Force sensors based on piezoresistive and MOSFET cantilevers for biomolecular sensing

Thesis presented to apply for the degree of Doctor in Electronic Engineering at the Department of Electronic Engineering of Universitat Autònòma de Barcelona

by,
Giordano Tosolini
Instituto de Microelectrónica de Barcelona
Centro Nacional de Microelectrónica
IMB-CNM (CSIC)

Joan Bausells Roigé
(Advisor and University Tutor)
Research Professor
Instituto de Microelectrónica de Barcelona
Centro Nacional de Microelectrónica
IMB-CNM (CSIC)
and
Associate Professor
Universitat Autònoma de Barcelona
UAB

September 2013

Joan Bausells, Research Professor at the *Instituto de Microelectrónica de Barcelona – Centro Nacional de Microelectrónica* (IMB-CNM, CSIC) and Associate Professor at the *Universitàt Autonoma de Barcelona* (UAB)

CERTIFIES:

That the thesis entitled "Force sensors based on piezoresistive and MOSFET cantilevers for biomolecular sensing" was carried out by Giordano Tosolini under his supervision within IMB-CNM.

Cerdanyola del Vallès, September 2013.

Prof. Joan Bausells

II

Abstract

Biorecognition processes between receptors and their conjugate ligands are very important in biology. These biomolecules can build up very specific complexes displaying a variety of functions such as genome replication and transcription, enzymatic activity, immune response, cellular signaling, etc. The unambiguous one-to-one complementarity exhibited by these biological partners is widely exploited also in biotechnology to develop biosensors for early-stage diagnostic applications in the environmental and biomedical fields. Depending on the nature of the transduction signals, biosensors can be classified in optical, electrical and mechanical.

Among mechanical biosensors, the microcantilevers play a prominent role. They have been used as stress or mass transducers in biomolecules detection for already more than a decade. The binding of molecules to their functionalized surface is detected by measuring either the deflection in static mode or the resonant frequency shift in dynamic mode. The deflection of the cantilever is converted optically by a laser and a photodetector in order to have the highest possible resolution. This limits the measurements in transparent liquids, the portability of the instrument and increases the complexity for multiplexing. The development of self-sensing cantilevers by integrating piezoresistors or metal-oxide-semiconductor field effect transistors (MOSFET) into the cantilever solves this issue. However, at the same time, this decreases the bending and frequency shift resolution due to the higher transducer noise.

On the other hand, the detection of a single molecule can be attained measuring the unbinding force between two molecules of a complex pulling them apart, using the atomic force spectroscopy (AFS) measuring approach. This technique is based on the atomic force microscope (AFM) and it has been used for more than 15 years. Despite the high force resolution, AFM has still not become an analytical instrument and it is mainly due to the complexity of the instrument and of its use. A biosensor based on AFS and on self-sensing cantilever would allow single molecule resolution, working in opaque fluids, easy multiplexing capability, and relatively easy integration in microfluidics cells.

In this perspective, and in view of the earlier work done in IMB-CNM on cantilever with piezoresistive deflection transduction, we worked to obtain self sensing-probes endowed with pN resolution and compatible with liquid media. Cantilevers based on single crystalline silicon have been modeled and the fabrication process has been optimized to improve the force sensitivity and to obtain high fabrication yield. At the same time we worked also on the modeling, development and fabrication of cantilevers with embedded MOSFET piezoresistive transducers. It turned out that the probes with integrated piezoresistor offer a more straightforward solution, but also the MOSFET cantilever can offer a good alternative.

Alongside the force sensors fabrication, new high-throughput set-ups and techniques have been developed and optimized to measure the electrical and electromechanical characteristics of micro-electro-mechanical systems (MEMS) in a precise and reliable way.

This was of key importance to correctly validate the new technological processes involved in production as well as characterize the final devices.

After achieving very good sensor performances (resolution < 10 pN in liquid environment) with high production yield, we used the force probes to investigate the biorecognition processes in the avidin-biotin complex. For this purpose we integrated the sensor into a commercial AFM to take advantage of the high mechanical stability of this equipment and the highly reliable displacement of the piezo actuator. We detected the forces related to the avidin-biotin complex formation, highlighting the possibility of biomolecule label-free recognition in nearly physiological conditions and at single molecule resolution. Beside the very high sensitivity attained, the sensor can be used with no restrictions in opaque media; it can be easily integrated in microfluidic cells and it displays a high multiplexing potentiality. This result opens new perspectives in highly sensitive label free biomarkers detectors in nearly physiological conditions.

Acknowledgments

Many people contributed to this thesis with their help, work, advices and support and I would like to acknowledge them all.

First of all, I would like to express my gratitude to my thesis director Prof. Joan Bausells, for giving me the opportunity to join the nanofabrication group and CNM, and to introduce me in the MEMS world. I appreciate, above all, the confidence he had in me and the freedom he gave me during these years.

I would like to thank Prof. Francesc Perez to introduce me to AFM, for helping me in the AFM characterization, in the development of new characterizations set ups and for all the useful discussions.

I would like to acknowledge the Prof. Salvatore Cannistraro for giving me the opportunity to work in his lab where we set up the biomolecular experiments, especially because of his enthusiasm and many ideas he had, since the first time he read my e-mail. Thanks also for teaching me to speak Italian again!

Even though I met Guillermo just 3 times, he helped me much at the beginning of the thesis explaining me all the practical things to start and telling me where he had hidden the "treasure box". His help didn't stop then, but continued also during these years with many advices. Thank you.

I would like to give a special thank to Prof. Jaume Esteve, Prof. Gabriel Gomila, Prof. Salvatore Cannistraro, Prof. Ramon Alcubilla and Prof. Nuria Barniol for accepting the invitation to be my thesis committee.

The device fabrication, modification and characterization wouldn't have been possible without the knowledge, suggestions and work of all the member of the ICTS crew! Carles, Roser, Mari and Carmen worked hard on dry etching and Marcos, Elena and Antonio on wet etchings; Erica, Josep Maria, Isabel and Julia, worked much on photolithography; Marta&Marta togheter with Nuria helped me with all non-standard etchings and other non standard fabrication experiments. Emilio, Miguel and Oihane took care of the wafers in the furnaces and in CVD and Josep, José and Sergio deposited all the metals on top of them. Jordi, Liber and Xevi showed me and thought me how to use the nano-equipments and to "cut and watch" the samples. Nieves organized all the RUNs and Javi did a bit of everything. Special thanks to the cleanroon bosses Ana and Miguel to give me priority to finish the RUN on-time for bio-experiments and to Javi and Josep to correct the errors in the RUNs. Finally to the encapsulation participated: Joan Puertas, Alberto and Maria. But the ICTS is also the SIAM: thanks to Sergi that explained me how to perform the electrical measurements.

Many thanks also to the "taller mecanico-mantenimiento" group to fabricate all the pieces I needed in the set ups and to take care of the cleanroom equipments.

Contents

VIII

x

Chapter I

Introduction

Introduction

This thesis will present the development, characterization and application of a force sensor based on silicon cantilever with an embedded piezoresistive transducer, for liquid environment, with sub-10 pN resolution, to be used as biomolecule detector.

In this chapter we will highlight the general objectives and motivations of the thesis and afterwards we will introduce the general concepts that have guided the development of the probe. We will point out the functions and the mechanical properties of the biomolecules, we will give some examples of cantilever-based biosensors and specifically we will present the atomic force spectroscopy technique applied in biomolecule recognition. Once we have pointed out the sensor requirements, we will review prior piezoresistive cantilever-based sensors and we will outline the reminder of the thesis.

1.1 – Aims and motivations of the thesis

The main objective of this thesis was to develop a highly sensitive force sensor (or biosensor) for liquid environment and to apply it as label-free detector of biomolecules.

Why develop a new sensor if there are many different techniques already commercially available and with very high sensitivity? Recently, the advances in micro and nanofabrication technologies have enabled the development of new highly sensitive platforms that can meet the new needs of the modern medical diagnosis. The diagnostic laboratories tend to be more specialized and centralized. They can process millions of samples in one year and they resemble more a factory assembly line. They have very expensive equipments (e.g. mass-spectroscopy, HPLC, SPR) for high throughput analysis with cost effective automation, quality assurance processes and very skilled personnel. At the same time, the decentralization of the laboratory test has gained much importance [1]. This test can be performed in small labs, at the clinic bedside, or even by the patients themselves at their home. This process is called "*near patient testing*" (NPT) or "*point of care testing*" (POC). A fundamental advantage of the NPT is the relative immediacy of the results. In NPT, the "total testing cycle" time is strongly reduced. The testing cycle is a loop starting with a request of a clinical test, which leads to the collecting of the sample and its arrival to the centralized diagnostic lab. After the analysis is performed, the results have to be sent back to the doctor and the patient. NPT allows shortening a lot the turnaround time mainly by shortening the pre- and post-analytical steps, which are the most time consuming. This leads to a faster diagnosis and therapeutic decision by the doctors, and reduces the waiting period of the patient, with clear advantages for his health. Moreover, the reduced testing time is of fundamental importance in some critical cases like emergencies or accidents.

Another very important need of the modern medicine is to move from a "general medicine" to a "*personal medicine*" [2]. This concept involves the prescription of a specific

treatment and medicine best suited for an individual, considering all the factors that influence the response to the therapy. In this perspective, the micro- and nano-fabrication offer big potential advantages to a personalized molecular diagnostics, which deals with the diagnosis and the monitoring of human diseases and is a part of the personal medicine [3-5]. It can offer new, very small and cheap diagnostics platforms for high-throughput, multiplexed detection of pM-level concentration of biomolecules. They can have thousand parallel sensors, each one properly functionalized to detect selectively a different molecule, at much higher density than it is achievable with current sensor array platforms, and can be massively produced. Their sensitivities are very high and they can approach single molecule resolution. Moreover this technology is also compatible with microfluidic systems, which allow a scale down of the whole analytical process resulting in faster and cheaper analysis [6]. Considering these aspects, they are very good candidates for early-stage diagnosis of diseases, which would allow more effective treatments. Among all the new microfabricated platforms, the cantilevers play an important role, as we will point out later on (paragraph 1.3).

1.2 – Functions of biomolecules

Biomolecule is any molecule that is produced by a living organism, including macromolecules like proteins, DNA, RNA as well as small molecules such as metabolites. Life relies on myriads of interactions between molecular components. Proteins in specific are a remarkable example. They are in charge of virtually every biological process in cells. Through specific recognition mechanisms, biomolecules can build reversible, or irreversible, complexes able to perform a variety of functions. These molecular interactions, or recognitions, are at the basis of the cell architecture, of genome replication and transcription, of signaling, of immune responses and can change the cell properties [7]. The ability of biomolecules to undergo these highly controlled processes is governed by molecular scale forces at pN levels (i.e ionic, hydrophobic, Van der Waals and hydrogen bonds).

A remarkable feature of living cells is their capacity to acquire different structural and functional capacity, whereas they share a common set of genes. Even though this differentiation mechanism is not fully understood, an extensive network of DNA and protein interactions clearly plays an important role [8]. Another fundamental property of cells is their adhesion, which influences almost all the steps of cell function. The survival and proliferation of a cell is very dependent on its ability to be strongly attached, or not, to a surface [9]. The aptitude of a cell to cope with various forms of aggression is also due to biorecognition processes. The key step for this, it is the adhesion of flowing leukocytes at the blood vessels walls and their transmigration into the infected tissues [10]. All these functions

are made possible by the presence of binding sites on their surface, called *receptors*, which interact only with specific molecules, the *ligands*.

The *immune system* of a living organism is also governed by the biological recognition of a wide variety of pathogenic agents. The task of immune cells consists of detecting a foreign and potentially harmful particle or molecule and to destroy it. The *antibodies* are molecules that are used by the immune system to identify and neutralize these foreign objects. Antibodies may be generated by the so-called *antigens*, which are the unique part of the foreign particle recognized by the antibodies. Disorders of the immune system can result in autoimmune diseases, inflammatory diseases and cancer [11, 12]. More in general, if a living organism has a certain disease, it produces the so-called *biomarkers*. They can be specific cells, molecules or genes, genes products, enzymes or hormones that can be used to measure the progress of the disease or the effect of a treatment.

As we saw with these examples, the biorecognition process between conjugate molecules, ligands and receptor, is very important for life. Because of this unambiguous one-to-one complementarity exhibited by these biological partners, the biorecognition is widely exploited also in biotechnology to develop *biosensors* for early-stage diagnostic applications in the environmental and biomedical field [13].

1.3 – Cantilever based biosensors

A *biosensor* is a device that combines a transducer with a biological sensitive layer [13]. The *biological sensitive element* (i.e. antibody, enzyme, protein or nucleic acid) interacts with the analyte under study while the *transducer* transforms the biological signal to a physical signal (i.e electrical) that can be more easily measured. As we saw in the previous paragraph 1.1, biosensors are gaining more and more importance in health science, clinical diagnostics and drug discovery but also in fundamental biological studies. Depending on the nature of the transduction, the biosensors can be classified in optical, electrical and mechanical sensors. Optical and electrical sensors are much more used in biological research than mechanical ones. This is mainly due to the fact that underlying technologies are mature and well established. On the other hand, the continuous improvements made in micro- and nanofabrication enables the development of more sensitive tools to sense and actuate on biological systems. The scale down of the tools dimensions led to outstanding mass resolution approaching single atom detection [14, 15]. Another consequence, of the scale down, is the reduction of the mechanical compliance of the devices, which is the ability of a structure to deflect under an applied load, and the enhancement of the force responsivity. We are now able to measure sub-10 pN forces, which are at the same order of magnitude of the rupturing of individual hydrogen bonds. This opens new opportunities in the study of inter- and intra-molecular forces that govern the life as pointed out in the previous paragraph 1.2.

The mechanical based biosensors [16-25] have a micro or nano-sized moving part, which in many cases is a cantilever. They can be batch fabricated and have arrays of hundreds sensitive transducers. They are mainly divided in two categories depending on the magnitude that they transform: *surface-stress* or *mass* (Figure 1.1). There is also a third category, in fact they can translate also *force*, but about this we will speak in the next paragraph 1.4. They can be classified also on the basis of the read-out method. The variation of the mechanical signals can be monitored by different techniques: *optical* or *electrical*. The deflection of a cantilever can be accurately measured by a laser beam focused on its surface and reflected into a position sensitive photodiode. This is the most common technique but some other methods are gaining importance. The integration of a deflection sensitive transducer, like a piezoresistor, into the structure is one of the most popular alternatives.

The *surface stress* sensitive devices measure the quasi-static deflection of the microcantilevers caused by the binding of the molecules to sensor surface. In fact, the adsorption of molecules onto a surface generates surface stress as a consequence of interactions between the molecules and the surface [26]. This technique has been used already to detect proteins [27], DNA [28, 29] and RNA [30]. The deflection is normally measured by the optical read out method, but the piezoresistive read out has also been used [31]. On the other hand, the molecules have also a certain *mass*, therefore if a sufficient number of them are bound on the cantilever, they can be easily detected due to the frequency shift of the resonance frequency of the beam. Cantilevers can have exquisite resolution when used in dynamic mode in vacuum or air, but this technique does not allow a continuous monitoring or fast detection. However, when the cantilevers are immersed in liquid, this becomes possible at expenses of the resolution. A proposed alternative is microfabricating a channel into the cantilever [32]. Such suspended microchannel resonators (SMR) allow continuous monitoring and in vacuum measurements with a very high quality factor, e.g. Q ~ 15000. Despite the high Q values attained, their performance is rather modest. A very promising alternative to the SMR is represented by the super-hydrophobic micropillars that allow wet functional surface and frequency shift detection in air with Q factors of about 1000 [33]. Even if chips with microcantilevers or nanocantilevers can be easily integrated in microfluidic cells, they have also some drawbacks. In order to have the highest possible resolution, the deflection of the cantilever is optically transduced. This limits the measurements in transparent liquids, the portability of the instrument and increases the complexity for multiplexing. The integration of a piezoresistor into the cantilever could be a solution but at the same time would decrease the resolution due to the higher transducer noise.

As pointed out above, cantilevers can detect also very small forces down to pN level. This is exactly the resolution needed to measure the unbinding forces between two conjugate molecules of a complex (i.e. avidin biotin [34]). This technique has been developed in 90s by Gaub [35, 36] and Hinterdorfer [37] and it is based on the atomic force microscope.
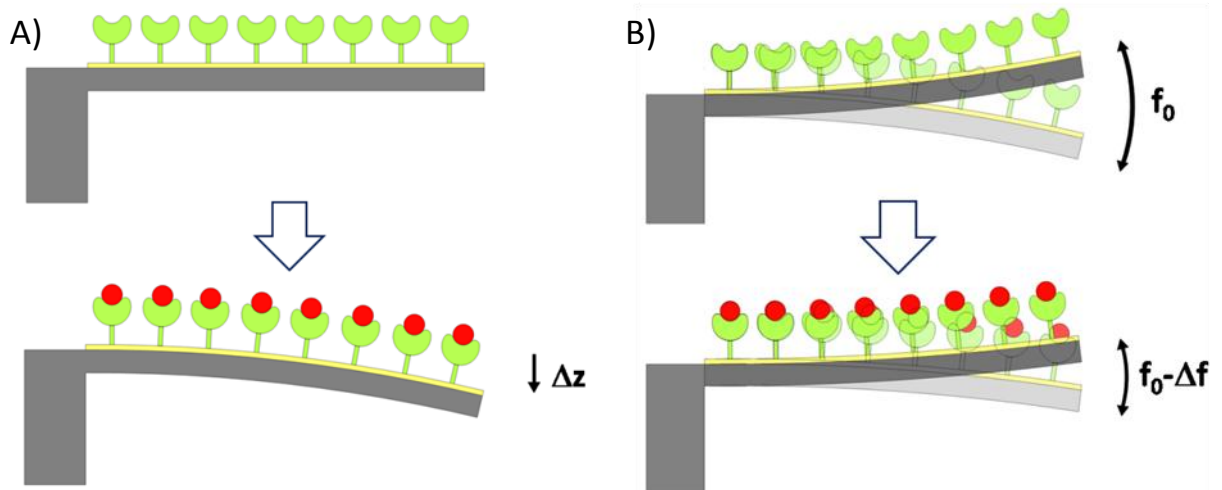
Figure 1.1. A) Cantilever as surface stress transducer: the ligands (red) attach to the receptors (green) provoke a bending in the cantilever (Δz) and a surface stress. B) Cantilever as mass transducer: after the binding of the ligands, the resonance frequency changes from f_0 to f_0-Δf.

1.4 – Atomic force spectroscopy in biomolecule recognition

The atomic force microscope (AFM) uses a microcantilever to measure the surface of a sample with nanometer precision. The cantilever, usually made of silicon or silicon nitride, has a sharp tip in its end with a radius of curvature of some nanometers. The cantilever or the sample is mounted on a piezoelectric actuator that allows positioning in the 3 dimensions with sub-nanometric resolution. When the tip is brought in close proximity to the sample surface, the interaction forces between the tip and the sample deflect the cantilever. The probe scans the sample to create an image of its surface. To measure the deflection of the cantilever, a laser is focused and reflected by the cantilever to a position sensitive photodiode [38]. Knowing the cantilever spring constant, k_C, the deflection, δ, can be converted into force by the Hooke's law:

$$F = k_C\delta \tag{1.1}$$

AFM has two main operating modes to create images: contact mode and dynamic mode. In the *contact mode*, or static mode, the tip is brought in contact to the samples with a certain force that is maintained during the raster scan. On the other hand, during the scanning in *dynamic mode,* the cantilever is oscillating near its resonant frequency with constant amplitude.

The AFM can be used also as a tool for measuring forces down to some pN [39], in the modality usually called *atomic force spectroscopy*, AFS [34, 40, 41]. In this mode, the tip is moved in the z vertical direction downwards and upwards with a constant speed and at a fixed location on the *x-y* plane (Figure 1.2). At the same time, the deflection of the cantilever

or the force actuating on the tip, are recorded as a function of *z* coordinate. The result is a force-distance (*F-z*) graph that is usually called *force curve*. This technique is therefore a perfect candidate to study the interaction between biomolecules undergoing a biorecognition process with high sensitivity, in physiological conditions and without labeling. For this purpose one molecular partner is bound to the apex of the AFM tip, while the other one is immobilized on a flat substrate (Figure 1.2). The functionalized tip is brought in contact with the substrate and the molecular complex may be formed. Afterwards, the tip is retracted from the substrate and when the cantilever restoring force overcomes the molecular interaction, the complex dissociation takes place and the tip jumps off sharply to a non-contact position. Such a jump-off process provides an estimation of the unbinding force. During AFS experiments hundreds or thousands *F-z* curves are recorded in a cyclic way, on different *x-y* positions and at different loading rates:

$$LR = \frac{dF}{dt} = k_c v \tag{1.2}$$

where *v* is the pulling speed. A representative force-distance is depicted in the Figure 1.2. Typical force distance curves for the avidin-biotin complex are reported in Figure 1.3. In the first graph (Figure 1.3.A) no unbinding event is visible since the retraction curve (red) follows faithfully the approach curve (green). The jump-off in Figure 1.3.B could be attributed to a non-specific adhesion between tip and sample, because the retraction curve has a constant slope. In Figure 1.3.C,D on the other hand, the slope of the curves changes during the retraction process. The cantilever is relaxed at the beginning but for further pulling the system becomes stretched. This behavior could be attributed to a specific biorecognition event.
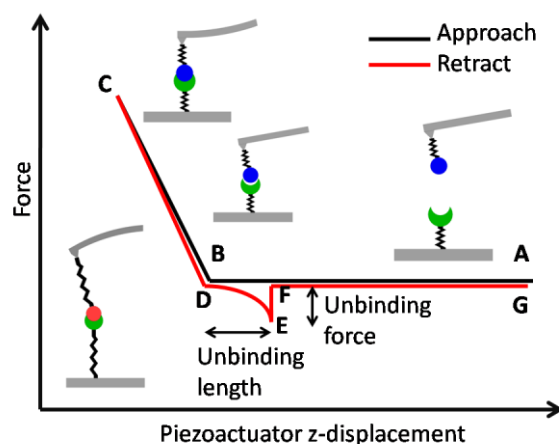
Figure 1.2. Schematic diagram of a typical AFS force curve representative of a specific unbinding event for a single bimolecular complex. At the beginning, point A, the cantilever has no deflection and it experiences null force. When the cantilever is moved towards the surface the two molecules start to interact (point B) and for further pushing, the cantilever is deflecting upwards due to repulsive forces. The approaching phase is stopped and the retraction can start. The bindings formed during the contact period, deflect the cantilever downwards (between point D and E). When the force applied by the cantilever overcomes the binding force, the cantilever jump off contact (point F).
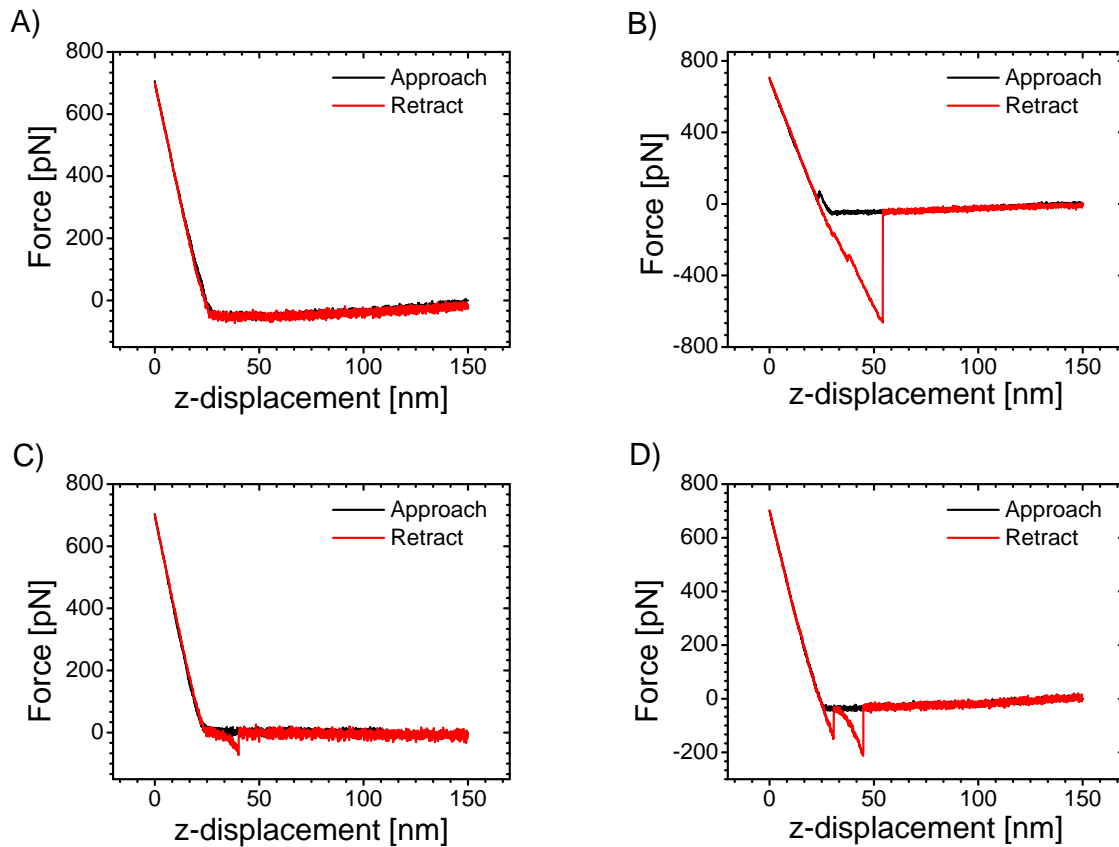
Figure 1.3 Typical AFS force curve for avidin-biotin complex. Approach curve in black and retract curve in red. A) No unbinding event. B) Non specific adhesion. C) Specific unbinding event related to the avidin-biotin complex. D) Adhesion plus specific unbinding event.
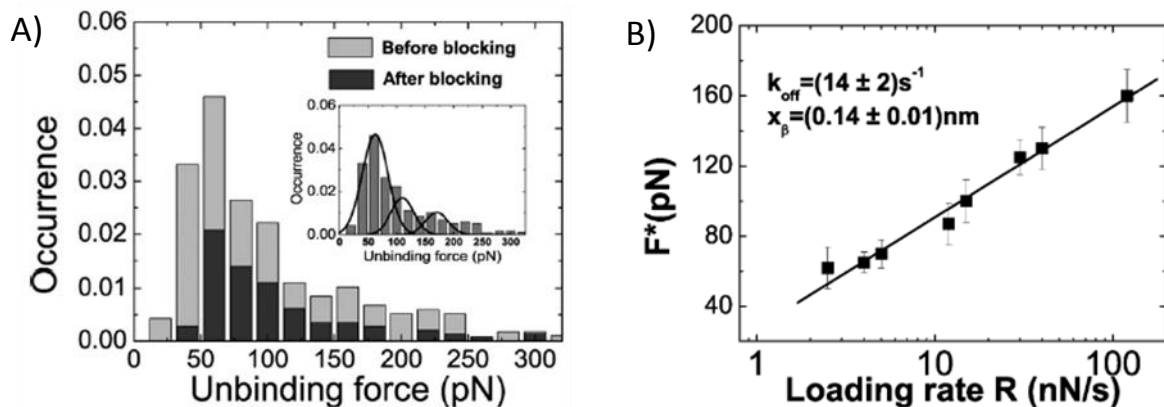
Figure 1.4. A) Example of unbinding force distribution at a fixed loading rate with Gaussian fitting to identify the most probable unbinding force value. B) Unbinding force at different loading rates. The data are fitted by the Bell-Evans model. Graphs extracted from [40].

The experiment is performed at different loading rates. After calculating the unbinding frequency (ratio between specific events and number of curves), the unbinding force distribution is plotted for each pulling speed (Figure 1.4.A). Afterwards, the unbinding force

is extracted from the distribution and plotted against the loading rate (Figure 1.4.B). Using the Bell-Evans model [40]:

$$F^* = \frac{k_B T}{x_\beta} \, ln \left(\frac{R x_\beta}{k_{off} k_B T} \right)$$

(1.3)

to fit the graph in Figure 1.4.B it is possible to extract information on the equilibrium properties of the molecular complex like its dissociation rate, k_{off}, at zero pulling force and the reaction coordinate corresponding to the separation between the bound and transition state , x_β (Figure 1.5).

Despite its very high force sensitivity, the AFM has still not become an analytical instrument for detecting single molecules in different specimens such as blood, tissues or cells. This is mainly due to the complexity of the instrument and of its use. Although the transduction optical system has very high resolution, down to Å level and few pN, it makes the AFM unfit to be used in the opaque fluids and introduces many laborious actions, which slow down considerably the detection process. Moreover the AFM can hardly be integrated into microfluidic cells and lacks in multiplexing and automation potentiality.
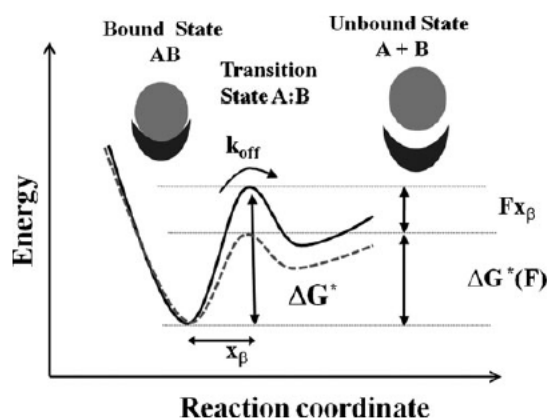
Figure 1.5. Energy diagram of a biomolecular complex. Upon an application of a force the energy state shift towards lower values (dashed line). Graphs extracted from [40].

1.5 – Sensor requirements

In this section we will discuss about the requirements of the new diagnostic tool and about the performance and design of the force probes, which is the principal part. The new diagnostic device should:

- Be for near patient testing or point of care testing. It should not require special sample preparation and offer fast response time.
- Be small in size
- Have high sensitivity and selectivity

- Have high reliability
- Multi-diagnosis (multiplexing) capability
- Be for liquid and opaque sample analysis
- Have no labeling need

As we saw in the previous sections, a very powerful method to detect a biomolecule is to detect the intermolecular force between the molecule under investigation and its conjugate molecule. This can offer much higher resolution than "traditional" methods like the detection of the surface stress or the detection of the molecules mass. As we pointed out before a candidate could be the AFM but has many intrinsic problems: it is unfit to be used with opaque fluids, necessitate of many laborious actions and it doesn't have multiplexing potentiality. A self-sensing cantilever, a cantilever with an integrated deflection transducer (i.e. a piezoresistor), could solve many problems that the AFM has. It wouldn't necessitate a laser and a photodetector and therefore it could work in opaque media. It would reduce laborious processes like the alignment of the laser and of the photodetector that slow down the analysis process. The chip could be integrated into a microfluidic system and therefore the functionalization of the surfaces would be faster and easier. It would have multiplexing potentiality because the chips could have arrays of hundreds of cantilevers.

On the other hand passing from an optical to and electrical read-out method can lead to a decrease in resolution and have problems in liquid environment. In this perspective, the probes have to be scaled down, especially in the thickness, to have a resolution similar to the one of the AFM (few pN) and all the conductive parts of the chip have to be electrically insulated. Moreover the probes should allow sensing frequencies up to 0.5-10 kHz. This means that their resonance frequency should be equal or higher than these values. In fact, typical AFS experiments are done at 0.1-1 seconds time scale, but the sampling frequency of the force acting on the cantilever tip is between 0.5 and 10 kHz. This frequency is needed to avoid the time average during the jump-off-contact.

1.6 – Piezoresistive cantilevers

In this chapter we aim to summarize the most relevant literature information about silicon cantilever with piezoresistive transduction (piezoresistor or MOSFET) that have been developed in the last two decades and have been used for different applications.

One of the first and perhaps the best know application, of a piezoresistive cantilever, has been the atomic force microscopy. Tortonese et al. in 1993 developed a p-doped piezoresistive silicon cantilever, integrated in a ¼ active Wheatstone bridge, obtaining atomic resolution images [42]. His best cantilever had a resolution of 0.1 Å (and 1 nN) in the bandwidth from 10 Hz to 1 kHz. In 1995 Linnemann et al. developed a cantilever with a complete Wheatstone bridge integrated into the cantilever. This solution allowed a

resolution of 0.2 Å (and 420 pN) in a bandwidth of 1 kHz. Su et al. in 1997 developed a cantilever with a triangular shape that achieved a resolution of 0.29 Å (and 100 pN)[43]. Brugger et al. developed an AFM cantilever for lateral force measurement [44] while Chui et al. made a dual axis cantilever using a sidewall implantation [45]. Hagleitner et al. fabricated, for the first time, an array of two cantilevers for parallel scanning [46]. Finally, Thaysen et. developed probes with highly symmetrical piezoresistive Wheatstone bridge for AFM purposes. They had a typical force sensitivity of 2.7×10^{-6} nN^{-1} and a noise of few μV considering a bandwidth of 1 kHz and bias voltage of 5V [47, 48]. This means a resolution of hundreds of pN in liquid environment.

Apart from these first works on AFM, many groups have developed different systems and applications based on cantilevers with integrated piezoresistors for force, displacement and surface-stress sensing. Piezoresistive cantilevers have been applied for torque magnetometry [44], materials characterization [49-51], data storage applications [52, 53] and to develop environmental [54], chemical [55] and biological [31, 56-60] sensors. Aeschimann et al. [61] developed a scanning probe array for liquid environment with a resolution of 160 pN, isolating the piezoresistor by 50 nm of silicon nitride and all the other conductors by 1 μm hard baked photoresist. Afterwards, Polesel-Maris et al. [62] used it to perform images and nanomechanical characterization of biological cells.

Regarding the cantilever optimization for force sensing, an impressive work has been done by Harley in the late 90s [63, 64] and recently by Doll [65, 66]. Harley attained a resolution of 0.5 pN in air, for a 10 Hz-1kHz bandwidth, with sub-100 nm thick cantilevers in which the doping atoms were confined on the surface using epitaxial growth [63]. Unfortunately these cantilevers were not electrically insulated and therefore were unfit to be used in liquid. Doll et al. in 2012 achieved sub-10 pN resolution in air and 12 pN resolution in liquid, for a wider bandwidth [66]. He used 200 nm of chemical vapor deposited parylene to insulate the conductors and the cantilevers.

At the Barcelona Microelectronics Institute (IMB-CNM-CSIC), Villanueva et al. made an impressive work about force sensors based on piezoresistive cantilevers made of doped polycrystalline silicon [67], between 2002 and 2005 in the scope of the Biofinger EU-project (IST 2001-20544). The goal of this project was the development and the testing of versatile, inexpensive, and easy-to-use diagnostic tools for health, environmental and other applications based on the measurement of molecular interactions by self-sensing nano-cantilever sensors. The cantilever had to act as a nano-"fishing tool" for molecules in a similar way like in the single molecule AFS. A requirement of the project was a complete compatibility with CMOS fabrication of the cantilevers, and for this reason the technology for the fabrication of submicron thick cantilever made of polycrystalline silicon was successfully developed. The monolithic integration of the cantilever and the amplifying circuit in the same chip allowed a resolution of 50 pN [68, 69]. However, this solution is an unnecessary complication if a high volume production is not required. In this perspective, in 2006, force sensors based on crystalline silicon cantilever were developed in the scope of

Spanish national projects. Due to the higher piezoresistive coefficient of the crystalline silicon, the sensor achieved a resolution of 65 pN with no amplification [70]. It has to be pointed out that these resolutions were measured in air.

The integration of a transistor into a cantilever is relatively a newer idea and it has been less exploited. Also in this case, one of the first applications has been the AFM. Akiyama et al. in 1998 developed a cantilever with an embedded p-MOSFET transistor for scanning force microscopy application [71]. Two years later, he integrated in the same chip an array of two self-sensing and thermally actuated cantilevers and the amplifying circuit [72]. In 2006 Shekhawat et al. developed a biomolecular sensor based on n-MOSFET-embedded microcantilevers [73]. He successfully detected low concentrations of avidin and goat antibody molecules and the results indicated that the sensitivity was comparable to the traditional optical transduction. Tark in 2009 [74] and Singh in 2011 [75], explored different p- and n-MOSFET cantilever designs. In the same years, Wang developed a sensor for observing the kinetics of chemical molecule interaction based on n-MOSFET cantilever [76, 77].

1.7 – Thesis outline

The following chapters are organized as follows:

- **Chapter 2 – Theoretical background**. In this chapter, the fundamentals of the linear elasticity theory, of the piezoresistive effect and of the noise in the electronic devices are discussed. These theories are at the basis of the analytical model of the piezoresistive cantilever.

- **Chapter 3 – Piezoresistive cantilever**. The electromechanical model that we used to optimize the resolution of the force sensor is presented. The mask design, the process fabrication and the fabrication issues of the piezoresistive force probes are also discussed. Afterwards, the development of new on-wafer characterization set-ups and techniques, fundamental for reliable and fast measurements, will be described. Finally, the mechanical, electrical and electromechanical performance of the different force probes will be reported.

- **Chapter 4 – MOSFET cantilever**. We will present the model, the mask design, the fabrication process and the characterization of the second option of force sensor: a cantilever with integrated a piezosensitive MOSFET.

- **Chapter 5 – Biomolecule recognition**. In order to perform biomolecule recognition experiments, we integrated the piezoresistive sensor into a commercial AFM to take advantage of the high stability of this equipment and highly reliable displacement of the piezo-actuator. In this chapter we will discuss the mechanical and electrical integration of the sensor into the AFM. The system

achieved a 10-pN resolution, which allowed us to detect biorecognition specific events underlying the biotin-avidin complex formation.

- **Chapter 6 – Summary**. We will highlight the most important results of the work and give suggestions for future research directions

References

1. Crook, M.A., *Near patient testing and pathology in the new millennium.* Journal of clinical pathology, 2000. **53**(1): p. 27-30.
2. Jain, K.K., *Nanobiotechnology and personalized medicine*, in *The Handbook of Nanomedicine*2012, Springer. p. 451-454.
3. Cheng, M.M.C., et al., *Nanotechnologies for biomolecular detection and medical diagnostics.* Current Opinion in Chemical Biology, 2006. **10**(1): p. 11-19.
4. Ferrari, M., *Cancer nanotechnology: Opportunities and challenges.* Nature Reviews Cancer, 2005. **5**(3): p. 161-171.
5. Ferrari, M. and A.P. Lee, *BioMEMS and biomedical nanotechnology*. Vol. 21. 2006: Springer.
6. Craighead, H., *Future lab-on-a-chip technologies for interrogating individual molecules.* Nature, 2006. **442**(7101): p. 387-393.
7. Wilchek, M., E.A. Bayer, and O. Livnah, *Essentials of biorecognition: the (strept) avidin-biotin system as a model for protein-protein and protein-ligand interaction.* Immunology letters, 2006. **103**(1): p. 27-32.
8. Badis, G., et al., *Diversity and complexity in DNA recognition by transcription factors.* Science, 2009. **324**(5935): p. 1720-1723.
9. Baszkin, A. and W. Norde, *Physical chemistry of biological interfaces*1999: CRC Press.
10. Lawrence, M.B. and T.A. Springer, *Leukocytes roll on a selectin at physiologic flow rates: distinction from and prerequisite for adhesion through integrins.* Cell, 1991. **65**(5): p. 859-873.
11. Coussens, L.M. and Z. Werb, *Inflammatory Cells and Cancer Think Different!* The Journal of experimental medicine, 2001. **193**(6): p. F23-F26.
12. O'Byrne, K.J. and A.G. Dalgleish, *Chronic immune activation and inflammation as the cause of malignancy.* British Journal of Cancer, 2001. **85**(4): p. 473.
13. Turner, A.P.F., *Biosensors: sense and sensibility.* Chemical Society Reviews, 2013. **42**(8): p. 3184-3196.
14. Yang, Y.T., et al., *Zeptogram-scale nanomechanical mass sensing.* Nano Letters, 2006. **6**(4): p. 583-586.
15. Lassagne, B., et al., *Ultrasensitive mass sensing with a nanotube electromechanical resonator.* Nano Letters, 2008. **8**(11): p. 3735-3738.
16. Arlett, J.L., E.B. Myers, and M.L. Roukes, *Comparative advantages of mechanical biosensors.* Nature Nanotechnology, 2011. **6**(4): p. 203-215.
17. Boisen, A. and T. Thundat, *Design & fabrication of cantilever array biosensors.* Materials Today, 2009. **12**(9): p. 32-38.
18. Boisen, A., et al., *Cantilever-like micromechanical sensors.* Reports on Progress in Physics, 2011. **74**(3): p. 036101.
19. Datar, R., et al., *Cantilever sensors: nanomechanical tools for diagnostics.* Mrs Bulletin, 2009. **34**(06): p. 449-454.
20. Fritz, J.r., *Cantilever biosensors.* Analyst, 2008. **133**(7): p. 855-863.
21. Raiteri, R., et al., *Micromechanical cantilever-based biosensors.* Sensors and Actuators, B: Chemical, 2001. **79**(2-3): p. 115-126.

22. Waggoner, P.S. and H.G. Craighead, *Micro- and nanomechanical sensors for environmental, chemical, and biological detection.* Lab on a Chip, 2007. **7**(10): p. 1238-1255.
23. Hansen, K.M. and T. Thundat, *Microcantilever biosensors.* Methods, 2005. **37**(1): p. 57-64.
24. Goeders, K.M., J.S. Colton, and L.A. Bottomley, *Microcantilevers: sensing chemical interactions via mechanical motion.* Chemical reviews, 2008. **108**(2): p. 522.
25. Tamayo, J., et al., *Biosensors based on nanomechanical systems.* Chemical Society Reviews, 2013. **42**(3): p. 1287-1311.
26. Godin, M., et al., *Cantilever-based sensing: the origin of surface stress and optimization strategies.* Nanotechnology, 2010. **21**(7): p. 075501.
27. Backmann, N., et al., *A label-free immunosensor array using single-chain antibody fragments.* Proceedings of the National Academy of Sciences of the United States of America, 2005. **102**(41): p. 14587-14592.
28. Wu, G., et al., *Bioassay of prostate-specific antigen (PSA) using microcantilevers.* Nature biotechnology, 2001. **19**(9): p. 856-860.
29. Mertens, J., et al., *Label-free detection of DNA hybridization based on hydration-induced tension in nucleic acid films.* Nature Nanotechnology, 2008. **3**(5): p. 301-307.
30. Zhang, J., et al., *Rapid and label-free nanomechanical detection of biomarker transcripts in human RNA.* Nature Nanotechnology, 2006. **1**(3): p. 214-220.
31. Rasmussen, P.A., et al., *Optimised cantilever biosensor with piezoresistive read-out.* Ultramicroscopy, 2003. **97**(1-4): p. 371-376.
32. Burg, T.P., et al., *Weighing of biomolecules, single cells and single nanoparticles in fluid.* Nature, 2007. **446**(7139): p. 1066-1069.
33. Melli, M., G. Scoles, and M. Lazzarino, *Fast Detection of Biomolecules in Diffusion-Limited Regime Using Micromechanical Pillars.* ACS nano, 2011. **5**(10): p. 7928-7935.
34. Bizzarri, A.R., Cannistraro, S., *Dynamic Force Spectroscopy and Biomolecular Recognition*2012: CRC Press, Boca Raton.
35. Florin, E.L., V.T. Moy, and H.E. Gaub, *Adhesion forces between individual ligand-receptor pairs.* Science, 1994. **264**(5157): p. 415-417.
36. Moy, V.T., E.-L. Florin, and H.E. Gaub, *Intermolecular forces and energies between ligands and receptors.* Science, 1994: p. 257-257.
37. Hinterdorfer, P., et al., *Detection and localization of individual antibody-antigen recognition events by atomic force microscopy.* Proceedings of the National Academy of Sciences of the United States of America, 1996. **93**(8): p. 3477-3481.
38. Meyer, G. and N.M. Amer, *Novel optical approach to atomic force microscopy.* Applied Physics Letters, 1988. **53**(12): p. 1045-1047.
39. Junker, J.P., F. Ziegler, and M. Rief, *Ligand-Dependent Equilibrium Fluctuations of Single Calmodulin Molecules.* Science, 2009. **323**(5914): p. 633-637.
40. Bizzarri, A.R. and S. Cannistraro, *The application of atomic force spectroscopy to the study of biological complexes undergoing a biorecognition process.* Chemical Society Reviews, 2010. **39**(2): p. 734-749.
41. Hinterdorfer, P. and Y.F. Dufrene, *Detection and localization of single molecular recognition events using atomic force microscopy.* Nature Methods, 2006. **3**(5): p. 347-355.

42. Tortonese, M., R.C. Barrett, and C.F. Quate, *Atomic resolution with an atomic force microscope using piezoresistive detection.* Applied Physics Letters, 1993. **62**(8): p. 834-836.

43. Su, Y., et al., *Fabrication of improved piezoresistive silicon cantilever probes for the atomic force microscope.* Sensors and Actuators A: Physical, 1997. **60**(1-3): p. 163-167.

44. Brugger, J., et al., *Microfabricated ultrasensitive piezoresistive cantilevers for torque magnetometry.* Sensors and Actuators A: Physical, 1999. **73**(3): p. 235-242.

45. Chui, B.W., et al., *Independent detection of vertical and lateral forces with a sidewall-implanted dual-axis piezoresistive cantilever.* Applied Physics Letters, 1998. **72**(11): p. 1388-1390.

46. Hagleitner, C., et al. *On-chip circuitry for a CMOS parallel scanning AFM*. in *1999 Symposium on Smart Structures and Materials*. 1999. International Society for Optics and Photonics.

47. Jacob, T., *Cantilever for bio-chemical sensing integrated in a microliquid handling system*, 2001, Technical University of Denmark.

48. Thaysen, J., et al., *Atomic force microscopy probe with piezoresistive read-out and a highly symmetrical Wheatstone bridge arrangement.* Sensors and Actuators A: Physical, 2000. **83**(1-3): p. 47-53.

49. Pruitt, B.L. and T.W. Kenny, *Piezoresistive cantilevers and measurement system for characterizing low force electrical contacts.* Sensors and Actuators A: Physical, 2003. **104**(1): p. 68-77.

50. Seel, S.C. and C.V. Thompson, *Piezoresistive microcantilevers for in situ stress measurements during thin film deposition.* Review of scientific instruments, 2005. **76**(7): p. 075103-075103-8.

51. Peiner, E., M. Balke, and L. Doering, *Form measurement inside fuel injector nozzle spray holes.* Microelectronic Engineering, 2009. **86**(4-6): p. 984-986.

52. Chui, B.W., et al., *Low-stiffness silicon cantilevers with integrated heaters and piezoresistive sensors for high-density AFM thermomechanical data storage.* Microelectromechanical Systems, Journal of, 1998. **7**(1): p. 69-78.

53. Ried, R.P., et al., *6-mhz 2-N/m piezoresistive atomic-force microscope cantilevers with incisive tips.* Microelectromechanical Systems, Journal of, 1997. **6**(4): p. 294-302.

54. Boisen, A., et al., *Environmental sensors based on micromachined cantilevers with integrated read-out.* Ultramicroscopy, 2000. **82**(1-4): p. 11-16.

55. Jensenius, H., et al., *A microcantilever-based alcohol vapor sensor-application and response model.* Applied Physics Letters, 2000. **76**(18): p. 2615-2617.

56. Baselt, D.R., et al., *A high-sensitivity micromachined biosensor.* Proceedings of the IEEE, 1997. **85**(4): p. 672-679.

57. Marie, R., et al., *Adsorption kinetics and mechanical properties of thiol-modified DNA-oligos on gold investigated by microcantilever sensors.* Ultramicroscopy, 2002. **91**(1-4): p. 29-36.

58. Yang, M., et al., *High sensitivity piezoresistive cantilever design and optimization for analyte-receptor binding.* Journal of Micromechanics and Microengineering, 2003. **13**(6): p. 864.

59. Wee, K.W., et al., *Novel electrical detection of label-free disease marker proteins using piezoresistive self-sensing micro-cantilevers.* Biosensors and Bioelectronics, 2005. **20**(10): p. 1932-1938.

60. Na, K.-H., Y.-S. Kim, and C.J. Kang, *Fabrication of piezoresistive microcantilever using surface micromachining technique for biosensors.* Ultramicroscopy, 2005. **105**(1): p. 223-227.

61. Aeschimann, L., et al., *Scanning probe arrays for life sciences and nanobiology applications.* Microelectronic Engineering, 2006. **83**(4-9): p. 1698-1701.

62. Polesel-Maris, J., et al., *Piezoresistive cantilever array for life sciences applications*, in *Proceedings of the International Conference on Nanoscience and Technology*2007. p. 955-959.

63. Harley, J.A. and T.W. Kenny, *High-sensitivity piezoresistive cantilevers under 1000 Å thick.* Applied Physics Letters, 1999. **75**(2): p. 289-291.

64. Harley, J.A., *Advances in Piezoresistive Probes for Atomic Force Microscope*, 2000, Stanford University.

65. Doll, J.C., *Advances in high bandwidth nanomechanical force sensors with integrated actuation*, 2012, Stanford University.

66. Doll, J.C. and B.L. Pruitt, *High-bandwidth piezoresistive force probes with integrated thermal actuation.* Journal of Micromechanics and Microengineering, 2012. **22**(9): p. 095012.

67. Villanueva, L.G., *Development of Cantilevers for Biomolecular Measurements*, 2006, Universitat Autonoma de Barcelona.

68. Villanueva, G., et al., *Piezoresistive cantilevers in a commercial CMOS technology for intermolecular force detection.* Microelectronic Engineering, 2006. **83**(4-9): p. 1302-1305.

69. Villanueva, G., et al., *Submicron piezoresistive cantilevers in a CMOS-compatible technology for intermolecular force detection.* Microelectronic Engineering, 2004. **73-4**: p. 480-486.

70. Villanueva, G., et al., *Crystalline silicon cantilevers for piezoresistive detection of biomolecular forces.* Microelectronic Engineering, 2008. **85**(5-6): p. 1120-1123.

71. Akiyama, T., et al., *Characterization of an integrated force sensor based on a MOS transistor for applications in scanning force microscopy.* Sensors and Actuators A: Physical, 1998. **64**(1): p. 1-6.

72. Akiyama, T., et al., *Integrated atomic force microscopy array probe with metal-oxide-semiconductor field effect transistor stress sensor, thermal bimorph actuator, and on-chip complementary metal-oxide-semiconductor electronics.* Journal of Vacuum Science & Technology B, 2000. **18**(6): p. 2669-2675.

73. Shekhawat, G., S.H. Tark, and V.P. Dravid, *MOSFET-embedded microcantilevers for measuring deflection in biomolecular sensors.* Science, 2006. **311**(5767): p. 1592-1595.

74. Tark, S.-H., et al., *Nanomechanoelectronic signal transduction scheme with metal-oxide-semiconductor field-effect transistor-embedded microcantilevers.* Applied Physics Letters, 2009. **94**(10): p. 104101-104101-3.

75. Singh, P., et al., *Microcantilever sensors with embedded piezoresistive transistor read-out: Design and characterization.* Sensors and Actuators A: Physical, 2011. **171**(2): p. 178-185.

76. Wang, J., et al., *100 n-type metal-oxide-semiconductor field-effect transistor-embedded microcantilever sensor for observing the kinetics of chemical molecules interaction.* Applied Physics Letters, 2009. **95**: p. 124101.

77. Wang, J., et al., *Chemisorption sensing and analysis using silicon cantilever sensor based on n-type metal–oxide–semiconductor transistor.* Microelectronic Engineering, 2011. **88**(6): p. 1019-1023.

Chapter II

Theoretical background

Theoretical background

In this chapter we will discuss the fundamentals of the linear elasticity theory especially in the case of the cantilever beam (section 2.1). We will report also about the piezoresistive effect in silicon for piezoresistors and MOSFET cases (section 2.2). In the third section (section 2.3) the noise in the electronic devices will be introduced. These theories are at the basis of the analytical model of the piezoresistive cantilever (chapter 3).

2.1 – Cantilever mechanics

2.1.1 – Mechanics of materials

Some basic concepts and definition about theory of the linear elasticity of the materials will be here briefly reminded. More detailed treatises can be found in [1-3].

Let's remind as first the concepts of *stress*, σ, and *strain*, ε, using a very simple example. If a cylindrical bar is subjected to a direct pull or push along its axis as shown Figure 2.1 then it is said to be subjected to tension (*σ>0*) or compression (*σ<0*) and it suffers elongation (*ε>0*) or shortening (*ε<0*), respectively.

The stress is defined as the total force, *F*, actuating on the bar divided by the cross sectional area, *A*, while the strain is defined as the change in length, *δL*, divided by the original length, *L*. A material is said to be elastic if it returns to its original, unloaded dimensions, when the load is removed. A particular form of elasticity which applies to a large range of materials, at least over part of their load range, produces deformations, and strains, which are proportional to the loads, and stresses. This proportionality is described by the Hooke's law and the coefficient of proportionality is the Young's modulus, E (or modulus of elasticity):

$$\sigma = E\varepsilon$$

(2.1)

We can speak therefore about linear elasticity and this is true for small displacements. Moreover a material which has a uniform structure throughout without any flaws or discontinuities is termed a homogenous material. Inhomogeneous materials have mechanical characteristics that vary from point to point. If a material exhibits uniform properties throughout in all directions it is said to be isotropic, conversely one which does not exhibit this uniform behavior is said to be anisotropic. Just to fix the ideas the crystalline silicon is homogeneous and anisotropic.

Let's now consider a general three dimensional case: an infinitesimal cube of material subjected to a general load condition (Figure 2.2).
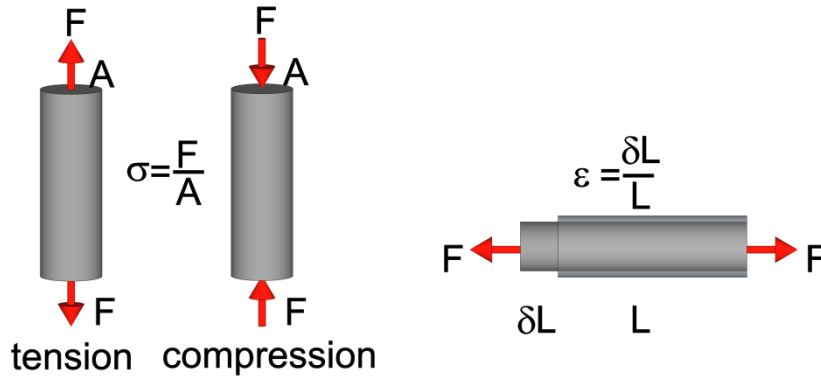
Figure 2.1. On the left: bar, with a cross-section A, subjected to tension and compression by a force F. On the right: bar subjected to tension showing the deformation, δL, and unloaded bar with original length, L.
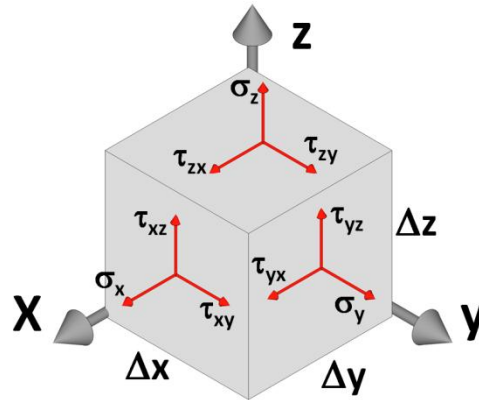
Figure 2.2. Infinitesimal cube of material under stress and fully described by normal (σ) and shear (τ) stresses.

In this case the stressed material is fully described by the *stress matrix*:

$$\bar{\bar{\sigma}} = \begin{bmatrix} \sigma_{xx} & \tau_{xy} & \tau_{xz} \\ \tau_{yx} & \sigma_{yy} & \tau_{yz} \\ \tau_{zx} & \tau_{zy} & \sigma_{zz} \end{bmatrix} \qquad (2.2)$$

The first position of the sub index refers to the surface normal upon which the stress acts and the second one refers to the direction of the stress component. Therefore σ_{xx} (written also σ_x) is the normal stress on the surface with the normal x acting in x direction while τ_{xy} (or σ_{xy}) is the shear stress acting on the surface with the normal x in the y direction and, by the way, it is possible to demonstrate that $\tau_{xy} = \tau_{yx}$, having a symmetric matrix. These stresses provoke related displacements and therefore strain is fully described by the strain matrix:

$$\bar{\bar{\varepsilon}} = \begin{bmatrix} \varepsilon_{xx} & \varepsilon_{xy} & \varepsilon_{xz} \\ \varepsilon_{yx} & \varepsilon_{yy} & \varepsilon_{yz} \\ \varepsilon_{zx} & \varepsilon_{zy} & \varepsilon_{zz} \end{bmatrix} \qquad (2.3)$$

If we consider for one moment just the x direction, all the points in the x direction are deformed and described by a displacement *u* (Figure 2.3).
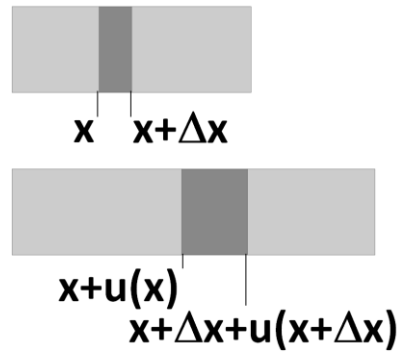
Figure 2.3. The displacement vector u(x,y,z) causes a deformation ε in x direction. The other two vectors v(x,y,z) and w(x,y,z) cause deformation in y and z directions respectively.

Therefore we can define the normal displacement ε_{xx} (written also ε_x) as:

$$\varepsilon_x = \frac{u(x + \Delta x) - u(x)}{\Delta x} = \frac{\partial u}{\partial x} \tag{2.4}$$

In general the displacement of one point P to P' in the body is described by one vector r with the 3 components u, v and w in the directions x, y and z respectively. The components u, v and w depend on the three coordinates:

$$u=u(x,y,z) \; ; \; v=v(x,y,z) \; ; \; w=w(x,y,z) \tag{2.5}$$

Now we can define the *shear strain*, ε_{xy} for example, as:

$$\varepsilon_{xy} = \frac{1}{2}\left(\frac{\partial v}{\partial x} + \frac{\partial u}{\partial y}\right) \tag{2.6}$$

And the *engineering shear strain*:

$$\gamma_{xy} = \frac{\partial v}{\partial x} + \frac{\partial u}{\partial y} \tag{2.7}$$

Also in this case it is possible to demonstrate that $\gamma_{xy}=\gamma_{yx}$ (symmetric matrix). Now, when the infinitesimal cube of material is stressed, let's say just in x direction, it presents a shrink in the other two direction y and z that are proportional to ε_x, if we are considering isotropic material:

$$\varepsilon_y = \varepsilon_z = \nu\varepsilon_x \tag{2.8}$$

ν is called Poisson's coefficient. Concluding, one infinitesimal cube of isotropic material under general load condition determines the following strain values:

$$\varepsilon_x = \frac{1}{E}\left(\sigma_x - \nu\left(\sigma_y + \sigma_z\right)\right) \; ; \; \gamma_{xy} = \frac{1}{G}\tau_{xy} \tag{2.9a}$$

$$\varepsilon_y = \frac{1}{E}\left(\sigma_y - \nu(\sigma_x + \sigma_z)\right) \; ; \; \gamma_{yz} = \frac{1}{G}\tau_{yz} \tag{2.9b}$$

$$\varepsilon_z = \frac{1}{E}\left(\sigma_z - \nu(\sigma_x + \sigma_y)\right) \; ; \; \gamma_{zx} = \frac{1}{G}\tau_{zx} \tag{2.9c}$$

Where G is the shear modulus:

$$G = \frac{E}{2(1+v)}$$

(2.10)

In the case of an anisotropic material the things are more complicated and for a general load case we must write:

$$\begin{bmatrix} \sigma_x \\ \sigma_y \\ \sigma_z \\ \tau_{yz} \\ \tau_{zx} \\ \tau_{xy} \end{bmatrix} = \begin{bmatrix} C_{11} & C_{12} & C_{13} & C_{14} & C_{15} & C_{16} \\ C_{12} & C_{22} & C_{23} & C_{24} & C_{25} & C_{26} \\ C_{13} & C_{23} & C_{33} & C_{34} & C_{35} & C_{36} \\ C_{14} & C_{24} & C_{34} & C_{44} & C_{45} & C_{46} \\ C_{15} & C_{25} & C_{35} & C_{45} & C_{55} & C_{56} \\ C_{16} & C_{26} & C_{36} & C_{46} & C_{56} & C_{66} \end{bmatrix} \begin{bmatrix} \varepsilon_x \\ \varepsilon_y \\ \varepsilon_z \\ \varepsilon_{yz} \\ \varepsilon_{zx} \\ \varepsilon_{xy} \end{bmatrix}$$

(2.11)

Or:

$$\sigma_i = \sum_j C_{ij} \varepsilon_j$$

(2.12)

And

$$\varepsilon_i = \sum_j S_{ij} \sigma_j$$

(2.13)

The stiffness matrix is traditionally represented by the symbol C, while S is reserved for the compliance matrix. This convention may seem backwards, but perception is not always reality. For cubic materials, like the silicon is, there are just three independent elastic constants:

$$C_{11} = C_{22} = C_{33}$$

(2.14a)

$$C_{12} = C_{23} = C_{31} = C_{21} = C_{32} = C_{13}$$

(2.14b)

$$C_{44} = C_{55} = C_{66}$$

(2.14c)

And all the other constants are zero. Therefore the stiffness matrix becomes:

$$\bar{\bar{C}} = \begin{bmatrix} C_{11} & C_{12} & C_{12} & 0 & 0 & 0 \\ C_{12} & C_{11} & C_{12} & 0 & 0 & 0 \\ C_{12} & C_{12} & C_{11} & 0 & 0 & 0 \\ 0 & 0 & 0 & C_{44} & 0 & 0 \\ 0 & 0 & 0 & 0 & C_{44} & 0 \\ 0 & 0 & 0 & 0 & 0 & C_{44} \end{bmatrix}$$

(2.15)

In the case of the silicon on the plane (100) the three constants are C_{11}=166 GPa, C_{12}=64 Gpa and C_{44}=80 Gpa [4]. From these values it is possible to calculate the Young's modulus, Poisson's ratio and shear modulus for different crystalline directions (Table 2.1, Figure 2.4):

Direction	Expression	Value [Gpa]
[100]	$C_{11} - 2\dfrac{C_{12}^2}{C_{11} + C_{12}}$	130
[110]	$4\dfrac{(C_{11}^2 + C_{12}C_{11} - C_{12}^2)C_{44}}{2C_{44}C_{11} + C_{11}^2 + C_{12}C_{11} + 2C_{12}^2}$	170
[111]	$3\dfrac{(C_{12} + 2C_{11})C_{44}}{C_{11} + 2C_{12} + C_{44}}$	189

Table 2.1. Young's moduli expressions for the most common silicon crystallographic directions.
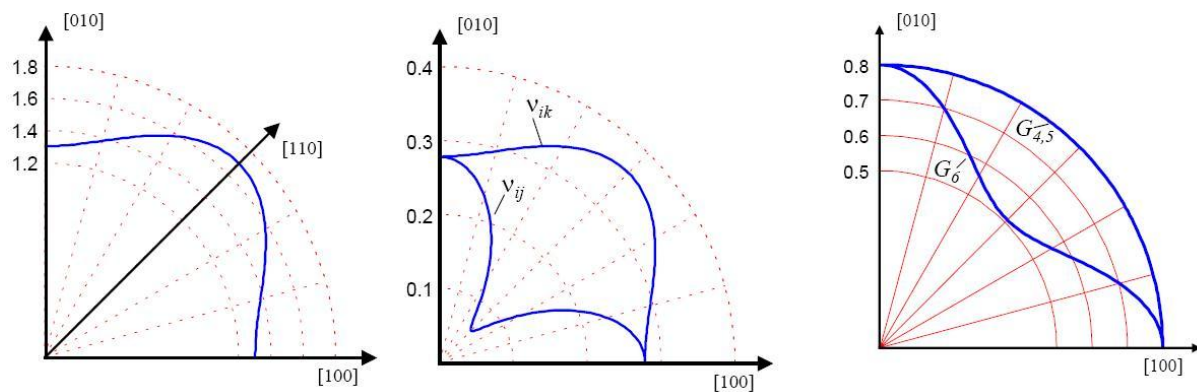
Figure 2.4. Young's modulus (x10^{11} Pa) (left), Poisson's ratio (center) and shear modulus (x10^{11} Pa) (right) calculated values for silicon in the (100) plane. [4]

2.1.2 – Loading, support and bending moment

In order to introduce the basic concepts as loads, supports and bending moments let's consider the simplest mechanical element: the beam. The beam can be subjected (Figure 2.5) to *point forces, F* (ideally are forces that are applied on one infinitesimal point of the surface), *distributed load, Q* (pressure, weight) and *concentrated moments, M*.

The boundary conditions, which avoid the beam to translate or rotate, are called supports and there are basically three types (Figure 2.5): *fixed* or *clamped* (the beam can't translate or rotate), *pinned* (the beam can just rotate) and *pinned on rollers* (the beam can translate and rotate but it is fixed on the surface).

In equilibrium the beam do not translate neither rotate, therefore the sums of the forces and of the moments applied on the beam must be zero. Let's consider as example one beam with a fixed end: a cantilever beam (or simply cantilever). If it is at equilibrium, because of the point force, *F*, at the fixed end there must be a force reaction, *F$_R$*, and a moment reaction, *M$_R$* (Figure 2.6). In other words if the support doesn't allow the translation, there can be a *force reaction* and if doesn't allowed rotation there can be a *moment reaction.*

Because of the equilibrium the total force, F_T, and the total moment, M_T, actuating on the cantilever must be zero, therefore:

$$M_T = M_R - FL \text{ (total moment about support)} \quad \rightarrow \quad M_R = FL \qquad (2.16)$$

$$F_T = F_R - F \qquad \qquad \rightarrow \quad F_R = F \qquad (2.17)$$

Now, each segment of the beam must be also in equilibrium, therefore if we section the beam at a certain length x, we have to suppose *internal shear force* (V) and *internal bending moment* (M) (Figure 2.6). For the case of the cantilever we have

$$M(x) = -F(L - x) \qquad (2.18)$$

Let's now consider just a differential beam element. It is convention to consider moments and force positive (or negative) like it is depicted in the figure below (Figure 2.7).
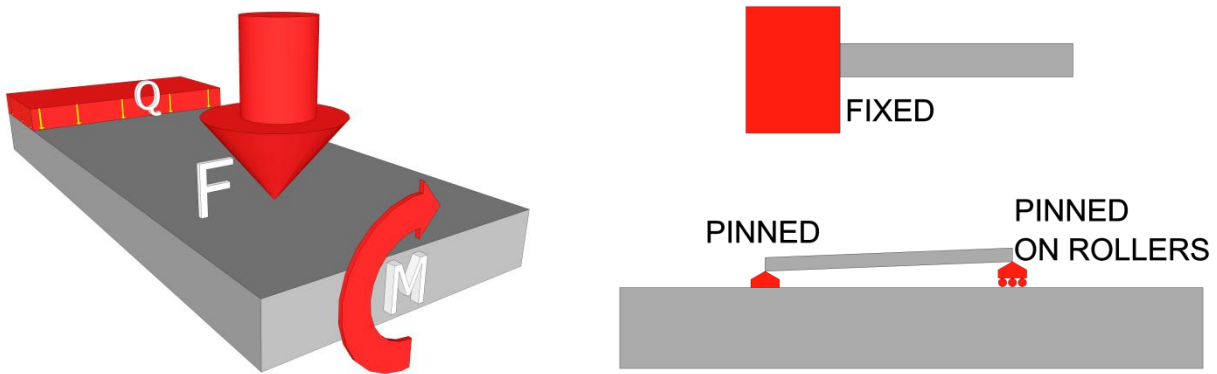
Figure 2.5. On the left: representation of a point force (F), distributed load (Q) and concentrated torque (M). On the right: representation of the boundary condition for a beam.
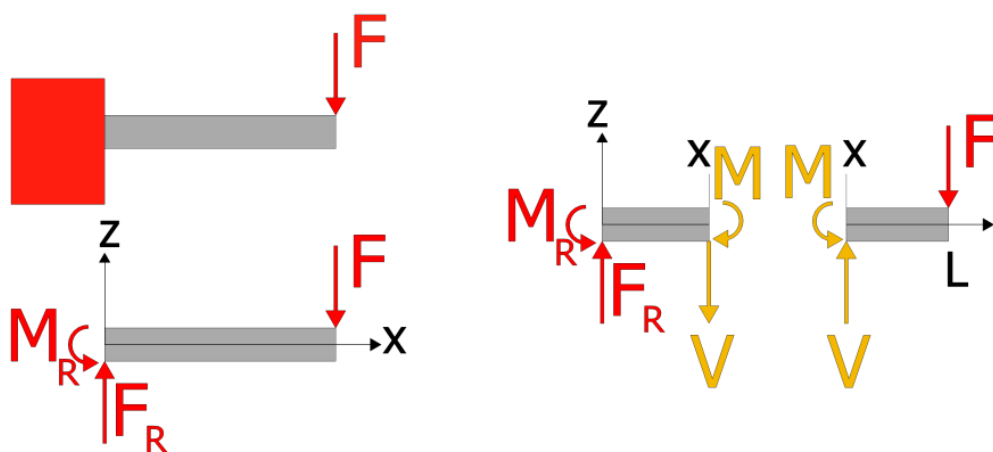
Figure 2.6. On the left: reactions of the clamped edge due to a force F actuating on one cantilever beam. On the right: representation of internal reaction in a beam.
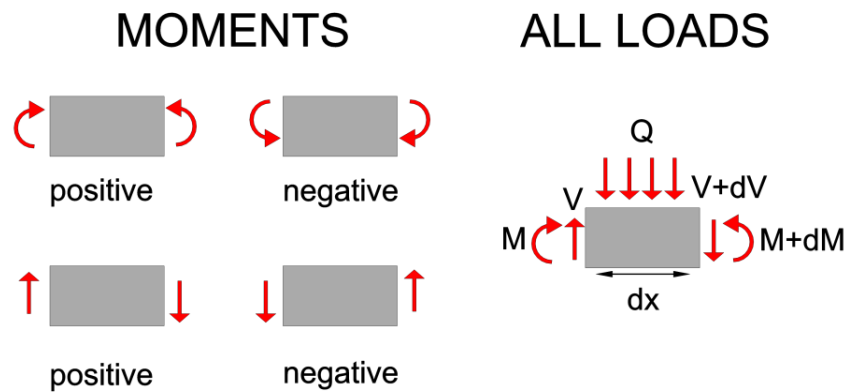
Figure 2.7. Conventions used for moments and shears.

This differential beam subjected to all the loads (point loads, distributed loads and moments), in equilibrium must obey governing differential equation for shear forces and moments:

$$F_T = q\,dx + (V + dV) - V \qquad \rightarrow \qquad \frac{dV}{V} = -q \qquad\qquad (2.19)$$

$$M_T = (M + dM) - M - (V + dV)dx - \left(\frac{q\,dx}{2}\right)dx \qquad \rightarrow \qquad \frac{dM}{dx} = V \qquad (2.20)$$

The change in the internal shear force is related to a distributed load and a change in internal moment is related to the internal shear force.

2.1.3 – Curvature and beam equations

In the previous paragraph we saw how the internal forces varies along the beam while in this one we will take into consideration stress, strain and deformation of the beam and we will see how they varies in its cross section.
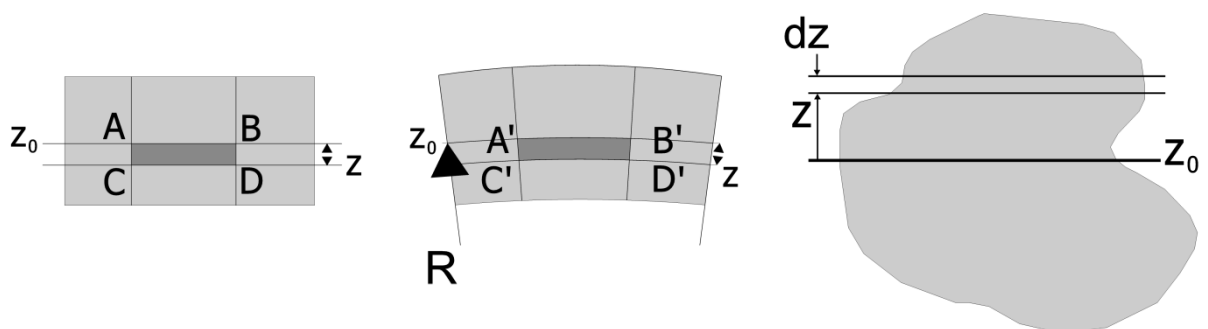
Figure 2.8. A beam initially unstressed (left), the same beam subjected to a bending moment (centre) and its cross sectional area.

If we now consider a beam initially unstressed and then subjected to a constant bending moment along its length, i.e. pure bending, as would be obtained by applying equal moment at each end, it will bend to a radius R as shown in (Figure 2.8). As a result of this bending the top fibres of the beam will be subjected to tension (the fibres are elongated) and the bottom to compression (the fibres are shortened). It is reasonable to suppose, therefore, that somewhere between the two there are points at which the stress is zero (and the fibres have the same length than before applying the moment). The locus of all such points is termed *neutral axis* and it located where the *centroid* is located. The radius of curvature R is then measured to this axis. For symmetrical sections the neutral axis is also the axis of symmetry while if the beam has not a symmetrical cross section the centroid is calculated by:

$$z_0 = \frac{\iint z \, dx \, dz}{\iint dx \, dz} \tag{2.21}$$

The fibre *AB*, distant *z* from the neutral axis, is stretched to *A'B'* if the bending moment is applied. The strain of fibre *AB*, along the *x* direction, is defined as the elongation divided by the original length:

$$\varepsilon_{AB} = \frac{A'B' - AB}{AB} \tag{2.22}$$

Since *AB=CD*, and the neutral axis is not strained *CD=C'D'*

$$\varepsilon_x = \varepsilon_{AB} = \frac{A'B' - C'D'}{C'D'} = \frac{(R-z)\theta - R\theta}{R\theta} = -\frac{z}{R} \tag{2.23}$$

Therefore the stress in *x* direction increases linearly with the *z* direction being zero on the neutral axis:

$$\sigma_x = -\frac{E}{R}z \tag{2.24}$$

where *E* is the Young's modulus.

On the strip of area, *dA*, of the cross section (Figure 2.8) is acting the force

$$dF = \sigma_x \, dA = -\frac{E}{R}z \, dA \tag{2.25}$$

and the moment about the neutral axis is:

$$dM = dF \, z = -\frac{E}{R}z^2 \, dA \tag{2.26}$$

Considering the whole cross section:

$$M = \int_A -\frac{E}{R}z^2 \, dA = -\frac{E}{R}\int_A z^2 \, dA \tag{2.27}$$

E and *R* are considered constant (independent of *dA*). The integral in the expression is called *second moment of area,* it is calculated taking as origin of *z* coordinate the neutral axis, and given the symbol *I*, therefore we can write:

$$M = -\frac{EI}{R} \tag{2.28}$$

If the beam is of uniform section, from the previous equation we have that the radius of curvature is constant if the material is homogeneous and we apply a constant bending moment. The radius of curvature of the beam is:

$$R = -\frac{EI}{M} \tag{2.29}$$

and is related directly with the term EI *bending stiffness* (or *flexural rigidity*) which depends on the Young's modulus of the material and on the area and shape of the cross section. Here we assumed the case of pure bending without any shear stress being present. In the most practical beam loading cases shear and bending occurs together at most points, however it would be possible to show that where the bending moment is maximum, in fact, the shear stress is zero and that the bending moment produces by far the greatest magnitude of stress.

Let's find now the relationship between the curvature and the applied load. Consider a beam *AB* (Figure 2.9) which is initially horizontal when unloaded. If this deflects to a new position *A'B'* under load, the slope at any point *C* is:

$$\theta = \frac{dz}{dx} \tag{2.30}$$

This is usually very small in practice, and for small curvatures is:

$$ds = dx = R \, d\theta \tag{2.31}$$

$$\frac{d\theta}{dx} = \frac{1}{R} \tag{2.32}$$
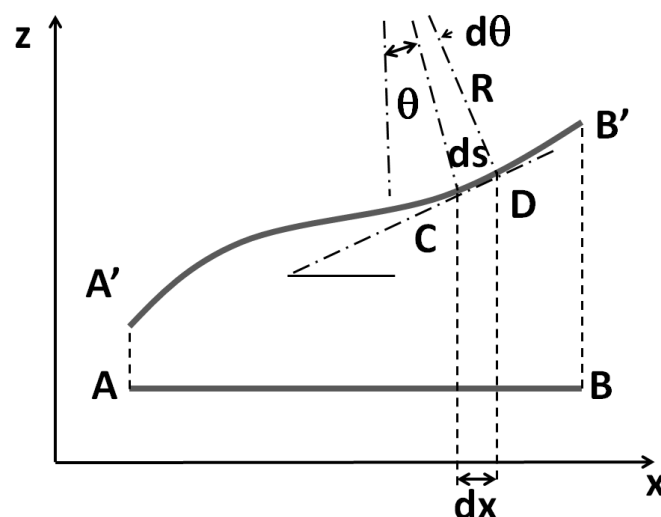
Figure 2.9. Representation of a beam initially unloaded (A-B) and after loading (A'-B')

Therefore considering (2.30)

$$\frac{d^2z}{dx^2} = \frac{1}{R} \qquad (2.33)$$

And considering the equation (2.29)

$$\frac{d^2z}{dx^2} = -\frac{M}{EI} \qquad (2.34)$$

Remembering also the previous equation we can summarize:

Displacement	$z \; or \; \eta$	(2.35)
Slope	$\theta = \dfrac{d\eta}{dx}$	(2.36)
Bending moment	$M = -EI\dfrac{d^2\eta}{dx^2}$	(2.37)
Shear force	$V = -EI\dfrac{d^3\eta}{dx^3}$	(2.38)
Loading	$q = -EI\dfrac{d^4\eta}{dx^2}$	(2.39)

2.1.4 – Cantilever with constant cross section and homogeneous material

2.1.4.1 – Static deflection

Let's now analyze the cantilever case (simple beam long *L* clamped at one end) with the transverse load, F, at its end (Figure 2.10). Considering the equations (2.18) and (2.37) we can write:

$$\frac{d^2\eta}{dx^2} = \frac{F}{EI}(L - x) \qquad (2.40a)$$

$$\frac{d\eta}{dx} = \frac{F}{EI}(Lx - x^2) + A \qquad (2.40b)$$

$$\eta = \frac{F}{EI}(Lx^2 - x^3) + Ax + B \qquad (2.40c)$$

Considering the boundary conditions at *x=0* (in the origin the deflection is zero and the beam is parallel to the x direction) we can calculate the coefficients *A* and *B*:

$$\eta(0) = 0 \rightarrow B = 0 \qquad (2.41a)$$

$$\left.\frac{d\eta}{dx}\right|_0 = 0 \rightarrow A = 0 \qquad (2.41b)$$

Therefore the equation of the elastic curve (deflection of the neutral axis) is:

$$\eta = \frac{F}{EI}\left(\frac{Lx^2}{2} - \frac{x^3}{6}\right) \tag{2.42}$$

where the bending stiffness is

$$EI = \int_A E(z)\, z^2\, dA = Ew \int_{-t/2}^{t/2} z^2 dz = E\frac{wt^3}{12} \tag{2.43}$$

Normally the end deflection of the cantilever is modelled as the deformation of a spring with elastic constant *k* (Figure 2.10):

$$F = k\,\eta(L) \tag{2.44a}$$

$$k = \frac{F}{\eta(L)} = \frac{F}{\dfrac{F}{EI}\left(\dfrac{L^3}{2} - \dfrac{L^3}{6}\right)} = 3\frac{EI}{L^3} = \frac{wt^3}{4L^3}E \tag{2.44b}$$

Finally considering the equations (2.23) and (2.33) we can write the strain and stress formulas for this case:

$$\varepsilon_x = -z\frac{d^2\eta}{dx^2} = \frac{z}{EI}(x - L)F \tag{2.45a}$$

$$\sigma_x = E\,\varepsilon_x = E\frac{z}{EI}(x - L)F \tag{2.45b}$$
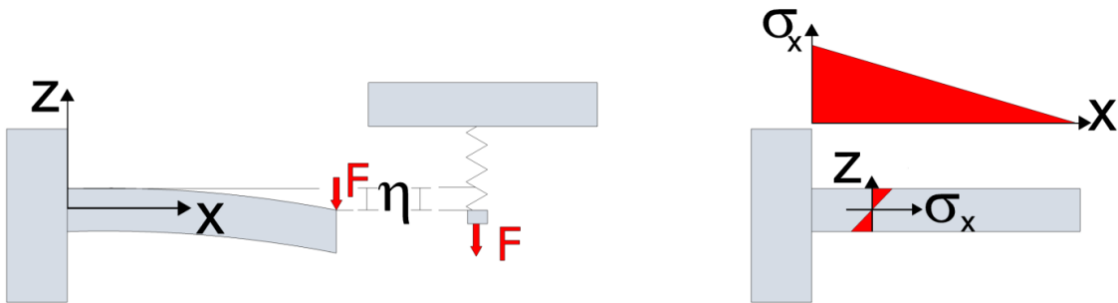
Figure 2.10. Cantilever model: the cantilever subjected to a point force can be modelled by a spring with constant k and mass m (left). On the right, the stress dependence on x and z axes is reported.

2.1.4.2 – Resonance frequency

Under the same conditions of linear elasticity and small deflection, the resonance frequency of the firs mode of the cantilever beam, in vacuum, can be calculated by the following formula [5]:

$$f_1 = \frac{1}{2\pi}\left(1.03\frac{E}{\rho_m}\right)^{1/2}\frac{t}{L^2} \tag{2.46}$$

where ρ_m is the mass density of the material of the beam.

2.1.5 – Cantilever with a multilayer structure and variable cross section

2.1.5.1 – Static deflection

Not to be confounded with beam made up of composite material, this composite (laminated) beam in this context refers to a beam with layering material having different Young's moduli and each material homogeneous. The difference in moduli will result in a beam having a shift in neutral axis under bending load. One way to work a composite beam problem is by using an *equivalent beam*. The basic idea is to make a beam out of just one material but expand or contract the substituted part laterally so that it has the same functionality as the original beam (Figure 2.11).

From these considerations the position of neutral axis is:

$$z_0 = \frac{\iint E(z) z \, dy \, dz}{\iint E(z) dy \, dz} = \frac{1}{2} \frac{\sum_i E_i \left(z_{ti}^2 - z_{di}^2 \right)}{\sum_i E_i (z_{ti} - z_{di})} \tag{2.47}$$

where *i* refers to the layer, z_t and z_d refer to the top and to the bottom of the layer respectively and *E* is the Young's modulus. Now that the position of the neutral axis is calculated it is possible to calculate the bending stiffness of the composite cantilever:

$$EI = \int_{-t/2}^{t/2} \int_{-w/2}^{w/2} E(z)(z - z_0)^2 dy \, dz = \frac{1}{3} w \sum_1 E_i ((z_{ti} - z_0)^3 - (z_{di} - z_0)^3) \tag{2.48}$$

Concluding, the stress (discontinuous) and strain (continuous) (Figure 2.11) are given by:

$$\varepsilon_x = -z \frac{d^2\eta}{dx^2} = \frac{z - z_0}{EI} (x - L)F \tag{2.49a}$$

$$\sigma_x = E_i \varepsilon_x = E_i \frac{z - z_0}{EI} (x - L)F \tag{2.49b}$$

Let's now consider instead that the beam is single layered and has not a constant cross section along the x direction like in the picture (Figure 2.12).

From the point of view of the displacement these two situations, U-cantilever or T cantilever, have the same solution (if the cross-sectional area is the same). For the two parts, 1 and 2, of the cantilever we can write:

$$\eta_1(x) = \frac{F}{EI_1} \left(\frac{L_2 x^2}{2} - \frac{x^3}{6} \right) \tag{2.50a}$$

$$\eta_2(x) = \frac{F}{EI_2} \left(\frac{L_2 x^2}{2} - \frac{x^3}{6} \right) + Ax + B \tag{2.50b}$$
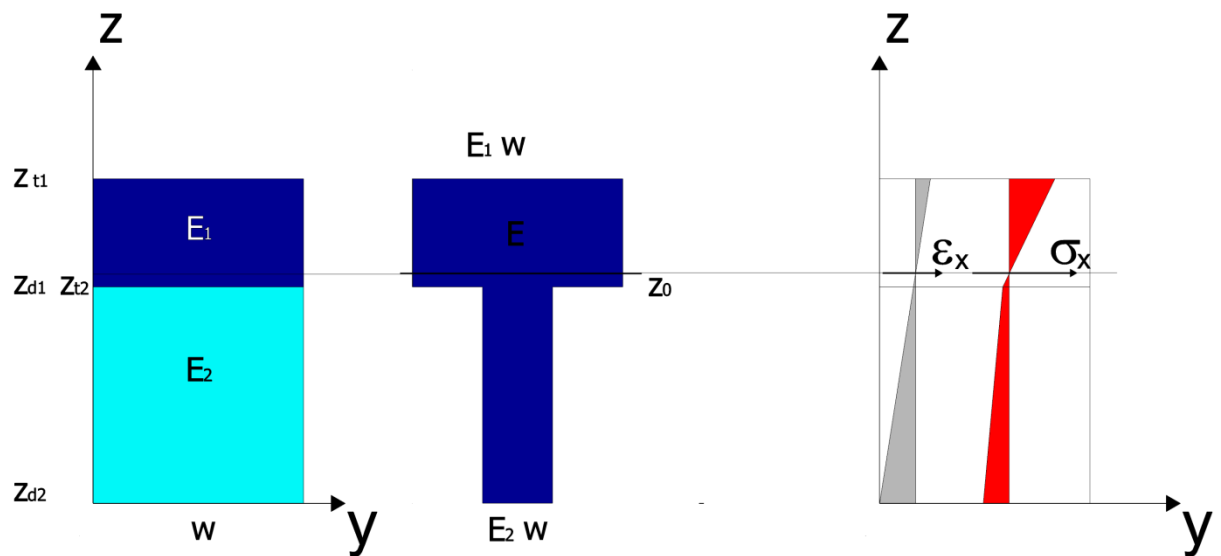
Figure 2.11. Two-layers-beam made of two materials with Young's moduli E_1 and E_2 and equivalent beam made of a single material with Young's modulus E. (left). On the right, representation of the x-component of strain and stress dependence on z-direction.
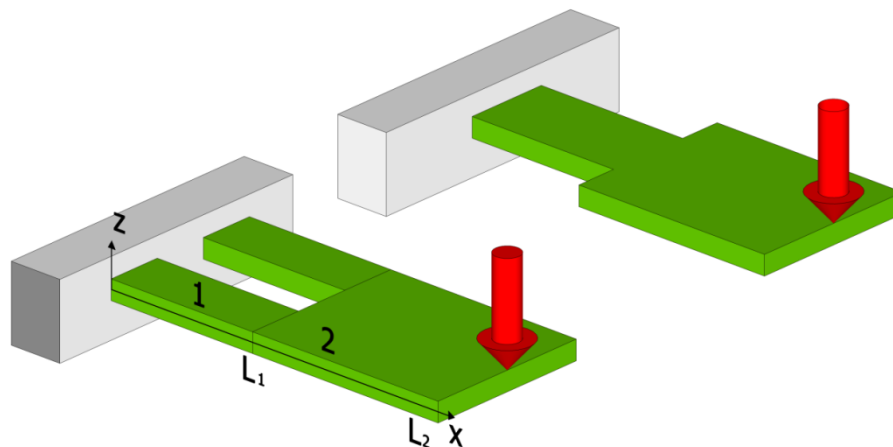
Figure 2.12. Cantilever with non constant cross sectional area: U or T shaped cantilevers. The cantilever can be modelled as two cantilevers in series. The first part [0,L_1] has smaller cross sectional area and lower bending stiffness. The second part [L_1,L_2] has bigger cross sectional area and higher bending stiffness.

EI_1 and EI_2 are the bending stiffness (or flexural rigidity) of the beam in the two different parts of the cantilever. These can be calculated from the previous equation (2.47-(2.48). Now in L_1 has to be $\eta_1 = \eta_2$ (the displacement has to be the same) and $\eta'_1 = \eta'_2$ (the tangent of the displacement is the same too). From these two boundary conditions we obtain A and B:

$$A = \frac{1}{2} \frac{L_1(L_1 - 2L_2)(EI_1 - EI_2)}{EI_1 EI_2} F \qquad (2.51a)$$

$$B = -\frac{1}{6} \frac{L_1^2(2EI_1L_1 - 3EI_1L_2 + 3EI_2L_2 - 2EI_2L_1)}{EI_1EI_2} F \tag{2.51b}$$

Finally the spring constant of the cantilever is:

$$k = \frac{F}{\eta_2(L_2)} \tag{2.52}$$

And stress and strain can be calculated as in the equation (2.49).

2.1.5.2 – Resonance frequency

Under the same assumptions, the resonance frequencies of a cantilever with non constant cross section can be numerically calculated using the following formulas [5]:

$$f_i = \frac{1}{2\pi}\sqrt{\frac{E}{12\rho_m}\frac{t}{L_2^2}\kappa_i^2} \tag{2.53}$$

$$
\begin{aligned}
&1 + \chi^2 - (\chi^2 - 1)\cos(\kappa_i L_2 \lambda)\cosh(\kappa_i L_2 \lambda) + 2\chi\cos(\kappa_i L_2)\sinh\big(\kappa_i L_2(\lambda - 1)\big)\sinh(\kappa_i L_2 \lambda) \\
&\quad = \cosh\big(\kappa_i L_2(\lambda - 1)\big)\Big((\chi^2 - 1)\cos\big(\kappa_i L_2(\lambda - 1)\big) \\
&\quad - \cosh(\kappa_i L_2 \lambda)\Big((\chi^2 + 1)\cos\big(\kappa_i L_2(\lambda - 1)\big)\cos(\kappa_i L_2 \lambda) \\
&\quad + 2\chi\sin\big(\kappa_i L_2(\lambda - 1)\big)\sin(\kappa_i L_2 \lambda)\Big)\Big)
\end{aligned}
\tag{2.54}
$$

Where $\chi = w_1/w_2$ and $\lambda = L_1/L_2$.

2.2 – Piezoresistive effect

The piezoresistive effect describes the change in the electrical resistivity of a semiconductor when a mechanical load is applied. Lord Kelvin reported for the first time on the change in resistance with elongation of metals (i.e. iron and copper) in 1856 [6]. After almost a century, and after Bardeen and Shockley predicted large conductivity change with elongation of single crystal semiconductors [7], Smith measured the exceptional large piezoresistive effect in silicon and germanium in 1953 [8]. Hereafter we will review the most important characteristics of the piezoresistive effect in doped crystalline silicon and in metal oxide semiconductor field effect transistors (MOSFET).

2.2.1 – Silicon piezoresistor

The electrical resistance, R, of a homogeneous conductor is a function of its length, l_R, of its cross section area, $A_R = w_R t_R$, and of the resistivity of the material, ρ_R:

$$R = \frac{l_R}{w_R t_R} \rho_R \tag{2.55}$$

When the resistor is under mechanical tension, the length increases while the thickness and width decrease, as explained in the previous section. Moreover, also the resistivity can vary. Therefore, the total relative change of the resistance is:

$$\frac{\Delta R}{R_0} = \frac{\Delta l_R}{l_{R_0}} - \frac{\Delta w_R}{w_{R_0}} - \frac{\Delta t_R}{t_{R_0}} + \frac{\Delta \rho_R}{\rho_{R_0}} \tag{2.56}$$

where the sub-index 0 is referred to the initial unstrained conditions. Dividing the two expressions by the strain ε, we can define the gauge factor as:

$$G_F = \frac{\Delta R/R_0}{\varepsilon} = 1 + 2\upsilon + \frac{\Delta\rho/\rho_0}{\varepsilon} \tag{2.57}$$

The first two terms represent the resistance change due to the geometrical variation of the resistor, while the third term refers to the variation of the resistivity. Geometric effects alone provide a G_F of approximately 2 and the contribution of the resistivity change add around 0.3 more in case of metals. However, for silicon, germanium and others semiconductors, the relative change in resistivity can be 50-100 times larger than the geometric term alone [9]. In silicon nanowires, it can become even 1000 times larger [10]. Considering a simple case of uniaxial applied stress, σ, along the current flow, we can write with good approximation that:

$$\frac{\Delta R}{R_0} = \frac{\Delta \rho_R}{\rho_{R_0}} = \pi_l \sigma \tag{2.58}$$

where π_l is the *longitudinal piezoresistive coefficient*. In the opposite case, when the stress and current flow are perpendicular, we have to speak about *transversal piezoresistive coefficient, π_t*. There is also a third piezoresistive coefficient that is called shear piezoresistive coefficient π_s, which relates the resistivity variation to the shear stress. In a more general case, we can have normal and shear stress in different direction and therefore we need a 6x6 matrix to relate the relative variation of the resistivity to the stress components [11]:

$$\frac{\Delta \rho_i}{\rho_i} = \sum_{j=1}^{6} \pi_{ij}\, \sigma_j \tag{2.59}$$

Considering the symmetry of the cubic crystal structure of the silicon, if the crystallographic axes [100], [010] and [001] are chosen as reference axes the piezoresistive matrix reduces to:

$$\bar{\bar{\pi}} = \begin{bmatrix} \pi_{11} & \pi_{12} & \pi_{12} & 0 & 0 & 0 \\ \pi_{12} & \pi_{11} & \pi_{12} & 0 & 0 & 0 \\ \pi_{12} & \pi_{12} & \pi_{11} & 0 & 0 & 0 \\ 0 & 0 & 0 & \pi_{44} & 0 & 0 \\ 0 & 0 & 0 & 0 & \pi_{44} & 0 \\ 0 & 0 & 0 & 0 & 0 & \pi_{44} \end{bmatrix} \tag{2.60}$$

37

The values of the three coefficients π_{11}, π_{12}, π_{44}, were measured, for the first time, by Smith, for relatively lightly doped silicon samples and are reported in Table 2.2 [8].

2.2.1.1 – Orientation, doping and temperature dependence

The relationships between longitudinal and transversal piezoresistive coefficients and the fundamental piezoresistive coefficients depend on the crystallographic orientation of the resistor (Table 2.2). Longitudinal and transverse piezoresistive coefficients can be calculated also for an arbitrary direction [12].

$$\pi_l = \pi_{11} - 2(\pi_{11} - \pi_{12} - \pi_{44})(l_1^2 m_1^2 + l_1^2 n_1^2 + m_1^2 n_1^2) \tag{2.61a}$$

$$\pi_t = \pi_{12} - 2(\pi_{11} - \pi_{12} - \pi_{44})(l_1^2 l_2^2 + m_1^2 m_2^2 + n_1^2 n_2^2) \tag{2.61b}$$

where *l*, *m* and *n* are the direction cosines respect to the crystallographic axes [13]. After Kanda [13, 14], π_l, π_t are normally reported in a graphical way. He represented the coefficients for lightly n- and p-doped silicon for an arbitrary direction on the (100), (110) and (211) wafer orientations (Figure 2.13).

Direction		coefficient			n-type	p-type
stress	current					
$\langle 100 \rangle$	$\langle 100 \rangle$	π_{11}	ρ [Ω cm]		11.7	7.8
$\langle 100 \rangle$	$\langle 010 \rangle$	π_{12}	π_{11} [10^{-11} Pa^{-1}]		-102.2	6.6
$\langle 110 \rangle$	$\langle 110 \rangle$	$\dfrac{\pi_{11} + \pi_{12} + \pi_{44}}{2}$	π_{12} [10^{-11} Pa^{-1}]		53.4	-1.1
$\langle 110 \rangle$	$\langle 1\bar{1}0 \rangle$	$\dfrac{\pi_{11} + \pi_{12} - \pi_{44}}{2}$	π_{44} [10^{-11} Pa^{-1}]		-13.6	+138.1

Table 2.2. First order piezoresistive coefficient in some typical configurations [9].

The piezoresistive factors don't change just on the crystallographic direction, but also on the doping concentration and temperature. In 1962 and 1963 Tufte and Stelzer measured the dependence of π_{11}, π_{44}, for n-doped silicon and p-doped silicon respectively, on the doping concentration ranging between 10^{15} and 10^{21} cm^{-3} and temperatures between 70 K and 370 K (Figure 2.14)[15, 16]. They found that the coefficients are decreasing when increasing the concentration and temperature. Considering the experimental results Kanda presented a theoretical model to calculate these variations, which were represented by the piezoresistance factor *P* (Figure 2.15). This fits pretty well for low doped silicon but it introduces an error between -24% and +14% for highly p doped silicon [13]. This error was attributed to the dopant scattering at high concentrations, whereas the calculations took into consideration just lattice scattering.

After Harley proposed an empirical fit for highly doped silicon [17], in 2008 this discrepancy was solved by Richter, who included all the relevant scattering mechanisms, acoustic phonon, non-polar optical phonon, and ionized impurity scattering [11]. This model predicts very well the piezoresistive factor at different temperatures and at concentrations between 10^{14} and 10^{20} cm^{-3}. After Richter, the piezoresistive factor $P=\pi_l/\pi_{l,0}$, can be calculated by:

$$P = \frac{\Theta^{-\vartheta}}{1 + \left(\dfrac{n}{N_B}\right)^{\alpha}\Theta^{-\beta} + \left(\dfrac{n}{N_C}\right)^{\gamma}\Theta^{-\eta}} \tag{2.62}$$
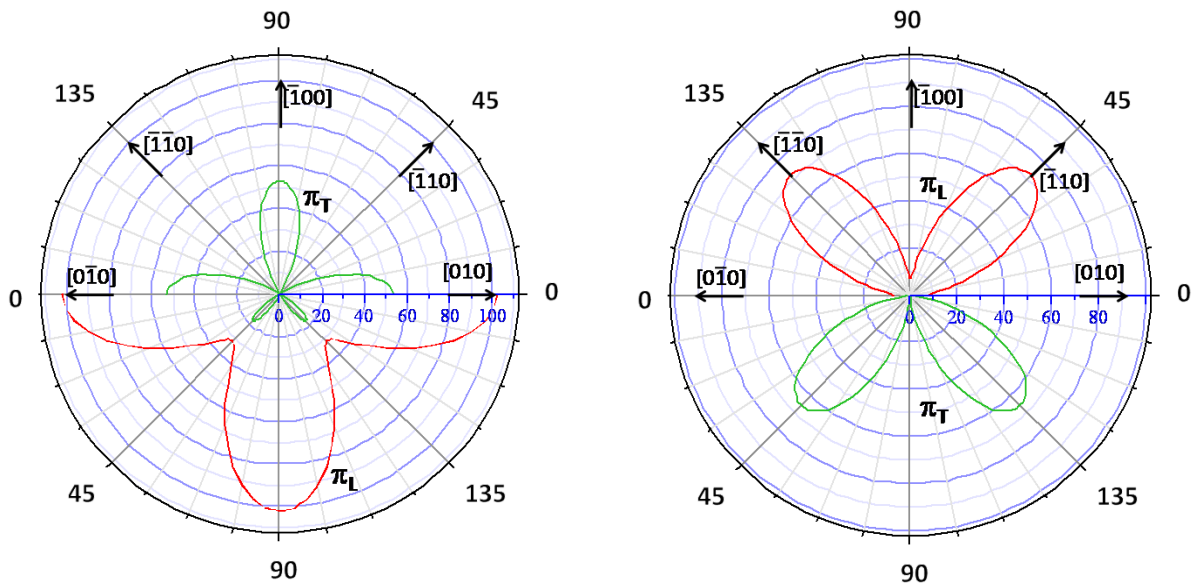
Figure 2.13. Longitudinal π_L (red) and transverse π_T (green) piezoresistive coefficients in n-doped silicon (left) and p-doped silicon (rigth). [13]
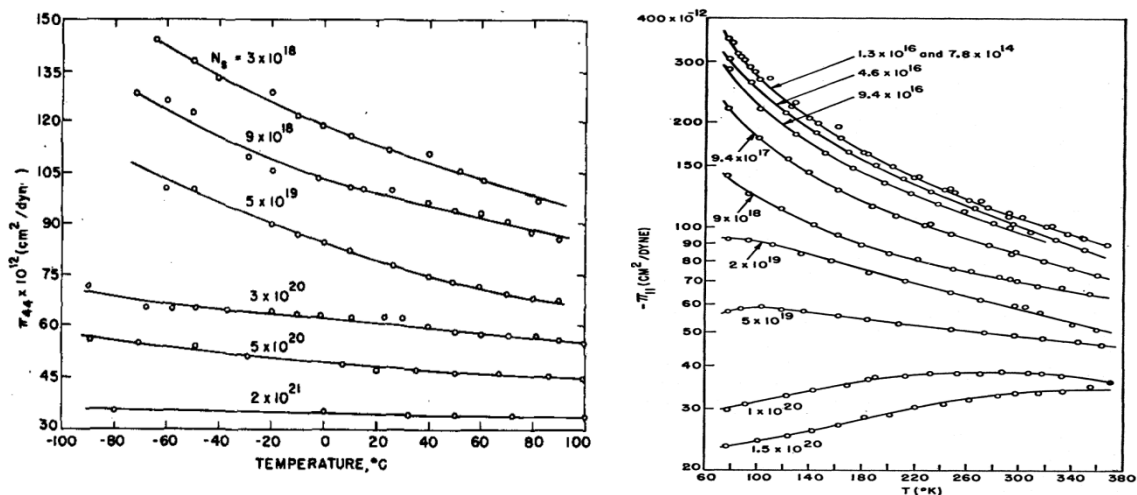
Figure 2.14. Experimental values of π_{44} in p-doped silicon (left) and π_{11} for n-doped silicon (right) for different doping concentrations and at different temperatures. [15, 16]

where n is the concentration, Θ is the normalized temperature T/300 and the fitting coefficients $\vartheta,\alpha,\gamma,\eta,N_B,N_C$, are 6×10^{19} cm^{-3}, 7×10^{20} cm^{-3},0.9, 0.43, 0.1, 1.6, 3 respectively (Figure 2.16).
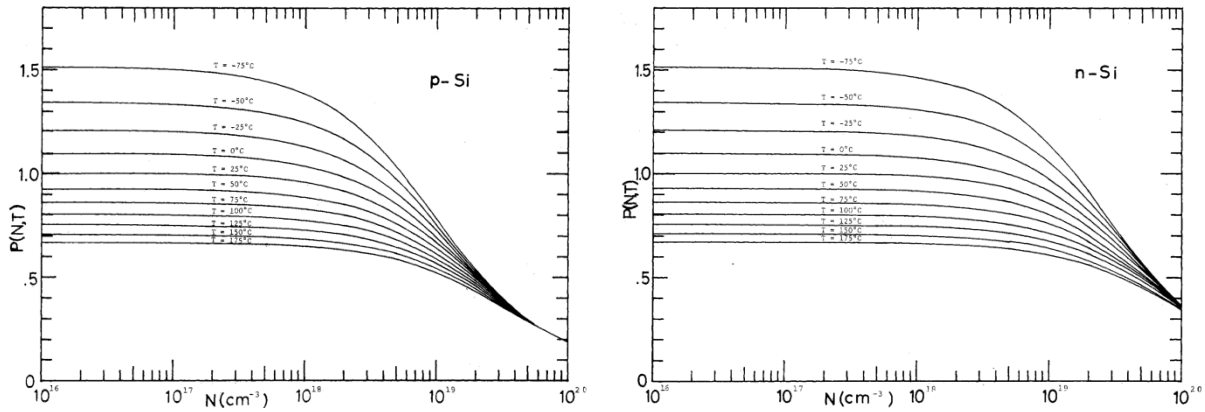
Figure 2.15.Theoretical values of piezoresistive factor calculated by Kanda for p-doped (left) and n-doped silicon (right) for different doping concentrations and at different temperatures. [13]
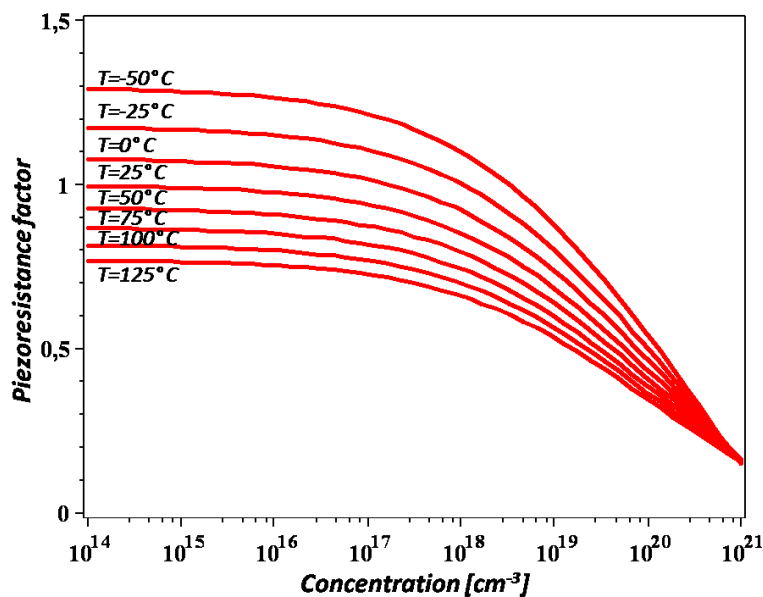
Figure 2.16. Theoretical values of piezoresistive factor calculated by Richter for p-doped silicon for different doping concentrations and at different temperatures [11].

2.2.2 – Silicon MOSFET

The metal-oxide-semiconductor field effect transistor (MOSFET) was made for the first time in 1959 at Bell Labs by D. Kahng and M. M. Atalla [18], after J. E. Lilienfeld patented the idea of this kind of transistor in 1925 [19]. Few years later, in 1967, 14 years after the

discovery of the piezoresistive effect in bulk silicon, Colman [20] from Texas Instruments, reported for the first time about piezoresistance in p-type MOSFET. In 1968, Dorey, from Bell Labs, confirmed the measurements of Colman [21] and just in 1970 and 1972, Dorda reported a much more detailed and complete work on the piezoresistive effect in p-type and n-type silicon inversion layer in MOSFETS [22, 23]. Even though, during the first years, this effect has been pointed out for mechanical transducers applications, in the last 15 years it has been of fundamental importance for improving the performance of the transistors in the logic technologies.

Hereafter, we will point out the working principles of the MOSFET transistors and afterwards we aim to summarize the literature information about their stress dependent characteristics.

2.2.2.1 – MOSFET model

The *MOSFET transistor* (Figure 2.17) is made by a capacitor, the metal-oxide-semiconductor (MOS) structure, which has two terminals: *gate* and *body*. Until the mid-1970s the gate was made of aluminum, but nowadays highly doped polycrystalline silicon is used for this purpose. The body is a lightly doped semiconductor, which is normally silicon. A thin oxide, normally silicon oxide, separates the two terminals. Source and drain complete the MOSFET structure. These two terminals are also made of silicon, but are doped in the opposite way than the body. The region between the source and drain, just under the gate oxide, is called *channel*.

The distribution of charges in the semiconductor can be modified by applying a voltage across the MOS structure. For sake of simplicity we consider just the n-MOSFET case. In this case, source and drain are n-doped and the body is p-doped. A positive voltage from gate to body, V_{GB}, force the positive conductive charges, the holes, to migrate far away from the silicon-silicon oxide interface. This creates a *depletion layer*, leaving exposed a carrier-free region of immobile, negatively charged acceptor ions. If the V_{GB} is high enough, higher than a threshold voltage (V_{TH}), then a high concentration of negative charge carriers, the electrons, forms a very thin layer (*inversion layer*) located just under the gate oxide. If a positive voltage is applied from drain to source, V_{DS}, then the electrons can flow and there is a current from source to drain, I_D.

The operation of a MOSFET can be separated into three different modes, depending on the voltages at the terminals (Figure 2.18):

- If the voltage between gate and source, V_{GS}, is lower than V_{TH} then there is no conduction between source and drain and therefore the transistor is turned off. This is called **sub-threshold mode**.

- If $V_{GS} > V_{TH}$ and $V_{DS} < V_{GS} - V_{TH}$ the transistor is turned on. Since V_{GS} is higher than V_{TH} the MOS is in inversion and there are electrons in the channel. Because of V_{DS}, there is current flow between source and drain. This state is called **linear region**, because the transistor operates like a resistor controlled by the gate, the source and drain voltages. The drain current is higher for higher V_{GS} and for higher V_{DS} and is modeled by:

$$I_D = \mu_n C_{ox} \frac{W_{CH}}{L_{CH}} \left((V_{GS} - V_{th})V_{DS} - \frac{V_{DS}^2}{2} \right) \tag{2.63}$$

where μ_n is the charge-carrier effective mobility, W_{CH} is the channel width, L_{CH} is the channel length and C_{ox} is the gate oxide capacitance per unit area.

- If $V_{GS} > V_{TH}$ and $V_{DS} > V_{GS} - V_{TH}$ the transistor is turned on, the current flows between source and drain and it depends mainly on V_{GS}. The drain voltage has just a weak influence. This behavior is explained by the fact that the voltage between the gate and the drain is lower than V_{TH} and therefore the channel is pinched-off near the drain. This state is called **saturation region** and is modeled by:

$$I_D = \frac{\mu_n C_{ox}}{2} \frac{W_{CH}}{L_{CH}} (V_{GS} - V_{th})^2 \left(1 + \lambda(V_{DS} - V_{DSsat})\right) \tag{2.64}$$

where λ is the channel length modulation parameter and sometimes is considered to be $\lambda{=}0$, especially for long channel MOSFET.
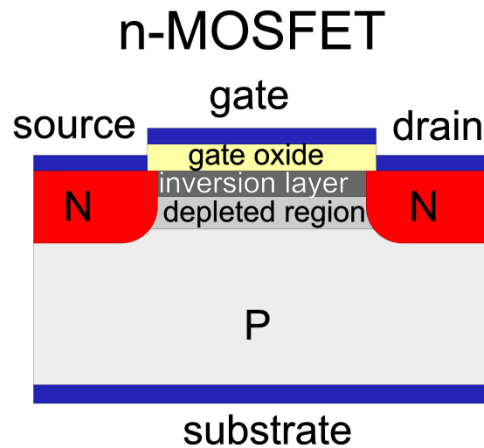
Figure 2.17. Representation of a n-type MOSFET transistor.
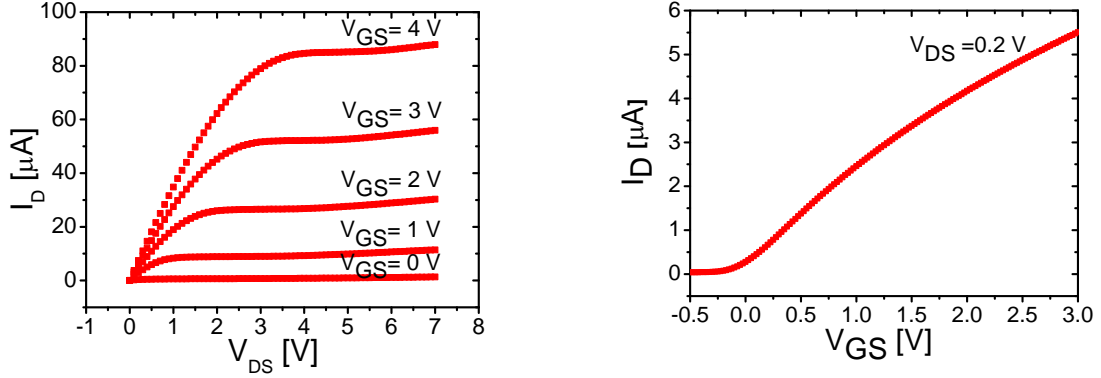
Figure 2.18. Electric characteristics of an enhancement mode n-MOSFET transistor. I_{DS} vs V_{DS} graph for different gate voltages (left) and I_{DS} vs. V_{GS} at low V_{DS} voltage.

2.2.2.2 – Piezoresistivity and carrier mobility enhancement in MOSFET transistors

The drain current of a MOSFET changes when the transistor is loaded by a compressive or tensile stress. When the transistor is in saturation, the mechanical stress can affect the carrier mobility, the threshold voltage and the channel dimensions. Like in the piezoresistor case, the changes in the W_{CH} and L_{CH} are not sufficient to explain the high current variation, and in fact they become negligible. Thus the relative change in the drain current is [24]:

$$\frac{\Delta I_D}{I_D} \cong \frac{\Delta \mu_D}{\mu_D} - 2\frac{\Delta V_{TH}}{V_{TH}}\left(\frac{V_{TH}}{V_{GS}-V_{TH}}\right) \qquad (2.65)$$

In literature, there has been some disagreement about the dependence of the threshold voltage variation with the stress, due mainly to a wrong way to measure it [24]. Bradley, in 2001, experimentally extracted the threshold voltage from MOSFET linear region measurements for different channel length and for three different technologies [24]. His results demonstrated that the threshold voltage is essentially independent of stress which is agrees with the theory of Mikoshiba [25]. Based upon this conclusion, the second term of the previous equation can be neglected. The mechanical stress, therefore, influence just the charge carrier mobility:

$$\frac{\Delta I_D}{I_D} \cong \frac{\Delta \mu_D}{\mu_D} \qquad (2.66)$$

If we consider that the transistor is subjected to uniaxial stress and that the drain current flows in the same direction, we can write:

$$\frac{\Delta I_D}{I_D} \cong \frac{\Delta \mu_D}{\mu_D} = -\pi_L \sigma \qquad (2.67)$$

where π_L is the longitudinal piezoresistive coefficient. It should be noted that, in this case, the piezoresistive coefficient is defined using the current variation instead than resistance variation (eq. (2.58)), and therefore a "-" is introduced in the formula. If the drain current

flows perpendicular respect to the stress, we have to introduce the transversal piezoresistive coefficient, π_T. In the same way like for the piezoresistors, the piezoresistive effect in silicon MOSFET is fully described by the piezoresistive matrix and by the three independent piezoresistive coefficients $\pi_{11}, \pi_{12}, \pi_{44}$ (Table 2.2).

2.2.2.3 – Orientation, doping, gate voltage, drain voltage, gate length and temperature dependence

Many works have been published about the piezoresistivity (or charge carrier enhancement) in MOSFET transistors. They agree that this effect varies with the crystallographic orientation of the channel, with the gate voltage, drain voltage and temperature while it does not depend on the doping level of the channel or on the channel length. Between 1967 and 90s, the piezoresistive coefficients have been studied systematically for p-type and n-type inversion layers in the fundamental directions and on different silicon substrates: (100), (110), (111). In these studies the fundamental piezoresistive coefficients $\pi_{11}, \pi_{12}, \pi_{44}$, have been measured or calculated. Later on, the attention has been directed more on the stress dependence of the electrons and holes mobility enhancement, to improve the transistor performance for logic technologies. In this perspective, the researchers measured mainly the piezoresistive properties in the common transistor direction, the <110>, and they didn't consider anymore fundamental the measurements of all the three primary piezoresistive coefficients. In Table 2.3 we report the values from Wang [26] and the maximum and minimum values obtained from other authors at low gate voltages. In appendix A, we report the most relevant values found by the researchers from 1967 until these days.

Considering the equations (2.61a) and the values of Wang, we can represent the piezoresistive coefficients for the different crystallographic directions in a graphical way, like is normally done for bulk silicon. In Figure 2.19 , we report π_L and π_T for n-type and p-type inversion layers on the (100) substrate.

Doping type	π_{11} x 10^{-11} [Pa^{-1}]	π_{12} x 10^{-11} [Pa^{-1}]	π_{44} x 10^{-11} [Pa^{-1}]
n-MOSFET	-90 (-84/-100)	40 (34/50)	-10 (-10/-21)
p-MOSFET	-15 (-1/-15)	30 (24/35)	115 (104/128)

Table 2.3. Piezoresistive coefficient values for n-and p-type inversion layer [26] . (Maximum and minimum values in literature).
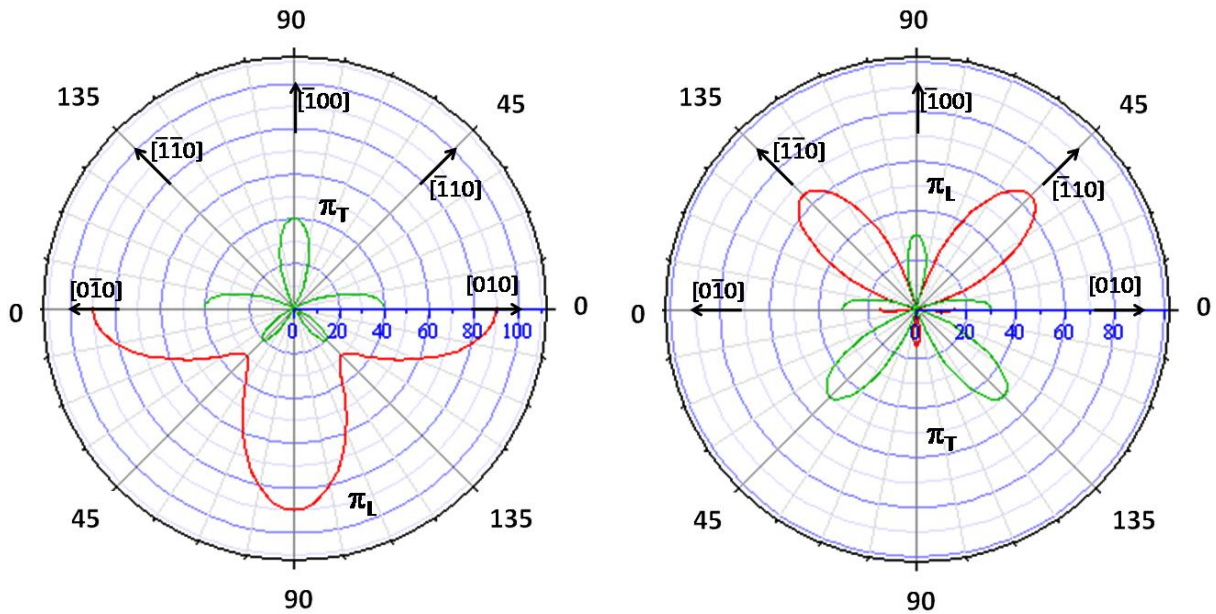
Figure 2.19. Longitudinal (red) and transverse (green) piezoresistive coefficients representation in n-doped silicon (left) and p-doped silicon (rigth) considering the values of Wang [26].
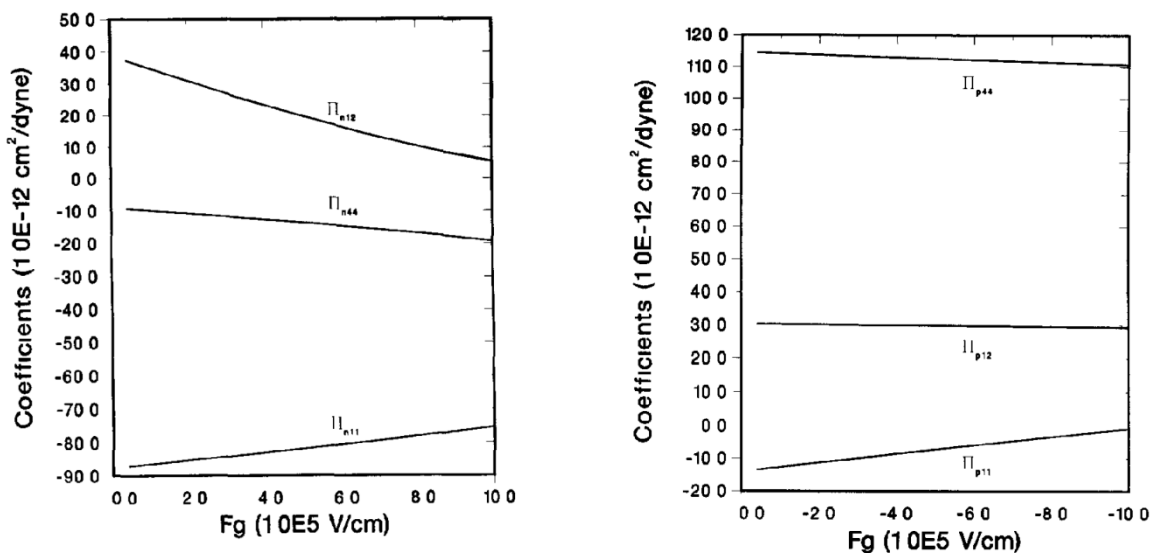
Figure 2.20. Variation of the piezoresistive coefficient with the transverse electric field at 300 K for n-MOSFET (left) and p-MOSFET (right) [26].

In the n-type inversion layer case, all the piezoresistive coefficients have around 10% or 20% lower values than the ones of the n-doped silicon. In the p-type inversion layer case, also π_{44} has 10% lower value, but π_{11} and π_{12} have opposite sign and higher absolute values with respect to the p-doped silicon case. Moreover these values are not at all constant. As reported by Dorda [22, 23], Canali [27], Mikoshiba [25] and Wang [26], the piezoresistive coefficient has a strong dependence on the gate voltage (or vertical electric field, E_G). They agree that in n-MOSFET case at low E_G, π_{11}, π_{12} tend to approach the corresponding values of the lightly doped silicon. The increase of the field strongly reduces their absolute values (Figure 2.20). On the other hand, π_{44} has an opposite behavior passing from around -10x10^{-11}

45

Pa^{-1} to -20 x10^{-11} Pa^{-1}. In the p-MOSFET case, this dependence is less marked and just the longitudinal piezoresistive coefficient firmly decreases from around -15x10^{11} Pa^{-1} to 0 Pa^{-1}.

Wang reported also about the variation of the piezoresistive coefficients with the drain voltage, for different stress values [26]. The decrease of the coefficients for high drain voltages is higher at higher stresses and is valid for n- and p-MOSFET, as reported in Figure 2.21. On the other hand, Vatedka measured the drain current for various V_{GS} and V_{DS} for an n-MOSFET with a gate length of 10 μm oriented in the <110> direction (Figure 2.22) [28]. He reported that the piezoresistive effect is higher for high drain voltages. Especially, the drain current relative variation just before drain breakdown can be 30% higher compared to the variation at lower drain voltages. At high drain voltages there is impact ionization which increases the number of electrons flowing to the terminal. The stress influences also the ionization with a final result of higher stress dependence of the drain current at high drain voltages.
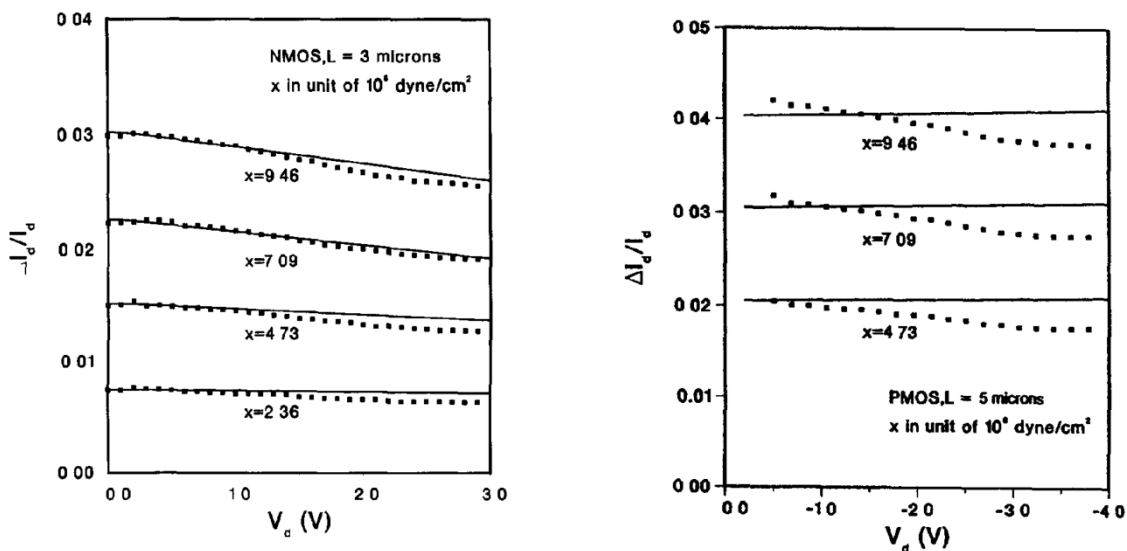
Figure 2.21. Relative drain current change (ΔI/I$_0$) depent on the drain voltage n-MOSFET (left) and p-MOSFET (right). Full lines are the simulation results and points are experimental values [26].
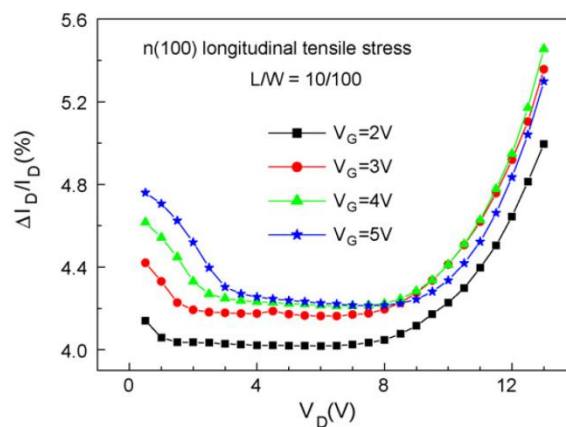
Figure 2.22. Drain voltage and gate voltage dependence of the relative drain current change (ΔI/I$_0$) [28].

46

In the last two decades, with the downscaling of the MOSFET transistor, it became evident that the piezoresistive characteristics were dependent on the transistor dimensions. The sensitivity of the devices to stress is constant for long gate length but falls off as the channel length is reduced below approximately 2 μm. Bradley and Gallon, in 2001 [24] and 2003 [29] respectively, attributed this phenomenon to the parasitic resistances of source and drain, that becomes more pronounced as the gate length decreases. The parasitic resistances, that are equal in source and drain, cause transconductance degradation and at the same time they are almost insensitive to the stress because are made of heavily doped silicon. In Figure 2.23 we report the uncorrected values and the relative corrected data of the longitudinal and transversal piezoresistive coefficients for p-MOSFET versus channel length.

Mikoshiba, in 1980, studied also the dependence of the piezoresistive coefficient on the channel doping [25]. In enhancement mode MOSFET transistors the coefficients do not depend on channel doping level also because the channels anyway are always lightly doped. It seems therefore that they are function mainly of the surface electric field. In the depletion mode transistor, we have to make a difference between n- and p-type MOSFETS. In the first case, the piezoresistive coefficients have similar values to the enhancement type transistor; however, they depend more weakly on the surface electric field. In fact, in this type of transistor, the current path exists partly in the surface accumulation layer and partly in the channel bulk region. In p-type depletion mode MOSFET the piezoresistive coefficients are almost equal to the corresponding bulk values at low vertical electric fields. Additionally, they show almost no field dependence. In Figure 2.24 we report the values measured by Mikoshiba for different type of n- and p-MOSFETs.

It is well known that the piezoresistive coefficients decrease with the temperature increase for bulk silicon and many authors studied it, as it has been pointed out in the previous section 2.2.1.1. On the other hand, for the silicon inversion layer there are not many studies about the carrier enhancement dependence with temperature. Canali [27] studied the variation of π_L and π_T between -20^{0}C and 120^{0}C for a p-MOSFET along the <110> and of π_L for a n-MOSFET along <111> direction. He reports piezoresistive coefficients variations between 500 ppm C^{-1} and 5000 ppm C^{-1} for different crystallographic directions, which are in the same order of magnitude of the variations reported by Tufte for low doped silicon (Figure 2.25) [15].
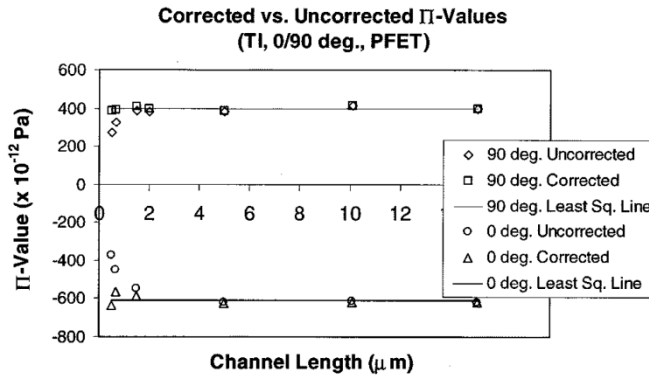
Figure 2.23. Piezoresistive coefficient dependence on the channel length. Uncorrected values and the relative corrected data of the longitudinal and transversal piezoresistive coefficients for p-MOSFET versus channel length [24].
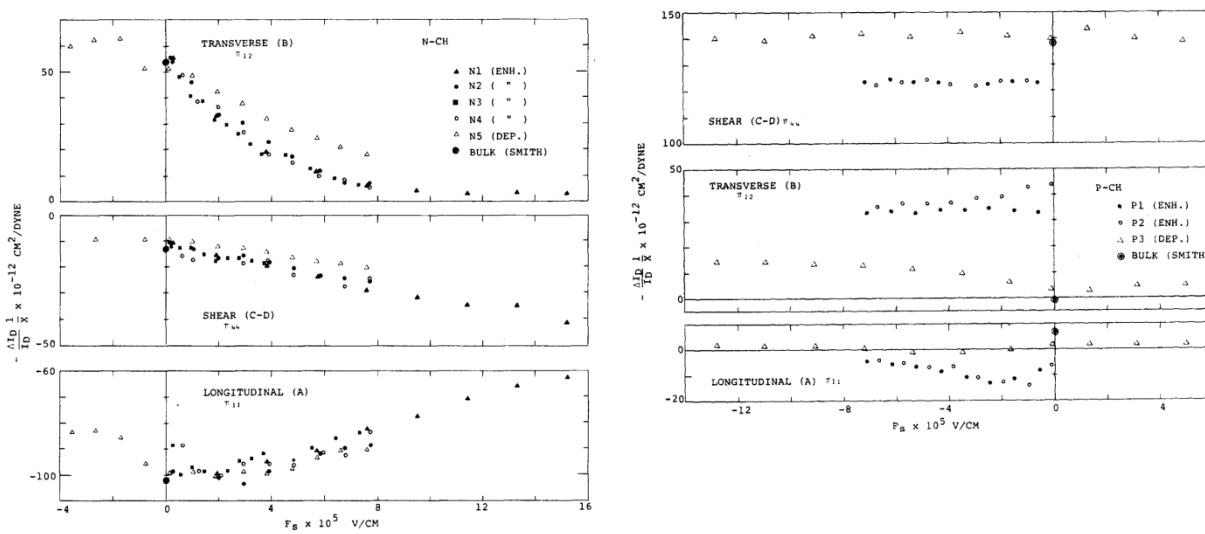
Figure 2.24. Piezoresistive coefficient dependence on channel doping and on transversal electric field for n-NOSFET (left) and p-MOSFET (right) transistors [25].
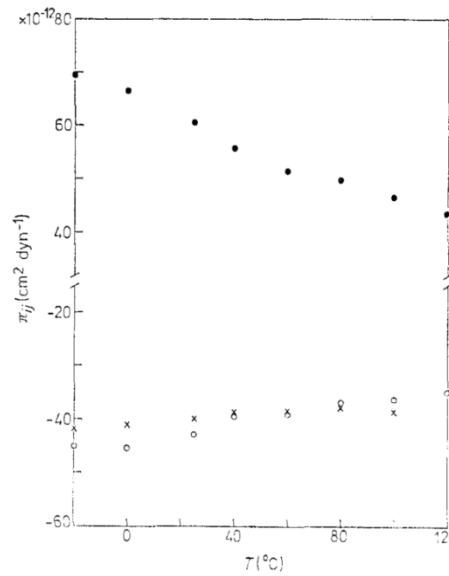
● $\pi_{1\langle 0\bar{1}1\rangle}$ (100) p-channels (3000 ppm °C^{-1}); × π_1 (111) n-channels (800 ppm °C^{-1});
○ $\pi_{t\langle 0\bar{1}1\rangle}$ (100) p-channels (1700 ppm °C^{-1}).

Figure 2.25. Temperature dependence of some piezoresistive coefficient for n- and p-MOSFET [27].

2.3 – Noise

In electronics, the *noise* is any unwanted random fluctuation in a measured signal. Let's consider for example a doped silicon resistor, *R*, biased by a noise-free constant current, *I*, which can be also 0. The voltage, *V*, has a constant mean value, but it has also fluctuations, at any frequency. These fluctuations are called noise (Figure 2.26). This can be *intrinsic* of the device under test or *extrinsic*, due to external sources. In general the extrinsic noise depends on the environment, it can vary a lot and it can be removed. A typical extrinsic noise is the 50 Hz (or 60 Hz) signal that is present almost everywhere and it is due to the power lines. Hereafter, therefore, we will focus just on the intrinsic noise of doped silicon resistors and of MOSFETs.
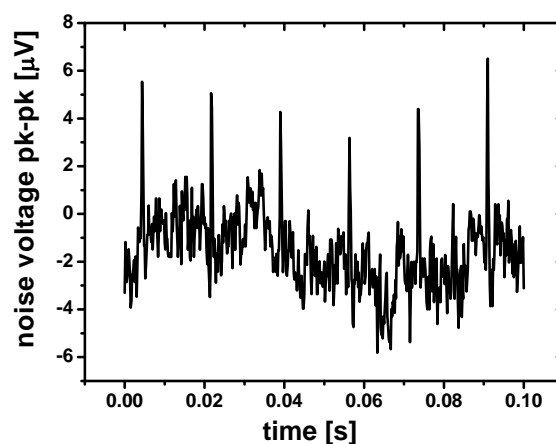
Figure 2.26. Noise in a resistor. Peaks are extrinsic noise at 60 Hz.

2.3.1 – Silicon resistor.

The intrinsic noise of a resistor can have different sources. The dominant one is the electrical noise although there are also some other important sources. A common way of representing the noise in frequency domain is to report the *power spectral density* (PSD) of the signal with [V^2/Hz] units (Figure 2.27). This is done transforming the signal from time domain to frequency domain, using the Fourier transform. A typical PSD for silicon doped resistor is the one reported in Figure 2.27. Two zones can be distinguished. At high frequencies there is no dependence. At lower frequencies there is 1/f dependence. The first is commonly called *thermal noise* (or Johnson-Nyquist noise), while the second is named *1/f noise* (or Hooge noise). If we analyze piezoresistive MEMS structures, like the cantilevers, then we have to consider also the *thermomechanical noise.*
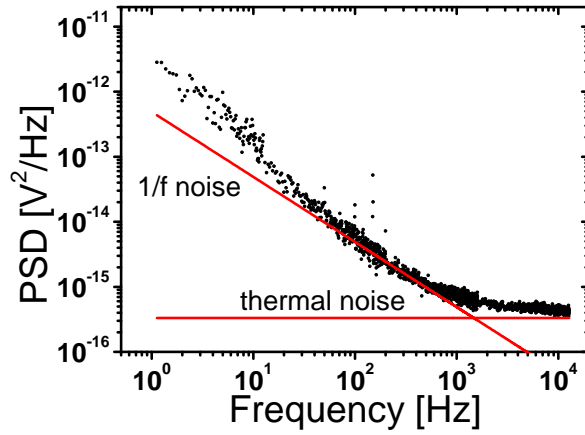
Figure 2.27. Power spectral density of a resistor. The data are fitted with thermal noise and 1/f noise expressions (eq. 2.64, 2.66).

2.3.1.1 – Thermal noise

Thermal noise was observed for the first time by Johnson [30] and explained by Nyquist [31]. This noise is caused by the thermal agitation of the charge carriers of the conductor. The PSD of this noise is independent of the frequency and it is proportional to the Bolzmann constant, k_B [J/K] the temperature, T [K], and the resistance, R [Ω]:

$$S_{R,J} = 4k_B TR \qquad (2.68)$$

The root mean square (RMS) noise voltage can be calculated by integrating the PSD in a certain bandwidth (f_{max}-f_{min}):

$$V_{R,J} = 2\sqrt{k_B TR(f_{max} - f_{min})} \qquad (2.69)$$

where f_{max} and f_{min} are the maximum and minimum frequency of the bandwidth that we choose.

2.3.1.2 – 1/f noise

1/f noise is maybe the most studied noise source. Despite this, it is not completely understood in semiconductors and it is still an active topic. During the years two main theories and models have acquired importance. In the McWhorter model [32], also called *number fluctuation model*, it is believed that the noise is caused by the random trapping and detrapping of the mobile carriers in the trap located at the Si-SiO$_2$ interface. On the other hand Hooge [33, 34] affirmed that this noise is due to fluctuation in the mobility of the free charge carriers when they collide with the crystal lattice. This model is therefore also called

mobility fluctuation model. According to this second empirical model, the PSD can be described by:

$$S_{R,H} = \frac{\alpha V_{bias}^2}{N} \frac{1}{f}$$

(2.70)

where V_{bias} [V] is the bias voltage of the resistor, N is the total number of charge carriers, f [Hz] is the frequency and α is the so called Hooge factor. The RMS noise voltage in a certain bandwidth is:

$$V_{R,H} = V_{bias} \sqrt{\frac{\alpha}{N} ln\left(\frac{f_{max}}{f_{min}}\right)}$$

(2.71)

α is dimensionless parameters that can vary in function of the doping technique and fabrication process details [35-37]. It is therefore ascribed to the lattice quality and the typical range of variation is 10^{-3} to 10^{-7}.

2.3.2 – MOSFET

The noise in the MOSFET case is pretty similar. We can identify electrical noise sources and mechanical noise sources. Hereafter we speak just about the electrical sources since the electromechanical noise is the same as in a piezoresistive cantilever. The electrical noise sources in a MOSFET transistor are [38-40]:

- Thermal noise in channel
- 1/f noise
- Noise in the resistive gate
- Noise due to the distributed substrate resistance
- Shoot noise associated with the leakage current of the drain source reverse diodes.

Also in this case the dominant sources are the thermal noise in the channel and the 1/f noise.

2.3.2.1 – Thermal noise

The current flowing between the drain and the source terminal in a transistor is based on the existence of an inverse resistive channel between them, as explained in the previous section 2.2.2. The inverse resistive channel is formed by the minority carriers in the substrate under the appropriate control of the gate voltage. In analogy to a resistance, the random motion of the free carriers within the inverse channel generates thermal noise at the device terminal. In the extreme case when the drain source voltage $V_{DS}=0$ the channel

can be treated as a homogeneous resistor. Therefore the thermal noise current spectral density is similar to the one of a resistor and is given by:

$$S_{ID,J} = 4k_B T g_0 \tag{2.72}$$

Where g_0 [1/Ω] is the channel conductance at V_{DS}=0 V. Normally V_{DS}>0 therefore it is not possible anymore to consider the channel as homogeneous resistor. It has to be divided in small parts, in these calculated the noise, and the noise integrated along the whole channel. Finally, for the saturation region, we can write [38]:

$$S_{ID,J} = \gamma(4k_B T g_m) \tag{2.73}$$

where g_m is the transconductance of the MOSFET and γ is a complex function of the basic transistor parameters and bias conditions. To give a value to γ a numeric approach is required. However typical values are between 2/3 and 1, for a gate oxide thickness of 50 nm and substrate concentrations around 10^{16} atoms/cm^{-3} [38]. If we integrate the spectral density in a certain bandwidth we obtain:

$$I_{D,J} = 2\sqrt{\gamma k_B T g_m (f_{max} - f_{min})} \tag{2.74}$$

2.3.2.2 – 1/f noise

Among all the active integrated devices, MOSFET transistors show the highest 1/f noise of all, due to their surface conduction mechanism [38]. This fact together with the lack of satisfactory theory resulted in an enormous number of papers in the literature on the discussion of 1/f noise in MOSFET both theoretically and experimentally. As it is for the resistors, also in the MOSFET case we find the mobility fluctuation and the number fluctuation models. Following the Hooge model the noise current spectral density is expressed by:

$$S_{ID,H} = \frac{\alpha I^2}{N}\frac{1}{f} \tag{2.75}$$

where α is the Hooge parameter, N is the total number of free carriers in the device, I the short circuit drain current and f the frequency. Like for the thermal noise, for a MOSFET in saturation region we have to divide the channel in small parts, in this calculate the noise, and integrate it along the whole channel. The total 1/f current noise power spectral density can be calculated by:

$$S_{ID,H} = \alpha \frac{q\mu_f (V_{Gs} - V_T)I_D}{L_{Ch}^2}\frac{1}{f} \tag{2.76}$$

where q is the elementary charge, μ_f is the so-called 1/f noise mobility which depends strongly on the bias conditions, V_{GS} and V_T are the gate voltage and the threshold voltage, I_{DS}

is the drain current and L_{CH} is the channel length. The noise current in a certain bandwidth can be calculated after integrating the previous formula:

$$I_{D,H} = \sqrt{\alpha \frac{q\mu_f(V_{Gs} - V_T)I_{DS}}{L_{Ch}^2} \ln\left(\frac{f_{max}}{f_{min}}\right)}$$

(2.77)

2.3.3 –Thermomechanical noise

A third noise source, the thermomechanical noise, is an electromechanical noise and derives from the fact that the cantilever is a moving beam. It is the mechanical analog of Johnson noise and consists of physical oscillations of the beam. Its origin is the Brownian movement of the particles surrounding the structure, which cause the vibrations. If a piezoresistor or a MOSFET are integrated into a beam then the resistivity or the drain current fluctuates, creating an additional noise in the signal. This places the lower limit on the resolution of all mechanical sensors. This noise is a white noise, at frequencies lower than the resonance frequencies and for beam with low quality factors. The power spectral density is [V^2/Hz] [35]:

$$S_{th} = S_F^2 \frac{4kk_BT}{\omega_0 Q}$$

(2.78)

Except at resonance, this noise source has always been smaller than 1/f and thermal noise [35], therefore, it will be neglected in the remainder of the thesis.

References

1. Love, A., *A treatise on the mathematical theory of elasticity,* 1944: New York: Dover Publications.
2. Timoshenko, S., *Strength of Materials,* 1949: D. Van Nostrand Company, Inc.
3. Hearn, E.J., *Mechanics of Materials I,* 1997: Butterworth Heinemann.
4. Wortman, J.J. and R.A. Evans, *Young's Modulus, Shear Modulus, and Poisson's Ratio in Silicon and Germanium.* Journal of Applied Physics, 1965. **36**(1): p. 153-156.
5. Villanueva, L.G., *Development of Cantilevers for Biomolecular Measurements*, 2006, Universitat Autonoma de Barcelona.
6. Thomson, W., *On the electro-dynamic qualities of metals: effects of magnetization on the electric conductivity of nickel and of iron.* Proceedings of the Royal Society of London, 1856. **8**: p. 546-550.
7. Bardeen, J. and W. Shockley, *Deformation potentials and mobilities in non-polar crystals.* Physical Review, 1950. **80**(1): p. 72.
8. Smith, C.S., *Piezoresistance effect in germanium and silicon.* Physical Review, 1954. **94**(1): p. 42-49.
9. Kanda, Y., *Piezoresistance effect of silicon.* Sensors and Actuators A: Physical, 1991. **28**(2): p. 83-91.
10. He, R. and P. Yang, *Giant piezoresistance effect in silicon nanowires.* Nature Nanotechnology, 2006. **1**(1): p. 42-46.
11. Richter, J., et al., *Piezoresistance in p-type silicon revisited.* Journal of Applied Physics, 2008. **104**(2): p. 023715-023715-8.
12. Mason, W.P. and R.N. Thurston, *Use of piezoresistive materials in the measurement of displacement, force, and torque.* The Journal of the Acoustical Society of America, 1957. **29**: p. 1096.
13. Kanda, Y., *A graphical representation of the piezoresistance coefficients in silicon.* IEEE Transactions on Electron Devices, 1982. **29**(1): p. 64-70.
14. Kanda, Y., *Graphical representation of the piezoresistance coefficients in silicon-shear coefficients in plane.* Japanese Journal of Applied Physics Part 1-Regular Papers Short Notes & Review Papers, 1987. **26**(7): p. 1031-1033.
15. Tufte, O.N. and E.L. Stelzer, *Piezoresistive properties of silicon diffused layers.* Journal of Applied Physics, 1963. **34**(2): p. 313-318.
16. Tufte, O.N. and E.L. Stelzer, *Piezoresistive properties of heavily doped n-type silicon.* Physical Review, 1964. **133**(6A): p. A1705.
17. Harley, J.A., *Advances in Piezoresistive Probes for Atomic Force Microscope*, 2000, Stanford University.
18. Kahng, D., *Electric field controlled semiconductor device*, U.S. Patent, Editor 1960.
19. Lilienfeld, J.S.E., *Method and apparatus for controlling electric currents*, U.S. Patent, Editor 1926.
20. Colman, D., R.T. Bate, and J.P. Mize, *Mobility anisotropy and piezoresistance in silicon p-type inversion layers.* Journal of Applied Physics, 1968. **39**(4): p. 1923-1931.
21. Dorey, A.P. and T.S. Maddern, *The effect of strain on MOS transistors.* Solid State Electronics, 1969. **12**(3): p. 185-189.
22. Dorda, G., *Piezoresistance in quantized conduction bands in silicon inversion layers.* Journal of Applied Physics, 1971. **42**(5): p. 2053-&.

23. Dorda, G., H. Friedrich, and E. Preuss, *Band Structure Investigation on p-Type Silicon Inversion Layers by Piezoresistance and Mobility Measurements.* Journal of Vacuum Science and Technology, 1972. **9**(2): p. 759-761.

24. Bradley, A.T., et al., *Piezoresistive characteristics of short-channel MOSFETs on (100) silicon.* IEEE Transactions on Electron Devices, 2001. **48**(9): p. 2009-2015.

25. Mikoshiba, H., *Stress-sensitive properties of silicon-gate MOS devices.* Solid State Electronics, 1981. **24**(3): p. 221-232.

26. Wang, Z.Z., J. Suski, and D. Collard, *Piezoresistive simulation in MOSFETs.* Sensors and Actuators A: Physical, 1993. **37-38**: p. 357-364.

27. Canali, C., et al., *Piezoresistivity effects in MOS-FET useful for pressure transducers.* Journal of Physics D-Applied Physics, 1979. **12**(11): p. 1973-1983.

28. Vatedka, R., et al., *Effect of high drain voltage on stress sensitivity in nMOSFETs.* Sensors and Actuators a-Physical, 2007. **140**(1): p. 89-93.

29. Gallon, C., et al., *Electrical analysis of external mechanical stress effects in short channel MOSFETs on (001) silicon.* Solid-State Electronics, 2004. **48**(4): p. 561-566.

30. Johnson, J.B., *Thermal agitation of electricity in conductors.* Physical Review, 1928. **32**(1): p. 97.

31. Nyquist, H., *Thermal agitation of electric charge in conductors.* Physical Review, 1928. **32**(1): p. 110-113.

32. McWhorter, A.L., *1/f noise and related surface effects in germanium*1955, Cambridge: MA: MIT Lincoln Laboratory.

33. Hooge, F.N., *1/f noise is no surface effect.* Physics Letters A, 1969. **29**(3): p. 139-140.

34. Hooge, F.N., *1/f noise sources.* Electron Devices, IEEE Transactions on, 1994. **41**(11): p. 1926-1935.

35. Harley, J.A. and T.W. Kenny, *1/f noise considerations for the design and process optimization of piezoresistive cantilevers.* Microelectromechanical Systems, Journal of, 2000. **9**(2): p. 226-235.

36. Mallon Jr, J.R., et al., *Low 1/f noise, full bridge, microcantilever with longitudinal and transverse piezoresistors.* Applied Physics Letters, 2008. **92**(3): p. 033508.

37. Yu, X.M., et al., *Optimization of sensitivity and noise in piezoresistive cantilevers.* Journal of Applied Physics, 2002. **92**(10): p. 6296-6301.

38. Zhong Yuan Chang, W.M.C.S., *Low-Noise Wide-Band Amplifiers in Bipolar and CMOS Technologies,* 1991: The Springer International Series in Engineering and Computer Science.

39. Haartman, M.V. and M. Ostling, *Low-frequency noise in advanced MOS devices,* 2007: Springer Publishing Company.

40. Van der Ziel, A., *Noise in solid state devices and circuits,* 1986: Wiley New York.

Chapter III

Piezoresistive cantilever

Piezoresistive cantilever

In this chapter the electromechanical model used to optimize the resolution of the force sensor will be introduce (section 3.1). Then the mask design, the fabrication process and the fabrication issues of the piezoresistive force probes will be pointed out (section 3.2). After presenting the development of new on-wafer characterization set-ups and techniques, the mechanical, electrical and electromechanical performance of the different force probes will be reported.

3.1 – Probe modeling

Here, the electromechanical model used to optimize the performance of the force probes with embedded piezoresistor is presented. This model can be also used to extract important materials parameters, like silicon piezoresistive coefficient, materials Young's modulus and Hooge factor for 1/f noise. The model is developed considering that the cantilever is loaded by a vertical (z- direction, Figure 3.1.A) point force in the free end and behaves according to the linear elastic theory (see previous section 2.1).

The most important parameters determining the performance of a quasi-static *force sensor* based on piezoresistive cantilevers are the spring constant k_C [N/m], the force sensitivity $S_{F,V}=\Delta V/F$ [V/N] (or deflection sensitivity $S_\delta=\Delta V/\delta$ [V/m]), the transducer noise, V_n [V], and the force resolution R_F [N], also called minimum detectable force (MDF). The spring constant is a parameter that relates the cantilever deflection with the force applied on the structure. The lower the spring constant, the higher the deflection for the same applied load. The force (or displacement) sensitivity is the parameter that says how much the transducer output signal varies upon the application of a load (or a deflection). Finally the resolution is the minimum force (or displacement) that the sensor can detect. An additional parameter that has to be taken into consideration is the resonance frequency of the beam. This tell us how fast a measurement can be performed: from the resonance frequency derives the frequency range over which the force probes can be used.

The electromechanical model is presented after assuming a suitable cantilever structure. Using this model we calculated the deflection and force sensitivities and considering the two main noise sources, we finally calculated the sensor resolution dependence on the various parameters.

A suitable structure for a piezoresistive force sensor based on a self-sensing cantilever that has to function properly in liquid environment is composed at least by (Figure 3.1.A):

- a mechanical layer (silicon in this case)
- a transducer layer (a piezoresistor in this case)
- an insulating layer (silicon nitride in this case).
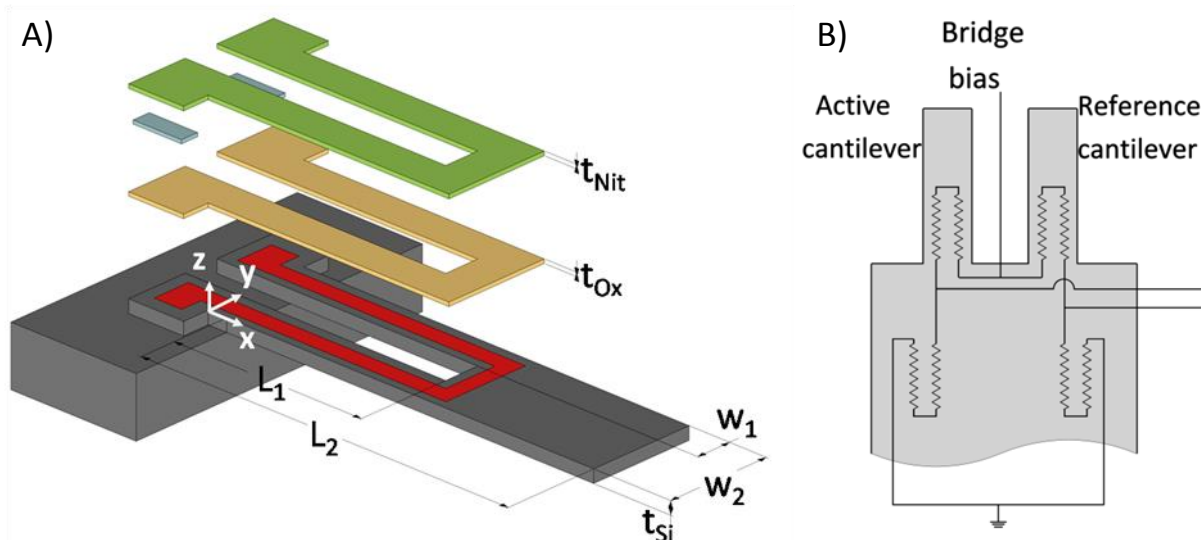
Figure 3.1 . A) Exploded view of the piezoresistive cantilever with typical dimensions. From the top there are: PECVD silicon nitride (t_{Nit} = 100 nm), thermal oxide (t_{Ox} = 38 nm), implanted crystalline silicon, and crystalline silicon (t_{Si} =325 nm). L_1 = 125 µm is half of the length of the piezoresistor and also the length of the multilayer part. L_2 = 250 µm is the total length of the cantilever. The implanted piezoresistor is visible on the silicon. z_{ti} and z_{di} are the top and the bottom z coordinates of the layers, with i = 1 for silicon nitride, i = 2 for silicon oxide, and i = 3 for silicon. B) Electrical scheme of the sensor. In each chip there are 4 piezoresistors: two are embedded into the cantilevers and two are integrated in the chip. They form two voltage dividers which can be externally connected to form a ¼ active Wheatstone bridge. The two cantilevers can be equal and one acts as reference, while the second one is be used as probe.

The *mechanical layer* is the one that contributes the most to the mechanical properties of the sensor: spring constant and resonance frequency. Silicon has been chosen because it has very good mechanical properties [1, 2], because the microfabrication processes are very well established and because doped silicon has high piezoresistive coefficients and therefore the transducer layer can be easily embedded. The *transducer layer* has to convert the mechanical bending into an easily measurable physical quantity. Doped silicon translates the mechanical elongation of the beam bending, into electrical resistance variation. The *insulating layer* has to electrically insulate the conductors (i.e. the piezoresistor) when they are in liquid environment. Silicon nitride has been chosen because it is a good barrier for water based solutions and it has good insulation and mechanical properties if compared to others materials like silicon oxide or polymers [3-6]. Finally, a thin layer of silicon oxide guarantees better electrical properties to the silicon piezoresistor reducing defect densities at the interface.

The cantilever can have constant or variable cross section along the x-axis. A smart way of fabricating the cantilever used already by many authors, and probably the most common one, is to choose the so called U-shaped cantilever [7]. With this structure we obtain the main advantage of reducing the spring constant and so increasing the force resolution. On

one hand the spring constant is reduced because part of cantilever is etched away. On the other hand this design allows higher downscaling of the cantilever width. If this design is not used, for very narrow piezoresistor legs the two depletion regions can come into contact if the lateral dopant diffusion is not considered very well. Even if the two legs are far from each other, in some cases there can be leakage current, reducing the sensitivity and increasing the noise [8]. If the two legs of the piezoresistor are physically separated we avoid this problem. This allows reducing more the cantilever width and therefore its spring constant.

A common way to read out the resistance change of the piezoresistor embedded into a deflected cantilever is to integrate it into a Wheatstone bridge (Figure 3.1.B). Choosing a symmetrical bridge (two piezoresistors embedded into two cantilevers and two into the chip) is beneficial for a linear response on deflection and reduced temperature dependence of the sensor [9].

3.1.1 – Mechanical model

The spring constant of a cantilever is defined as:

$$k_c = \frac{F}{\delta} \tag{3.1}$$

where *F* is the force actuating at the cantilever end and δ the deflection. In the case of a multilayer, U-shaped cantilever (Figure 3.1) k_c can be calculated taking into consideration the equations (2.47(2.52) (section 2.1.5):

$$k_c = -\frac{3EI_1 EI_2}{(L_1 - L_2)^3 (EI_1 - EI_2) - L_2^3 EI_2} \tag{3.2}$$

where *EI₁* is the bending stiffness of the multilayer part of the beam, *x=[0,L₁]*, and *EI₂* is the bending stiffness of the second part, *x=[L₁,L₂]*.

3.1.2 – Sensitivity

In the previous section 2.2.1, we saw that, when a piezoresistor is mechanically stressed, the relative change of the resistance value (*ΔR/R₀*) is the result of the change of the resistor dimensions (length *l*, width *w* and thickness *t*) and of the resistivity (*ρ*). In the case of low doped crystalline silicon, the change of the resistivity in certain directions (i.e. <100>) is larger than the dimensional changes by a factor of 50, thus:

$$\frac{\Delta R}{R_0} = \frac{\Delta \rho_R}{\rho_{R_0}} = \pi_l \sigma \tag{3.3}$$

where the π_l is the longitudinal piezoresistive coefficient for that certain direction. The cantilever under study is modeled as a linear elastic beam with a point load at the tip, as explained in the previous section. This leads to a longitudinal stress (σ_x) along the two legs of the cantilever that varies linearly along x and z and to a negligible transverse stress along y. Considering that the resistor, thus the current, and the stress are parallel and along the <100> direction we can write:

$$\frac{\Delta R}{R_0} = \pi_{11}\langle\sigma_{R,x}\rangle = \frac{G}{E_{R,100}}\langle\sigma_{R,x}\rangle \tag{3.4}$$

where π_{11} is the longitudinal piezoresistive coefficient for the crystallographic direction <100> , <$\sigma_{R,x}$> is the longitudinal mean stress in the resistor in the x direction and $E_{R,100}$ is the young modulus of the piezoresistor in the 100 crystallographic direction. We have chosen the <100> direction as example, because it is also the one that optimize the piezoresistive coefficient for n-doped silicon. We used this direction also for fabricating the cantilevers.

Knowing the deflection of the cantilever between 0 and L_1 (2.49), we can calculate the stress in the piezoresistor:

$$\sigma_R = -(z - z_0)\left(\frac{d^2}{dx^2}\delta_1\right)E_{R,100} = \frac{(z - z_0)}{EI_1}(x - L_2)E_{R,100}F \tag{3.5}$$

The average stress in the piezoresistor is obtained integrating the stress in the length and thickness and dividing the result by the length and thickness:

$$\langle\sigma_{R,x}\rangle = \frac{1}{L_1 t_R}\frac{E_{R,100}F}{EI_1}\int_0^{L_1}(x - L_2)dx\int_{-t_R}^{0}(z - z_0)\,dz$$
$$= -\frac{1}{4}\frac{E_{R,100}F(-L_1 + 2L_2)(t_R + 2z_0)}{EI_1} \tag{3.6}$$

where t_R is the thickness of the resistor (in this case we have approximated the doping profile with a step profile). Now, considering that for a ¼ active Wheatstone bridge (Figure 3.1.B) biased by a certain voltage, V_{BIAS}, it is:

$$\frac{\Delta V}{V_{BIAS}} = \frac{1}{4}\frac{\Delta R}{R_0} \tag{3.7}$$

the force sensitivity is:

$$S_{F,V} = \frac{\Delta V}{F} = -\frac{1}{16}\frac{G(-L_1 + 2L_2)(t_R + 2z_0)}{EI_1}V_{BIAS} \tag{3.8}$$

or in terms of piezoresistive coefficient:

$$S_{F,V} = -\frac{1}{16}\frac{E_{R,100}\pi_{11}(-L_1 + 2L_2)(t_R + 2z_0)}{EI_1}V_{BIAS} \tag{3.9}$$

This model is valid in principle if the piezoresistance is homogeneously doped and has a sharp p-n junction. This is possible just when epitaxial growth is used. In the case of implantation followed by annealing, the doping concentration is not constant through the thickness. It should be, therefore, developed a model that takes into consideration the z

dependence of the conductivity and piezoresistive coefficient. Tortonese [7] has been the first taking into consideration this aspect introducing the efficiency factor, β. Park [10, 11] slightly modified this factor, including the piezoresistance factor, *P*, just in the numerator:

$$\beta^* = \frac{2}{t_c} \frac{\int_{-t_c/2}^{t_c/2} P\mu n z \, dz}{\int_{-t_c/2}^{t_c/2} \mu n z \, dz} \tag{3.10}$$

In any case, the efficiency factor can be calculated by dividing the force sensitivity for an arbitrary dopant concentration profile, by the theoretical maximum force sensitivity. The maximum sensitivity is obtained for an infinitesimally thin and low doped piezoresistor located on the silicon surface. The maximum force sensitivity in our case would be:

$$S_{F,V} = -\frac{1}{8} \frac{E_{R,100} \pi_{11} (-L_1 + 2L_2) z_0}{E I_1} V_{BIAS} \tag{3.11}$$

At IMB-CNM, we have a large experience in ion implantation. In our case we use As to obtain a shallow junction, due to its low penetration and small diffusion. Due to the concentration-dependence of the diffusion coefficient of As in silicon [12], the profiles after a thermal annealing are fairly abrupt [13-15], which have been previously characterized by spreading resistance. We have therefore approximated the abrupt dopant profile by a step function in order to obtain a simpler analytical approximation for the force sensitivity.

3.1.3 – Noise and bandwidth

The performance of the cantilever is limited by the noise. Here we will take into consideration just the two major noise sources: thermal noise and 1/f noise, called also Hooge noise. The thermomechanical noise in fact has lower power for similar force probes and therefore we didn't take it into consideration [16, 17], as discussed in 2.3.3.

The thermal noise of a balanced Wheatstone bridge is equal to the noise of a single resistor, so that the overall noise power for the Wheatstone bridge in the frequency bandwidth from f_{min} to f_{max} is [18]:

$$V_{R,J}^2 = 8k_B T R_S \frac{L_1}{w_R} (f_{max} - f_{min}) \tag{3.12}$$

where $R_S = \rho/t_R$, is the sheet resistance, which can be easily measured, $L_1 = 1/2 \, L_R$ is half of the length of the resistor and w_R is the width of the resistor.

A piezoresistive Wheastone bridge can be made by 1, 2 or 4 silicon doped resistors. In our case we use 4 doped resistors for temperature compensation therefore the Hooge noise is [19]:

$$V_{R,H}^2 = \frac{1}{2} \frac{\alpha V_{BIAS}^2}{L_1 w_R dose} ln\left(\frac{f_{max}}{f_{min}}\right) \tag{3.13}$$

where V_{BIAS} is the bias voltage of the bridge and *dose* is the implantation dose.

The sheet resistance depends on the concentration and therefore on the doping dose and it is calculated from the following empirical carrier mobility expression and resistivity expressions [20]:

$$\mu_n = \mu_{min} + \frac{\mu_{max} - \mu_{min}}{1 + \left(\frac{n}{N_r}\right)\alpha_\mu} \tag{3.14}$$

$$\rho = \frac{1}{q\mu_n n} \tag{3.15}$$

In the case of arsenic, the fitting parameters are μ_{min}=52.2 cm^2/Vs, μ_{max}=1472 cm^2/Vs, N_r=9.68 10^{16} and α_μ=0.68, *n* is the doping concentration ($n=dose/t_R$) and q=1.6 10^{-19} C is the elementary charge.

Typically the atomic force spectroscopy biomolecule recognition experiments are done in a timescale of 1 second and the data are acquired at frequency between 0.5 kHz and 10 kHz, depending on pulling speed and on the atomic force microscope. In the calculation and in the measurements of the noise, we consider therefore always the maximum bandwidth of 1Hz-10 kHz.

3.1.4 – Resolution

The force resolution, which is defined as the *minimum force* that can be *detected* (**MDF**), is commonly considered as the RMS force noise:

$$MDF = \frac{\sqrt{V_{R,J}^2 + V_{R,H}^2}}{S_{F,V}} = -\frac{8\sqrt{32k_B T R_S \frac{L_R}{W_R}(f_{max} - f_{min}) + 2\frac{\alpha V_{bias}^2}{L_R W_R dose}ln\left(\frac{f_{max}}{f_{min}}\right)}}{E_{100}\pi_{11}(2L_2 - L_1)(t_R + 2z_0)V_{bias}}EI_1 \tag{3.16}$$

And it has been calculated from the equations (3.11)-(3.13).

3.1.5 – Optimization

In order to improve the force resolution, we have to maximize the force sensitivity and minimize the total noise or in other words to minimize the *MDF*. This is not at all a simple task, in fact many parameters influence both sensitivity and noise. For example, for higher doping concentration, we decrease the 1/f and the thermal noises. At the same time also the force sensitivity decreases because the piezoresistive coefficient drops.

In the electromechanical model presented in the previous sections we take into consideration 9 parameters that can be divided in design, process and operation

parameters. The *design parameters* are the ones that depend completely on our choice and we fix them during the design of the masks for the photolithography and during the wafer selection. They are the length (L_2 or L_C), silicon thickness (t_{Si}) and arm width (w_1) of the cantilever and the relative length ($\lambda_R = L_R/L_2$) and width ($\omega_R = w_R/w_1$) of the piezoresistor. The *process parameters* depend on the fabrication process. They are the dopant implantation dose (*dose*), the Hooge factor (α) of the 1/f noise and the relative piezoresistor thickness ($\tau_R = t_R/t_{Si}$). Finally we consider just one *operation parameter*: the bias voltage of the Wheatstone bridge (V_{BIAS}). Also the bending stiffness of the multilayer part, EI_1, influences the sensitivity. However, it depends on the cantilever arm width, on the silicon thickness and on the thicknesses of the silicon oxide and silicon nitride. The first two parameters have been taken already into account and the oxide and nitride should be as thin as possible because thicker they are, lower the sensitivity. At the same time, considering the PECVD silicon nitride deposited in the IMB-CNM cleanroom, this should have a minimum thickness of 100 nm in order to insulate well the conductors. Therefore the nitride is always considered to be 100 nm thick and the silicon oxide 38 nm thick, even though, because of the fabrication process it is thinned at around 10 nm (see next section 3.2).

Hereafter we will present the $S_{F,V}$ and *MDF* dependence on these 9 parameters. For this, we fix suitable starting values (Table 3.1) of all parameters except one, which is varied in a range constrained by technological and practical issues. Starting lengths and widths are chosen according to the previously designed masks (section 3.2.1) and the silicon thickness accordingly to 4'' SOI wafer available at IMB-CNM. The dose corresponds to a concentration of 10^{-20} atoms/cm^3 considering the relative resistor thickness, which was chosen according to the previous studies of Harley [21]. For the Hooge factor we have chosen a typical value for implanted piezoresistors [19] and for the bias voltage a typical value used in literature.

All the results are reported in normalized graphs.

L_C [μm]	w_1 [μm]	t_{Si} [μm]	$\lambda_R = L_R/L_2$	$\omega_R = w_R/w_1$	$\tau_R = t_R/t_{Si}$	*dose* [cm^{-2}]	α	V_{bias} [V]
250	2	0.325	0.5	1	0.33	1 10^{15}	1x10^{-3}	5

Table 3.1. Starting values for the different parameters: cantilever length L_C, cantilever arm width w_1, silicon cantilever thickness t_{Si}, relative piezoresistor length λ_R, relative piezoresistor width ω_R, relative piezoresistor thickness τ_R, implantation dose, Hooge factor α, bias voltage V_{BIAS}.

Cantilever length

The cantilever length has big influence on the force resolution. An increase in the length from 100 μm to 1 mm improves the resolution by more than 20 times. This is due to the linear increase of the sensitivity and to the decrease of the noise. The noise decreases

because we fixed a ratio $\lambda_R = L_R / L_c$ and therefore for longer cantilevers, the piezoresistor becomes longer and it has higher total number of charge carriers. However, we should strike a balance between the resolution and the mechanical characteristics of the cantilever, especially considering the resonance frequency. According to eq. (2.53) and to FEM simulations, the resonance frequency of the described cantilever with a length of 250 μm is around 6.5 kHz, which is enough fast for biomolecule detection purposes. Additionally we have to consider that longer cantilevers are far more prone to break during the fabrication and have more sticking problems that leads to much lower fabrication yield.
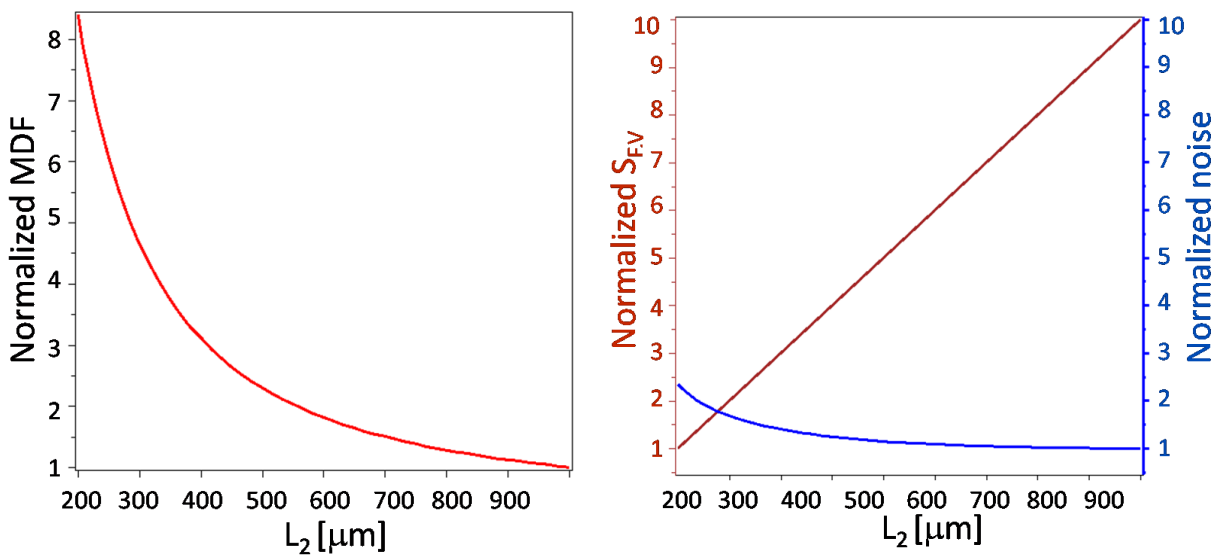
Figure 3.2. Normalized force resolution (left) and normalized force sensitivity and noise voltage (right) dependence on the cantilever length

Cantilever arm width

The decreasing of the width of the cantilever arms from 20 μm to 1 μm leads to a decrease of the cantilever bending stiffness and therefore an increase of the force sensitivity. On the other hand, the resistance becomes narrower and this increases both, 1/f and thermal noises. By decreasing the width from 20 μm to 1 μm, the final result is an improvement of the resolution of more than 4 times. However, we have chosen the minimum width to be 2 μm because the resolution of the photolithographic process is, in practice, approximately 2 μm, with an overlay tolerance of 1 μm.
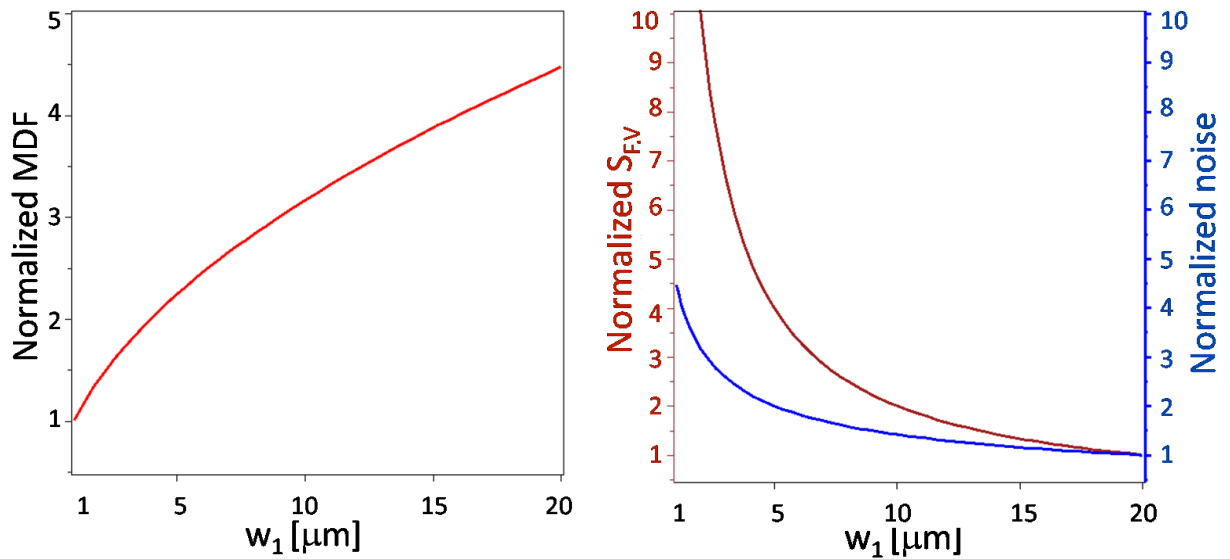
Figure 3.3 Normalized force resolution (left) and normalized force sensitivity and noise voltage (right) dependence on the cantilever arm width.

Silicon thickness

The reduction of the silicon thickness influences the bending stiffness, the position of the neutral axis and also the piezoresistive factor because we fixed the dose and the relative piezoresistor thickness. These variation leads to a sensitivity increase of around 3 times when the thickness decreases from 1 μm to around 300 nm. The 1/f noise, which is the one that contributes the most to the total noise, does not depend on the relative piezoresistor thickness and therefore the total noise is almost unaffected. The final result is that also the force resolution improves by 3 times for the same thickness reduction.
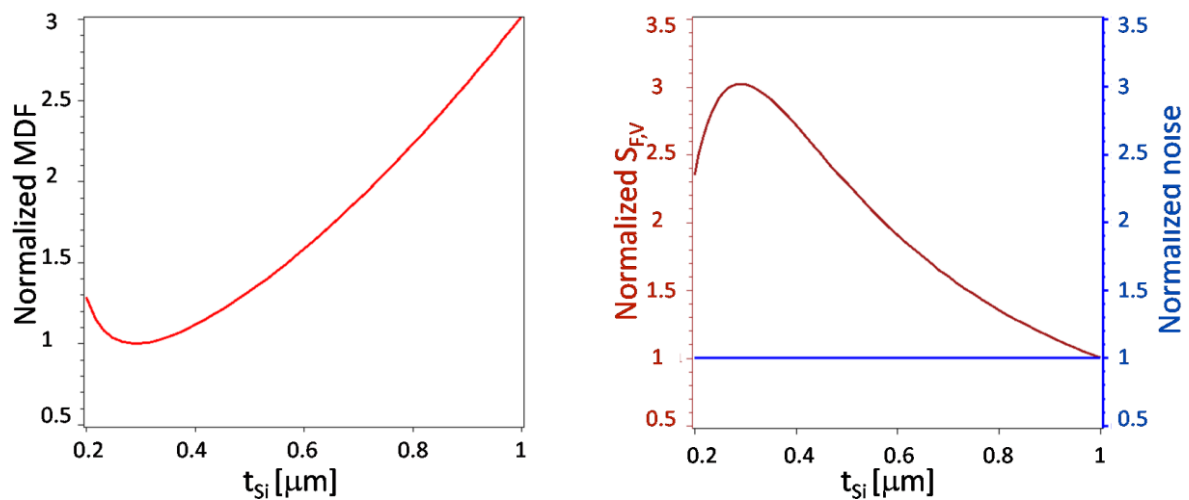
Figure 3.4. Normalized force resolution (left) and normalized force sensitivity and noise voltage (right) dependence on the cantilever thickness.

Piezoresistor length

If the relative length of the piezoresistor, λ_R, is increased from 0.1 to 0.6 of the total length of the cantilever, the resolution improves by a factor of 2. However, the resolution does not change much if λ_R varied between 0.3 and 1 and it has the minimum for λ_R=0.6. The sensitivity decreases by a factor of 2 and the noise decreases by a factor of 5. In fact for longer piezoresistor the 1/f noise decreases because the number of charge carriers increases. Additionally we have to consider that when a piezoresistive cantilever is used in a biomolecular application, the temperature increase due to Joule heating could be an issue. A temperature increase of few tens of degrees of the cantilever end could lead to denaturation of the molecules [22]. For this reason λ_R=0.5 is better than λ_R=0.6.
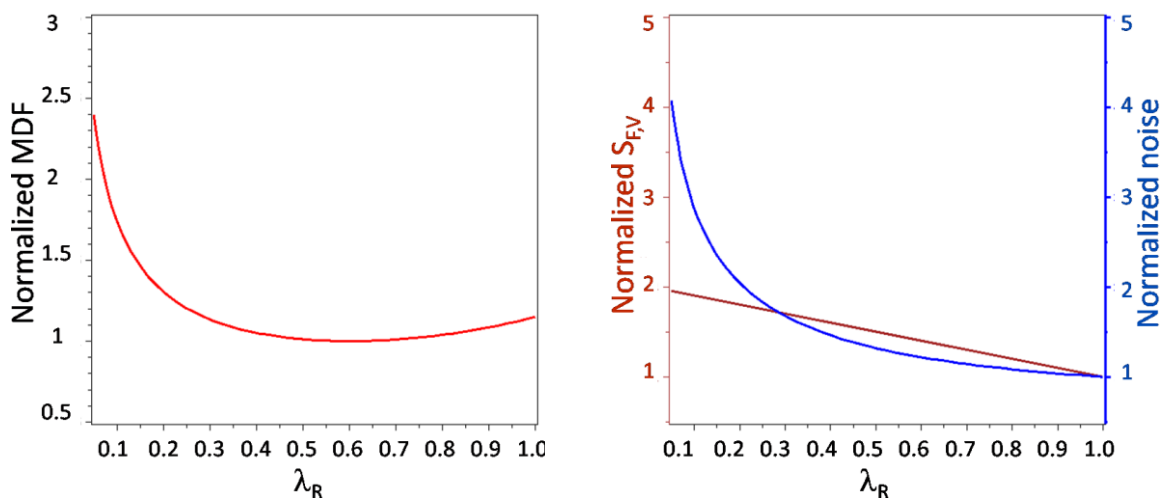
Figure 3.5. Normalized force resolution (left) and normalized force sensitivity and noise voltage (right) dependence on the relative length of the piezoresistor.

Piezoresistor width

For a fixed cantilever arm width, the increase of the relative piezoresistor width, ω_R, from 0.1 to 1, improves the resolution of about 4 times, through the reduction of the noise (i.e. higher number of charge carrier). On the other hand the sensitivity is not affected by the piezoresistor width. The best option is therefore to make the piezoresistor as wide as the cantilever arm.
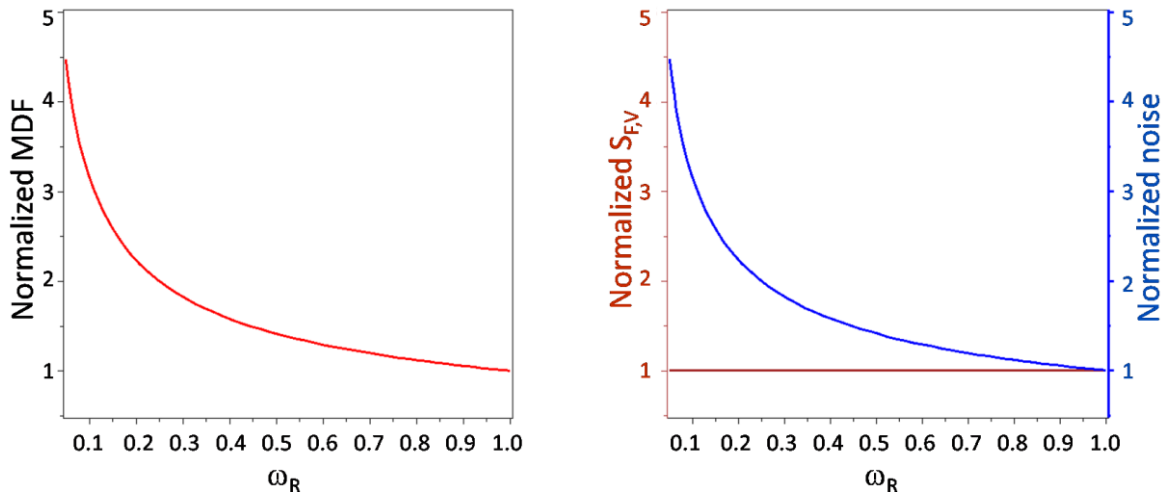
Figure 3.6. Normalized force resolution (left) and normalized force sensitivity and noise voltage (right) dependence on the relative width of the piezoresistor.

Piezoresistor thickness

The reduction of the relative piezoresistor thickness, τ_R, has almost no effect on the noise, but has a strong effect on the sensitivity. For a fixed doping dose, thinner is the piezoresistor, higher the doping concentration and therefore smaller the piezoresistive coefficient. On the other hand, thinner piezoresistors have higher mean mechanical stress. The result is that the sensitivity is maximized for a certain thickness. In this case we have the maximum sensitivity and resolution for relative thickness of τ_R=0.2. The piezoresistor thickness, or better said junction depth, is controlled indirectly by two process parameters: doping implantation energy and doping diffusion length. In order to obtain thin junctions, atomic species with low penetration range and low diffusion coefficient (i.e. arsenic), low implantation energies and low diffusion length thermal treatments should be chosen.
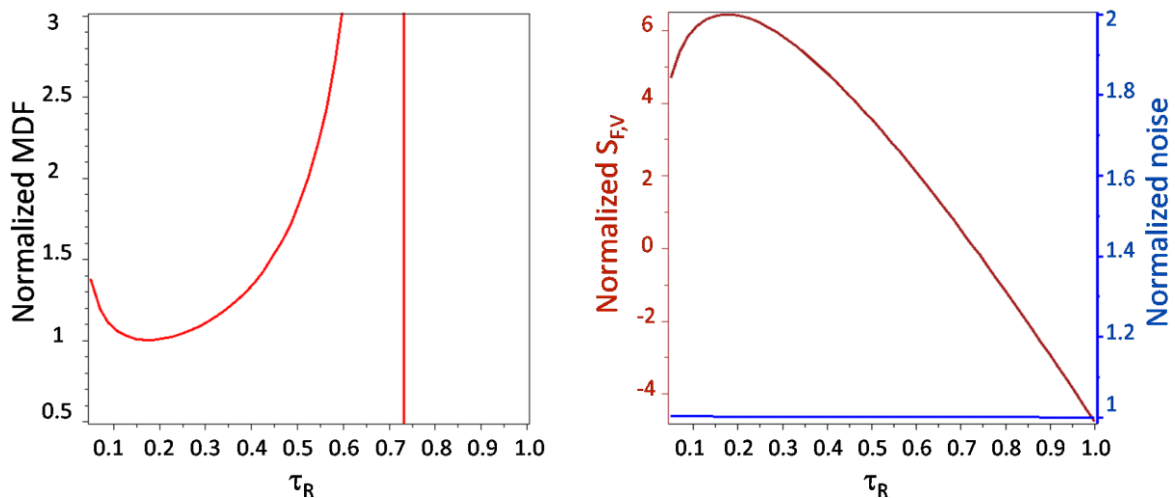
Figure 3.7. Normalized force resolution (left) and normalized force sensitivity and noise voltage (right) dependence on the relative thickness of the piezoresistor.

Dopant implantation dose

The increase in dopant dose increases the dopant concentration, therefore on one hand decreases the gauge factor and the sensitivity, but on the other hand the total noise decreases much faster due to higher number of charge carriers. For doping doses of 1×10^{15} and 1×10^{16} we can have the best performances. Higher doping has also a second positive consequence: the piezoresistive coefficient depends less on the piezoresistor temperature.
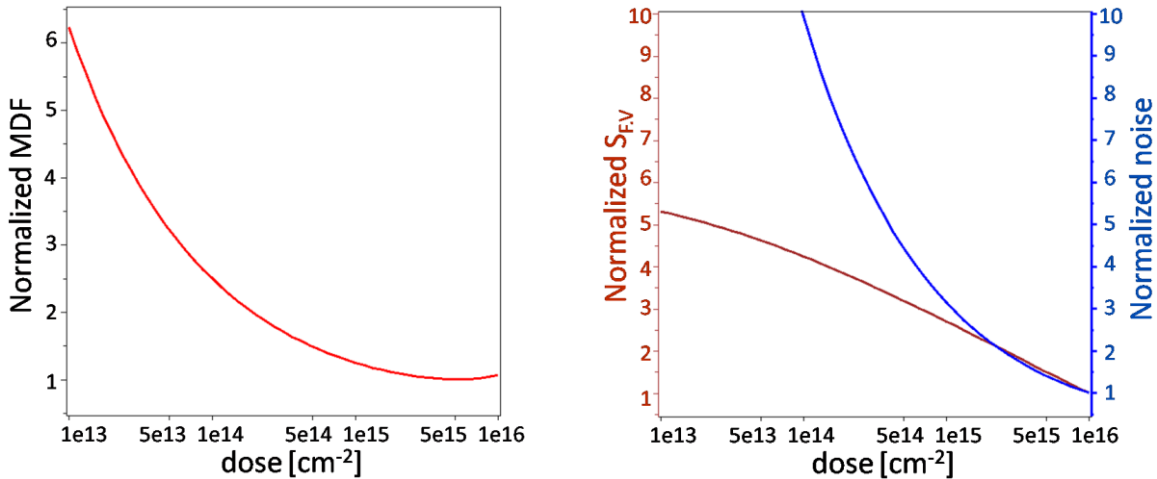
Figure 3.8. Normalized force resolution (left) and normalized force sensitivity and noise voltage (right) dependence on the implantation dose.

Hooge factor

The Hooge factor α is a process parameter that we cannot control directly; it affects just the 1/f noise and depends on the crystalline quality of the piezoresistor. For the best silicon piezoresistor, it can be as low as 10^{-6} and for low quality and implanted silicon piezoresistor can be as high as 10^{-3} [23]. Improvements in the fabrication process and therefore on the silicon crystalline structure can decrease the noise up to 4 times and improve the resolution by the same factor. This factor does not influence the sensitivity.
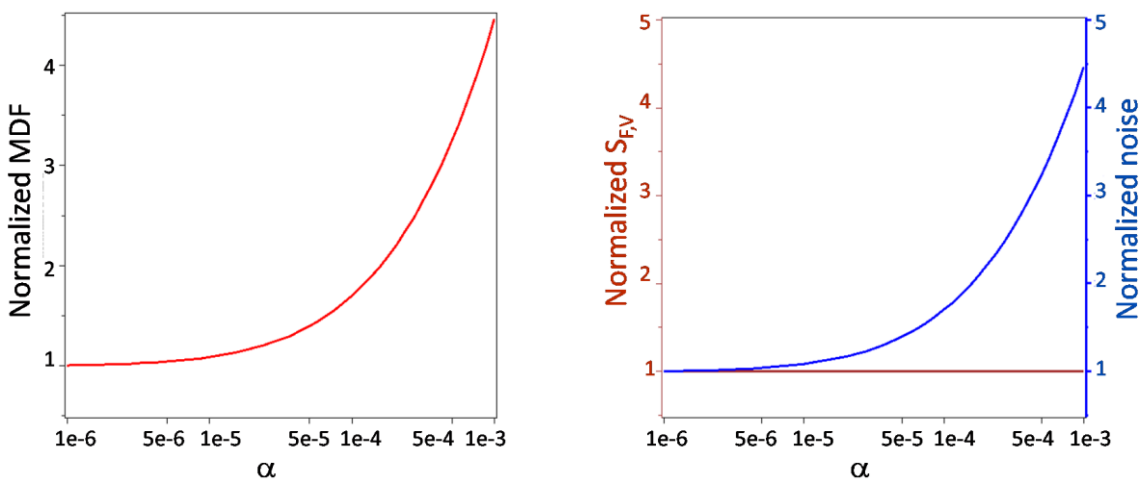
Figure 3.9. Normalized force resolution (left) and normalized force sensitivity and noise voltage (right) dependence on the Hooge factor.

Bias voltage

While using the sensor, we can improve the resolution of around 50% by increasing the bias voltage. In fact, if on one side we increase the 1/f noise, at the same time we increase also the sensitivity. On the other hand, we have to consider that the electrical power dissipated in the piezoresistor scales as V_{BIAS}^2 and excessive power dissipation can increase the temperature of the cantilever with potential damage to sensitive samples, like biomolecules are.
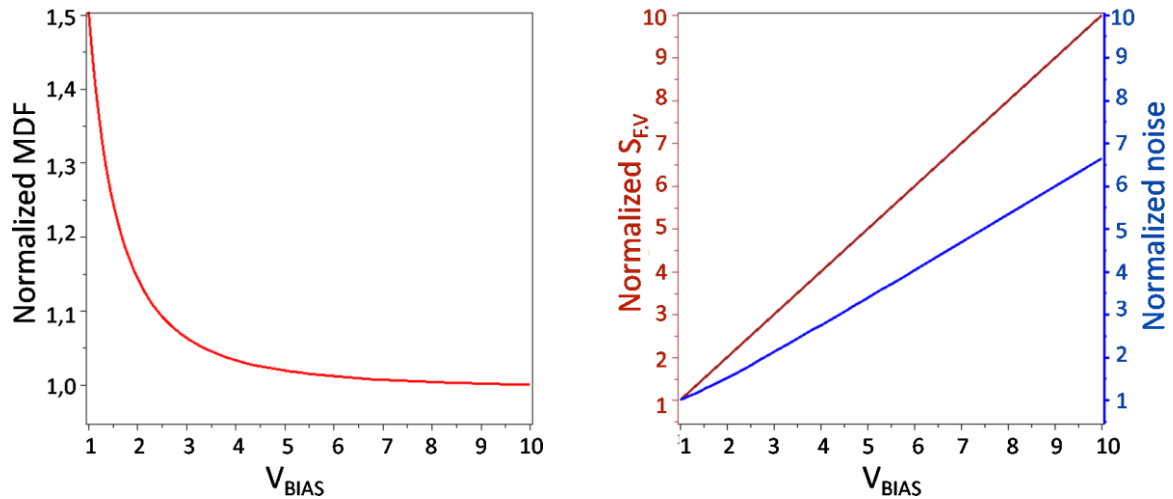
Figure 3.10. Normalized force resolution (left) and normalized force sensitivity and noise voltage (right) dependence on the bias voltage.

Optimization

In Table 3.2 are reported, as example, some values that optimize the force sensitivity. For practical reasons (i.e. available photolitographic masks and SOI wafers at IMB-CNM) we have considered the same widths, lengths and silicon thickness. We have kept constant the implantation dose in order not to exceed the saturation limit and the piezoresistor thickness resulted to be to τ_R=0.2 and. Considering these values the model predicts the following noise, sensitivity and resolution values:

$$noise = 2.4 \ [\mu V]$$
$$S_{F,V} = 3.2 \ 10^5 \ [V/N]$$
$$MDF = 8.3 \ [pN]$$

with a gauge factor G≈52 and a sheet resistance R_S≈117 [Ω/□]. Considering the results is therefore possible a sub-10 pN resolution.

L_C [μm]	w_1 [μm]	t_{Si} [μm]	$\lambda_R = L_1/L_C$	$\omega_R = w_R/w_1$	$\tau_R = t_R/t_{Si}$	dose [cm^{-2}]	α	V_{bias} [V]
250	2	0.325	0.5	1	0.2	$1\ 10^{15}$	$1\ 10^{-4}$	5

Table 3.2. Optimized values of the different parameters: cantilever length L_C, cantilever arm width w_1, silicon cantilever thickness t_{Si}, relative piezoresistor length λ_R, relative piezoresistor width ω_R, relative piezoresistor thickness τ_R, implantation dose, Hooge factor α, bias voltage V_{BIAS}.

3.2 – Microfabrication

In this section, the mask layouts and the microfabrication process of the sensors will be presented. We will point out the several issues encountered during the processing and the solutions we took in order to obtain high process yields and better sensor performances.

3.2.1 – Piezoresistive cantilever design

A set of 7 masks (CNM 671) were designed for the fabrication of the sensors. The masks have been inspired from a previous set of masks (CNM 295) designed by Dr. Luis Guillermo Villanueva. The sensor chips have been designed to have final dimensions of 4.3 mm x 1.5 mm that are approximately the same dimensions of AFM chips. In this way, each chip can be mounted on a commercial AFM and several measurements can be performed: sensitivity, resonance frequency, AFS. Moreover, with these small dimensions, around 400 chips can be microfabricated in a 4'' wafer, therefore, even for relatively low fabrication yields (20%) and relatively high performance deviation, we can have a sufficient number of sensors to perform biological experiments. In every wafer there are also 18 chips for electrical and mechanical characterization and 2 double side alignments widows.

An overview of the different mask levels for a single chip (design 2x250) is reported in the Figure 3.11.A while in the Figure 3.11.B-H we report a close-up of the masks of the most important part of the chip: the cantilevers. On every chip there are alignment marks (bottom-left), name of the chip design (up-left, i.e. 2x250) and name of every single chip (up-right, i.e. M9). In order to name all the 400 chips in the wafer, we choose a battleship stile name (letter-number). In this way every chip can be monitored very easily during production, on-wafer characterization, encapsulation and application.

Every chip has 4 piezoresistors that form a Wheatstone bridge (Figure 3.1.B-H): two are embedded into the cantilevers and two integrated into the chip.

1. The first mask (red, Figure 3.11.B) defines the regions for the implantation and the first alignment marks for the whole process.
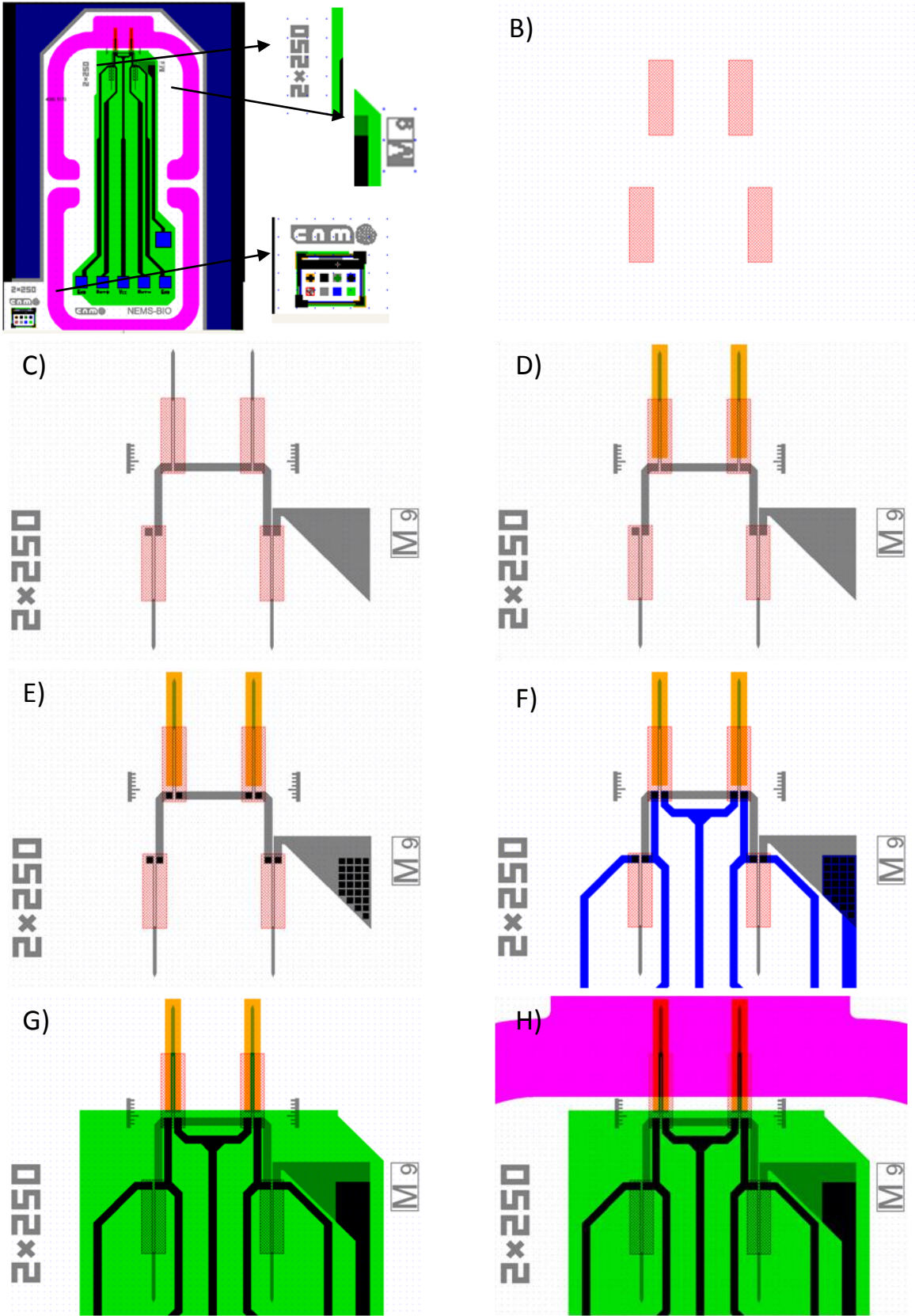
Figure 3.11. A) Overlapping of the 7 mask levels for a single chip (design 2x250). B-H) Close-up of the masks of the cantilever area. B) implantation area; C) cantilever and SOI silicon; D) active area of the cantilever; E) contact windows; F) aluminum interconnections ; G) Silicon nitride passivation area; H) backside DRIE.

2. The second mask (gray, Figure 3.11.C) defines the silicon cantilevers. The piezoresistors are formed, therefore, by implanting (Arsenic) in a big region followed by the etching of the unwanted silicon. All the cantilevers are connected one to each other, so that the lightly p-doped silicon substrate has the same bias.

3. The third mask (orange, Figure 3.11.D) defines the active region of the cantilever. In these windows it is etched away the silicon oxide previously deposited, which was used for the alignment marks and as mask for implantation and etching.

4. The forth mask (black, Figure 3.11.E) defines the windows that allow to contact the two terminals of every piezoresistor and lightly p-doped silicon.

5. The fifth mask (blue, Figure 3.11.F) defines the interconnection between the piezoresistors and the pads which are present in the bottom part of the chip.

6. The sixth mask (green, Figure 3.11.G) defines the area where the conductive parts have to be electrically insulated from the environment: all the piezoresistors and the interconnections (except the pads).

7. The seventh mask (rose, Figure 3.11.H) is the backside mask and delimits the dimension of the chip. It defines the region where the bulk silicon and the buried oxide of the SOI wafer have to be etched. In this step the cantilever will be released and two anchor beams will be also defined at the center of the chip, one at each side. These two beams hold the chips in the wafer after the microfabrication process ends. Upon a soft pulling, a chip can be detached from the wafer with no risk for the device.

As it is visible in the Figure 3.11.A, there are 6 pads: five in row and one above. The central pad of the row, is to bias the bridge, the other two, next to it, are the two output voltages of the Wheatstone bridge and the last two are the two grounds of each side of the bridge that can be externally connected. The pad above the row can be used to bias the lightly p-doped silicon substrate.

In total we have 3 designs, 2, 6 and 8, and each of them has three sub-designs (Table 3.3 and Figure 3.12). The first number of the sub-design reflects the width of the cantilever arm while the second the length of the sensing cantilever. All the sensing cantilevers and all the piezoresistors are 250 μm and 125x2 μm long, respectively. The piezoresistor has the same width of the cantilever arm in 2 and 6 designs (Figure 3.12.A) while in design 8 it is just 2 μm wide (Figure 3.12.B). The cantilever with a width of 6 μm has been included because is less fragile than the one of 2 μm, even though has around 3 times less resolution. In the cantilever 8, the piezoresistor is aligned inside the cantilever. In this way the piezoresistor is somehow more "protected" from the external environment. The sub-designs 2x250, 6x250 and 8x250 have two cantilevers with the same length. One is used as sensing probe and the other acts as the reference. The sensing cantilever of the sub-designs 2x250-, 6x250- and 8x250- is 250 μm long while the reference one is 140 μm long (Figure 3.12.C).

Design	sub-design	w₁ [μm]	w_R [μm]	w₂ [μm]	L₁ [μm]	L₂ [μm]
2	2x250	2	2	8	125	250
	2x250-	2	2	8	125	250 & 140
	2x250+	2	2	8	125	250
6	6x250	6	6	16	125	250
	6x250-	6	6	16	125	250 & 140
	6x250+	6	6	16	125	250
8	8x250	8	2	20	125	250
	8x250-	8	2	20	125	250 & 140
	8x250+	8	2	20	125	250

Table 3.3. Different designs and sub-designs of the sensor present in the set of masks. w_1, w_R, w_2 are the cantilever arm width, the piezoresistor width and the cantilever width respectively. L_1 and L_2 are the half of the piezoresistor length and the cantilever length.
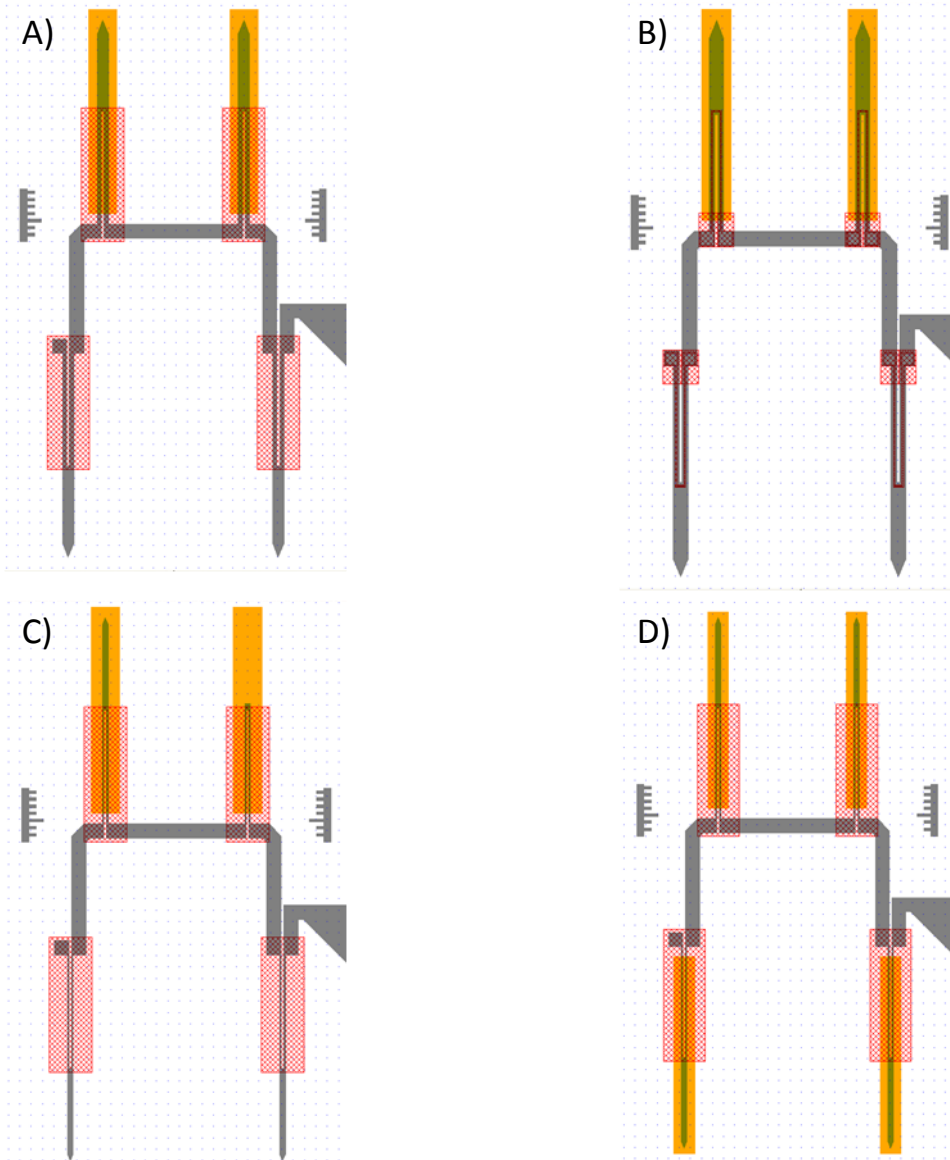
Figure 3.12. Close-up of the masks of the cantilever area for different designs. A) 6x250; B) 8x250; C) 2x250- ; D) 2x250+.

In the sub-designs 2x250+, 6x250+ and 8x250+, the 3rd photolithographic mask is different: the windows-etching is performed on the cantilevers and on the substrate piezoresistors (Figure 3.12.D). Later on in this chapter, we will point out the effects of these differences.

In Figure 3.13, finally, we report the test structures included in the test chip. Here several types of structures are defined and are useful to perform mechanical and electrical measurements. In the Figure 3.13.A, two voltage dividers with two piezoresistors, one embedded into the cantilever and one placed on the substrate, are useful for sensitivity characterization, even though all the sensor chips are characterized. On the top side of the windows, there are 4 cantilevers with different layers. These are useful to extract interesting materials parameters like young modulus and residual stress gradient [24, 25]. The rotating point arms, similar to crosses, in Figure 3.13.B are used to measure the mean residual stress of the different layers of the cantilever [26]. The squares in Figure 3.13.C are test areas for the secondary ion mass spectrometry (SIMS) and for the spectroscopic reflectometry to evaluate the doping profile and the film thicknesses, respectively. In the last Figure 3.13.D there are Van der Pauw Greek crosses, Kelvin bridges and resistors to evaluate the contact and the sheet resistances.
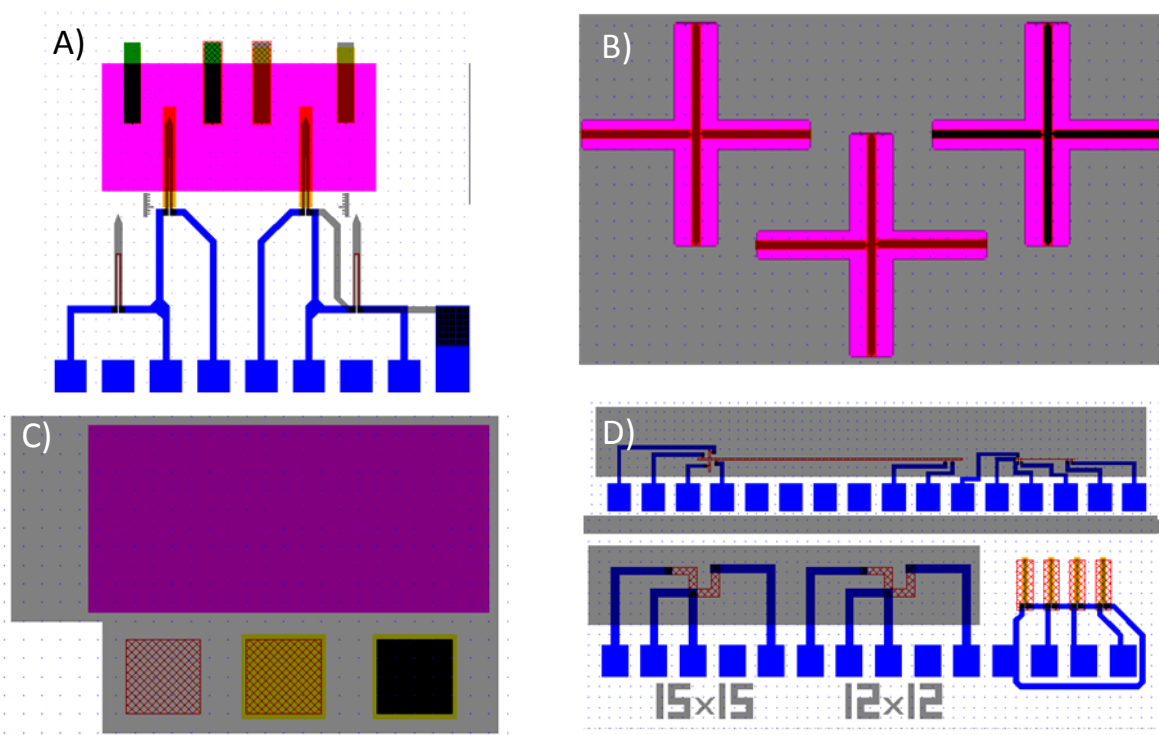
Figure 3.13. Test structures in the wafer. A) piezoresistive cantilevers in semi Wheatstone bridge plus 4 cantilevers with different layers for beam bending tests; B) Crosses to measure the mean residual stress in the different layers; C) 3 squares for TOF-SIMS measurements and rectangle for spectroscopic reflectometry measurements to evaluate the layers thicknesses; D) Van der Pauw Greek cross, Kelvin bridges and resistors to evaluate the contact and the sheet resistances.

3.2.2 – Piezoresistive cantilever process flow

In this section, just the optimized microfabrication process that allowed a high fabrication yield (RUN 6481) will be described. Different technological processes have been tried before and they will be pointed out in the next section together with the fabrication issues and other improvements that can be done.

The sensors were fabricated from double side polished (100) silicon-on-insulator (SOI) wafers, from Soitec, with a 340 nm thick device layer, a 1 μm thick buried oxide (BOX) and total wafer thickens of 450 μm (Figure 3.14.A). The device layer was p-type silicon with a resistivity of 0.1-10 Ωcm. In the RUN 6481, 4 SOI wafers plus one standard p-doped wafer with a resistivity of 0.1-10 Ωcm, as test wafer, were processed.

At the start of the process the device layer thickness was mapped in 49 points, because, even though the majority of the wafer didn't present any unusual standard deviation, we found that in some wafers the thickness was at least 15% above the nominal thickness. Afterwards, the wafers were labeled with a laser scriber on the backside; we measured the silicon oxide thickness on the backside, and, in case of oxide presence, we completely etched the layer by SiOetch solution. On the front side, a layer of 168 ± 4 nm of oxide was deposited via tetraethylorthosilicate(TEOS)/O_2-plasma enhanced chemical vapor deposition (PECVD) at 400º C in the Applied Materials Precision 5000 CVD equipment.

The *first photolithography* was performed in order to define the windows for implantation and the alignment marks for the following photolitographies. During this and all the following photolithographies, the wafers are rotated by 45° respect to a standard orientation. In this way the piezoresistors and the cantilevers are defined along the <100> crystallographic direction to have the highest piezoresistive factor and they form an angle of 45º with respect to the wafer flat. The oxide was etched by SiOetch solution and the photoresist hard baked at 180º C to remove possible solvent left after the photolithography before the implantation. Arsenic was implanted at a relatively low energy (50 keV) with a dose of 1×10^{15} ions/cm^2. Then, the wafers were cleaned from the resist in an O_2 plasma asher (Figure 3.14.B).

The *second photolithography* was performed to pattern the cantilevers in the <100> direction. The TEOS PECVD oxide was etched away in SiOetch solution and the silicon was etched via SF_6/C_4F_8 deep reactive ion etching (DRIE) in an Alcatel 601 etcher (P601POLI conditions) (Figure 3.14.C). In the test wafer we measured an etching speed of 540 nm/min, so we etch the SOI wafer for 45'' with just 7 second of over-etching, in order to avoid silicon undercut at the Si-SiO$_2$ interface. The thickness of the silicon and of the buried oxide (BOX) was measured by Nanospec® to ensure that the silicon was completely etched. The wafers were cleaned from the resist and in piranha solution. Afterwards a TEOS PECVD silicon oxide layer of 307 ± 9 nm thick was deposited at 400º C. This oxide insulates the low doped p-type silicon from the aluminum interconnections.
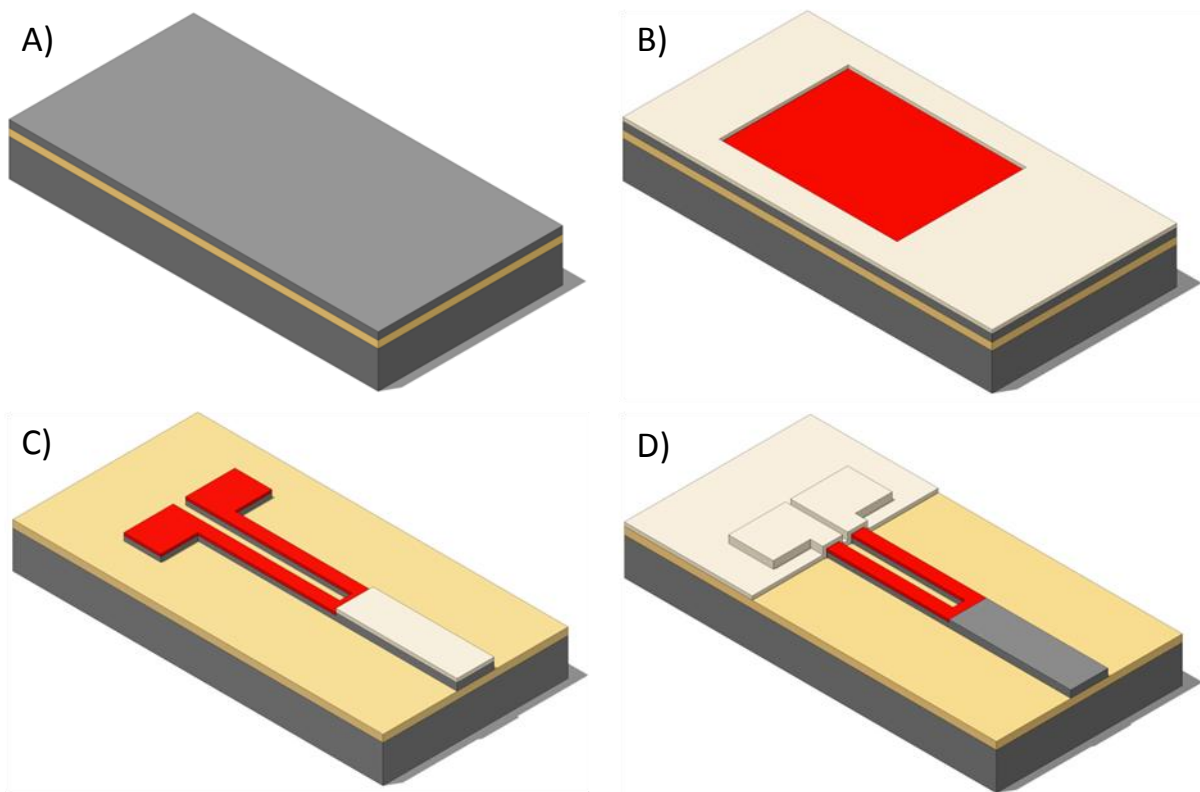
Figure 3.14. Cantilever area during different fabrication processes. A) SOI wafer before the process. B) The implanted area is highlighted in red. C) The SOI layer is etched to define the cantilever. D) PECVD silicon oxide is deposited and etched away from the active area of the cantilever.

The *third photolithography* was performed to pattern windows on the cantilevers. The PECVD oxide was etched away by SiOetch solution and the resist removed in the plasma asher (Figure 3.14.D). After a piranha cleaning, the wafers were annealed at 950 ºC for 75' in oxidizing atmosphere in order to activate the doping ions. In this step also a layer of 39 ± 11 nm of thermal oxide was grown (Figure 3.15.A). The thermal oxide protects the piezoresistors and the crystalline silicon against the following surface micromachining processes.

The *fourth photolithography* was performed to pattern the contact-windows: windows in the oxide that allow to contact the piezoresistors. The 300 nm thick TEOS PECVD silicon oxide was etched by SiOetch solution (Figure 3.15.B). After the resist was removed, the wafers were etched without mask in commercial SuperQ etch solution to etch the native oxide that could have grown on the n-doped silicon contacts. Just afterwards, a 1 μm thick layer of aluminum-copper-silicon alloy (98.75% Al, 0.5% Cu, 0.75% Si) was sputtered in the Varian 3180 equipment. The Al-alloy with silicon was used in order to avoid spikes of metal into the silicon. These spikes could short circuit the p-n junction which is very superficial in our case [27].

The *fifth photolithography* was performed to pattern the metal interconnections and the pads of the chip. The metal etching is performed via BCl$_3$/Cl$_2$/N$_2$ RIE in the Drytek Quad

etcher (PQ2ALC25 conditions) with automatic final point detection (Figure 3.15.C). In case of presence of metal particles or spacers at the end of RIE, commercial Defreckling Aluminum Etch (DAE, Fujifilm Electronic Materials) solution was used for 45'' to remove the metal particles. We preferred to use wet etching instead than a RIE over-etch to avoid as much as possible damages in the silicon piezoresistor. On the other hand we didn't want to perform the etching using just DAE solution because it would damage the interconnections in critical points like the vertical steps (see later). During this step, between 20 nm and 30 nm of the thermal protective oxide were etched by RIE and around 6 nm by wet etching. Even though we etched almost all the silicon oxide, it was very important to remove the metal particles because they could be responsible of pinholes in the insulation layer. After a cleaning in water, the wafers were thermally treated at 350º C in N_2/H_2 atmosphere for 35 minutes to reduce the contact resistance [28]. To insulate all the conductive parts of the sensor, a layer of 99 ± 1 nm thick silicon nitride was deposited by SiH_4/NH_3-PECVD at 375 ºC in the Applied Materials Precision 5000 CVD equipment in two steps of 50 nm. The silicon nitride layer provides a good electrical insulation to the sensors, once they are in liquid environment. The deposition of thin layers of PECVD silicon nitride was performed in two steps because this reduces the possibility of pinholes in the layer [3].

The *sixth photolithography* was performed to pattern the silicon nitride. The 100 nm thick nitride layer was etched via CHF_3/CF_4 RIE in Alcatel Gir 160 (PGNISEN conditions) (Figure 3.15.D). In this step also the underneath TEOS PECVD silicon oxide was completely etched however this was not an issue because the piezoresistors were protected and just the structural part of the cantilever was exposed to the etching. The wafer was cleaned in O_2 plasma asher and in water. With this process, we finished the microfabrication process in the wafer front part.

A 1 μm thick aluminum layer was deposited on the wafer backside. The *seventh photolithography* was performed on the backside to define the areas that have to be etched by deep reactive ion etching (DRIE) until the buried oxide (BOX). The aluminum is etched via $BCl_3/Cl_2/N_2$ RIE in the Drytek Quad etcher (PQ2ALC25 conditions) with automatic final point detection. On the front side a 1.5 μm thick resist is deposited and hard backed for 30' at 200º C to protect the component side from the following processes. The 450 μm of bulk silicon are etched via SF_6/C_4F_8 Bosch deep reactive ion etching process (DRIE) (Figure 3.15.E). The etching stops at the BOX but additional 30 seconds of SF_6 RIE is performed in order to eliminate all the residues of the passivating polymer. The BOX is etched by 49% HF vapors at 32º C, in a custom made HF vapor etcher (Figure 3.15.F). Finally, the protective resist is etched by O_2 plasma.

In Figure 3.16, we report 3 SEM micrographs of a chip at the end of the fabrication process
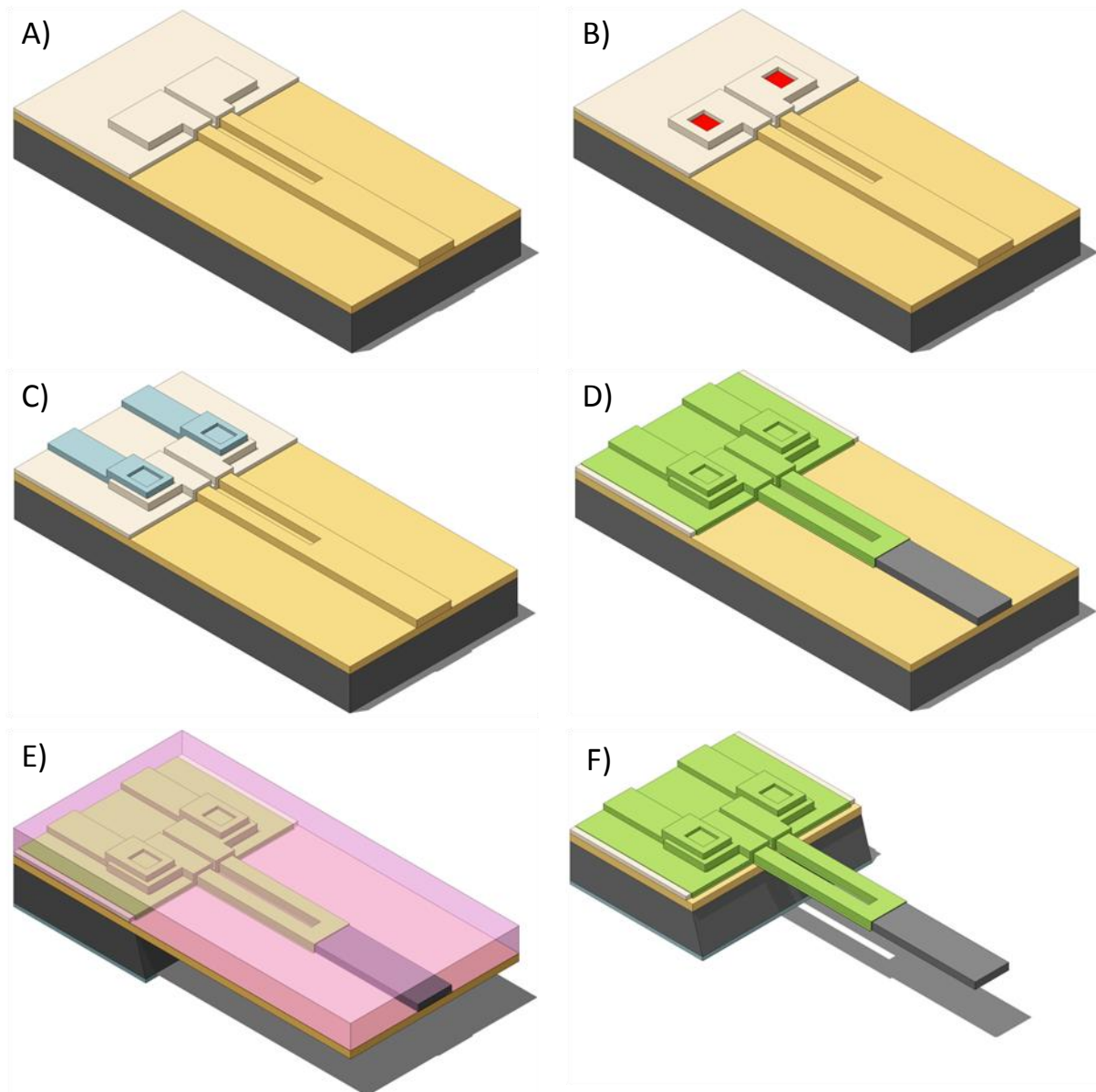
Figure 3.15. Cantilever area during different fabrication processes. A) The wafer is annealed in oxidizing atmosphere and a 39 nm thick silicon oxide layer is grown. B) Two contact windows are opened in the PECVD silicon oxide on the n-doped silicon. C) aluminum is sputtered and etched to define the interconnections. D) A layer of 100 nm thick PECVD silicon nitride is deposited and etched to passivate all the conductive parts. E) Aluminum is deposited on the backside and patterned. Resist is deposited on the front side to protect the device in the following processes. DRIE of bulk silicon is performed and stopped at the buried oxide. F) the buried oxide is etched by vapor HF and the resist is removed in O_2 plasma asher.
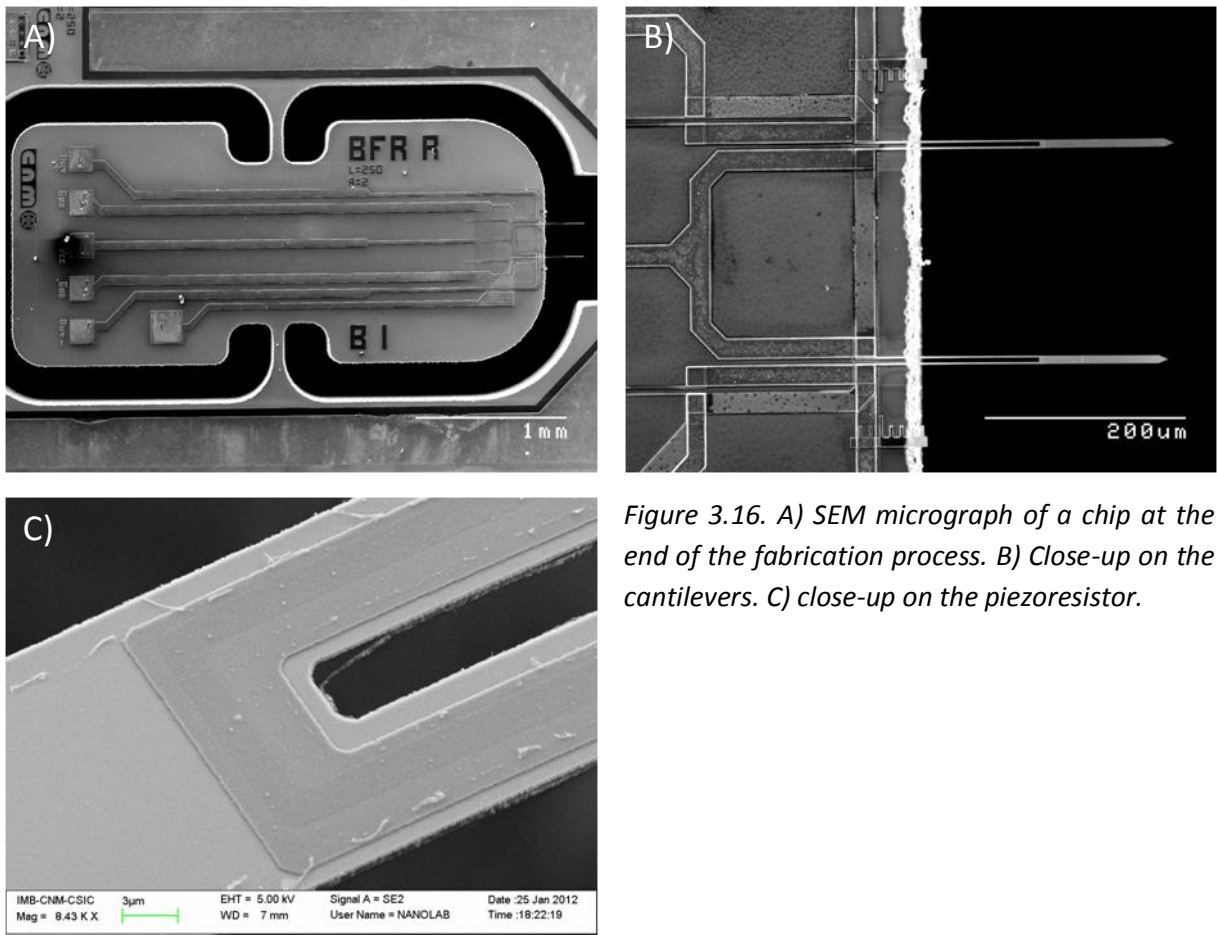
Figure 3.16. A) SEM micrograph of a chip at the end of the fabrication process. B) Close-up on the cantilevers. C) close-up on the piezoresistor.

3.2.3 – Different process solutions and fabrication issues

In this section we will point out the process steps that we used in other RUNs and the fabrication issues we encounter during the microfabrication, giving advices for future optimizations.

Implantation dose

Three different doses (0.5 and 1 x 10^{15} atoms/cm^2 in the RUN 4972 and 5 x 10^{15} atoms/cm^2 in the RUN 6141) have been implanted in order to check the different sensitivity and noise performances. Unfortunately due to the big challenges encountered during the fabrication process, especially in the BOX and interconnections etchings, we have been able to evaluate just the performances of the cantilevers with an arsenic implantation of 1 x 10^{15} atoms/cm^2 of the RUN 4972.

My suggestion, for the future research directions on this point, to improve the sensor performance, is to evaluate the piezoresistive and noise properties of doped silicon, in

structures that are much easier to fabricate. An interesting and straightforward alternative is the one proposed by J. Richter [29]. He proposed a chip with several integrated piezoresistors in different crystallographic directions [30] that can be fabricated by a combination of 4 photolitographies, doping, RIE and DRIE processes. The chip is then bent by a relatively simple and compact 4 point bending setup [31] in which the stress can be also applied by placing loads on a weight [32].

Post implantation annealing

Four different post implantation annealing have been performed: oxidation (OXPTAA process) at 950ºC for 75' (RUN 6481), OXPTAA plus annealing in inert atmosphere at 900ºC for 60' (RUN 4972 wafer 4), OXPTAA plus annealing in inert atmosphere at 1050ºC for 30' (RUN 4972 wafer 4) and rapid thermal annealing (RTA) in oxidizing atmosphere at 1050ºC for 30 seconds (RUN 6141 wafer 6). The post implantation thermal treatment is of fundamental importance for the final resolution of the sensor. In fact, if on one side we have to decrease the diffusion length to achieve thinner piezoresistors, on the other side the 1/f noise decreases for higher diffusion lengths [23]. We wanted therefore to evaluate the best annealing conditions in the case of arsenic implantation.

Out of these experiments, we could evaluate the doping profiles, electrical, electromechanical and noise characteristics of the first three options (chapter 3.3). Due to issues encountered in the aluminum etching of the wafer 6141-6, the device layer of the SOI wafer was partly etched and therefore we couldn't evaluate the characteristics for the last option. Also in this case is valid the previous suggestion about the implantation dose: the evaluation should be performed on much simpler structures.

Metal interconnections

For the metal interconnections, 0.5 μm or 1 μm thick layer of aluminum-copper-silicon alloy (98.75% Al, 0.5% Cu, 0.75% Si) was used. While the presence of copper helps against electromigration [33], the presence of silicon reduces the probability of aluminum spikes that can penetrate few microns into the silicon [27]. This aspect is very important for very thin n-p junctions to avoid short circuit between the resistor and the substrate. While on first two RUNs 4972 and 6141 we deposited just 0.5 μm, we opted to increase the thickness of the metal layer to 1 μm to avoid possible discontinuities and to increase the cross sectional area of the interconnections in the RUNs 6330 and 6481.

Even though in the first RUN 4972 we didn't detected any problem during the aluminum etching via BCl$_3$/Cl$_2$/N$_2$ RIE, we encounter big issues in the following three RUNS 6141, 6330 and 6481. While in Figure 3.17.A-B (run 4972) we didn't appreciate any particle after the

aluminum RIE, in the Figure 3.17.C-D (RUN 6141) we could appreciate bright spots in some areas of the device, especially on the side of height steps and black points on the cantilever. These defects are much more visible in the live images respect to the recorder micrographs.

This behavior was emphasized in the next two RUN 6330 where we deposited 1 µm thick aluminum layer. In Figure 3.18.A are visible many dark spots on the cantilever and aside. These are probably rests of the Al-alloy that it was not possible to etch via RIE with the automatic end point detection. To etch away these particles, in this occasion, we used the so called "isotropic solution" (i.e. H_2O + HNO_3 + HF 49% (1200/3000/60)). This solution is normally used in IMB-CNM to defreckle Al/Si particles. The result was positive: after 15'' the cantilever surface was much cleaner than before (Figure 3.18.B). However, I would discourage the use of this solution when a very thin layer of silicon oxide is protecting the crystalline silicon because even though it has high selectivity against the silicon oxide (17:1) it has no selectivity against silicon (1:1.2). The result is that it is possible to damage the piezoresistor very easily.
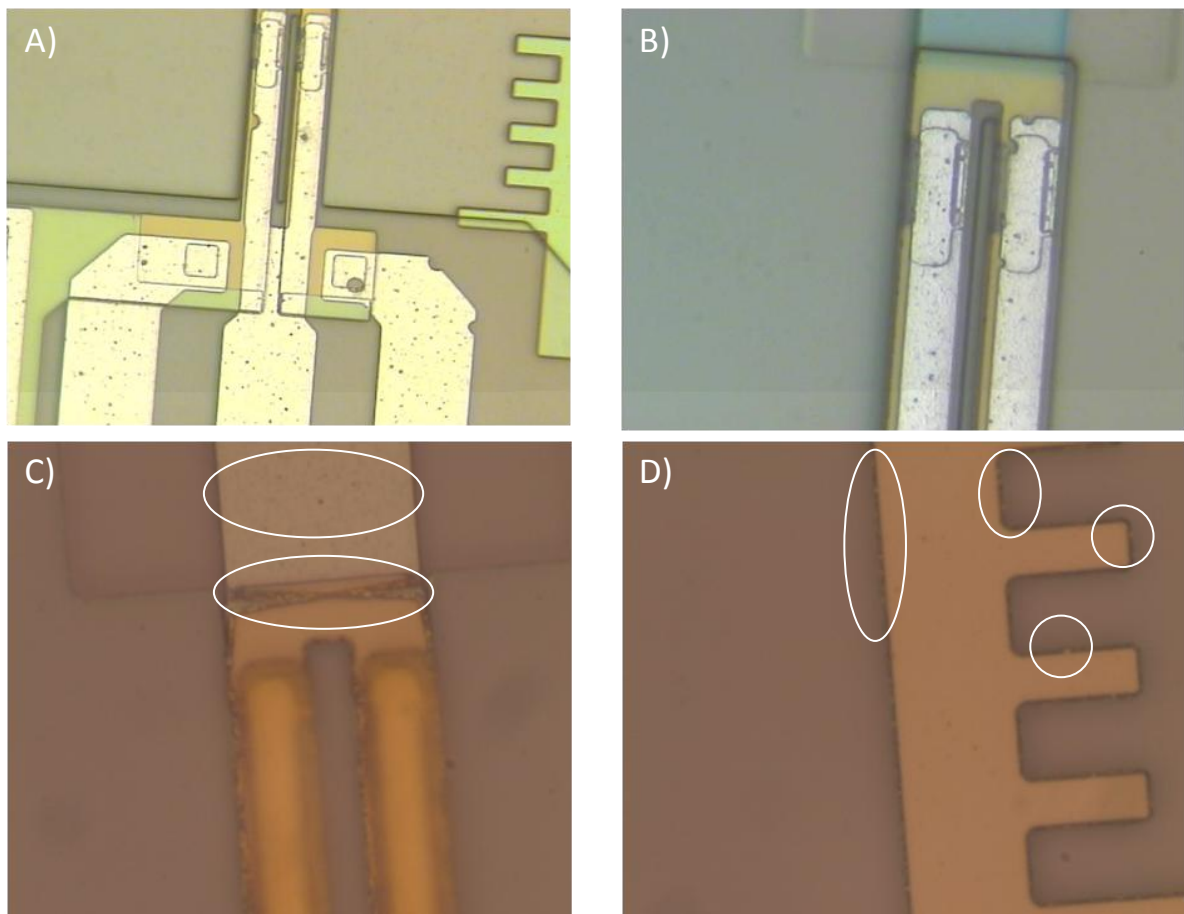
Figure 3.17. Optical microscope images. Details of the wafer after the aluminum RIE. A-B) Wafer 4972-4: no bright or black particle is visible on the cantilever or on the height steps. C-D) Black particles are visible on the cantilever. Bright particles are visible at the border of the structures. In the live image these spots are much more visible.
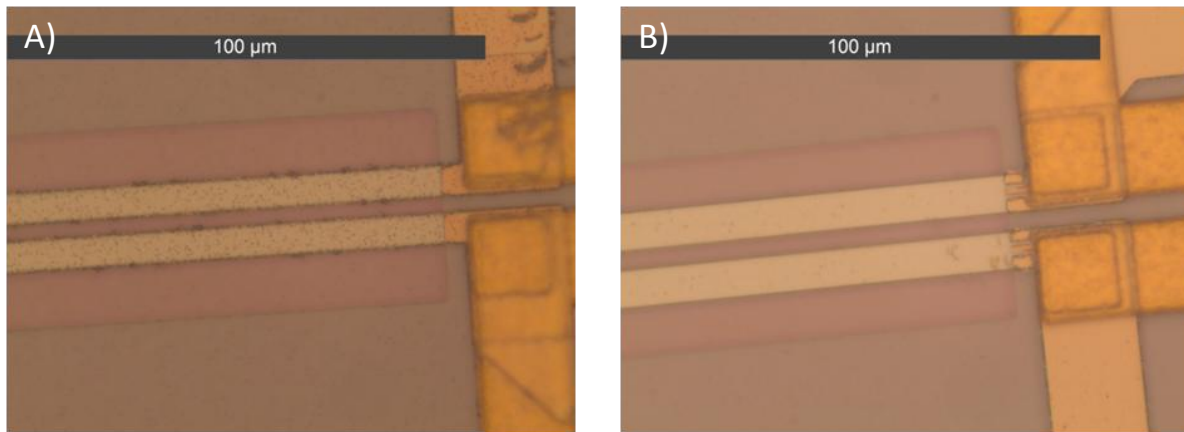
Figure 3.18. Optical microscope images of wafer 6330-3. A) Cantilever after the aluminum RIE: many black spots are visible on the cantilever and aside. C) The cantilever appear clean after wet etching with the "isotropic solution"
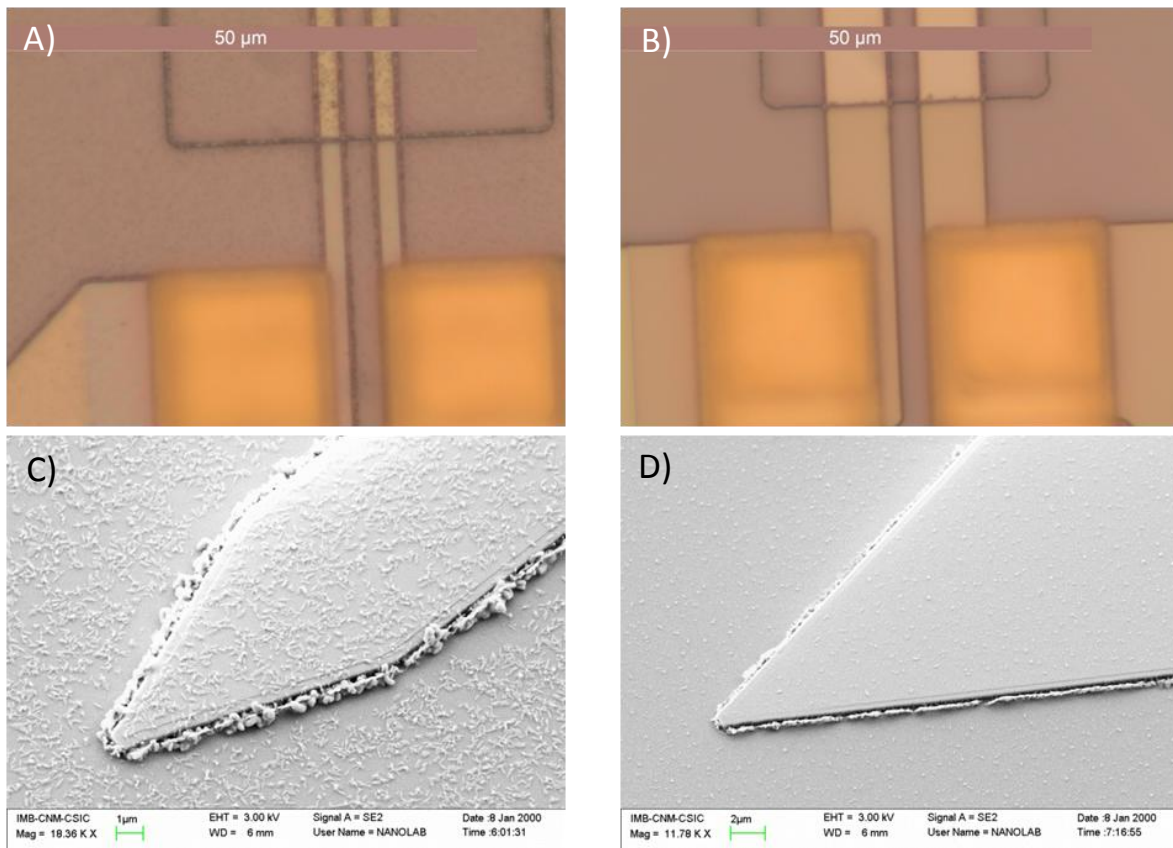
Figure 3.19. Optical microscope (A,B) and SEM (C,D) images of wafer 6481-2. A, C are taken at the center of the wafer. B, D are taken on the external part of the wafer. In the central part, there are more aluminum rests because the etching is slower.

Also in the RUN 6481 we encountered the same problem. Additionally, we noticed that while in the center we end up with many particles (Figure 3.19.A,C), in the border of the wafer, the surfaces were much cleaner (Figure 3.19.B,D). This can be explained considering that the etching speed in the external wafer area is higher than in the center. In the external part, therefore, the aluminum is over-etched and just very few particles remain on the wafer.

If the photoresist is not promptly removed, after the aluminum etching, the results can be very bad. The RIE is performed using Cl_2 gas for the etching and the BCl_3 gas for the sidewall passivation. At the end of the etching, therefore, we have chlorine in the photoresist and in the passivation polymer on the sidewall that can react with the atmospheric moisture and continue the corrosion of the aluminum [34, 35]. In Figure 3.20 we see the results of leaving the wafer with the photoresist for two days, even if they were promptly cleaned in DI water after the RIE. It's very interesting to notice the different morphology of the residues in contact with the polymer, more rounded, and the particles away from the polymer that have a long shape and probably didn't reacted with the Cl_2. The reaction then can go very deep in the metal and break the photoresist (Figure 3.20.D). In order to remove the metal particles we decided this time to perform a 45'' wet etching by using DAE solution, as pointed out in the section 3.2.1. In Figure 3.21 we can appreciate the difference between before and after the etching. The use of DAE solution should be preferred respect to the "isotropic" solution because has much higher selectivity against silicon and silicon oxide and because it is specially developed for Al-alloys that contain Si and Cu.
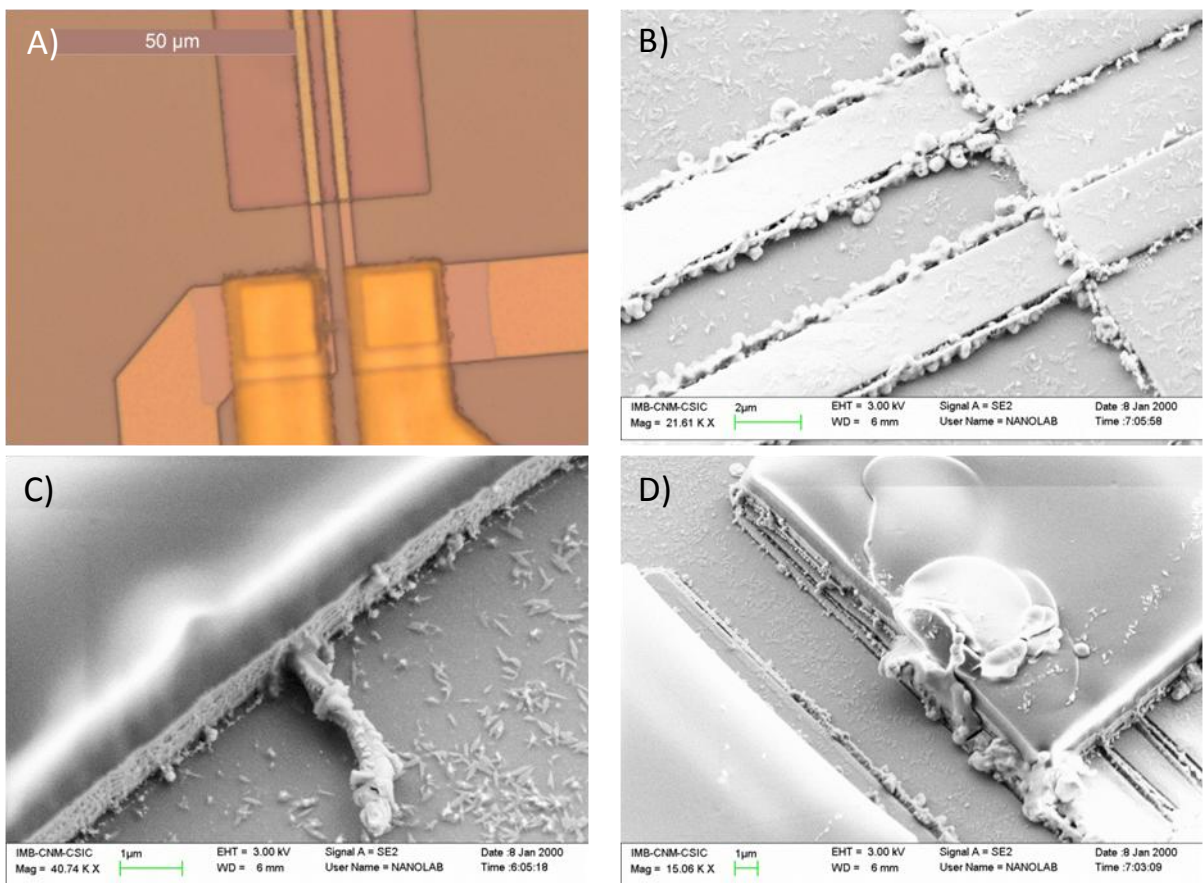
Figure 3.20. Optical microscope and SEM images of wafer 6481-2 after 2 days from the aluminum etching without removing the resist. B) The aluminum particles in contact and the ones that are not in contact with the passivating polymer have completely different morphology one from each other probably because they reacted with chlorine present in the polymer. C,D) The Al in contact with the photoresist is corroded by the chlorine and it form chloride structures that can break the resist (D).
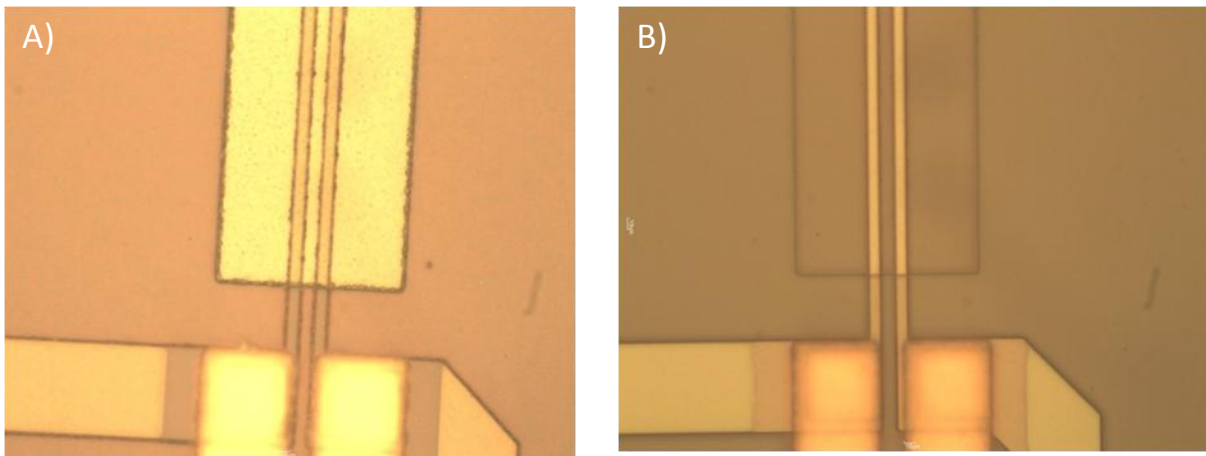
Figure 3.21. Optical microscope images of wafer 6481-4: A) after the Al RIE and B) after 45" DAE wet etching. After the wet etching the particles are not visible anymore.
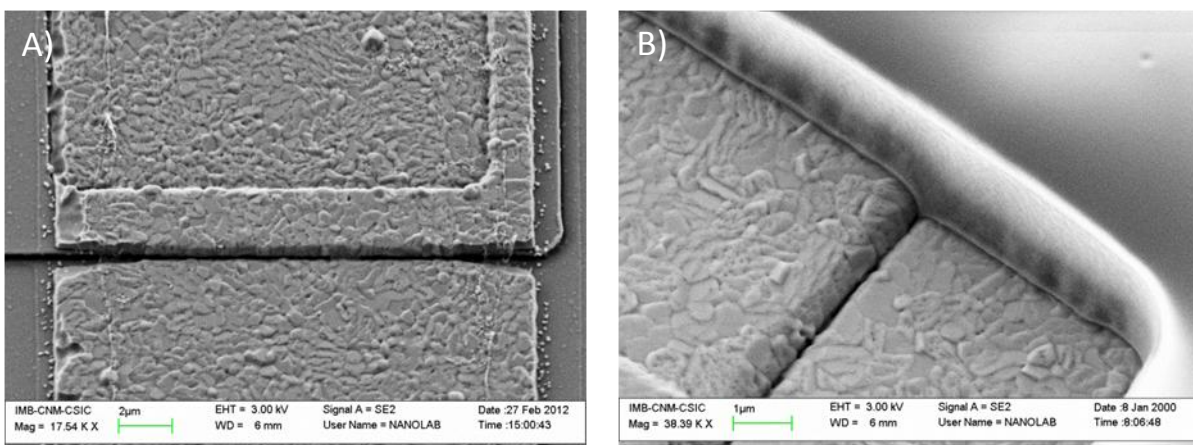
Figure 3.22. SEM microscope images of wafer 6141-3. A) The aluminum interconnection is severely etched by DAE. B) The photoresist has very good step coverage and it seems that it adheres very well on the aluminum.

We tried also to perform the etching completely in DAE solution (RUN 6141). Even though it is a good option to etch well all the aluminum alloy (Figure 3.22), it under-etches the aluminum interconnections far inside beneath the photoresist in presence of a height step (Figure 3.22.A). This is hardly explainable considering that the photoresist has very good step coverage as it is visible in Figure 3.22.B.

Considering all the experiments about the aluminum etching I would exclude that the residual particles on the wafer surface are made of Al/Si because the BCl_3/Cl_2 RIE etches pretty well also the silicon. They are probably, in part, residues of aluminum due to the very rough morphology of the sputtered layer, and in part copper chloride ($CuCl_3$) which has very low volatility [34, 35]. This problem can be solved with longer etching times, as it happened in the external areas of the wafers we have processed. This is not at all an issue in standard CMOS process but can become an issue in MEMS when very thin layers are used. To this purpose a relatively thick oxide should protect the silicon underneath. I would suggest at least a 100 nm thick thermal oxide or relatively thicker LPCVD or PECVD silicon oxides.

However, in our case, this wouldn't have been possible because we worked with very thin device layers (340 nm). On the other hand, to deposit a thicker layer of oxide is possible but the drawback is that its excess should be etched away afterwards, which could lead to other problems.

In my opinion a very straightforward improvement in the fabrication would be achieved by using a lift-off process. To this purpose a reversible resist with a thickness between 3 µm and 5 µm with a pronounced undercut could work pretty well (i.e. TI 35ES from MicroChemicals GmbH) [36]. Using the lift-off process we wouldn't need the protective oxide and the silicon surface would be more preserved because we wouldn't perform a RIE process. This option could lead also to a decrease in Hooge factor and 1/f noise of the piezoresistor.

In this context we performed just preliminary experiments (RUN 6427). We performed a photolithography using a 1.7 µm thick 5214 reversible photoresist and we sputtered a bi-layer of Ti/Al (30 nm/400 nm). Ti/Al was used for practical reasons: the sputtering system that was compatible with resist didn't have a target of Al-Cu-Si alloy. In this case the aluminum spikes are avoided by the 30 nm of titanium [27]. In the SEM Figure 3.23.A we see that in the most part of the chip the metal went off after 2 hours of acetone, flushing the wafer with a syringe and 30'' of ultrasounds. However in the regions in between the interconnections, the lift off was not successful. In the close up Figure 3.23.B we can appreciate that the metal layer is continuous throughout the height and the walls form 90° with the horizontal plane. The lift off was not successful because the undercut of the photoresist was probably not sufficiently pronounced. In this sense the different photolithographic steps (exposure, backing and development) should be improved to obtain a more negative angle [36] and evaporator, instead than sputtering equipment, should be used to deposit the metal layer.
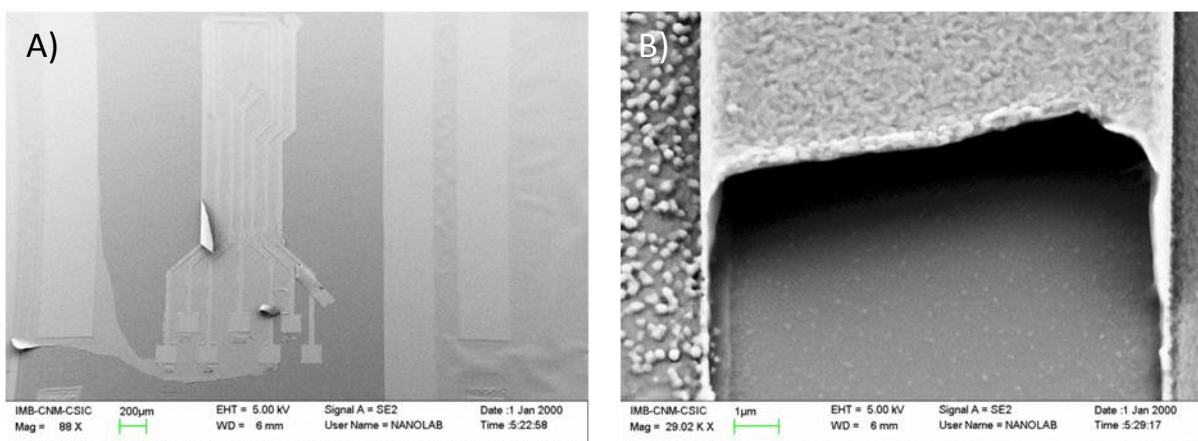
Figure 3.23. SEM microscope images of wafer 6427-1after the lift-off process. A) The Ti-Al bi-layer lift-off in a big area of the chip but not in between the interconnections. B) A close-up image which shows that the layer is continuous on the vertical walls.

DRIE of bulk silicon

The deep reactive ion etching of the bulk silicon from the backside of the wafer is done by a standard Bosch process with SF_6 and c-C_4F_8 gases for etching and passivation steps respectively. At the end of this process, it is very important to perform an additional 30'' of SF_6 etching in order to eliminate all the residues of the passivating polymer on the buried oxide. In general we found that the etching has an undercut angle between 1° and 2° so that the total undercut can be as low as 10 μm for a wafer thickness of 450 μm. In this sense care should be taken in designing the backside mask. This value varies a lot across the wafer and in general is between 10 and 20 μm (Figure 3.24). For a longer SF_6 over-etching times this value can be increased of 10 or 20 μm, decreasing at the same time the roughness of the chips borders.

Much care should be taken when the SOI wafer is chosen, because the thickness of the buried oxide during this step is very important. From the Figure 3.25 we can see how the DRIE evolves for different etching times. The first area of the bulk silicon that is etched is approximately in the center of the etching window (Figure 3.25.A). For additional 30'' etching, a bigger silicon area is etched (Figure 3.25.B) and after additional 30'' the etched area increases more (Figure 3.25.C). At the same time, in other parts of the wafer, bulk silicon is still present and no window is visible (Figure 3.25.D). In order to etch the bulk silicon in a large area of the wafer an over-etching should be performed but during this time also the BOX is being etched. Typical over-etching times are between 5' and 7' during which around 200 nm of oxide can be etched away. It is clear that if a wafer with 200 nm thick silicon BOX is used, we would etch completely the oxide and we would start to etch the silicon of the SOI (Figure 3.25.E). I would suggest choosing an SOI wafer with at least 500 nm of oxide. The fact that etching of the bulk silicon is not homogeneous across the wafer, even in a single window, is a drawback also for the etching of the buried oxide as we will see it later. A SOI wafer with a starting BOX of 1 μm, can have a variable oxide thickness between 1 μm and 700 nm, at the end of the DRIE.
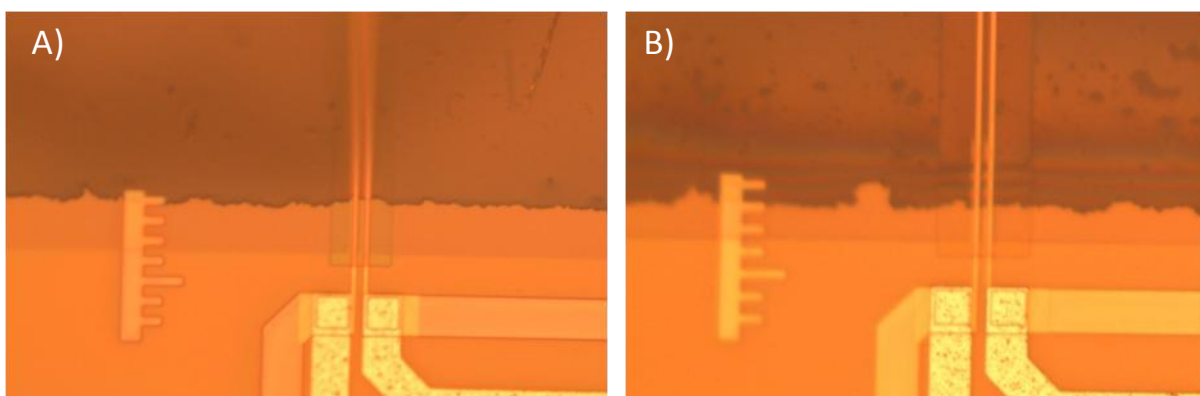
Figure 3.24. Optical microscope images of two chips in wafer 6481-4: A in the center of the wafer, B in the border of the wafer. A) The bulk silicon is in line with the first line of the ruler on the left so that the total undercut of the bulk silicon is 10 μm. In B) the total undercut is 20 μm since it is in line with the second line.
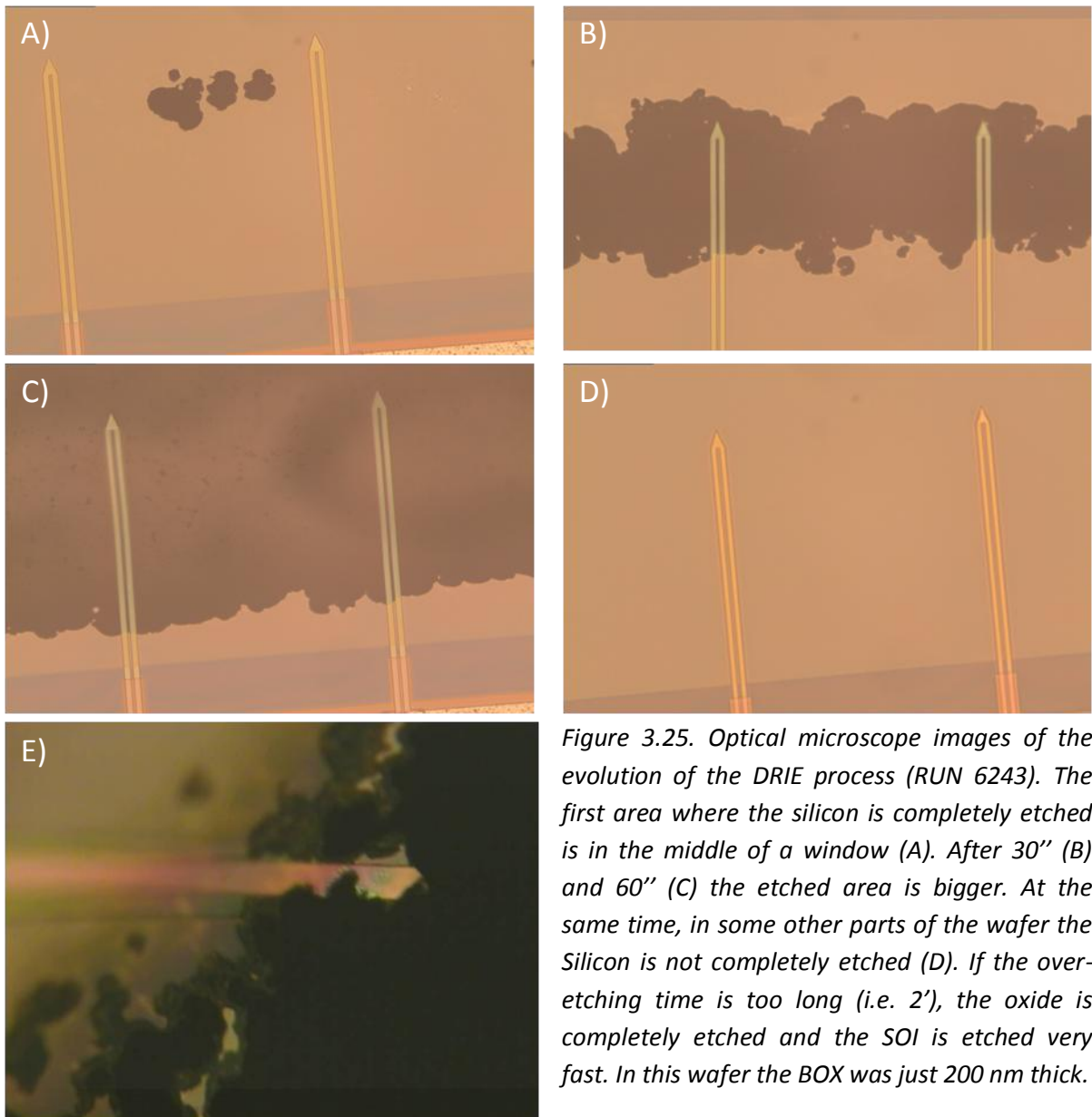
Figure 3.25. Optical microscope images of the evolution of the DRIE process (RUN 6243). The first area where the silicon is completely etched is in the middle of a window (A). After 30'' (B) and 60'' (C) the etched area is bigger. At the same time, in some other parts of the wafer the Silicon is not completely etched (D). If the over-etching time is too long (i.e. 2'), the oxide is completely etched and the SOI is etched very fast. In this wafer the BOX was just 200 nm thick.

BOX etching

The last step of the process, the etching of the buried oxide, is also the most challenging. In this step we have to etch away the buried oxide to release the cantilever but at the same time we have to avoid any damage to the layers in the front side. For this purpose we have tried different fabrication options: wet etching, dry etching and quasi-dry vapor HF etching. The device side was protected by standard photoresist that was deposited before the bulk silicon DRIE and hard backed at 200º C for 30'.

As first option (RUN 4444) we tried wet etching. We performed the etching pouring SiOetch solution onto the wafer backside while the wafer was hold by a screw-tightened wafer holder to protect the component side. This solution etches the thermal silicon oxide at a speed of around 900 nm/min. Unfortunately after 10 minutes there was still oxide. We over-etched for 10 minutes more and we could appreciate that in some areas the resist detached from the oxide and the component side was partially etched (Figure 3.26.A-B). This was probably due to the fact that the buried oxide got broken in some points and the solution could reach the component side. For an additional over-etch of 5 minutes we just made the situation worse: the silicon oxide was still present and bigger areas of the device side were etched (Figure 3.26.C). The very low etching speed may be due to reduced diffusion of the reagents and of the products into and outside the cavities, considering especially that that rest of DRIE passivation polymer was not likely to be present on the oxide because we over-etch the wafer via SF_6 RIE for 30''. If the etching was performed from the component side, therefore without any protective resist, the etching speed of the silicon oxide was the usual one but in this case the oxide, the nitride and the metal were also etched.

Concluding, wet etching from the backside is not a good option because long etching times are needed and the detaching of the protective resin is likely to happen, causing the etching of the oxide, nitride and aluminum on the component side of the wafer. As a second option we used two different oxide RIE conditions in an Alcatel Gir 160 etcher: CHF_3/CF_4-PGIOXXX (RUN 5214) and CHF_3-PGIOXGUI (RUN 6481). In the Figure 3.27 and Figure 3.28 we can appreciate that for both conditions, around the chip it remains an oxide shadow even for long etching times (Figure 3.27.B-C). This is due mainly to the fact that the DRIE etching is not vertical but it has a negative angle so that the bulk silicon acts as a mask for the BOX etching and that the oxide RIE is very anisotropic because it is more a physical than a chemical etching [37, 38]. In RUN 5214, the oxide near the chip outline didn't go away even for longer etching times, on the other hand the cantilever changed the color due probably to the fact that the plasma started to etch the silicon. In fact the selectivity between oxide and silicon is 5:1. The etching of the SOI should be avoided when working with very thin SOI wafer with integrated piezoresistors.
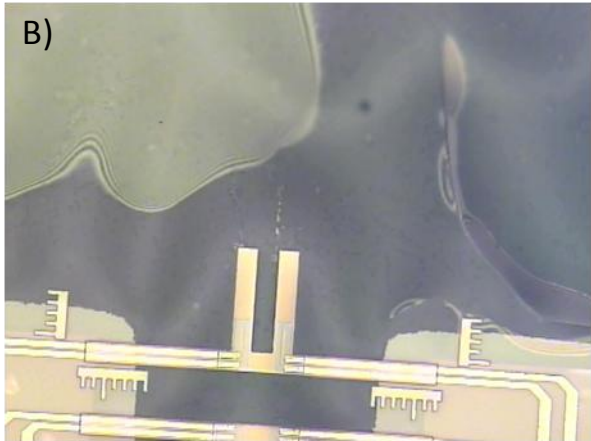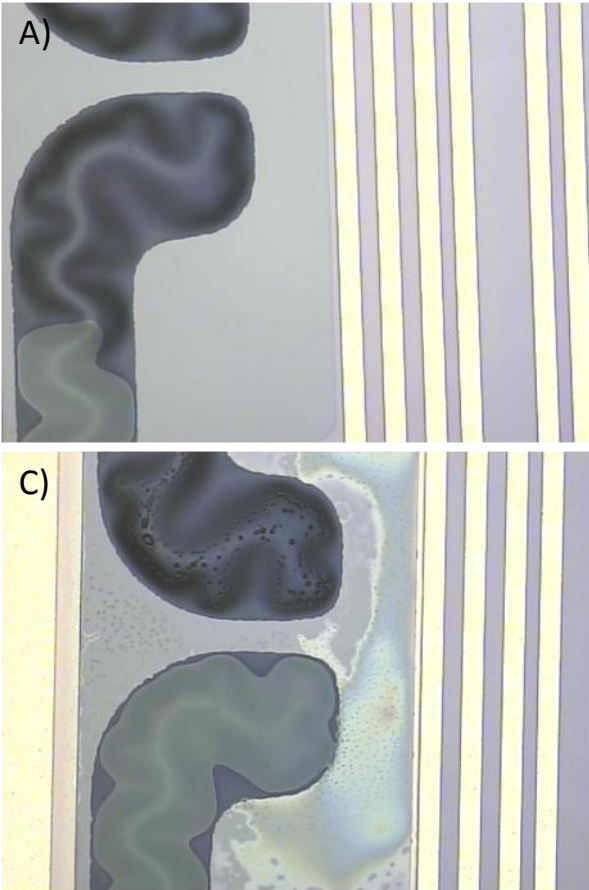
Figure 3.26. Optical microscope images of the evolution of the BOX etching by SiOetch. A and B are after 20' etching. In A the oxide is still present and can be recognized by the wave morphology. The resist start to detach from the oxide. In B, we can see that the oxide is broken and therefore the etching solution can penetrate to the component side. C) After additionally 5' etching the resist is even more detached and the components side of the chip is damaged.
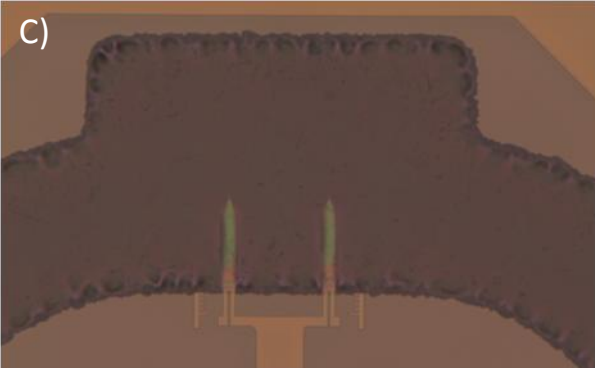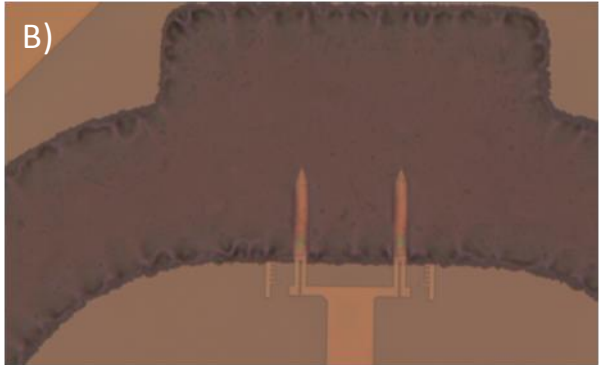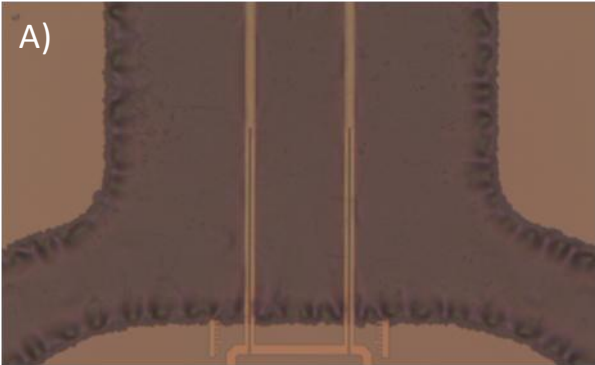
Figure 3.27. Optical microscope images of the evolution of the BOX etching by RIE (PGIOXXX conditions). In A) we see the wafer after 9' minutes etching, in B) after 9'+2' and in C) after 9'+2'+1'. We can notice that the oxide is completely etched away except near the chip and that for higher etching times the cantilever changes color because probably is etched too.

We had an improvement switching the conditions to PGIOXGUI, which have a selectivity of 12:1. Even if we could perform longer etching times with lower risks to etch the silicon, also in this case, after a total etching time of 14 minutes, we couldn't etch completely the oxide near the chip (Figure 3.28). In these pictures we can notice also that if there is still oxide, the cantilevers are not in focus on the same plane of the chip because they are deflected (Figure 3.28.A). The cantilevers are in focus on the same plane when the oxide is etched (Figure 3.28.B). Since the oxide is transparent, it is quite challenging to detect its presence through the resist by an optical microscope, therefore this fact can be used to qualitatively evaluate the presence of the oxide underneath the cantilever. In SEM pictures (Figure 3.28.C) we can see the final results. The oxide is etched away just in the cantilever windows while around the chip is still present because the opening is two times narrower. Finally, in Figure 3.28.D, we can notice that even if the oxide seems completely etched, on the front part of the cantilever there is a kind of network. This is probably very thin silicon oxide which folded on the cantilever. To eliminate this network longer etching time would be needed with the risk to etch considerably also the silicon. In chapter 5, we will see that even though this cantilevers can be used and have good sensitivity and noise performances, they cannot be used to perform biomolecule force spectroscopy measurements.

As third option, we used HF vapors (RUN 4972). For this purpose we poured 100 ml of 49% HF into a 3.5'' teflon beaker and we placed the wafer on the top. During these trials we found three very important aspects. First: the etching speed of the HF vapors is affected a lot by the atmosphere humidity [39]. In more humid days we saw that the etching was 2 times faster than during less humid days. Second: recently deposited photoresist provide much better barrier than "older" photoresist. The process should be performed just after the silicon DRIE. In case that few weeks or months pass the resist detaches from the oxide much faster. Third: the wafer should not be placed into water just after the vapor. When the wafer is cleaned in DI water, we found that the resist and the component side had much worse aspect than in the case that the wafer was left in air. This can be explained by the fact that just after the process, absorbed HF is still present on the wafer surfaces and in contact with water the HF-water solution penetrates faster and easier into the component side. Even if we obtained very good results with this technique (wafer 4972-9), we didn't manage to obtain the same result in other wafers.
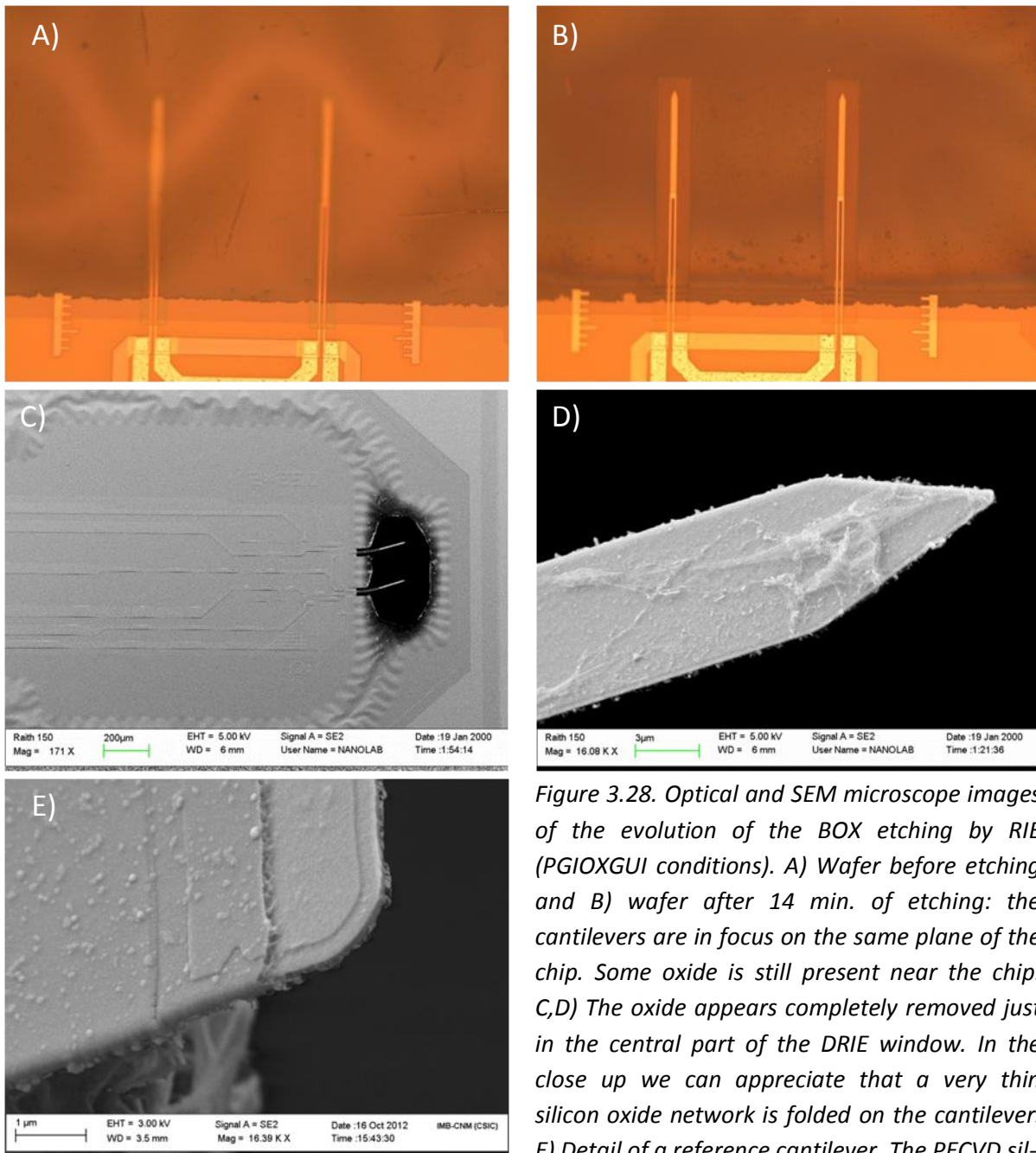
Figure 3.28. Optical and SEM microscope images of the evolution of the BOX etching by RIE (PGIOXGUI conditions). A) Wafer before etching and B) wafer after 14 min. of etching: the cantilevers are in focus on the same plane of the chip. Some oxide is still present near the chip. C,D) The oxide appears completely removed just in the central part of the DRIE window. In the close up we can appreciate that a very thin silicon oxide network is folded on the cantilever. E) Detail of a reference cantilever. The PECVD silicon nitride covers pretty well the sidewalls of the cantilevers, providing therefore a good insulation to the piezoresistor.

In this perspective it was important to have an equipment to have more repeatable HF vapor etching. For this purpose we used an old custom made HF vapor etcher. After the first trials we reported a very inhomogeneous etching speed across the wafer, which could vary up to one order of magnitude. Therefore, as first, we modified the position of the holes of the HF vapor "shower" to be as equidistant as possible one from each other. Then we used a dummy silicon wafer to have a more homogenous temperature distribution across the wafer that has to be etched (Figure 3.29). Additionally we inserted a 3 ways valve to choose a flow of pure N_2 or N_2+HF+H_2O vapors in order to condition the reaction chamber before and after

the etching (Figure 3.30). Thanks to these three modifications we achieved relatively low etching speed variations across the wafer (Figure 3.31). The first two valves that control the N_2 flow were turned for 360°, for an approximate value of 2 l/min (the flow meter has a maximum value of 1 l/min). If lower flow was chosen we found that the etching was less homogeneous. Unfortunately we have not been able to vary the etching speed tuning the temperature as reported in literature [40]. We had a kind of on-off etching behavior dependent on the temperature (Figure 3.31). For values below 30° C we had etching speeds (v_{etch}) of 300 nm/min or higher. For temperatures higher than 33° C, we found almost no etching (v_{etch}<10 nm/min). At 32° C we had v_{etch}≈180 nm/min but with big deviation. In the literature the etching does not depend so strongly by the temperature. This strong dependence can be explained by the fact that the thermocouple of the heater is not so accurate. The temperature could be set with a 1° C of accuracy but during the use, the temperature read on the display could vary ± 1° C. Considering these aspects I would suggest to try using commercial HF vapor phase etcher from AMMT or Idonus or the more complex etcher form Primaxx.

However we found that at 30° C we could have a relatively controlled etching speed of 300±50 nm/min (Figure 3.31). Before the etching we placed the wafer on the heating substrate, we closed the reaction chamber and we let pass a N_2 flow to condition the chamber for 10 minutes. After the etching we conditioned the chamber for 10 minutes as well to remove all the HF vapors.

Label	Level (°C)	Emissivity
3	38.37090	1.000
4	38.17552	1.000
6	35.47609	1.000
7	32.18684	1.000
8	33.22650	1.000

Label	Level (°C)	Emissivity
3	28.09489	1.000
4	27.93197	1.000
6	27.99994	1.000
7	27.57652	1.000
8	27.64514	1.000
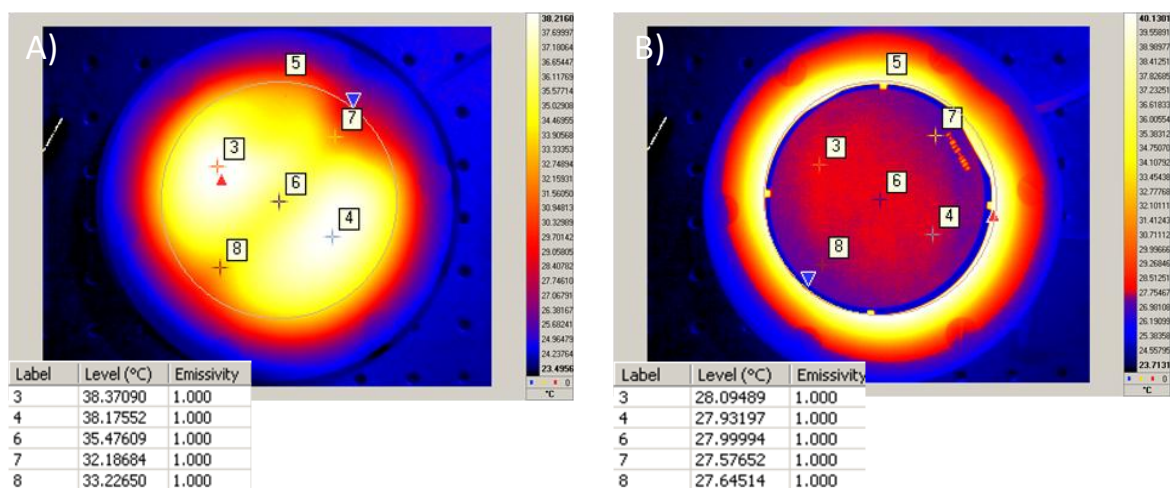
Figure 3.29. Thermoreflectance images of the temperature distribution of the chuck surface of the HF vapor etcher (A): the temperature can vary up to 5°C in the central area where the wafer is placed during the etching. B) After placing a wafer, the temperature has better distribution and varies 0.5 °C as maximum. Just the temperature variation should be taken into consideration in these measurement and not the absolute values.
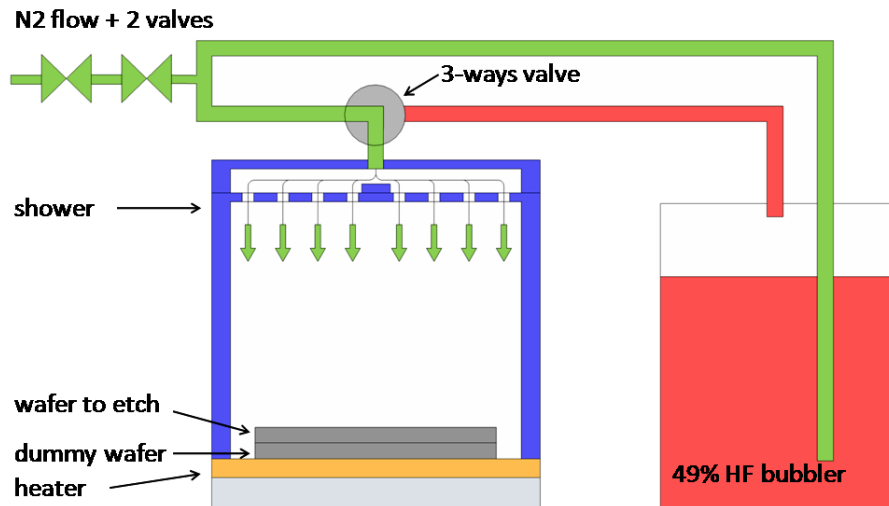
Figure 3.30. Schematics of the modified HF vapor etcher. The tubes with N₂ flow are highlighted in green. The tubes with N₂+HF+ H₂0 flow are highlighted in red. Two valves control the N₂ flow, while a 3-ways valve controls which gas enters in the reaction chamber. The gas is dispersed into the chamber flowing through a "shower". On the heater (orange), we place a dummy wafer to improve the temperature homogeneity. On this, we place the process wafer. All the parts of the etcher are made of teflon or HF resistant polymers.
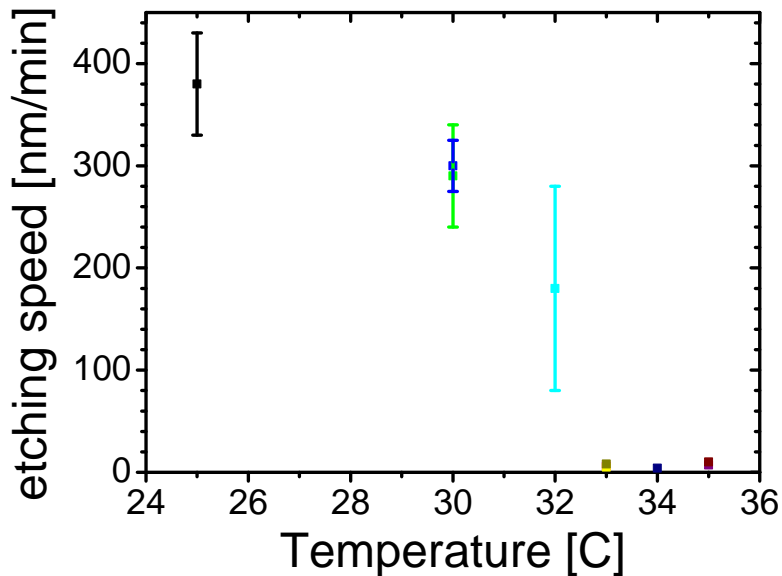
Figure 3.31. Silicon oxide etching speed vs. heater temperature.

In Figure 3.32 and Figure 3.33 we report SEM pictures of the device in which the buried oxide was etched by HF vapor.
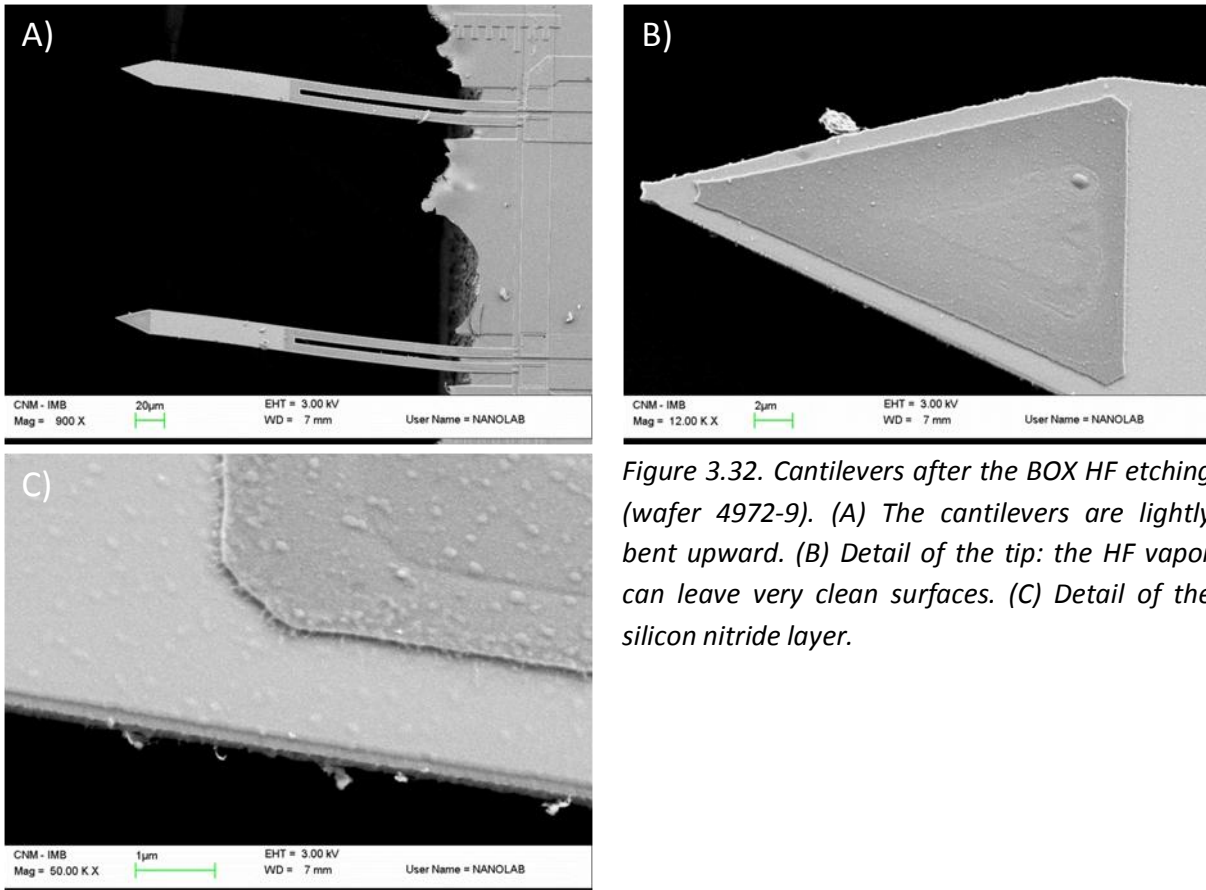
Figure 3.32. Cantilevers after the BOX HF etching (wafer 4972-9). (A) The cantilevers are lightly bent upward. (B) Detail of the tip: the HF vapor can leave very clean surfaces. (C) Detail of the silicon nitride layer.
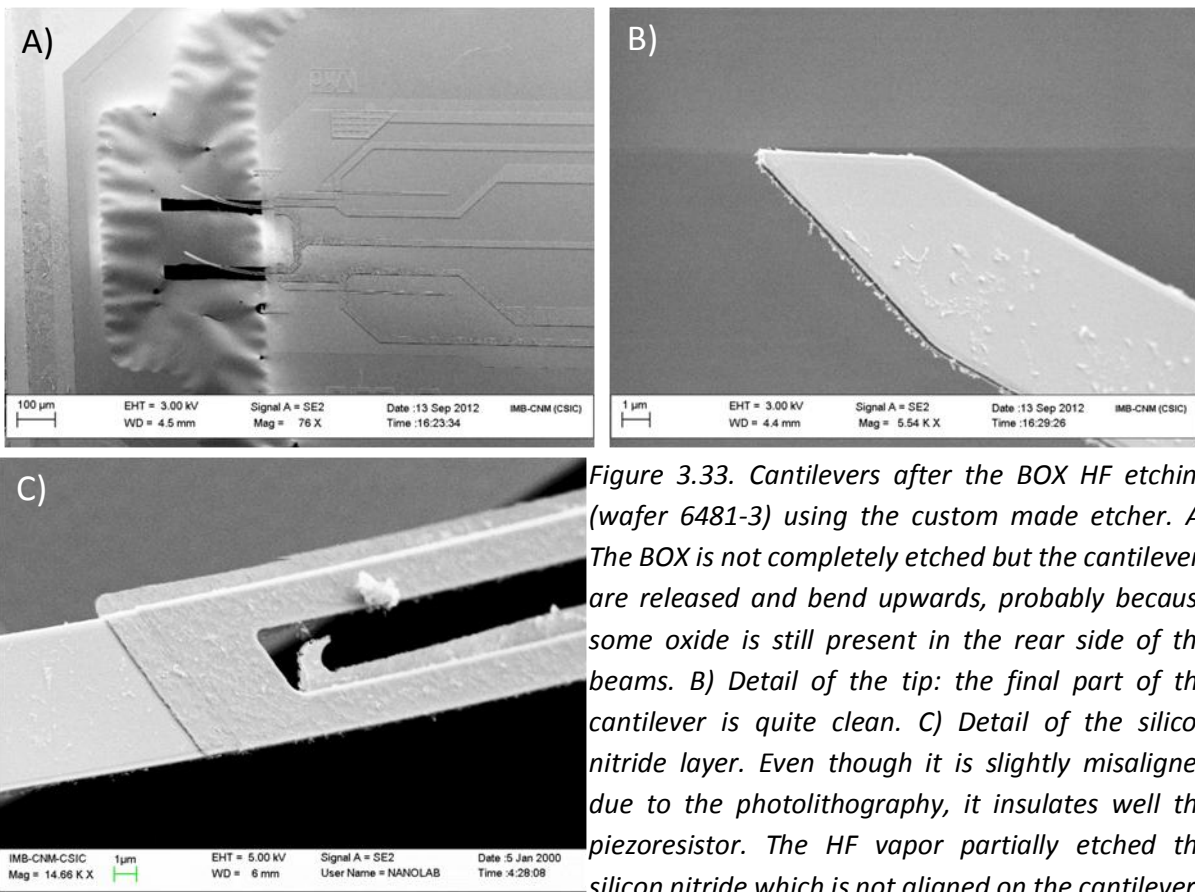
Figure 3.33. Cantilevers after the BOX HF etching (wafer 6481-3) using the custom made etcher. A) The BOX is not completely etched but the cantilevers are released and bend upwards, probably because some oxide is still present in the rear side of the beams. B) Detail of the tip: the final part of the cantilever is quite clean. C) Detail of the silicon nitride layer. Even though it is slightly misaligned due to the photolithography, it insulates well the piezoresistor. The HF vapor partially etched the silicon nitride which is not aligned on the cantilever.

Using the custom made etcher we could achieve quite satisfactory results (RUN 6481). All the tested devices (25% of the total) were working and all the chips had no broken cantilever, therefore we can consider a fabrication yield of 100%. Although other researchers faced problems related with the BOX cracking during the release process that led to the breaking of the cantilevers [41], we did not encounter similar problems. This is probably due to the protective hard backed photoresist deposited on the component side. Unfortunately, due to HF vapor release the insulating layer was partially etched from many cantilevers. Considering the SEM images and the characterization in water (chapter 5) we consider that at least 25% of the sensors function well in liquid environment. Improvements in this direction can be achieved by using commercial HF etchers and changing the component side protective layer. As reported [42], the photoresist has no good barrier properties against HF vapors, but we used it for practical reasons. On the other hand aluminum can be an option. From preliminary experiments we saw that a 500 nm thick Al-layer offers a good barrier for the HF vapors (Figure 3.34) and can be used also to produce very sharp silicon oxide tips. Of course the release of the cantilever from the aluminum layer could lead to other problems like nitride etching, sticking, etc.

As we saw in the previous Figure 3.32 and Figure 3.33, the cantilever can be quite horizontal or have strong bending. This difference can be seen comparing different wafers of different RUNs but also comparing two chips across a single wafer. Considering this aspect, it becomes quite challenging to reduce the curvature to desired values: for the same fabrication process the layers can have different residual stresses in different wafers. The bending, in part, can be due to residual oxide on the rear part of the beam and in part to the variation of the layer thickness across the wafer. The layer thickness variation is not an issue when relative thick cantilevers are fabricated, but can become a problem when we produce nanomechanical structures. In this perspective, much job should be done in order to tune in a repeatable way the residual stresses of the layers [6, 43]. For our purposes, the functionality of the sensor is not compromised and as we will see in chapter 5 the cantilevers function very well as biomolecule detectors and have very high resolution.
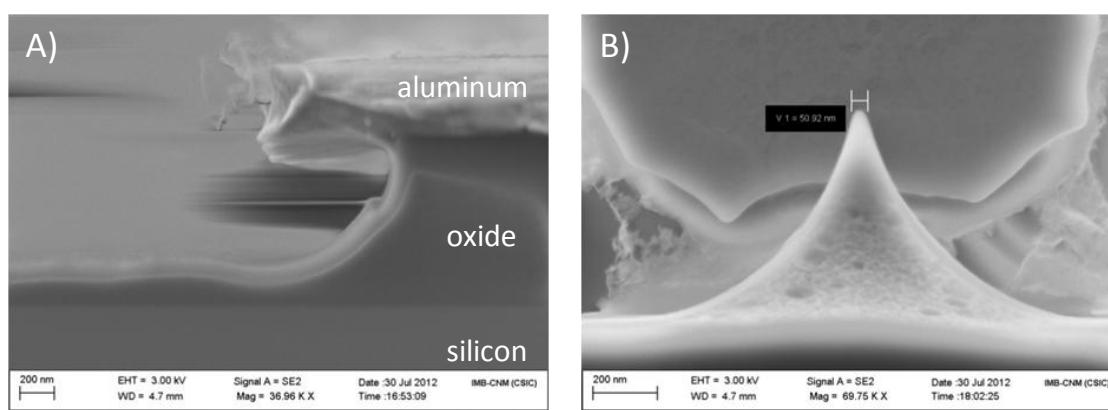
Figure 3.34. Cross section SEM images. The HF vapor etched approximately 850 nm of the exposed thermal SiO$_2$. The 500 nm thick Al- layer protected the oxide underneath. The etching has a typical shape of an isotropic etching, as result tips with radius of 25 nm can be produced. The etching was performed with the custom made etcher at 30 C for 2'30''.

3.3 – Characterization

In this section we will present the different techniques that we used and developed to measure the electrical, mechanical, electromechanical and noise characteristics of the sensors to calculate their resolution. This part was of key importance for the success of the project because if on one side it was very important a reliable fabrication process, on the other side the validation of a technological process requires an intensive characterization of the performances of the devices. Performing fast, accurate and repeatable mechanical, electrical and electromechanical characterization of the device properties is necessary in order to prove the reliability of the sensor and to validate the fabrication technology. For these reasons, we decided to develop set ups that allows on-wafer properties characterization, which results in a considerable reduction of the testing time respect to previous set ups [44].

The most important parameters determining the performance of a quasi-static *force sensor* based on piezoresistive cantilevers are the spring constant k [N/m], the force sensitivity ($S_{F,V}$) [V/N], the transducer noise [V_{NOISE}] and the minimum detectable force (MDF) [N].

3.3.1 – Mechanical

Due to the fact that that the cantilevers are very soft, it is not possible to measure directly the spring constant, but it is calculated according to eq. (3.2). The thicknesses are measured using an optical interferometer (Nanospec AFT 200 from Nanometrics). The widths and lengths are verified using optical microscope and SEM images. The Young's modulus for silicon along <100> direction is taken as E_{Si}= 130 GPa[45] and E_{SIO2}= 75 GPa for thermal oxide [46]. PECVD silicon nitride has been reported to present a wide range of values for its Young's modulus, instead, from 60 to 300 GPa [47-49] depending on the deposition conditions and the layer thickness. Thus, it is necessary to experimentally determine such value for our material. We performed micromechanical measurements with a beam bending based technique [50] on stiffer (specifically designed) test cantilevers (see section 3.2.1) using a commercial AFM (Bruker Dimension 3100). From these measurements it is easy to calculate the spring constants of the test cantilevers. Then, it is possible to extract the Young's modulus of the silicon nitride layer using eqs. (2.47), (2.48), (2.52).

When the AFM probe is in contact with a cantilever, in the contact point we can write the following equation to balance the forces (Figure 3.35.A):

$$F = k_c \delta_c = k_{Peff} \delta_P \qquad (3.17)$$

where k_C and δ_C are the spring constant and deflection of the cantilever while k_{Peff} and δ_P are the effective spring constant ($k_{Peff}=k_P/cos^2\alpha$ and $\alpha=12º$ is the mounting angle of the probe)

and the deflection of the AFM probe. We know also that the total probe displacement (z_P) is the sum of the deflection of the probe and the one of the cantilever under test:

$$z_P = \delta_c + \delta_P \tag{3.18}$$

therefore we can write:

$$F = k_{Peff} \frac{\delta_P}{\delta_c} = k_{Peff} \frac{\delta_P}{z_P - \delta_P} = k_{Peff} \frac{tan\theta}{1 - tan\theta} \tag{3.19}$$

where $tan\theta$ is the slope of the deflection curve of the AFM probe while deflecting the cantilever (Figure 3.35.B).

For these measurements we used an AFM probe with a measured spring constant K_{Peff}= (0.055 ±0.002) N/m (calibrated using Sader's tune method [51]) in agreement with the theoretical one (0.05 N/m). We initially performed multiple force curves on a single cantilever to study the repeatability of the method from which we obtained a relative standard deviation of 5%. This was then repeated on 9 cantilevers, to study the variation of the spring constant in different points of the wafer. The mean value of the slope, for the different cantilevers, is tanθ=0.306 (with a relative standard deviation of 6%) that indicates a spring constant k_C=(0.0240±0.0014) N/m and therefore an E_{nit}=(70±7) Gpa. This value was confirmed measuring the Young's modulus of the 100 nm thick silicon nitride layer on silicon oxide and aluminum substrate by the nanoindentantion technique performed via a XP MTS Nano Indenter. With this value of the silicon nitride Young modulus, we calculated the spring constant for the various cantilever designs (Table 3.4). Note that the rest of piezoresistive cantilever designs have much lower spring constants and it was therefore not possible to perform the spring constant calibration directly on them with this method. Finally, the value of the spring constant of the cantilever design 2x250 has been also simulated in order to verify the analytical model. The result agrees pretty well being just 1% higher.
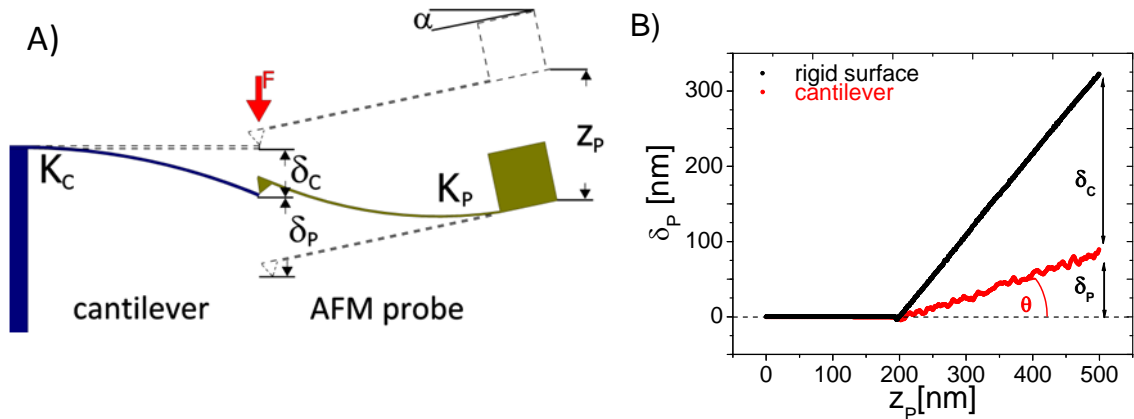
Figure 3.35. A) Beam bending spring constant measurement: the AFM probe is deflecting the test cantilever). The initial positions are shown in dashed lines. B) AFM probe deflection curves (δ_P) against the total AFM probe displacement (z_P). In black the AFM probe is deflected against a stiff surface. This curve is used to calibrate the AFM photodetector sensitivity. In red the AFM probe is deflected against the cantilever under test: the difference between the two curves represent the deflection of the cantilever under test (δ_c).

Cantilever design	w_1 [μm]	w_2 [μm]	L_1 [μm]	L_2 [μm]	k_C [mN/m]	k_C^* [mN/m]	$(k_C^* - k_C)/k_C$
2x250	2	8	125	250	0.62±0.04 (0.617)	0.620	+ 0.5%
6x250	6	16	125	250	1.73±0.11	-	-
8x250	8	20	125	250	2.02±0.13	-	-

Table 3.4. Spring constant for different cantilever designs. The spring constants are calculated from eq. 3.5-3.7, considering the following Young's moduli for silicon, silicon oxide and silicon nitride: 130 GPa, 75 GPa and 70 GPa. The standard deviation is calculated considering that the silicon nitride modulus varies between 63 GPa and 77 GPa. k_C^* has been simulated by finite element method (using Ansys), taking into consideration the same dimensions and young moduli.

3.3.2 – Electrical

The electrical characteristics of the piezoresistors are measured using a semiautomatic probe station (PA200 from Karl Süss) and a semiconductor parameter analyzer (HP4155). I-V curves are acquired for each piezoresistor by sweeping the bias voltage from -2.5 V to 2.5 V in steps of 0.1 V while recording the current. We find a good ohmic contact between aluminum and n-type silicon (Figure 3.36.A), very high fabrication yield (90%-100%) for the best wafers (4972 wafers 4, 9, 10 and 6481 wafers 2, 3, 4, 5), and low relative standard deviation of the resistance values for both the resistors implanted in the substrate and embedded in the cantilevers (Table 3.5). In Figure 3.36.A, we reported the I-V graph for a substrate resistor and a cantilever resistor from a chip of the wafer 6481-3. It is visible the linear behavior of both resistors and that the cantilever resistor has higher resistivity. This difference is in part explained by the different process that the two resistors have, as it will be pointed out here afterwards (i.e. difference between the 2x250 and 2x250- designs). If the results are plotted in R-V graph (Figure 3.36.B) we can notice that while the substrate resistor is constant in this range, the cantilever has a U dependence. This is explained by the fact that at higher voltages (positive or negative), the piezoresistor dissipate more power by joule effect and as consequence the temperature of the cantilever increases and therefore also the resistivity. For an increase of 500 Ω at 2.5 V (with a power ~300 μW) and considering a temperature coefficient of resistance between 500 and 1000 ppm/k [23], the piezoresistor can have a maximum temperature increase of 125 °C and 250 °C. Even though this seems a lot, we have to consider that since the cantilever has a very small volume it has a very small heat capacity. This effect is not visible for substrate resistor since they are on the chip which can be considered a heat sink.

In Table 3.5 we compare the resistance and the square resistances for three different wafers (4972-4, 4972-9, 6481) that had different annealing times and temperature after the OXPTAA annealing (75' at 950 C in oxidizing atmosphere). The sheet resistances were

calculated considering that the total resistor length was 325 μm, the width was 2 μm and that the contact resistance was negligible (less than 200 Ω for each contact). As expected from the model developed in the section 3.1, the sheet resistance decreases by increasing the diffusion length.

From the wafer 6481-3 we can appreciate two main differences in three different designs 2x250, 2x250+ and 2x250- (Table 3.6). First, for the design 2x250+ the substrate resistance has a value 10% higher than the other two designs. In this design the annealing to activate the doping atoms is done after removing the oxide deposited above the implantation (i.e. in the same way that is done also for the cantilever piezoresistors). This is probably due to a loss in arsenic that can derive in part from arsenic pile-up in the Si-SiO$_2$ interface [52-54] and in part from exodiffusion [13]. According to the model and the measurements, around 20% of the As atoms can be lost in wafers 6481-3 and 4972-4.
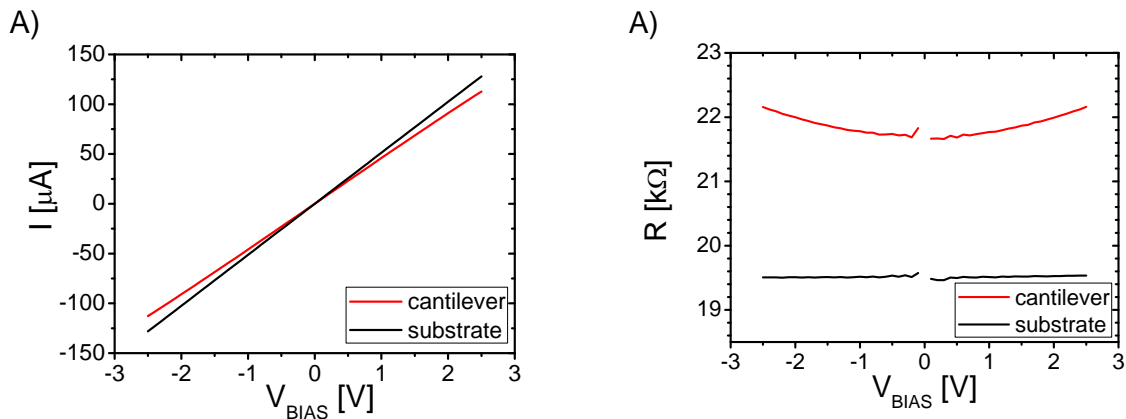
Figure 3.36. I-V (A) and R-V (B) graphs for a chip in the wafer 6481-3. The red corresponds to the cantilever resistor and the black to the substrate resistor.

	2x250 S [kΩ]	2x250 C [kΩ]	2x250 S [Ω/□]	2x250 C [Ω/□]	n° R	t$_{ANN}$ [min]	T$_{ANN}$ [°C]
6481-3	20.3±0.5	22.7±0.7	125±0.3	140±0.4	20	No	No
4972-4	19.3±0.4	23.2±0.5	119±0.3	143±0.3	46	60	900
4972-9	16.3±0.3	18.2±0.7	100±0.2	112±0.4	46	30	1050

Table 3.5 Resistance and sheet resistance mean values ± standard deviation in 3 different wafers. The values are divided between substrate resistor (S) and cantilever resistors (C). n° R is the number of measured resistors, t$_{ANN}$ and T$_{ANN}$ are the time and temperature of post oxidation annealing.

	2x250 S [kΩ]	2x250 C [kΩ]	2x250 S [Ω/□]	2x250 C [Ω/□]	n° R
2x250	20.3±0.5	22.7±0.7	125±0.3	140±0.4	20
2x250+	22.0±0.4	23.0±0.5	135±0.3	142±0.3	20
2x250-	20.0±0.4	22.3±0.7	123±0.3	137±0.4	20

Table 3.6. Resistance and sheet resistance mean values ± standard deviation for 3 different designs in wafer 6481-3. The statistic is made measuring 20 resistances for each design.

The second main difference is relative to the design 2x250- in which the reference cantilever is long just 140 µm instead than 250 µm. From the I-V measurement, plotted in R-V graphs (Figure 3.37), we can see that, if both cantilevers have the same length, they have the same resistance dependence on the bias voltage. On the other hand in shorter cantilevers, the piezoresistors have 15% stronger voltage dependence. This can be explained by the fact that shorter cantilevers can dissipate less heat because of smaller surface area even though the piezoresistor has the same length. This leads to higher temperature and therefore higher resistance variation.

A)   B)
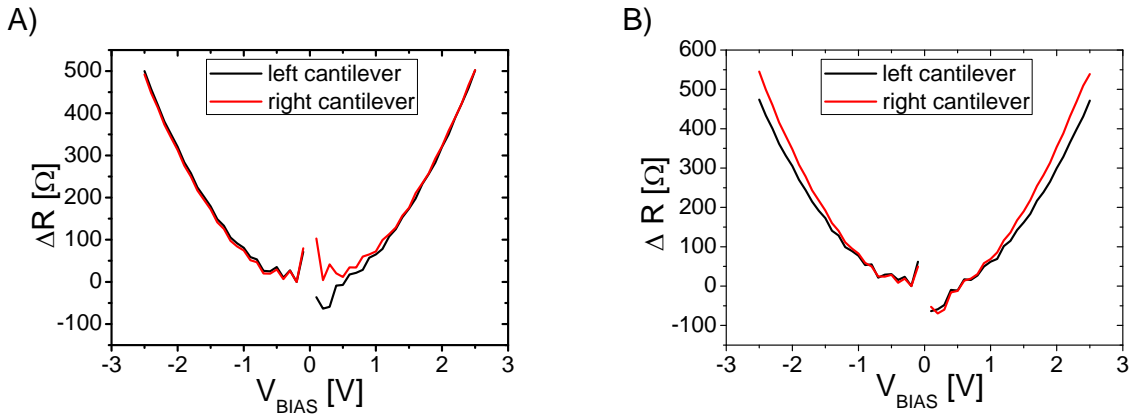
Figure 3.37. R-V graphs for the two cantilevers (red and black) of a chip. A) 2x250 design and B) 2x250- design.

3.3.3 – Noise

The measurement of noise is a complex task because the signals that have to be measured can be very weak, ranging from µV down to nV. Moreover, a DC bias current is usually present as well as disturbances from electronic equipment, which complicates the task even more. The measurement setup must be designed carefully with appropriate shielding and preferably using batteries as power sources to avoid disturbances to be injected in the circuits [19, 55]. Here we will report the developed and optimized set up that we used for the measurement of low-frequency (1 Hz -10 kHz) noise voltage.

We measured the noise power spectral density (PSD) by using a low noise voltage amplifier (LNA) (SR560 from Stanford Research) and a spectrum analyzer (SR785 from Stanford Research). The pads are contacted by using the probe card specifically designed for the sensitivity characterization (see next paragraph). The measurements are performed in a probe station (KS PA200 from Karl Suss), which provides also a good electronic shielding from external noise sources. The wiring system and the supply voltage are adapted to reduce as much as possible the non-intrinsic noise [56]. For this purpose, we use 4 AA rechargeable batteries (Eneloop from Sanyo) that give a DC bias voltage of 5 V and 30 cm long coaxial cables. The differential signal is amplified 1000 times by the LNA and the spectra

recorded by the spectrum analyzer (Figure 3.38). It is of key importance that the device under test, the wirings and the LNA are placed inside the probe station to acquire a PSD free as much as possible from non-intrinsic noise. Moreover, the LNA is operated in "battery" mode which allows having lower amplifier noise. This set-up allows us also to have a single ground (i.e. the ground of the signal analyzer) avoiding possible ground loops. In Table 3.7 we report the parameters for the LNA and the signal analyzer we used for all measurements. The final PSD graph between 1Hz and 10 kHz (Figure 3.39) is the result of 4 different bandwidth measurements: 0.125-12.5 Hz, 0.5-200 Hz, 2-1600 Hz and 16-12800 Hz. Each bandwidth had different number of fast Fourier transform (FFT) lines and therefore different binwidth: 0.125 Hz, 0.5 Hz, 2 Hz and 16 Hz respectively. Each PSD was the average of 50 curves. Finally, we unfortunately noticed that during the weekends the measurements were more stable, repeatable and there were less external interferences. This is due to the fact that almost all the equipments in the IMB-CNM are shut down, which provokes to have less interference. In this perspective, the quasi totality of the noise measurements has been performed during non-working hours.

SR560		SRS785				
Coupling	AC	Coupling	AC			
Inputs	A-B	Input	A			
filters	0.03-300K	Window	Hanning			
Gain	1000	Span [Hz]	12.5	200	1600	12800
Input	100 MΩ, 25pF	FFT lines	100	400	800	800
Output	50 Ω	Binwidth [Hz]	0.125	0.5	2	16

Table 3.7. Parameters of the low noise voltage amplifier (SR560) and the dynamic analyzer (SRS785) for the noise measurements.
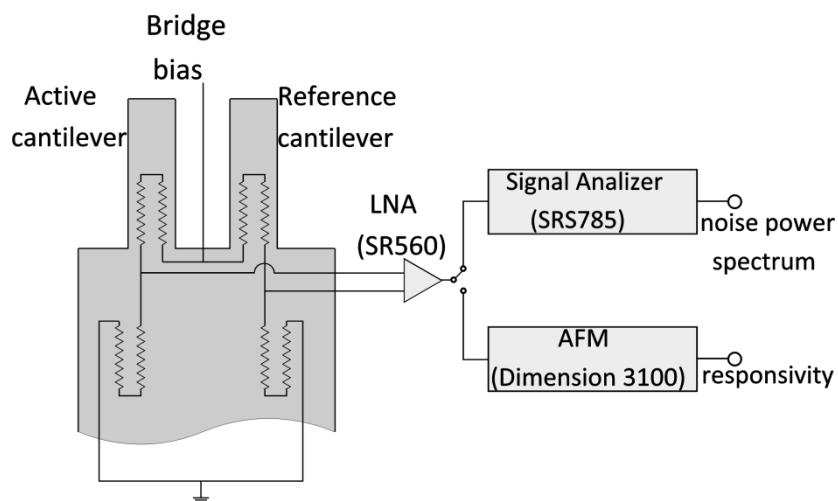
Figure 3.38. Noise and sensitivity measurements electrical scheme. The differential voltage of the Wheatstone bridge is amplified by the low noise voltage amplifier. The noise spectrum is recorded by the signal analyzer while the sensitivity signal is recorded by the AFM electronics (see next section).

After the optimization of the set up, we tested the repeatability of the measurement, recording the noise spectrum 9 times for a single chip taking on and off the set up each time. We obtained a relative standard deviation of 2% for the integrated noise in the 1 Hz-10 kHz bandwidth. Then we measured the noise spectra of all the chips across the wafer for one wafer (4972-9) and of fewer chips for two other wafers (4972-4 and 6481). In Figure 3.39, we report typical input referred noise power spectral density for the three different wafers. In Table 3.8, we report the mean voltage noise value referred to input (V_{noise}) measured between 1Hz and 10 kHz and the Hooge factor.

As we can see from the graphs and the average voltages there are substantial differences between the wafers 4972 and 6481. Although in the literature it is reported that for thermal treatments with higher diffusion length the 1/f noise and Hooge factor decrease, we found the opposite behavior. While α substantially agree with literature values for wafer 6481 [23], it is much higher for wafers 4972. This can be explained by the fact that the aluminum RIE damaged the crystalline structure of the implanted silicon in wafer 4972 because longer over-etching has been used. On the other hand in wafer 6481, we reduced as much as possible the etching time and the aluminum residues have been etched by wet etching. Extreme care should be taken for the back end of line process, after the piezoresistor is formed. Reactive ion etching should be avoided whenever possible and they should be replaced by wet etching or better by lift-off processes.

A second important point is that a good nitride passivation, which insulates the piezoresistor in liquid environment, is of fundamental importance for both air and water environments. The noise spectral density of a device (wafer 6481-3) immersed in water, shown in Figure 3.39.E, shows that the silicon nitride layer provides a good insulation for the conductors immersed in liquid. On the other hand, in Figure 3.40.A, we can see the noise spectra of a chip (4972-4) measured just after biasing and after few minutes. The low frequency noise spectra increases of around 1 order of magnitude and loose the typical 1/f noise shape. This is probably due to the fact that in wafer 4 the nitride passivation layer has been damaged during the HF vapor release (Figure 3.40.B).

Finally, for the sensors of the wafer 6481-4, the noise spectra have a $1/f^n$ behavior between 1 Hz and 10 Hz (Figure 3.39.C). This has been reported already by other researchers [11] and it has been explained by "temperature fluctuations or thermomechanical coupling due to unstable convection around the cantilever, leading to temperature fluctuations which are electrically coupled via a change in piezoresistivity with temperature"
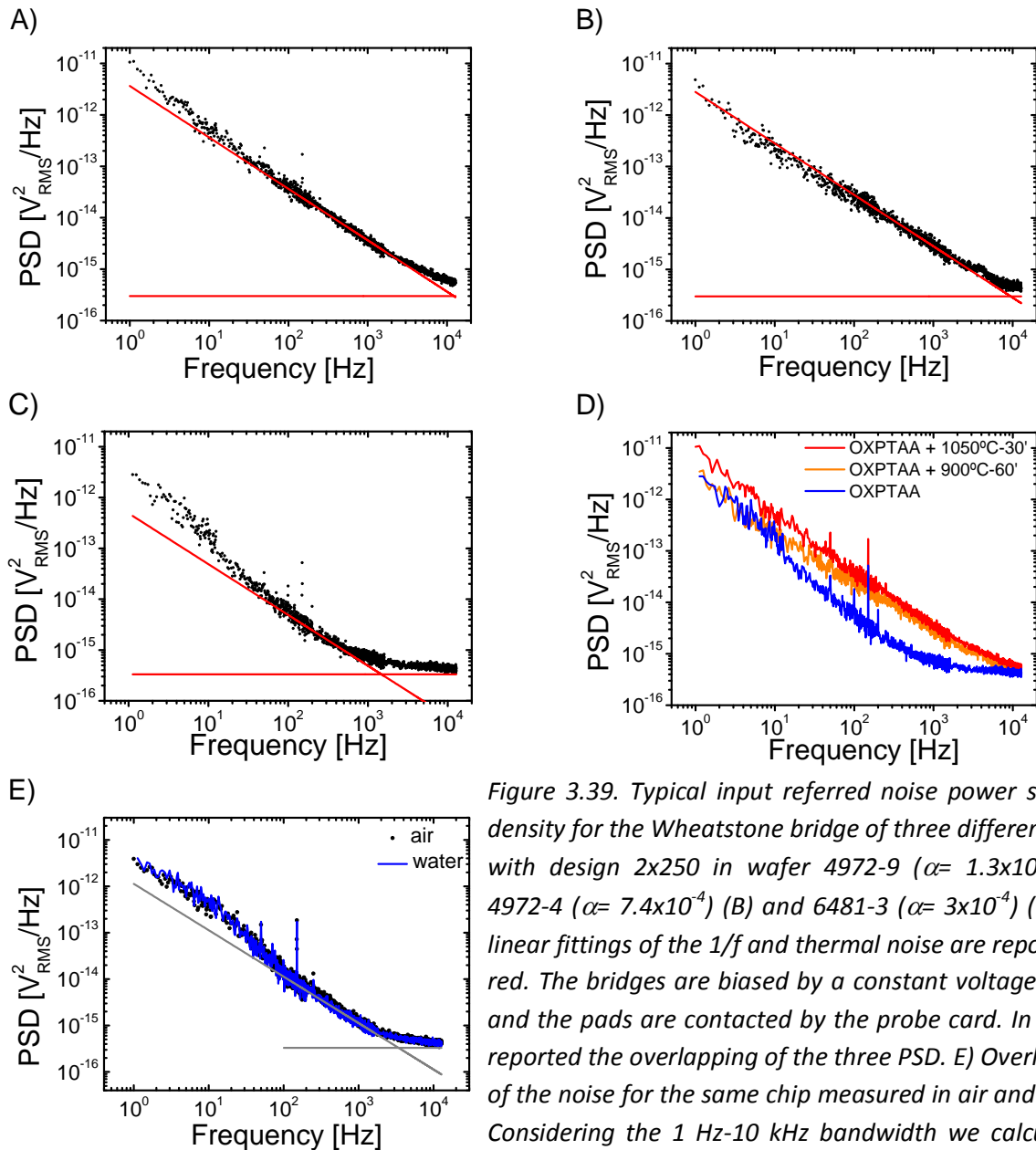
Figure 3.39. Typical input referred noise power spectral density for the Wheatstone bridge of three different chips with design 2x250 in wafer 4972-9 (α= 1.3x10^{-3}) (A), 4972-4 (α= 7.4x10^{-4}) (B) and 6481-3 (α= 3x10^{-4}) (C). The linear fittings of the 1/f and thermal noise are reported in red. The bridges are biased by a constant voltage of 5 V and the pads are contacted by the probe card. In D) it is reported the overlapping of the three PSD. E) Overlapping of the noise for the same chip measured in air and water. Considering the 1 Hz-10 kHz bandwidth we calculate a noise of 3.7 µV in air (black) and 3.8 uV in water (blue)

WAFER	DESIGN	$2\sqrt{Dt}$ [nm]	V_{noise} [µV]	α (x10^{-3})	n° sensors
4972-9	2x250	95	6.7±1.0	1.3±0.2	24
4972-9	6x250	95	5.5±0.6	2.8±0.3	24
4972-9	8x250	95	6.9±0.7	1.4±0.1	24
6481-4	2x250	42	3.9±0.8	0.3±0.1	10

Table 3.8. Diffusion length($2\sqrt{Dt}$), input referred noise integrated in the 1 Hz - 10 kHz bandwidth (V_{noise}), Hooge factor (α), for different cantilever designs and in different wafers. The statistics are made out of 24 or 10 sensors across the wafer.
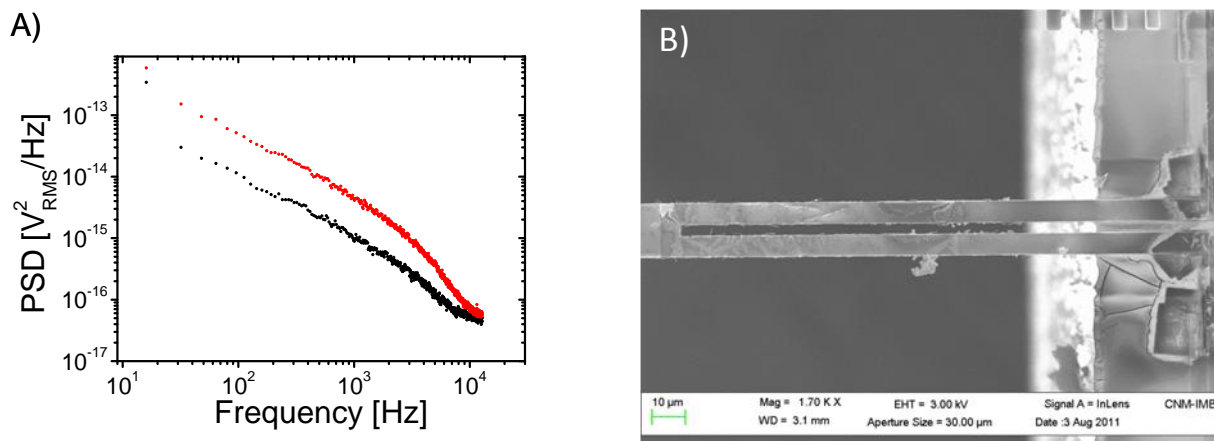
Figure 3.40. A) Input referred noise power spectral density for the Wheatstone bridge of the majority of the chips from the wafer 4972-4. In black the PSD when the chip is just biased; in red the PSD when the chip is biased for 10 minutes. B) SEM image of the cantilever: it is visible how the silicon nitride passivating layer is damaged.

3.3.4 – Sensitivity and resolution

The displacement sensitivity, $S_{\delta,V}=\Delta V/\delta$, can be measured by performing an accurate deflection of the cantilever while recording the resistance variation or, in our case, the voltage variation of the Wheatstone bridge. In order to deflect the cantilever with high accuracy, various approaches have been used, such as a needle mounted on a bimorph piezodisk [57], a calibrated piezotube [58], an AFM in contact mode [59] or in tapping mode [60], etc. A parallel approach, only valid for very low stiffness devices, measures the resonant thermomechanically-driven displacement fluctuations [21, 59]. All these methods allowed a precise estimation of the device deflection sensitivity but were carried out on a chip level, therefore making technology validation a tedious and long process. An alternative, which allows for on-wafer testing, is to deflect the cantilever by a needle mounted on a micromanipulator [61]. However, this method is far less accurate than the previously mentioned solutions.

Here, we present a novel set-up and technique that allows on-wafer characterization with high accuracy, good repeatability and unprecedented reduction in testing time. For this purpose, we designed a special probe-card (Figure 3.41.A), which was fabricated by HTT.GmbH in Dresden (Figure 3.41.B). It allowed us to contact the pads of a chip and simultaneously deflect them by other means. In particular, its reduced size permitted the use of an AFM (Dimension 3100 or Dimension Icon of Bruker) to deflect the cantilevers, thus benefiting from the high motional precision of such equipment. The probe-card presented here was specifically designed to be used in the Dimension 3100 AFM, could access all the devices across the 4'' wafer, using a micropositioner (500 MIS from Quater). The probes had to be long and almost horizontal in order to avoid any interaction with the head and probe

holder of the AFM (Figure 3.41.C) and were correctly aligned onto the chip pads using the optical microscope of the AFM. In addition, the PCB had to be small to fit onto the AFM chuck. The two grooves (visible in the left part of the top view) increased the travel range of the micropositioner. To bias the chips, we used a voltage source (2636 from Keithley) or 4 AA rechargeable batteries (Eneloop from Sanyo) in series, which provided a constant voltage of 5 V. A low noise voltage amplifier (SR 560 from Stanford Research) was used to amplify the differential output signal (Figure 3.38). In Figure 3.42 and Figure 3.43, it is possible to see the complete set up. The wafer was placed on the chuck of the AFM and the probecard was moved on a chip to contact the pads. Then, a stiff AFM probe (k≈40 N/m) was used to deflect the cantilevers at a certain distance from the clamping edge (namely at 140±3 μm or at the free end). The output differential voltage was amplified and recorded continuously together with the AFM probe displacement (Figure 3.44).
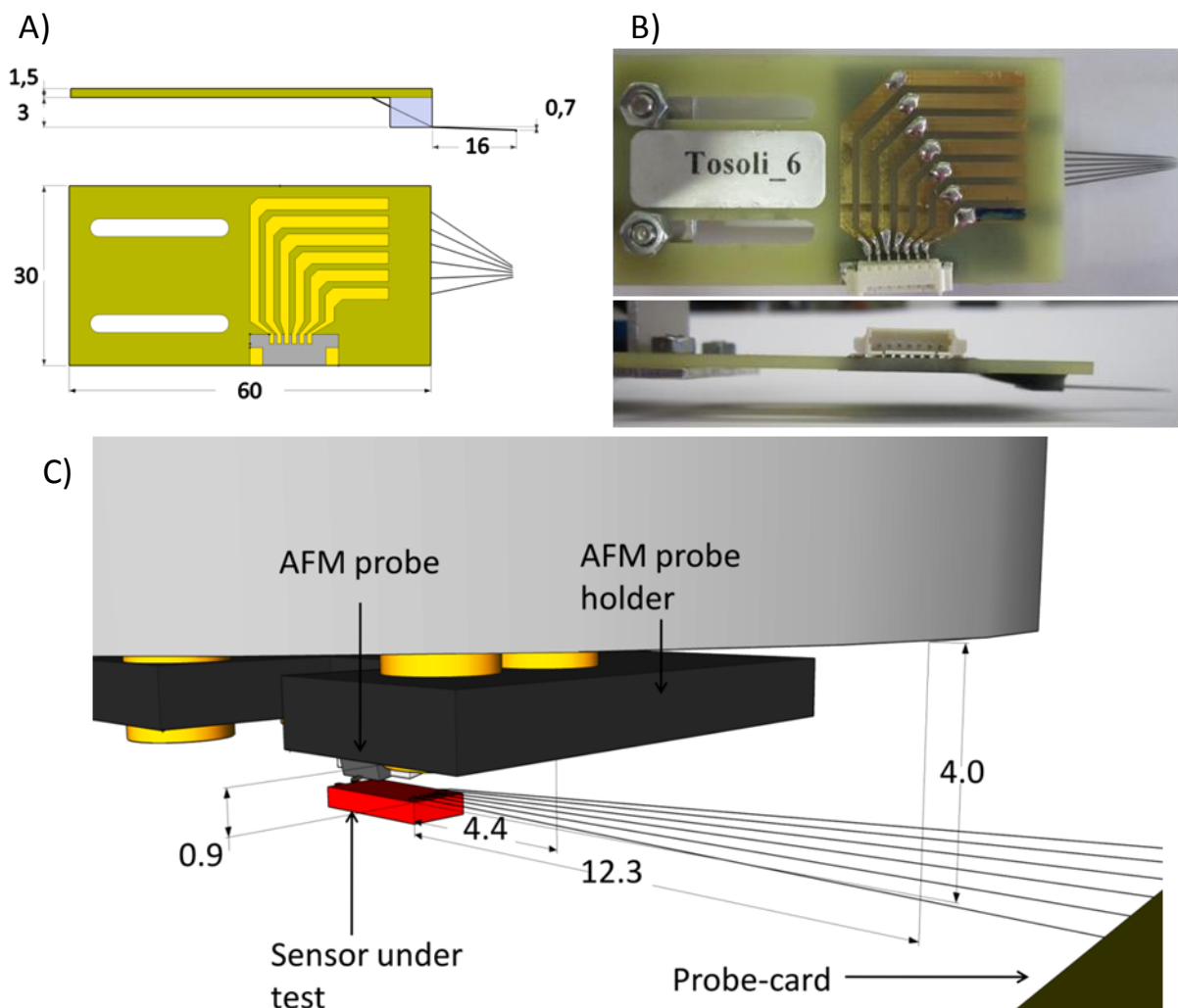
Figure 3.41. A) Lateral view (up) and top view (down) of the probe card design (dimensions in mm). For the probes we fixed the maximum vertical drop to 0.7 mm and the length to 16 mm to avoid any interaction with the AFM head. B) Probecard fabricated by HTT.GmbH in Dresden. C) The probes have to contact the pads of the chips without interacting with the AFM probeholder or with the AFM head while the AFM probe is in contact (dimensions in mm).
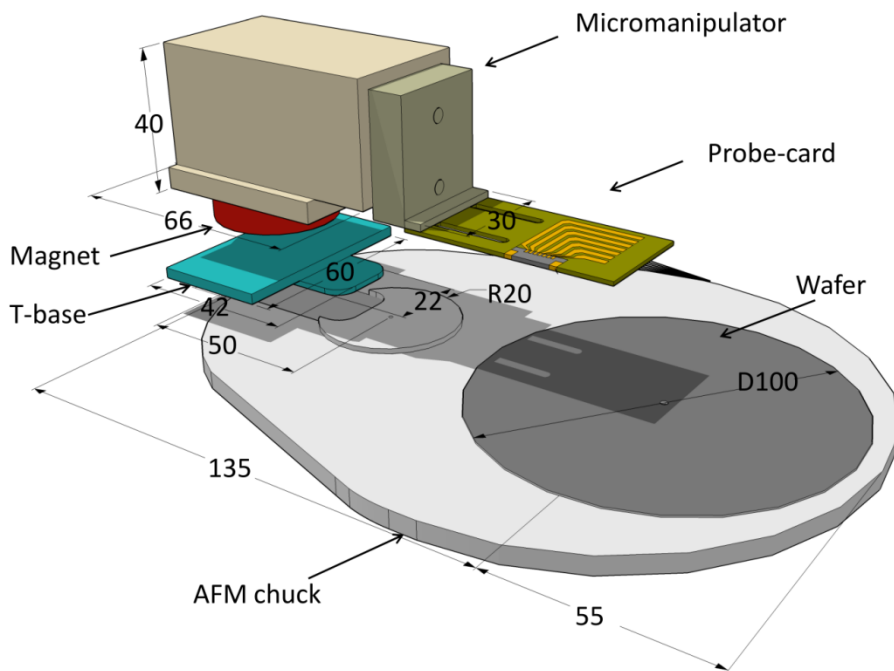
Figure 3.42. Representations of the probecard held by the micromanipulator on the AFM chuck (dimensions in mm). The micromanipulator (orange) is fixed on a substrate by a magnet (red). Unfortunately the non compatible CMOS AFM chuck is made of non-magnetic steel therefore we made a T shaped base (blue) from magnetic steel, which can be fixed on the AFM chuck by a screw.
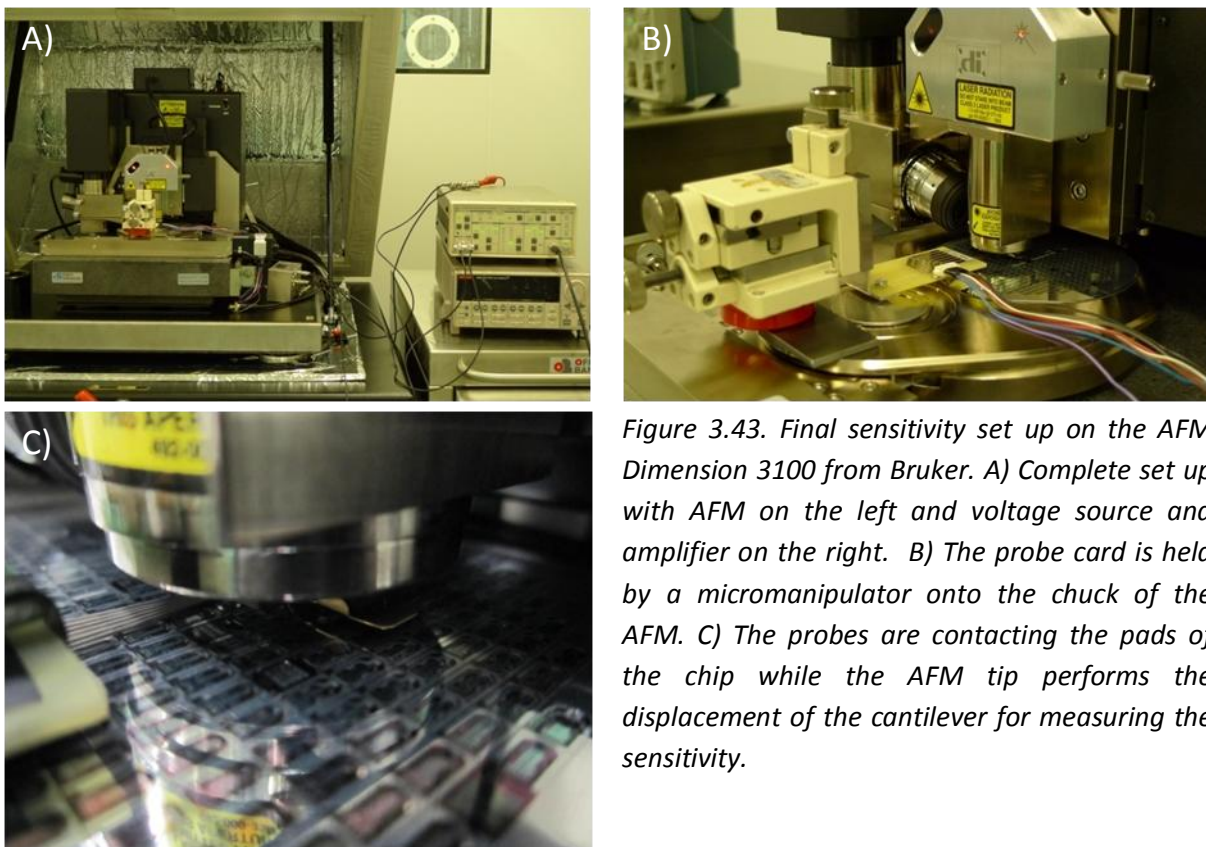
Figure 3.43. Final sensitivity set up on the AFM Dimension 3100 from Bruker. A) Complete set up with AFM on the left and voltage source and amplifier on the right. B) The probe card is held by a micromanipulator onto the chuck of the AFM. C) The probes are contacting the pads of the chip while the AFM tip performs the displacement of the cantilever for measuring the sensitivity.

In order to precisely position the AFM tip on top of the device and work under low interaction forces, the AFM was operated in dynamic mode. In this mode, the tip-sample interaction is controlled by maintaining fixed amplitude of AFM probe oscillating at its resonance frequency. This gave us another advantage and was the ability to detect when the AFM probe contacts the piezoresistive cantilever, which was when the oscillation amplitude dropped to zero. Since the stiffness of the AFM probe was much bigger than the one of the cantilever under investigation (4 or 5 orders of magnitude), its static deflection was negligible. After one measurement that typically was performed at 1 Hz, the probe card could be moved to the next chip by using the micromanipulator. The AFM allowed a precise positioning of the probe along the cantilever thanks to the optical microscope and to the motorized positioning stage which has a repeatability of $\pm$ 3 μm. We had also very good control of the deflection, due to the piezoactuator of the AFM.

Figure 3.44 shows a typical deflection experiment. From these measurements, we obtained the displacement sensitivity ($S_\delta = \Delta V/\delta$) and we calculated the gauge factor (G) or piezoresistive coefficient (π_{11}) and the force sensitivity ($S_{F,V} = \Delta V/F$) for a force F applied in the end of the cantilever (3.8).

In Figure 3.45, we report the difference deflection sensitivity for the same cantilever deflected at 140 μm and 250 μm far from the clamping edge. In the first case, the force sensitivity at the tip was calculated from the sensitivity model (3.8). If the cantilever was deflected at the tip, then the force sensitivity was calculated considering the nominal spring constant. In this example we can appreciate that the two calculated values (180 μv/nN and 170 μv/nN) are in a good agreement.

In order to check the repeatability of the measurement method, we performed multiple force curves on the same piezoresistive cantilever with the AFM probe being always in contact and we obtained a relative standard deviation of less than 2% out of 8 measurements (Figure 3.46.A). This variability is mainly due to low frequency noise and to the linear fitting. In addition, we performed repeatability experiments also taking on and off the set up each time performing the force distance curve on the same cantilever at the same point. As expected, we obtained a higher relative standard deviation of around 3% out of 5 measurements (Figure 3.46.B). The higher variability should be addressed to the uncertainty of the positioning system. The variation agrees with the electromechanical model developed in section 3.1.

In addition to the repeatability, we studied also the variation of the sensitivity of the chips across the wafers (Figure 3.47). In Table 3.9 we report the mean value of the sensitivities, noise and MDF. This shows that our measurement system is particularly suited to technology characterization where several device types and several device geometries within a type have to be measured.
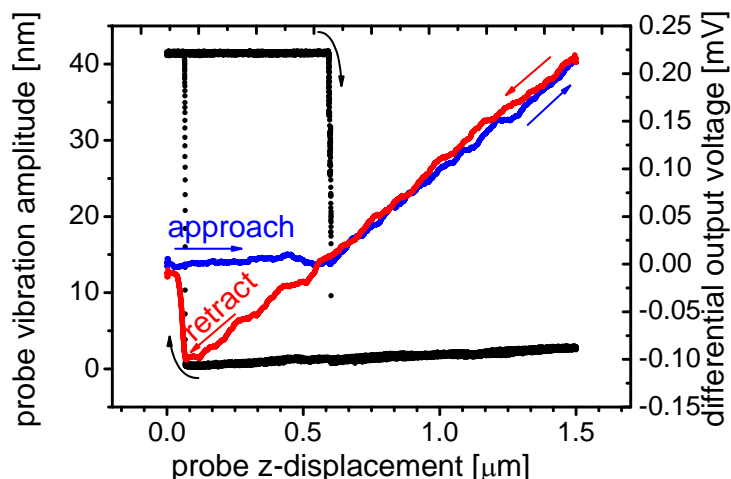
Figure 3.44. Electromechanical response of a piezoresistive cantilever (8x250). At a length of 140 μm, a stiff probe (in tapping mode) starts to deflect downwards the cantilever when the vibration decreases from around 40 nm to almost 0 nm. At the same time the output differential voltage of the Wheatstone bridge (WB) starts to increase (blue line) from 14.03 mV to 14.24 mV for a deflection of 0.91 μm. This means a displacement sensitivity of around 231 μV/um at the deflection point and a force sensitivity of 46 μV/nN at the tip. In the retract curve (red) is also visible the strong interaction between the AFM tip and the cantilever under test which is bending upwards for 0.5 μm. The force curve (approach and retract) is performed over 1 second.
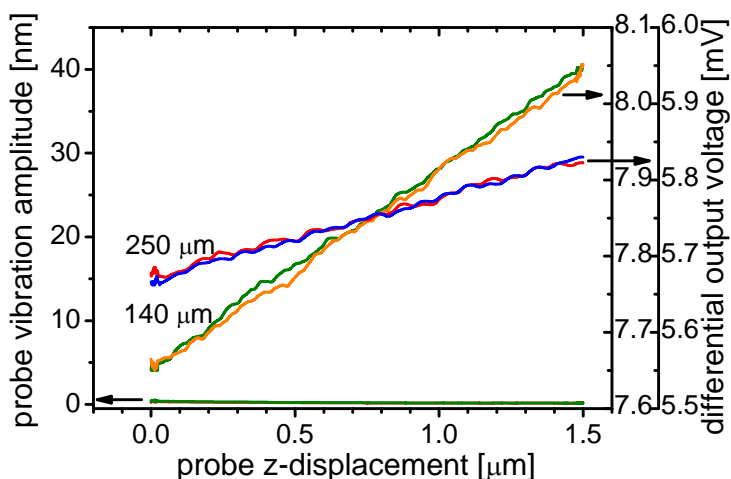
Figure 3.45. Sensitivity measurements on a piezoresistive cantilever (2x250). The AFM probe performs a force curve on the test cantilever at 140 μm from the clamping edge or at 250 μm (i.e. at the cantilever end). In the first case, the output voltage goes from 7.65 mV to 8.04 mV. This correspond to a displacement sensitivity of 261 μV/μm and to a force sensitivity at the tip of 180 μV/nN. In the second case the voltage varies between 5.67 mV and 5.83 mV, which means a displacement sensitivity of 106 μV/μm and a force sensitivity at the tip of 170 μV/nN in agreement with the previous measurement. The vibration amplitude of the AFM probe is stable at 0 nm for all the measurement (i.e. the probe is always in contact).
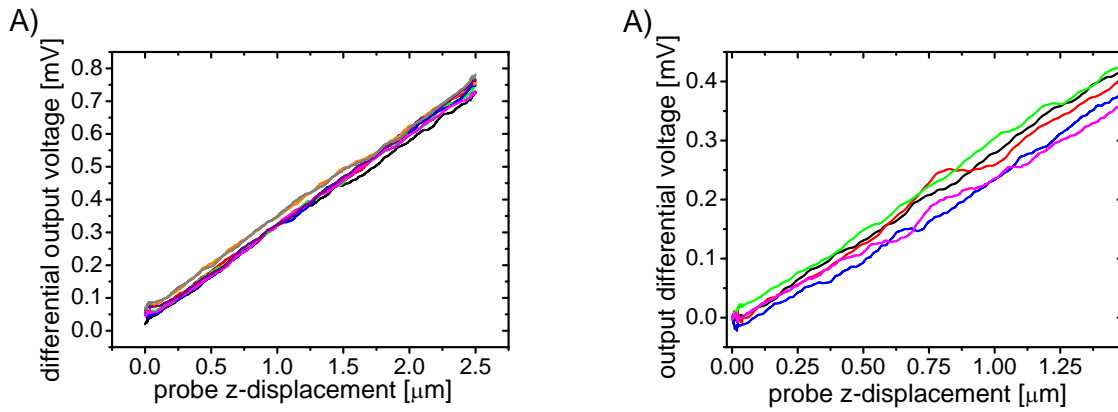
Figure 3.46. Repeatability measurements. A) The AFM probe is in contact and it performs 8 force curves. B) The measurements are performed on the same cantilever and at the same length taking on and off the set up between each measurement.
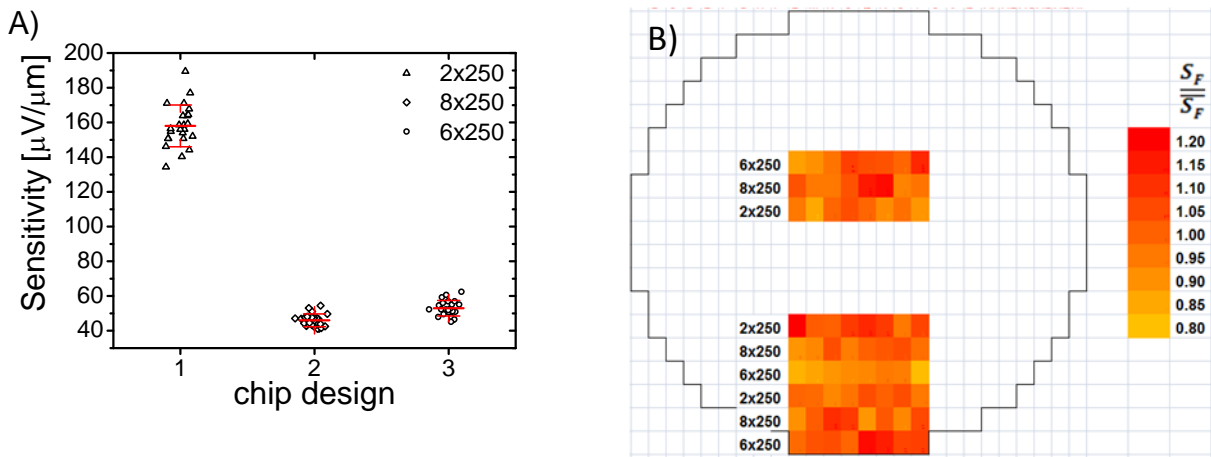
Figure 3.47. A) Sensitivity results for 72 chips (24 per each design) of wafer 4972-9. Triangles, squares and circles refer respectively to the designs 2x250, 8x250 and 6x250. Averaged values and standard deviation are reported in red for each design. B) Sensitivity wafer-map. The 24 chips of each design are positioned in 3 different rows of 8 chips each. The relative sensitivity (sensitivity divided by the averaged sensitivity, $S_F/\overline{S_F}$) increases from yellow to red as reported in the legend.

From Table 3.9, it is possible to see that going to lower diffusion lengths and thinner piezoresistors (Figure 3.48) is beneficial to the sensitivities and to the efficiency factor, β. This was calculated considering a maximum deflection sensitivity of 1670 µV/µm and 700 µV/µm for deflection points of 140 µm and 250 µm respectively. For calculating the maximum sensitivity, an infinitely thin piezoresistor with the highest piezoresistive coefficient was considered. Taking into account the noise and the sensitivity values for the wafer 6481 we achieved a maximum resolution of 6±2 pN (design 2x250).

Wafer	Design	S_δ	Deflection Point	t_R	β	$S_{F,V}$	π_{11} x10^{-11}	nº chips	Noise 1Hz-10kHz	MDF
		[µV/µm]	[µm]	[nm]		[µV/nN]	[Pa^{-1}]		[µV]	[pN]
4972-4	2x250	510±28	140	115	0.31	320±18	61±3	23		21
	8x250	470±40	140	115	0.28	100±9	56±5	23		69
	6x250	510±25	140	115	0.31	120±6	62±3	20		46
4972-9	2x250	240±19	140	185	0.14	160±13	67±5	24	6.7±1.0	42±9
	8x250	230±20	140	185	0.14	40±3	64±6	24	6.9±0.7	170±30
	6x250	230±18	140	185	0.14	50±4	64±5	24	5.5±0.6	110±19
6481	2x250	400±50	250	70	0.57	650±75	88±10	10	3.9±0.8	6±2

Table 3.9. Deflection sensitivity (S_δ), deflection point from the clamping edge, piezoresistor thickness (t_R) from TOF-SIMS measurements (Figure 3.48), efficiency factor, force sensitivity ($S_{F,V}$), piezoresistive coefficient, number of measured chips, input referred noise in the 1Hz 10 kHz bandwidth, force resolution (MDF). The force resolution of the three designs of the wafer 4972-4 it has been calculated considering the noise of the designs of the wafer 4972-9.
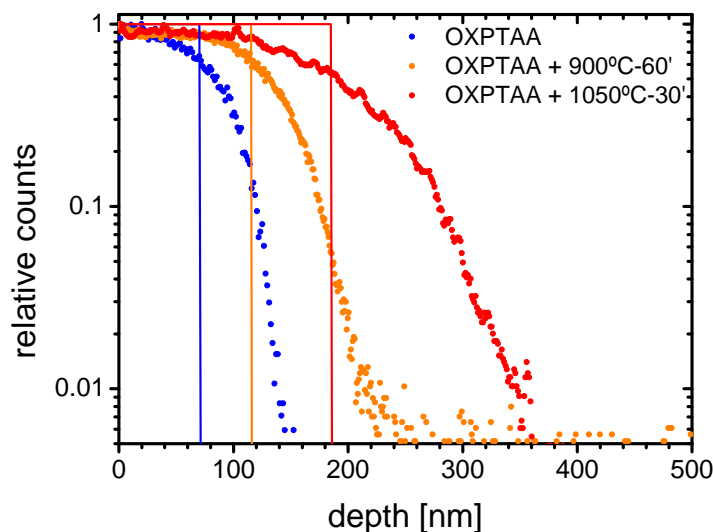
Figure 3.48. TOF-SISM measurements of the implantation for the three different wafers. For higher diffusion length the junction has also higher depth. The real profiles have been approximated with step profile functions (continuous line) to calculate the average piezoresistive coefficient in Table 3.9. The depths of the step profiles are calculated supposing that all the atoms are within this profiles which have a constant concentration.

In Table 3.10, the sensitivity calculated from the model is compared to the measured sensitivity, for the three different wafers. The results agree quite well for the first two wafers while for the wafer 6481 the experimental sensitivity is almost two times higher respect to the predicted one. This can be due to many factors related to the model and to the

measured devices, as for example: sub-estimation of the piezoresistive coefficient in the model, initial bending of the cantilever, BOX not completely etched. Considering the deviation, an upgrade of the model that takes into account the real dopant profile, could be beneficial also for an improvement of the sensor performance. This would require also process simulations [18] and piezoresistance experiments [30].

Concluding, the use of the probe-card together with a manual micromanipulator allowed characterizing a considerable number of chips in a relatively short time (20-30 chip/hour for expert users) across the whole wafer. This constitutes a definite improvement with the way these measurements were done up to date [60], where the chip had to be pulled apart from the wafer, attached on a PCB board and wire bonded, which is a time consuming, risky and not robust process. In addition, with the new method we reduced also the risk to damage the sensor. An additional way to decrease the measurement time would be to automate in part the measurement set up using a motorized micromanipulator. However, there is a limit to the amount of the automation due to the complex nature of the electro-mechanical measurement. Finally from the sensor point of view, we achieved our target to fabricate, in a reliable way, sensors endowed with sub-10 pN resolution suitable to be used in biomolecule detection.

Wafer	Design	$S_{F,V}$ [μV/nN]	$S_{F,V}^*$ [μV/nN]	
4972-4	2x250	320	282	+13%
4972-9	2x250	160	128	+25%
6481	2x250	650	342	+91%

Table 3.10. Measured force sensitivity ($S_{F,V}$), calculated sensitivity ($S_{F,V}^*$), relative difference between model and experimental values.

Summary and future research directions

The main objective of the work presented in this chapter was to obtain a high number of force sensors based on piezoresistive cantilevers, enabled with a resolution of around 10 pN in liquid environment, to be used in the detection of intermolecular forces. Such a high force resolution was needed in view of the very low unbinding forces of single pairs of receptor and ligand molecules, which are in the order of 10 - 100 pN.

In the first section, the electromechanical model to evaluate the resolution of the sensor has been presented. This was used to find the right parameter values to improve the performance of the cantilevers which were previously developed at CNM and had a resolution of 65 pN, which was not sufficient for our purposes.

Afterwards, it has been presented the microfabrication process that allowed a fabrication yield between 90% and 100%, in the best wafers. The main fabrication issues have been also addressed (i.e. metal and buried oxide etchings). Different fabrication solutions have been taken to improve especially the sensitivity and the noise. Thanks to the optimization of two key process steps (i.e. relatively low annealing temperature, a combination of dry and wet metal etching), we obtained sensors with a sensitivity of 650±75 µV/nm, a noise of 3.8±0.8 µV and a resolution of 6±2 pN. A big improvement in the yield was then represented by the upgrading of a custom made HF vapor etcher. Thanks to it, we could etch the buried oxide more homogeneously and in a more reliable way. This translated to lower risk to damage the silicon nitride insulation layer and to higher number of well passivated sensors (between 25% and 50% of all the chips in a wafer).

A third, very important, aspect to achieve the objective, was the development of highly precise and high-throughput electro-mechanical characterization techniques and set-ups to correctly validate the technological processes involved in production as well to characterize all the final devices. In particular, the integration of a probe-card into an AFM allowed a fast and precise on-wafer sensitivity measurement and the use of a preamplifier and a spectrum analyzer with a probe-station allowed a reliable on-wafer noise characterization. The complete characterization of an entire wafer became possible in a reasonable time (≈1 week). Mechanical, electrical, noise and electromechanical average properties have been reported for 3 different wafers.

In different points of the chapter, several advices to improve the performance and the yield of the sensor have been point out:

- Improvement of piezoresistive and noise properties of doped silicon in structures those are much easier to fabricate than cantilevers.
- Fabrication of the chip metal interconnections by lift-off process instead than sputtering and etching. To this purpose a reversible resist with a thickness between 3 µm and 5 µm with a pronounced undercut could work pretty well (i.e. TI 35ES from MicroChemicals GmbH)

- Upgrade further the HF vapor etcher or better use a commercial one to etch in a more uniform way the BOX. Commercially available equipment exists from AMMT GmbH, Idonus or SPTS Primaxx.

References

1. Petersen, K.E., *Silicon as a mechanical material.* Proceedings of the IEEE, 1982. **70**(5): p. 420-457.
2. Hopcroft, M.A., W.D. Nix, and T.W. Kenny, *What is the Young's Modulus of Silicon?* Journal of Microelectromechanical Systems. **19**(2): p. 229-238.
3. Yota, J., *Effects of Deposition Method of PECVD Silicon Nitride as MIM Capacitor Dielectric for GaAs HBT Technology.* ECS Transactions, 2011. **35**(4): p. 229-240.
4. Osenbach, J.W., *Corrosion-induced degradation of microelectronic devices.* Semiconductor science and technology, 1996. **11**(2): p. 155.
5. Lin, H., et al., *Moisture-resistant properties of SiNx films prepared by PECVD.* Thin Solid Films, 1998. **333**(1-2): p. 71-76.
6. Wei, J., et al., *A new fabrication method of low stress PECVD SiNx layers for biomedical applications.* Thin Solid Films, 2008. **516**(16): p. 5181-5188.
7. Tortonese, M., R.C. Barrett, and C.F. Quate, *Atomic resolution with an atomic force microscope using piezoresistive detection.* Applied Physics Letters, 1993. **62**(8): p. 834-836.
8. Harjee, N., *Coaxial-tip Piezoresistive Cantilever Probes for High-resolution Scanning Gate Microscopy*2011: Stanford University.
9. Thaysen, J., et al., *Atomic force microscopy probe with piezoresistive read-out and a highly symmetrical Wheatstone bridge arrangement.* Sensors and Actuators A: Physical, 2000. **83**(1-3): p. 47-53.
10. Park, S.-J., J.C. Doll, and B.L. Pruitt, *Piezoresistive Cantilever Performance-Part I: Analytical Model for Sensitivity.* Journal of Microelectromechanical Systems, 2010. **19**(1): p. 137-148.
11. Park, S.-J., et al., *Piezoresistive Cantilever Performance-Part II: Optimization.* Journal of Microelectromechanical Systems, 2010. **19**(1): p. 149-161.
12. Jones, S.W., *Diffusion in Silicon,* 2008: ICKnowledge LLC.
13. Guia, G.B., *recuita termica rapida de silici implantat amb arsenic per a la fabricacio d'unions poc profundes*, 1989, Universidad Autonoma de Barcelona.
14. Tsai, M.Y., et al., *Shallow junctions by high-dose As implants in Si: experiments and modeling.* Journal of Applied Physics, 1980. **51**(6): p. 3230-3235.
15. Liu, T.M. and W.G. Oldham, *Sheet resistance-junction depth relationships in implanted arsenic diffusion.* Electron Device Letters, IEEE, 1981. **2**(10): p. 275-277.
16. Harley, J.A. and T.W. Kenny, *1/f noise considerations for the design and process optimization of piezoresistive cantilevers.* Microelectromechanical Systems, Journal of, 2000. **9**(2): p. 226-235.
17. Doll, J.C., et al. *High frequency force sensing with piezoresistive cantilevers*. in *Solid-State Sensors, Actuators and Microsystems Conference, 2009. Transducers 2009. International*. 2009.
18. Doll, J.C., *Advances in high bandwidth nanomechanical force sensors with integrated actuation*, 2012, Stanford University.
19. Dieme, R., *Investigation of process fabrication for low-noise p-type diffused piezoresistors* 2009, University of Florida.
20. Zeghbroeck, B.V., *Principles of semiconductor devices*2011: online book at http://ecee.colorado.edu/~bart/book/.

21. Harley, J.A., *Advances in Piezoresistive Probes for Atomic Force Microscope*, 2000, Stanford University.
22. Pritchard, A.B., D.B. McCormick, and L.D. Wright, *Optical rotatory dispersion studies of the heat denaturation of avidin and the avidin-biotin complex.* Biochemical and Biophysical Research Communications, 1966. **25**(5): p. 524-528.
23. Barlian, A.A., et al., *Review: Semiconductor piezoresistance for microsystems.* Proceedings of the IEEE, 2009. **97**(3): p. 513-552.
24. Serre, C., et al., *Determination of micromechanical properties of thin films by beam bending measurements with an atomic force microscope.* Sensors and Actuators A: Physical, 1999. **74**(1-3): p. 134-138.
25. Cassard, J., et al. *The MEMS 5-in-1 Reference Materials (RM 8096 and 8097)*. in *Microelectronic Test Structures (ICMTS), 2012 IEEE International Conference on*. 2012. IEEE.
26. Van Drieenhuizen, B.P., et al., *Comparison of techniques for measuring both compressive and tensile stress in thin films.* Sensors and Actuators A: Physical, 1993. **37-38**(0): p. 756-765.
27. Ting, C.Y. and M. Wittmer, *The use of titanium-based contact barrier layers in silicon technology.* Thin Solid Films, 1982. **96**(4): p. 327-345.
28. Faith, T.J., et al., *Contact resistance: Al and Al-Si to diffused N+ and P+ silicon.* Journal of Vacuum Science & Technology A: Vacuum, Surfaces, and Films, 1983. **1**(2): p. 443-448.
29. Richter, J., *Piezoresistivity in Microsystems*, 2008, Technical University of Denmark.
30. Richter, J., et al., *Piezoresistance of silicon and strained Si0.9Ge0.1.* Sensors and Actuators A: Physical, 2005. **123-124**: p. 388-396.
31. Richter, J., et al., *Four point bending setup for characterization of semiconductor piezoresistance.* Review of scientific instruments, 2008. **79**(4): p. 044703-044703-10.
32. Richter, J., *Piezo resistivity in silicon and strained silicon germanium*, 2004, Technical University of Denmark.
33. Kim, C. and J.W. Morris, *The influence of Cu precipitation on electromigration failure in Al-Cu-Si.* Journal of Applied Physics, 1992. **72**(5): p. 1837-1845.
34. Xiao, H., *Introduction to Semiconductor Manufacturing Technology*2001: Prentice Hall PTR.
35. James D. Plummer, M.D.D., Peter B. Griffin, *Silicon VLSI Technology: Fundamentals, Practice and Modeling*: Prentice Hall PTR.
36. Microchemicals, *Lift-off Processes with Photoresists*, www.microchemicals.eu/technical_information.
37. Gabriel, C., *CMOS Application of Plasma Etching*, in *International Courses in Semiconductor Technology*, CEI-EUROPE, Advanced Technology Education.
38. Pearton, S.J. and D.P. Norton, *Dry etching of electronic oxides, polymers, and semiconductors.* Plasma Processes and Polymers, 2005. **2**(1): p. 16-37.
39. Helms, C.R. and B.E. Deal, *Mechanisms of the HF/H2O vapor phase etching of SiO2.* Journal of vacuum science and technology. A. Vacuum, surfaces, and films, 1992. **10**(4): p. 806-811.
40. Witvrouw, A., et al. *Comparison between wet HF etching and vapor HF etching for sacrificial oxide removal*. in *Micromachining and Microfabrication*. 2000. International Society for Optics and Photonics.

41. Hill, G.C., et al., *Patterned cracks improve yield in the release of compliant microdevices from silicon-on-insulator wafers.* Journal of Micromechanics and Microengineering, 2011. **21**(8): p. 087001.

42. Bakke, T., et al. *Etch stop materials for release by vapor HF etching*. in *16 MicroMechanics Europe Workshop (MME)* 2005. Göteborg, Sweden.

43. Fang, W. and J.A. Wickert, *Determining mean and gradient residual stresses in thin films using micromachined cantilevers.* Journal of Micromechanics and Microengineering, 1996. **6**(3): p. 301-309.

44. Villanueva, L.G., *Development of Cantilevers for Biomolecular Measurements*, 2006, Universitat Autonoma de Barcelona.

45. Wortman, J.J. and R.A. Evans, *Young's Modulus, Shear Modulus, and Poisson's Ratio in Silicon and Germanium.* Journal of Applied Physics, 1965. **36**(1): p. 153-156.

46. Halg, B. *On a nonvolatile memory cell based on micro-electro-mechanics*. in *Micro Electro Mechanical Systems, 1990. Proceedings, An Investigation of Micro Structures, Sensors, Actuators, Machines and Robots. IEEE*. 1990.

47. Gavan, K.B., et al., *Size-dependent effective Young's modulus of silicon nitride cantilevers.* Applied Physics Letters, 2009. **94**(23).

48. Huang, H., et al., *Effect of deposition conditions on mechanical properties of low-temperature PECVD silicon nitride films.* Materials Science and Engineering: A, 2006. **435-436**: p. 453-459.

49. McShane, G.J., et al., *Young's modulus measurement of thin-film materials using micro-cantilevers.* Journal of Micromechanics and Microengineering, 2006. **16**(10): p. 1926-1934.

50. Langlois, E.D., et al., *Spring constant calibration of atomic force microscopy cantilevers with a piezosensor transfer standard.* Review of Scientific Instruments, 2007. **78**(9).

51. Sader, J.E., *Frequency response of cantilever beams immersed in viscous fluids with applications to the atomic force microscope.* Journal of Applied Physics, 1998. **84**(1): p. 64-76.

52. Shibahara, K., et al. *Dopant loss origins of low energy implanted arsenic and antimony for ultra shallow junction formation*. in *Material Research Society Symposium Proceedings*. 1998. Materials Research Society.

53. Rubio, J.E., et al., *Dose loss and segregation of boron and arsenic at the Si/SiO2 interface by atomistic kinetic Monte Carlo simulations.* Materials Science and Engineering: B, 2005. **124**: p. 392-396.

54. Koh, M., et al., *Quantitative Evaluation of Dopant Loss in Low Energy As Implantation for Low-Resistive, Ultra Shallow Source/Drain Formation.* Solid State Devices and Materials, 1998: p. 18-19.

55. Von Haartman, M., *Low-frequency noise characterization, evaluation and modeling of advanced Si-and SiGe-based CMOS transistors*, 2006, KTH.

56. Dieme, R., *Characterization of noise in MEMS piezoresistive microphones*, 2005, University of Florida: Gainesville.

57. Akiyama, T., et al., *Characterization of an integrated force sensor based on a MOS transistor for applications in scanning force microscopy.* Sensors and Actuators A: Physical, 1998. **64**(1): p. 1-6.

58. Linnemann, R., et al., *Characterization of a cantilever with an integrated deflection sensor.* Thin Solid Films, 1995. **264**(2): p. 159-164.

59. Arlett, J., *Properties of piezoresistive silicon nano-scale cantilevers with applications to BioNEMS*, 2006, California Institute of Technology: Pasadena.

60. Villanueva, G., et al., *Crystalline silicon cantilevers for piezoresistive detection of biomolecular forces.* Microelectronic Engineering, 2008. **85**(5-6): p. 1120-1123.

61. Thaysen, J., *Cantilever for bio-chemical sensing integrated in a microliquid handling system*, in *Mikroelektronik Centret*2001, Technical University of Denemark.

Chapter IV

MOSFET cantilever

MOSFET cantilever

In this chapter, the electromechanical model, the microfabrication and the characterization of the force sensor based on crystalline silicon cantilever with an embedded metal-oxide-semiconductor field-effect transistor piezoresistive deflection transducer (MOSFET cantilever) will be presented. The aim of this part of the project was:

- the development of the technological processes to obtain MOSFET cantilevers.
- to measure the sensitivity and noise and extract important materials parameters like the piezoresistive factor of silicon inversion layer.
- to compare the performances of MOSFET and piezoresistive cantilever and to select the best one for using it in biomolecule recognition.

4.1 – Probe modeling

This section presents the sensitivity and noise models used to develop the cantilever with and embedded MOSFET deflection transducer. The most important parameters that have to be taken into account, also in this case, are: the cantilever spring constant, k_C [N/m], the force sensitivity $S_{F,I}=\Delta I/F$ [A/N] (or deflection sensitivity $S_{\delta}=\Delta I/\delta$ [V/m]), the transducer noise, I_n [A], and the force resolution R_F [N], which is also called minimum detectable force (MDF). The sensitivity can be expressed also by the relative change of the drain current per unit of force or displacement, $(\Delta I_D/I_{D,0})/F$ [N^{-1}] or $(\Delta I_D/I_{D,0})/\delta$ [m^{-1}]. Respect to the piezoresistor case, in this case, the drain current variation is measured and therefore the sensitivity and the noise are expressed in [A/N] and in [A] respectively. In the past, different cantilever structures and MOSFETs design have been used [1-5] but none of them was U-shaped or optimized for force sensing. We proposed, also for the MOSFET cantilevers, a U-shaped beam, to decrease the spring constant and increase the force sensitivity. In the exploded view (Figure 4.1), we can see the different parts composing the self-sensing probe for liquid environment:

- the silicon mechanical layer (gray)
- the transducer (the MOSFET channel)
- the gate silicon oxide (orange)
- the field silicon oxide (white)
- the aluminum gate (blue)
- the silicon nitride insulation layer (green)

In the cantilever, there are two MOSFET in series, one in each arm of the beam. Source and drain of the series are depicted in red and are placed at the clamping edge of the cantilever (x=0). The two transistors are connected by a short transversal resistor (red) made of implanted silicon.

A)

B)
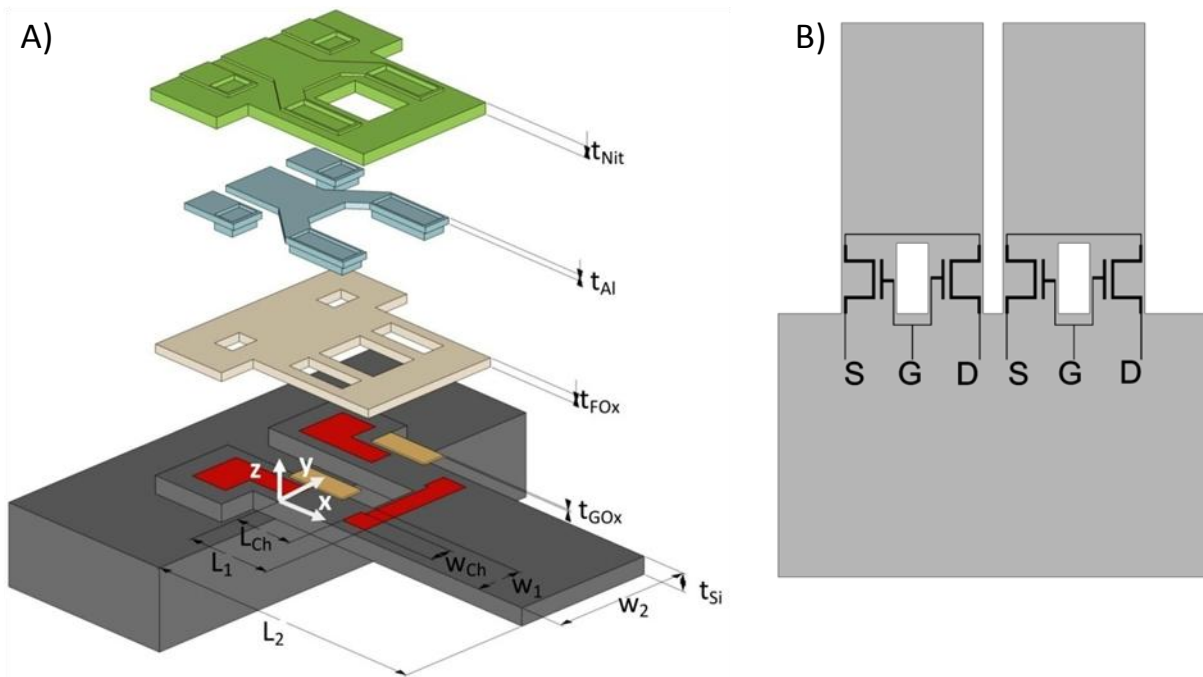
Figure 4.1. A) Exploded view of the MOSFET cantilever. From the top there are: PECVD silicon nitride (t_{Nit} = 100 nm), aluminum (t_{Al} = 500 nm), field oxide (t_{FOx}=300-500 nm), thermal oxide (t_{GOx} = 38 nm), implanted crystalline silicon, and crystalline silicon (t_{Si} =325 nm). B) In each arm of the cantilever there is one MOSFET and they are connected in series by an implanted resistor. The second cantilever acts as current reference.

4.1.1 – Mechanical model

The mechanical behavior of the cantilever with integrated MOSFETs can be described by the equations (2.47)-((2.52) of the section 2.1.4. Even though the MOSFET structure is much different from the piezoresistor structure, we can adapt those equations also in this case. The cantilever can be modeled as a series of two beams with different bending stiffness EI_1 and EI_2. For the calculation of EI_1 (2.48) the contribution of 4 layers have to be considered: silicon, silicon oxide, aluminum and silicon nitride. While silicon, aluminum and nitride have a constant thickness in x direction, this is not the case for the oxide, because there are the field oxide and the gate oxide that have two different thicknesses, t_{FOx} and t_{GOx} respectively. We introduced, therefore, a simplification, calculating the volume-weighted average thickness and considering it constant between $x = [0, L_1]$. Then, it is possible to calculate neutral axis (z_0), bending stiffness (EI_1) and spring constant (k_C). As we will see later on, this analytical simplification agrees with FEM simulations.

4.1.2 – Sensitivity model

In order to calculate the force sensitivity for the MOSFET cantilever we modeled the probe in a similar way like the piezoresistive one (section 3.1.2). The cantilever is loaded by a point force, *F*, in its end so that in its arms we can consider that the stress is uniaxial along

the cantilever axis. Considering that also the transistor channel is oriented in the same direction and disregarding the contribution of the resistive source and drain, which have much lower resistivity than the channel, the relative variation of the current is proportional to the average stress in the channel, $\langle\sigma_{Ch}\rangle$:

$$\frac{\Delta I_D}{I_{D,0}} \cong -\pi_{L,Ch}\langle\sigma_{Ch}\rangle \tag{4.1}$$

where $\pi_{L,Ch}$ is the piezoresistive coefficient of the n- or p-channel inversion layer of the MOSFET, which has constant value across the channel. The stress into the channel is (eq. (2.49.b):

$$\sigma_{Ch} = \frac{(z_{Ch} - z_{0,Ch})}{EI_1}(x - L_2)E_{Ch}F \tag{4.2}$$

where z_{Ch} and $z_{0,Ch}$ are the z-positions of the channel and neutral axis in the channel region respectively. EI_1 is the bending stiffness of the multilayer part of the cantilever and E_{Ch} is the Young's modulus of the channel material (i.e silicon). The conduction into the cannel is due to a very thin layer of electrons on the surface of the silicon near the gate oxide, so that the average stress in the channel is:

$$\langle\sigma_{Ch}\rangle = \frac{(z_{Ch} - z_{0,Ch})}{EI_1}E_{Ch}F\int_0^{L_{Ch}}(x - L_2)dx = -\frac{1}{2}\frac{(L_{Ch} - 2L_2)(z_{Ch} - z_{0,Ch})E_{Ch}}{EI_1}F \tag{4.3}$$

Therefore the force sensitivity is:

$$S_{F,I} = \frac{\Delta I_D}{F} = \frac{1}{2}\frac{(L_{Ch} - 2L_2)(z_{Ch} - z_{0,ch})\pi_{L,Ch}E_{Ch}}{EI_1}I_{D,0} \tag{4.4}$$

Considering the piezoresistive coefficient of the silicon inversion layer (section 2.2.2), the sensitivity is optimized when the cantilever and the transistor (n-MOSFET case) are oriented in the <100> crystallographic direction. It should be pointed out that in the previous equations (4.2)-(4.4), we used $z_{0,Ch}$ which is different from z_0, which is an "averaged" neutral axis used just for a mechanical point of view to calculate the bending stiffness. The neutral axis in the channel region, $z_{0,Ch}$, is calculated considering silicon, gate oxide, aluminum and silicon nitride. In this case the field oxide is not taken into consideration because it is not present in the channel region. Also in this case, the position of the neutral axis in the channel area has been simulated by FEM analysis and the results are very similar.

4.1.3 – Noise and resolution

The force resolution of the cantilever is limited by the noise. Also in this case we take into consideration just the thermal noise (eq. (2.69) and 1/f noise (eq. (2.71). Considering the expression of the force sensitivity we can calculate the minimum detectable force:

$$MDF = \frac{\sqrt{I_{D,J}^2 + I_{D,H}^2}}{S_{F,I}} = \frac{2\sqrt{4\gamma k_B T g_m(f_{max} - f_{min}) + \alpha \dfrac{q\mu_f(V_{Gs} - V_T)I_D}{L_{Ch}^2} ln\left(\dfrac{f_{max}}{f_{min}}\right)}}{(L_{Ch} - 2L_2)(z_{Ch} - z_{0,Ch})\pi_{L,Ch}E_{Ch}I_D} EI_1 \tag{4.5}$$

When the MOSFET is in saturation, the I_D can be rewritten using eq. (2.63) and the transconductance, g_m, is constant and is expressed by:

$$g_m = \mu_f C_{Ox} \frac{W_{CH}}{L_{Ch}}(V_{Gs} - V_T) \tag{4.6}$$

Considering that the 1/f is the predominant noise source at low frequencies (i.e. below 10 kHz), we can simplify the equation (4.5):

$$MDF = \frac{2\sqrt{2}\sqrt{\dfrac{\alpha\, q}{C_{Ox}\, L_{Ch}\, W_{Ch}(V_{Gs} - V_T)} ln\left(\dfrac{f_{max}}{f_{min}}\right)}}{(L_{Ch} - 2L_2)(z_{Ch} - z_{0,Ch})\, \pi_{L,Ch}\, E_{Ch}} EI_1 \tag{4.7}$$

4.1.4 – Optimization

Like for the piezoresistive case, also for the MOSFET cantilever it is possible to improve the force resolution increasing the sensitivity and decreasing the noise, varying the different parameters. The main difference with the piezoresistive cantilever is inherent to the conduction mechanics. In the MOSFET, the conduction through the channel is due to electrons underneath the gate oxide that are confined to the semiconductor-oxide interface, the so called "two dimensional electron gas". However they are free to move in a direction parallel to this interface. This specific mechanism can improve the sensitivity because the conduction is on the surface of the silicon where the stress is the highest.

The force resolution depends on many parameters (4.5), nevertheless for the same technology we can consider that α, C_{Ox} and V_T are constant. Also E_{Ch} and $\pi_{L,Ch}$ are constant once we fixed the MOSFET and cantilever crystallographic direction. Finally the sensitivity depends on the dimensions of the cantilever, on the dimensions of the MOSFET and on the gate voltage. Particularly important is the effect of the thickness of the various layers (silicon, aluminum and nitride) above and underneath the channel. The sensitivity and the resolution depends on the width and length of the cantilever and of the channel in similar way like in the piezoresistive cantilever 3.1.5. The resolution increases for longer and narrower cantilever and longer and wider channel.

In Figure 4.2, we reported the variation of resolution, sensitivity and noise against the silicon thickness. For very thin cantilevers the channel lays under the neutral axis (in compression) and therefore the cantilever has negative sensitivity. In this region the sensitivity and the resolution vary strongly. For thicker cantilever the sensitivity is positive

and has less dependence, and so the resolution. Resolution and sensitivity vary in a similar way if the aluminum thickness is changed.

Considering a cantilever thickness of 325 nm, like in the case of the piezoresistive cantilever, and the values for the other variables reported in Table 4.1, we can expect a resolution of 277 pN. If we increase the silicon thickness to 1 μm and decrease the thicknesses of the field oxide and the aluminum, to reach a spring constant comparable to the softer piezoresistive cantilever, we could obtain a resolution of 32 pN. In the calculations, we have considered the following typical values for the other parameters: α=2 10^{-6}, q=1.6 x 10^{-9} C, C_{Ox}= 1.12 mF/m^2 (t_{Ox}=30 nm) and V_T= 0.1 V, E_{Ch}= 130 Gpa, $\pi_{L,Ch}$= -90, t_{Nit}=100 nm. It should be pointed out that the Hooge factor is two orders of magnitude lower than in the piezoresistor case. We decided to use this value because was fitting the first noise results on MOSFET devices and it is an average value in the literature [6]. Such a lower value can be explained by the fact that the MOSFET channels has a very low doping and this turns into a much better crystal quality, especially when they compared to piezoresistors made by ion implantation.
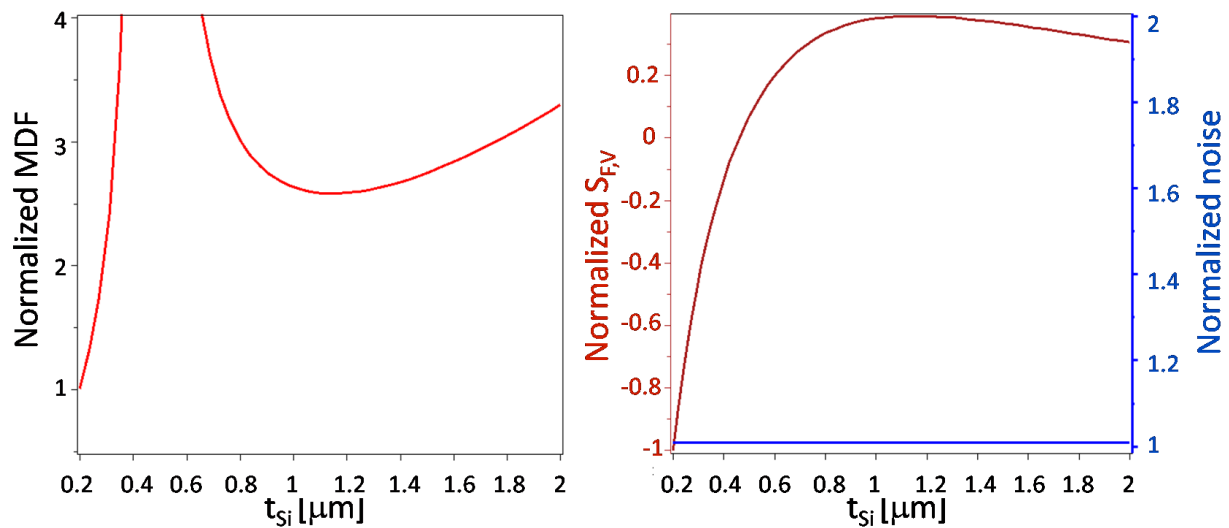
Figure 4.2. Normalized force resolution (left) and normalized force sensitivity and noise current (right) dependence on the silicon thickness.

L_2 [μm]	w_1 [μm]	t_{Si} [μm]	t_{Al} [μm]	t_{FOx}	k_C mN/m	L_{Ch} [μm]	w_{Ch} [μm]	$I_{D,H}$ [pA]	$S_{F,I}$ [pA/pN]	MDF [pN]
200	6	0.325	0.5	0.23	3.57	20	4	184	-0.67	277
330	6	1	0.1	0.1	0.65	40	4	90	2.32	32

Table 4.1. Values of the different variables used in (4.5) to obtain a MDF of 277 pN and 32 pN. L_2= cantilever length, w_1= cantilever arm width, t_{Si}=thickness of the silicon layer, t_{Al}= thickness of the aluminum gate, t_{FOx}= volume-weighted average thickness of the field oxide, k_C= cantilever spring constant, L_{Ch}= channel length, w_{Ch}= channel width, $I_{D,H}$= integrated 1/f noise between 1 Hz and 1 kHz, $S_{F,I}$=force sensitivity, MDF= force resolution.

4.2 – Microfabrication

In this section we will present the mask layout and the microfabrication process flow of the sensors. The fabrication issues will be also pointed out.

4.2.1 – MOSFET cantilever design

A set of 7 masks (CNM 295) had previously been designed by Dr. Guillermo Villanueva to fabricate the sensors. Also in this case, the chips were designed to have final dimensions of 4.3 mm x 1.5 mm that are approximately the same dimensions of an AFM chips. In the same mask, also other type of sensor structures had been designed, like the piezoresistive cantilevers, so that in one 4'' wafer there are 48 MOSFET cantilever force sensors. Even though this is a small number compared to 400 sensors based on piezoresistors, the aim of this new sensor based on MOSFET transduction, was to check the performance (sensitivity, noise, resolution), materials parameters like the piezoresistive coefficient for inversion layer, and to develop the fabrication process to obtain such a cantilever.

An overview of the different mask levels for a single chip (design A1) is reported in the Figure 4.3.A while in the Figure 4.3.B-H the different mask level relative to the cantilever area are reported. Each chip has alignment marks in the bottom left and the design name in the up-right part. Every chip has two nominally identical cantilevers (one acts as reference) and two MOSFETs are embedded in each cantilever.

1. The first mask (red, Figure 4.3.B) it is used to define the implantation areas: drain and source.
2. The second mask (gray, Figure 4.3.C) is used to define the cantilever. Sources and drains are formed, therefore, by implantation of arsenic in a bigger area followed by silicon etching. In this way, in each arm of the cantilever, there is a channel (lightly p-doped) plus source and drain (heavily n-doped). The two cantilevers are connected, so that the lightly p-doped silicon substrate has the same bias in all the MOSFETs.
3. The third mask (orange, Figure 4.3.D) is used to define the channel and to etch away the silicon oxide previously deposited, which was used for the alignment marks and as mask for implantation and etching.
4. The fourth mask (black, Figure 4.3.E) defines the windows that allow to contact the "first" source and the "last" drain of the two MOSFETs in series on each cantilever. The same windows are defined in the central part to contact the lightly p-doped silicon substrate.
5. The fifth mask (blue, Figure 4.3.F) defines the metal interconnection and the pads which are designed in the bottom part of the chip.
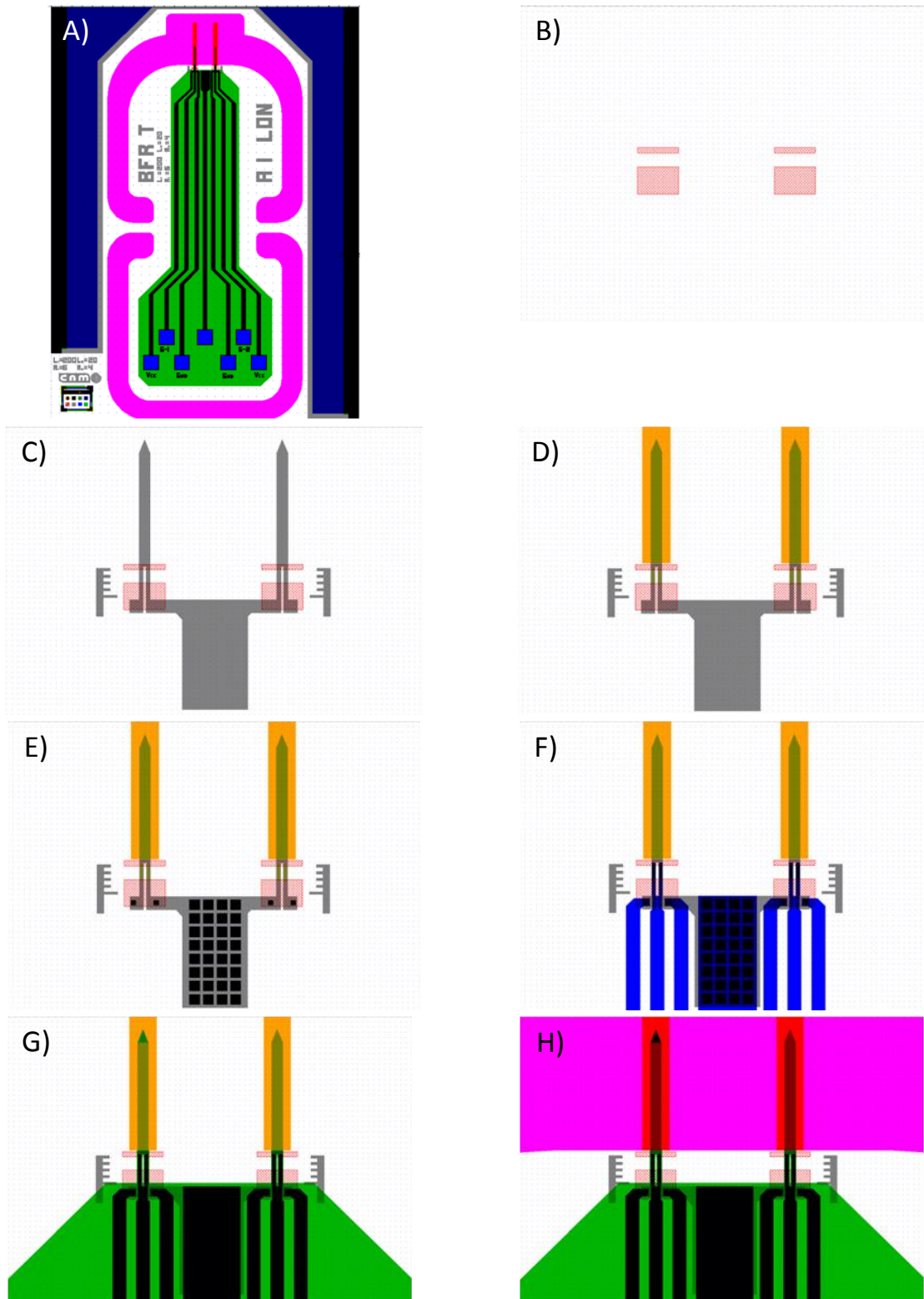
Figure 4.3. A) Overlapping of the 7 mask levels for a single chip (design A1). B-H) Close-up of the masks of the cantilever area. B) implantation area; C) cantilever and SOI silicon; D) Channel and active area of the cantilever; E) contact windows; F) aluminum interconnections ; G) Silicon nitride passivation area; H) backside DRIE.

6. The sixth mask (green, Figure 4.3.G) defines all the conductive areas that have to be electrically insulated from the environment: the MOSFETs and the interconnections (except the pads).

7. The seventh mask (rose, Figure 4.3.H) is the backside mask and delimits the dimension of the chip. It defines the region where the bulk silicon and the buried oxide of the SOI wafer have to be etched. In this step the cantilever will be released and two anchor beams will be also defined at the center of the chip, one at each side, holding the chips in the wafer.

In each chip there are seven pads (Figure 4.3.A) which are defined in the bottom part of the chip. The first and the last three pads are used for the source, gate and drain respectively, while the central pad is used to bias the substrate.

There are 2 main designs of MOSFET transistors which are embedded in 4 different cantilevers designs for a total number of 8 different sub-designs (Table 4.2).

design	sub-design	w_{Ch} [μm]	L_{Ch} [μm]	w_1 [μm]	w_2 [μm]	L_1 [μm]	L_2 [μm]
A	1	4	20	6	16	30	200
	2	4	20	6	16	30	400
	3	4	20	10	24	30	200
	4	4	20	10	24	30	400
B	1	4	10	6	16	20	200
	2	4	10	6	16	20	400
	3	4	10	10	24	20	200
	4	4	10	10	24	20	400

Table 4.2. Various MOSFET and cantilever designs. w_{Ch}= channel width, L_{Ch}= channel length, w_1= cantilever arm width, w_2= cantilever width, L_1= cantilever length of the multilayer part, L_2= total cantilever length

The channel width is 4 μm for all the transistors while the length varies between design A and B, in which it is 20 μm or 10 μm, respectively. The length of the transistors is reflected also in the length of the multilayer part of the cantilever which is 30 μm and 20 μm, respectively. The other main difference between sub-designs 1-2 and 3-4 is the width of the cantilever arms. In 3 and 4 the drain and source implantation are aligned inside the cantilever so that the arm had to be wider to respect the photolithographic tolerance (Figure 4.4). This leads also to wider cantilever. Finally, the cantilever can have two different lengths of 200 μm and 400 μm. Also in the set of mask CNM 295 there were similar test structures for the electrical characterization, like in the set CNM 671.
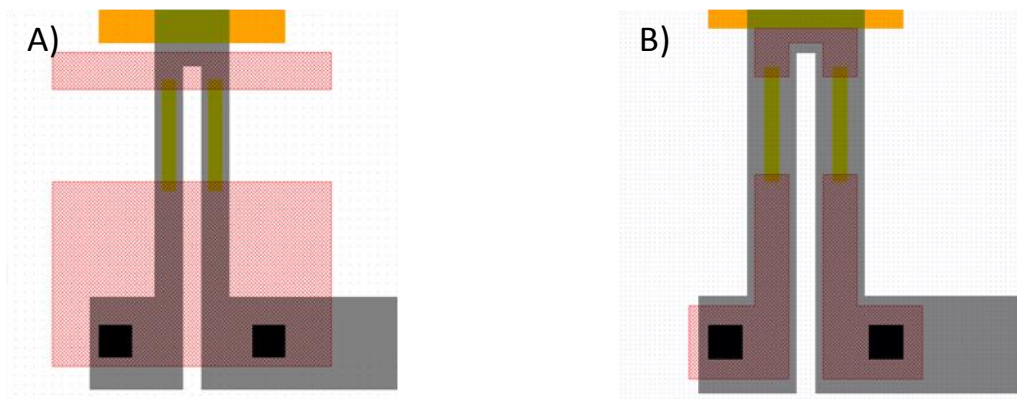
Figure 4.4. Close-up of the masks of the cantilever area for different designs: A1 (left) and A3 (right).

4.2.2 – MOSFET cantilever process flow

In this section, the fabrication process flow used in the RUN 4972 is reported. Since the MOSFET cantilevers and the piezoresistive cantilever are fabricated on the same wafer, we used the same process flow described in section 3.2.2. Nevertheless, the results are completely different because of the differences in the photolithographic masks.

The sensors were fabricated from double side polished (100) silicon-on-insulator (SOI) wafers, from Soitec, with a 340 nm thick device layer, a 1 µm thick buried oxide (BOX) and total wafer thickness of 450 µm (Figure 4.5.A). The device layer was p-type silicon with a resistivity of 0.1-10 Ωcm. In the RUN 4972, 8 SOI wafers plus two standard p-doped wafers with a resistivity of 0.1-10 Ωcm, as test wafers, were processed. Unfortunately we had high yields just in wafers 4972-4 and 4972-9, while in the other wafer we have very poor yield.

At the beginning the wafers were labeled with a laser scriber on the backside; we measured the silicon oxide thickness on the backside, and, in case of oxide presence, we completely etched the layer by commercial SiOetch solution. On the front side, a layer of 190 ± 4 nm of oxide was deposited via tetraethylorthosilicate(TEOS)/O_2-plasma enhanced chemical vapor deposition (PECVD) at 400º C in the Applied Materials Precision 5000 CVD equipment.

The *first photolithography* was performed in order to define the windows for source and drain implantation and the alignment marks for the following photolitographies. Also in this case, the wafers were rotated by 45° respect to a standard orientation in order to align source, channel and drain in the <100> crystallographic direction to have the highest piezoresistive coefficient. The oxide was etched by SiOetch solution and the photoresist hard baked at 180º C. Arsenic was implanted at a relatively low energy (50 keV) with a dose of 1×10^{15} ions/cm^2 (Figure 4.5.B). Then, the wafers were cleaned from the resist in an O_2 plasma asher.

131
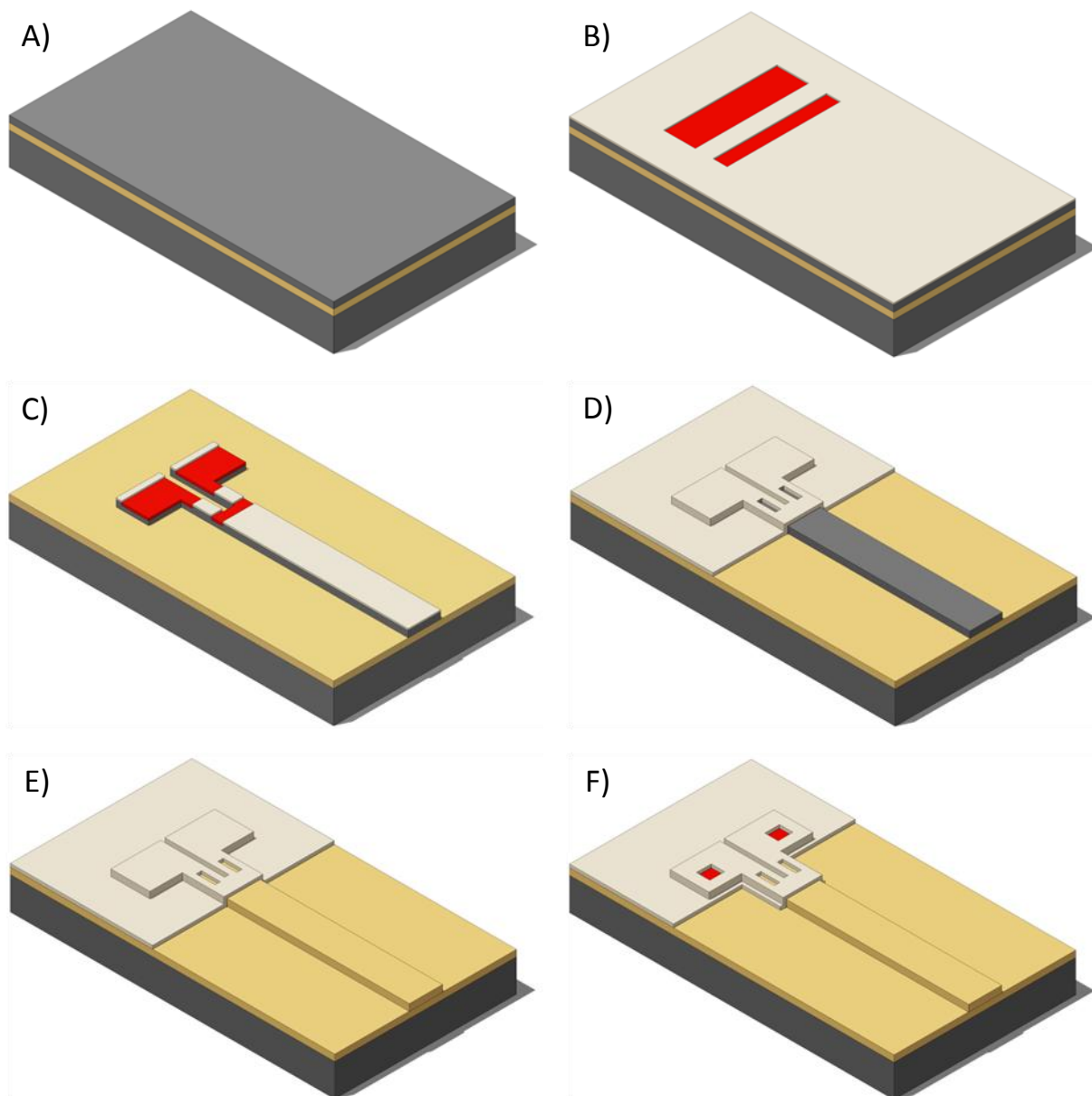
Figure 4.5. Cantilever area during different fabrication processes. A) SOI wafer before the process. B) The implanted area is highlighted in red and PECVD in white. C) The SOI wafer is etched to define the cantilever. D) PECVD silicon oxide is deposited and etched away from the channel and the active areas of the cantilever. E) The wafer is annealed in oxidizing atmosphere and a 38 nm thick silicon oxide layer is grown. F) Two contact windows are opened in the PECVD silicon oxide on the n-doped silicon.

The *second photolithography* was performed to pattern the cantilevers in the <100> direction. The TEOS PECVD oxide was etched away in SiOetch solution and the silicon was etched via SF_6/C_4F_8 deep reactive ion etching (DRIE) in an Alcatel 601 etcher (P601POLI conditions) (Figure 4.5.C). Afterwards a TEOS PECVD silicon oxide layer of 314 ± 15 nm thick was deposited at 400º C. This oxide is the field oxide of the MOSFET and insulates the source drain and substrate.

The *third photolithography* was performed to pattern windows on the MOSFET channel and on the cantilevers. The PECVD oxide was etched away by SiOetch solution and the resist removed in the plasma asher (Figure 4.5.D). Afterwards, a thermal treatment to grow 38 nm of the gate oxide was performed (OXPTAAA standard process). Wafer 4972-4 was annealed further at 900° C for 60 minutes and wafer 4972-9 at 1050° C for 30 minutes in N_2 atmosphere (Figure 4.5.E).

The *fourth photolithography* was performed to pattern the contact-windows: windows in the oxide that allow contacting the source and drain of the transistor (Figure 4.5.F). Also in this case, after resist removal, we performed 20'' etching with SuperQ to etch the native oxide that could have grown on the contacts. In this step also between 5-8 nm of gate oxide were etched away. Just afterwards, a 0.5 µm thick layer of aluminum-copper-silicon alloy (98.75% Al, 0.5% Cu, 0.75% Si) was sputtered.

The *fifth photolithography* was performed to pattern the metal gate, the interconnections and the pads of the chip. The metal etching was performed via $BCl_3/Cl_2/N_2$ RIE in the Drytek Quad etcher (PQ2ALC25 conditions) with automatic final point detection (Figure 4.6.A). During this etching we didn't have any drawbacks as detected in the following RUNs (i.e. 6481). After a cleaning in water, the wafers were thermally treated at 350º C in N_2/H_2 atmosphere for 35 minutes to reduce the contact resistance. To insulate all the conductive parts of the sensor, a layer of 99 ± 1 nm thick silicon nitride was deposited by SiH_4/NH_3-PECVD at 375 ºC in the Applied Materials Precision 5000 CVD equipment in two steps of 50 nm.

The *sixth photolithography* was performed to pattern the silicon nitride. The 100 nm thick nitride layer was etched via CHF_3/CF_4 RIE in Alcatel Gir 160 (PGNISEN conditions) (Figure 4.6.B). The wafers were cleaned in O_2 plasma asher and in water. With this process, we finished the microfabrication process in the wafer frontal part.

A 1 µm thick aluminum layer was deposited on the wafer backside. The *seventh photolithography* was performed on the backside to define the areas that have to be etched by deep reactive ion etching (DRIE). Aluminum and silicon were respectively etched via $BCl_3/Cl_2/N_2$ RIE in the Drytek Quad etcher (PQ2ALC25 conditions) and via SF_6/C_4F_8 Bosch DRIE process, until reaching the buried oxide. Standard photoresist was protecting the device side (Figure 4.6.C). Finally the BOX was etched by 49% HF vapors. The wafers were placed on a Teflon beaker filled with 100 ml of 49% HF solution. Wafer 4 was etched for 3'+1.5'. Wafer 9 was etched for just 2' in vapors and wet etched using the SiOetch solution for a total time of 6'. Finally, the protective resist was ashed by O_2 plasma (Figure 4.6.D). A SEM micrograph of a sensor chip (RUN 4972-4), a close-up of the cantilevers and a close-up on the MOSFET transducers, are reported in Figure 4.7.A-C.
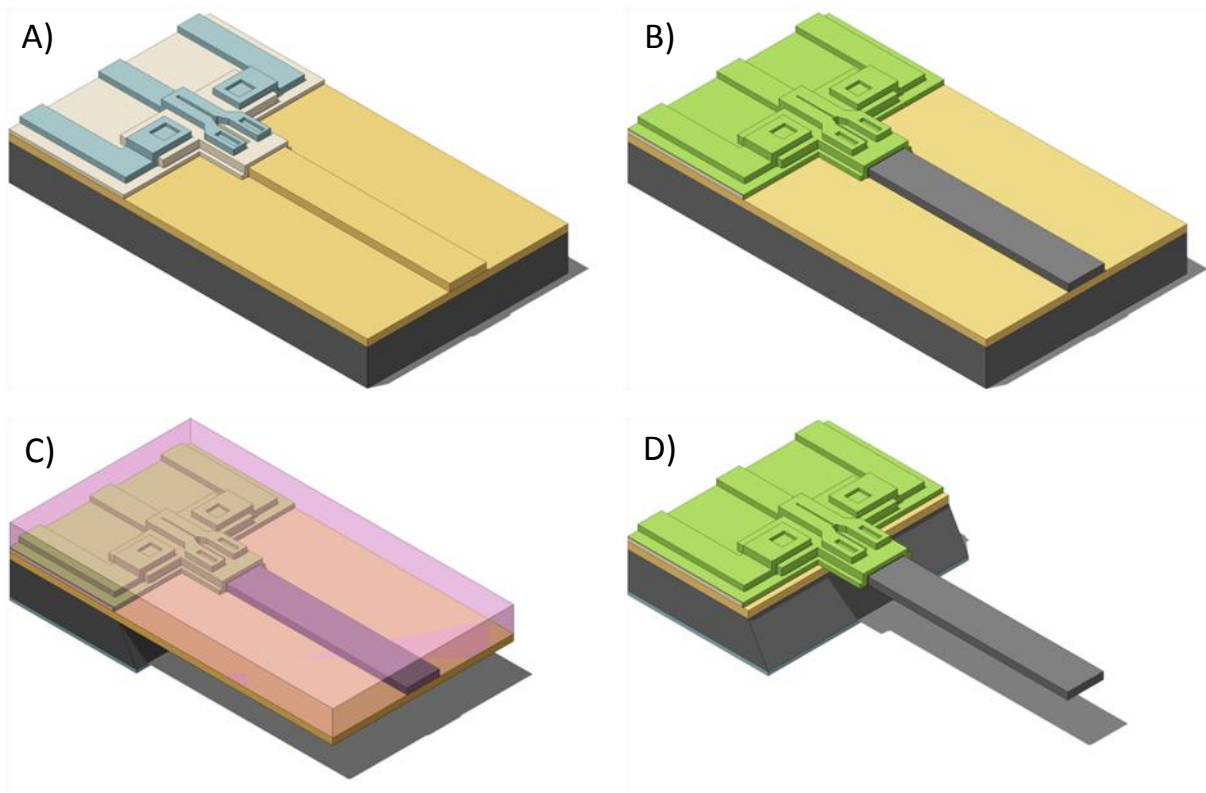
Figure 4.6. Cantilever area during different fabrication processes. A) Aluminum is sputtered and etched to define the interconnections. B) A layer of 100 nm thick PECVD silicon nitride is deposited and etched to passivate all the conductive parts. C) Aluminum is deposited on the backside and patterned. Resist is deposited on the front side to protect the device side. DRIE of bulk silicon is performed and stopped at the BOX. B) The BOX is etched by vapor HF and the resist is removed in O₂ plasma asher.
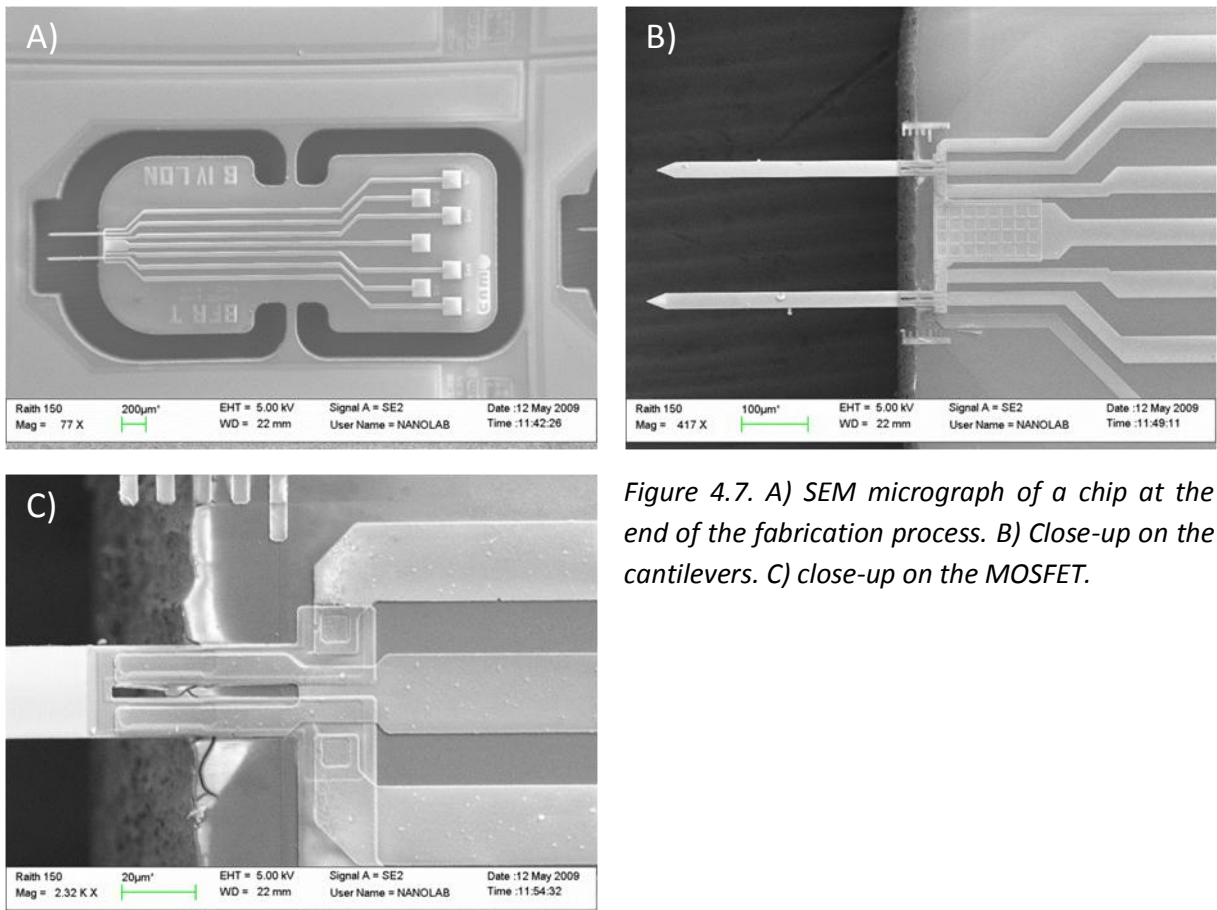
Figure 4.7. A) SEM micrograph of a chip at the end of the fabrication process. B) Close-up on the cantilevers. C) close-up on the MOSFET.

4.2.3 –Fabrication issues

Most of the fabrication issues were similar like in the case of piezoresistive cantilevers (section 3.2.3): bulk silicon DRIE and BOX etching. However, due to the particular structure of the MOSFET transducer, they influenced much more the final result and the performance variation. The DRIE of the bulk silicon has not homogeneous speed across the wafer as mentioned earlier. This fact provokes that the undercut can vary up to 10 μm and it represents a big issue for MOSFET with "short" channel of 10 μm or 20 μm. The result is that the channel can be in the zone of maximum stress (Figure 4.8.A,C) or in a part of almost zero stress (Figure 4.8.B,D) because the silicon and BOX underneath are not etched, resulting in a very big sensitivity variation (section 4.3.4).

In a similar way, the sensitivity can be also affected by problems in BOX etching (section 4.3.4). The relative distance between the neutral axis and the channel can be affected, when the oxide is not completely etched underneath the transistor, like in the case of wafer 4972-9 (Figure 4.9.A,B). On the other hand, if the BOX etching is performed for too long time, there is the risk of damage the aluminum gate, as it happened in the other wafers of the RUN 4972.
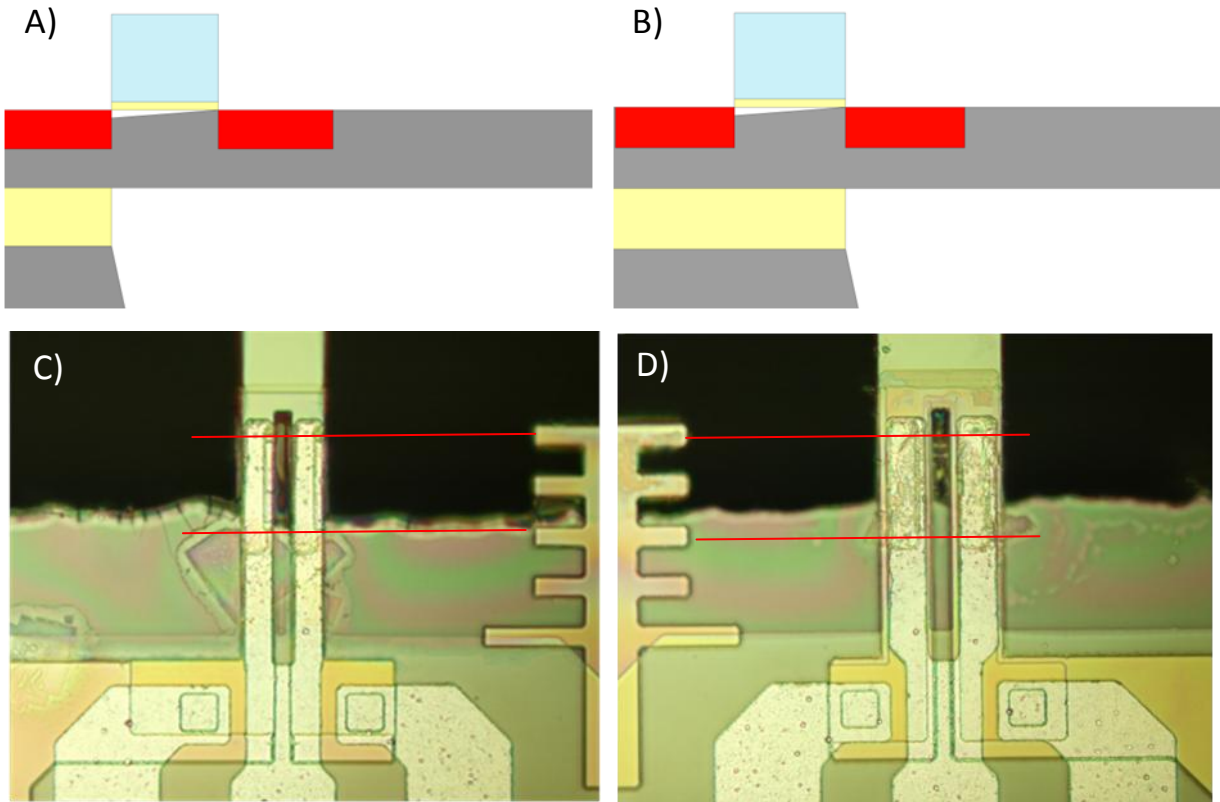
Figure 4.8. A, B) Longitudinal cross section scheme of the MOSFET cantilever. The DRIE has different etching speed across the wafer so that in one wafer a MOSFET can be in the highest stress region of the cantilever (A) or still on the substrate , where the theoretical stress is null (B). C, D) Optical micrographs of finished devices in the wafer 4972-4: the MOSFET is completely suspended (C) or partially on the substrate (D).
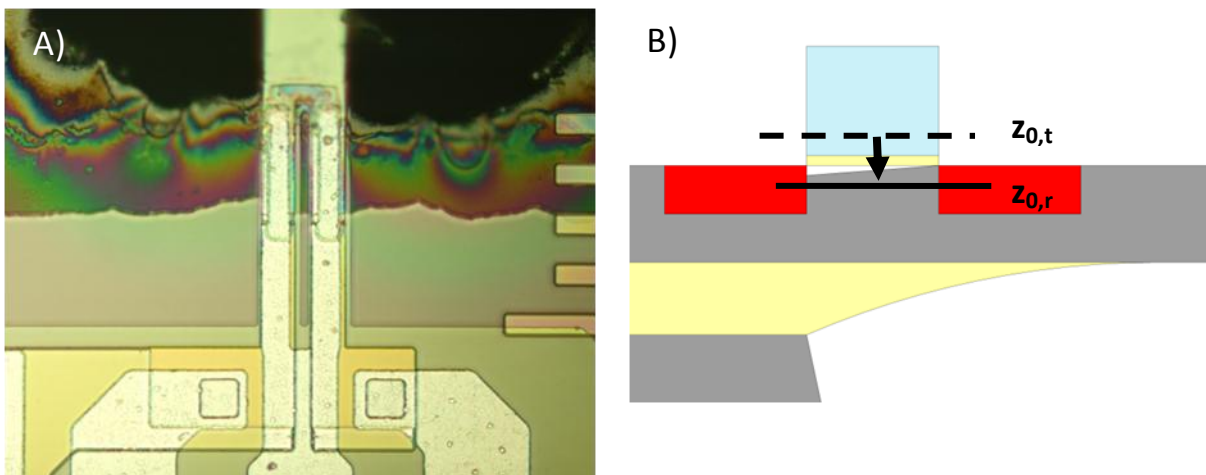
Figure 4.9. A) Optical micrograph of a finished device in the wafer 4972-9: After the BOX etching, there is still some oxide remaining under the MOSFET. B) Longitudinal cross section scheme: the oxide shifts the neutral axis downwards. Depending on oxide thickness the shift can be bigger or smaller and channel can be in compressive or tensile strain.

In order to study and improve the piezoresistive and noise properties of MOSFETs in a more reliable way, my suggestion is to fabricate and perform these studies in structures that are much easier to fabricate.

4.3 – Characterization

In this section, mechanical, electrical and electromechanical characteristics of the cantilevers with embedded MOSFET transistors will be presented. The set up for the on-wafer measurements have been already presented in the previous chapter, therefore here we will just point out the differences.

4.3.1 – Mechanical characterization

Also in this case, like in the case of the cantilever with embedded piezoresistor, it was not possible to measure directly the spring constant, due to the fact that the probes were very soft. They have been calculated, therefore, using the eq. (2.47)-(2.52). Length and width of the cantilevers were measured by using optical and SEM microscopes and the thicknesses by the optical interferometer. Young's moduli of the silicon, silicon oxide, aluminum and silicon nitride were considered to be E_{Si}= 130 GPa [7], E_{SIO2}= 75 GPa [8-11], E_{Al}=70 Gpa [12, 13] and E_{Nit}=70 Gpa. Here below, in Table 4.3, the spring constant are calculated for the different probe designs. The cantilever A-1 has been simulated by FEM (Ansys, Figure 4.10) and the spring constant agrees well with the calculated one being around 2.9% lower than the one estimated by the analytical model. In view of this difference, we don't make big error by considering a constant oxide thickness in the multilayer part of the cantilever (section 4.1.1).

design	sub-design	k_C [mN/m]	k_C^* [mN/m]	$(k_C^* - k_C)/ k_C$
A	1	3.57	3.47	-2.9%
	2	0.35	-	-
	3	5.37	-	-
	4	0.53	-	-
B	1	3.03	-	-
	2	0.33	-	-
	3	4.55	-	-
	4	0.49	-	-

Table 4.3. Spring constant of the different cantilever designs by analytical model (k_C) and by simulation (k_C^*). It has been calculated considering literature values of the Young's moduli of Si, SiO$_2$ and Al. The Young's modulus of the silicon nitride has been measured (section 3.3.1).
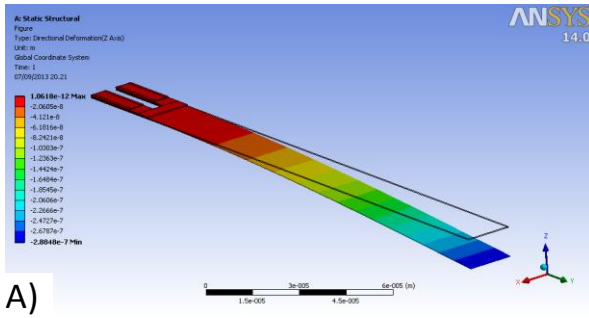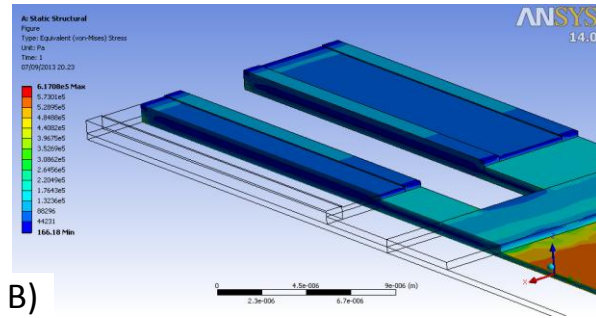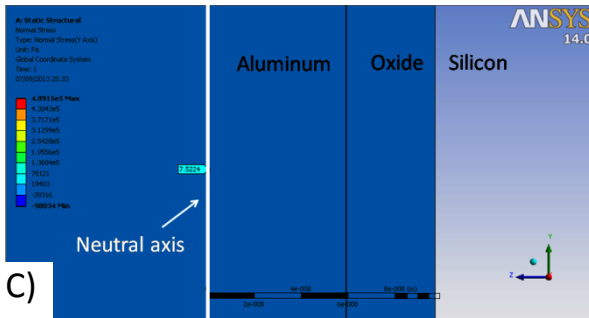
Figure 4.10.A) Deflection of the cantilever under a static load of 1 nN. The cantilever bends 288 nm and therefore the k_C*=3.47 mN/m. B) Cross section of the multilayer part of the cantilever representing the equivalent stress. C) The white line represents the locus where the stress is minimum ≈0 Pa (i.e. neutral axis). It is placed at z≈+98 nm respect to the silicon-oxide interface.

4.3.2 – Electrical characterization

The electrical characteristics of the MOSFET transistors were measured using a semiautomatic probe system Karl Süss PA200 and a semiconductor parameter analyzer HP4155. The drain current (I_D) was recorded as a function of the voltage between source and drain (V_{DS}) for several gate voltages (V_{GS}) (Figure 4.11.A,B). Additionally, I_D was recorded sweeping V_{GS} between -0.5 and 2 V for a fixed V_{DS} = 0.2 V (Figure 4.11.C,D) in order to determine the threshold voltage V_T. In Table 4.4 we report the average values and standard deviations for the different MOSFET designs.

	$I_{D,sat}$ [μA] at V_G=4V wafer 4972-4	SD. [μA]	$I_{D,sat}$ [μA] at V_G=4V wafer 4972-9	SD. [μA]]	$I_{D,sat}$ of 4972-4/ $I_{D,sat}$ of 4972-9
A1	68	10 (15%)	40	3 (8%)	1.7
A2	62	6 (10%)	39	7 (18%)	1.6
A3	88	9 (10%)	48	8 (17%)	1.8
A4	86	9 (10%)	58	6 (10%)	1.5
B1	140	37 (26%)	61	16 (26%)	2.3
B2	139	27 (19%)	68	17 (25%)	2.0
B3	159	39 (25%)	85	17 (20%)	1.9
B4	141	35 (25%)	100	15 (15%)	1.4

Table 4.4. Averaged saturation drain current for a gate voltage of 4 V in wafer 4672-4 and 4972-9. Standard variation (SD.) is reported in absolute and (relative) values.

The $I_{D,sat}$, increases by decreasing the gate length. For example, if we compare the transistors A1 and B1 of the wafer 4972-4 with a channel length of 20 μm and 10 μm respectively, the $I_{D,sat}$, at V_{GS}=4 V, increases from 68 μA to 140 μA, which is two times higher, as expected (2.64). We can notice, also, that the current increases if the source and drain are formed just by implantation (designs 3 and 4) respect to the design 1 and 2 in which the source and drain are formed by implantation and dry etching. This fact does not have a clear origin. Finally the transistors from the wafer 4972-4 have almost two times higher drain current compared to the transistors of the wafer 4972-9 and it is consequence of a lower threshold voltage (Figure 4.11.C,D). This difference shouldn't be related to the different annealing conditions, which is the only nominal difference between the two wafers. After the oxide growth, the wafer 4 was annealed further at 900⁰ C for 60' while the wafer 9 was annealed at 1050⁰ C for 30'. The difference could be due, more probably, to different oxide thickness as consequence of the gate oxide etching during the processing, for example.
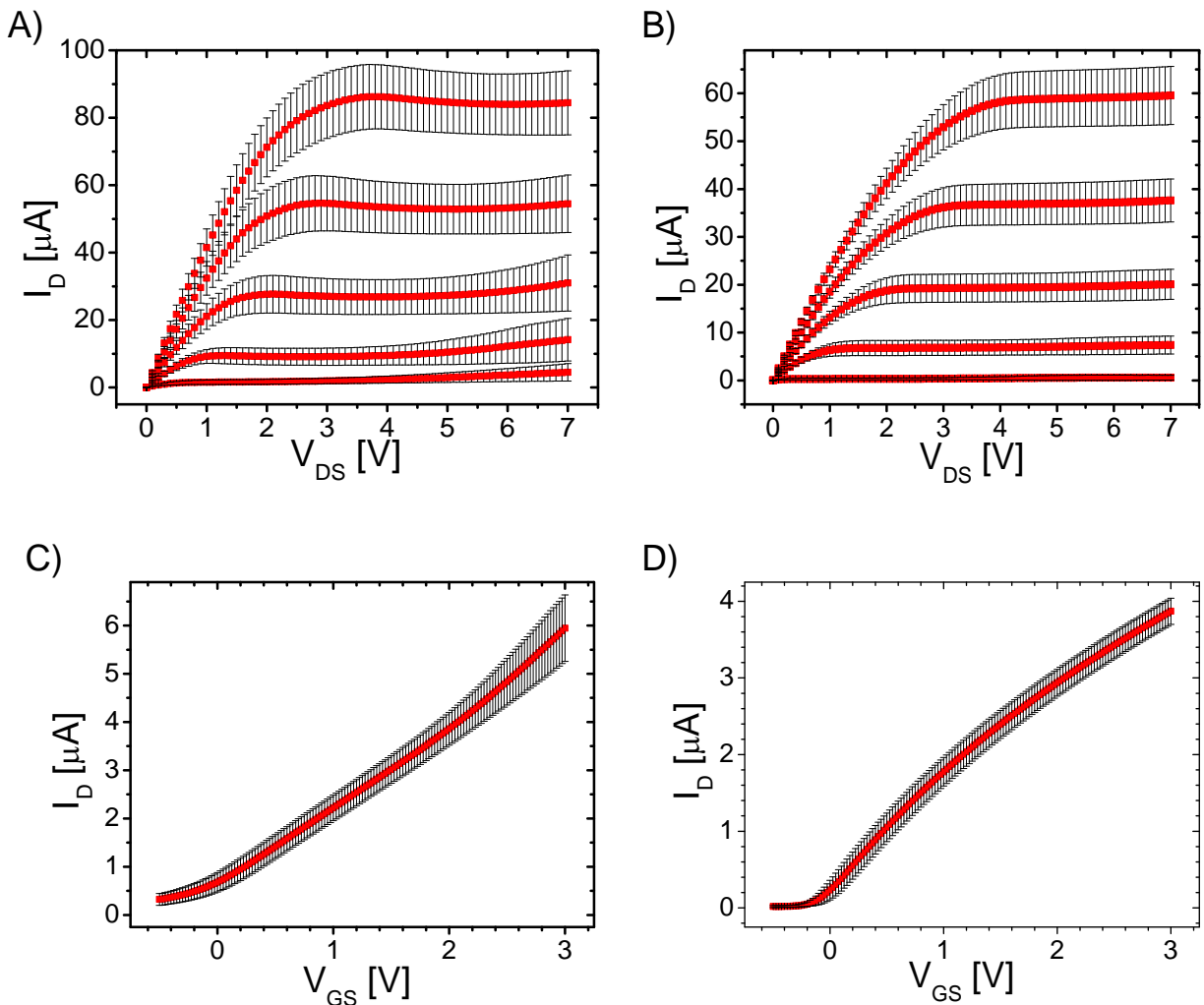
Figure 4.11. A,B) I_D vs. V_{DS} measurements for different V_{GS} (V_{GS} =0, 1, 2, 3, 4 V) for wafers 4972-4 and 4972-9 respectively. C,D) I_D vs. V_G at constant V_{DS}=0.2 V for wafers 4972-4 and 4972-9, respectively. Design A4.

The saturation currents present a relatively high relative standard deviation, which is in between 8% and 26% for the best and the worst case respectively. The variation is between 1.5 and 4 times higher than in the piezoresistive case. This result was expected because the integration of transistors with a channel width of 4 μm and a length of 10 μm or 20 μm is much more challenging than the integration of a comparable resistor. In fact, we have to consider that the resolution limit of the photolithography is around 2 μm with an overlay tolerance of 1 μm. This fact can explain also that the standard variation (Table 4.4) of the characteristics is lower for transistors with longer channel (designs A), and higher for transistors with shorter channel (designs B). Another source of variations can derive from the fact that the gate oxide is partially etched by wet etching before the metallization. Even though the wet etching is performed just for 20´´ this can lead to bigger variation of the gate thickness from chip to chip.

4.3.3 – Noise

The noise power spectral density (PSD) was measured using a low noise current amplifier (LNA) (SR570 from Stanford Research) and a spectrum analyzer (SR785 from Stanford Research). The measurements were performed on-wafer, in the KS PA200 probe station, contacting the source, drain, gate and substrate by the four probes of the probe station. The use of these probes, allowed the use of triaxial cables, which provide much better shielding against the external electromagnetic interferences, respect to the coaxial ones. The LNA was powered by batteries for low noise operations. The LNA input is a source measurements unit (SMU) so that it can bias the device under test (DUT) and can measure the drain current at the same time. The drain and gate were connected to the input of the LNA and were biased at 4 V (V_{GS}=V_{DS}=4V), so that the transistor was in saturation region. The drain current was "taken up" by the SMU unit and a DC current, with the same intensity, was subtracted not to drive the amplifier into saturation (Figure 4.12.A). The sensitivity (or amplification) was fixed at 100 nA/V, which means that a signal of 100 nA is transformed to a signal of 1 V by the LNA. This sensitivity allowed having a relatively low amplifier noise of $600 \text{ fA}/\sqrt{\text{Hz}}$ (Figure 4.12.B) and a measuring bandwidth of 2 kHz with a low DC input impedance of 10 kΩ which is much lower compared to the impedance of the DUTs (i.e. 100 kΩ) [14]. The source and substrate were biased by the ground of the LNA. After the amplification the signal was processes and recorded by a dynamic signal analyzer (SRS785). In this way, the set up had a single physical ground (the one of the SR785) avoiding possible ground loops which could invalidate the measurements.

After the set up development, and before testing the transistors, amplification and noise measurement had to be performed to assure the correct performance of the amplifier because the LNA had several years and new batteries had to be installed. In Figure 4.12.C, we can see the open circuit current noise of the amplifier, which is comparable to the amplifier specifications (Figure 4.12.B).

140

The final PSD graph of the MOSFETs in Figure 4.13 is the result of three different bandwidth measurements: 0.125-12.5 Hz, 0.5-100 Hz and 2-1600 Hz. Each bandwidth had different number of FFT lines and therefore different binwidth: 0.125 Hz, 0.5 Hz and 2 Hz respectively. Each PSD was the average of 50 curves. In Table 4.5, we report the parameters of the LNA and the signal analyzer we used for all measurements.
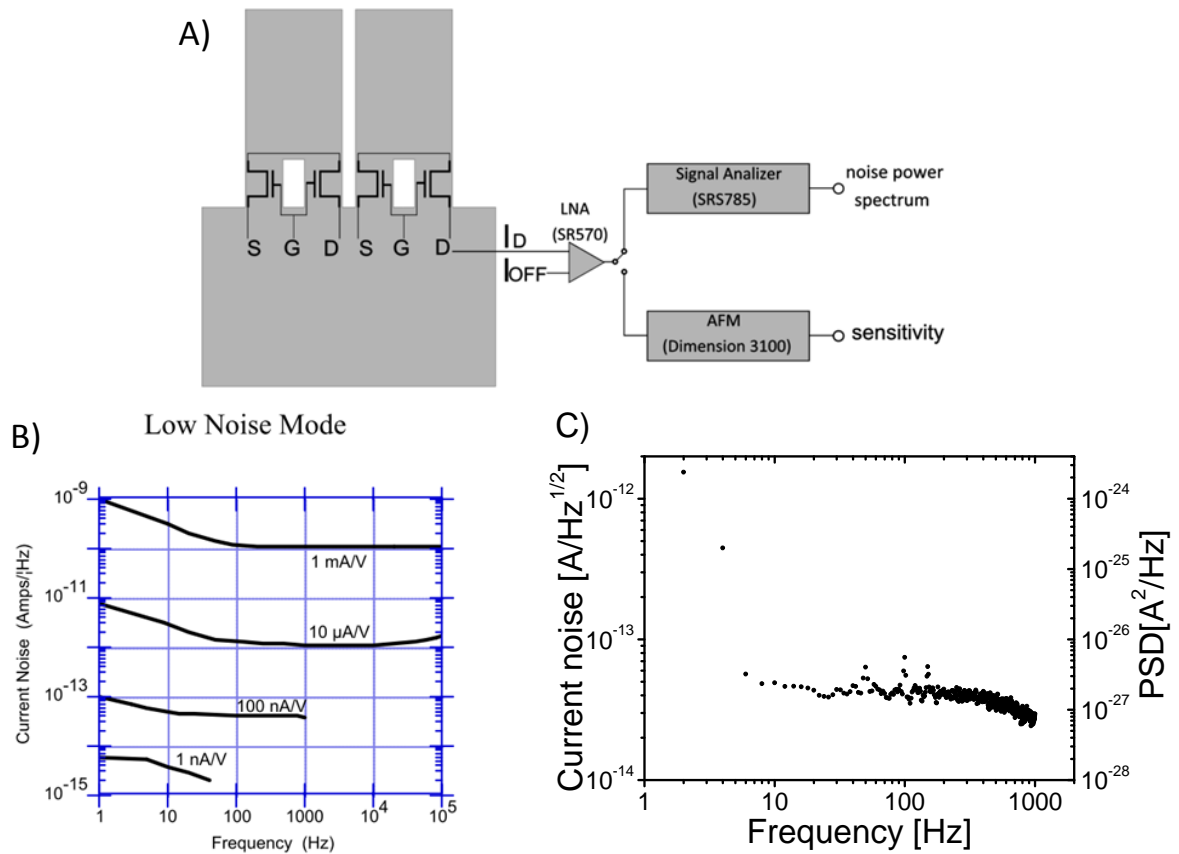
Figure 4.12. A) Noise and sensitivity measurements electrical scheme. An offset current is subtracted to the drain current and the difference is amplified. The noise spectrum is recorded by the signal analyzer while the sensitivity signal is recorded by the AFM electronics (see next section). B) Current spectral density for different amplifier sensitivities. C) Current noise and power spectral density of the measurement set-up.

SR560		SRS785			
Coupling	Not available	Coupling	AC		
Inputs	A	Input	A		
filters	0.03-300K	Window	Hanning		
Sensitivity	100 nA/V	Span [Hz]	12.5	200	1600
Input	10 kΩ,	FFT lines	100	400	800
Output	50 Ω	Binwidth [Hz]	0.125	0.5	2

Table 4.5. Parameters of the low noise current amplifier (SR570) and the dynamic analyzer (SRS785) for the current noise measurements.
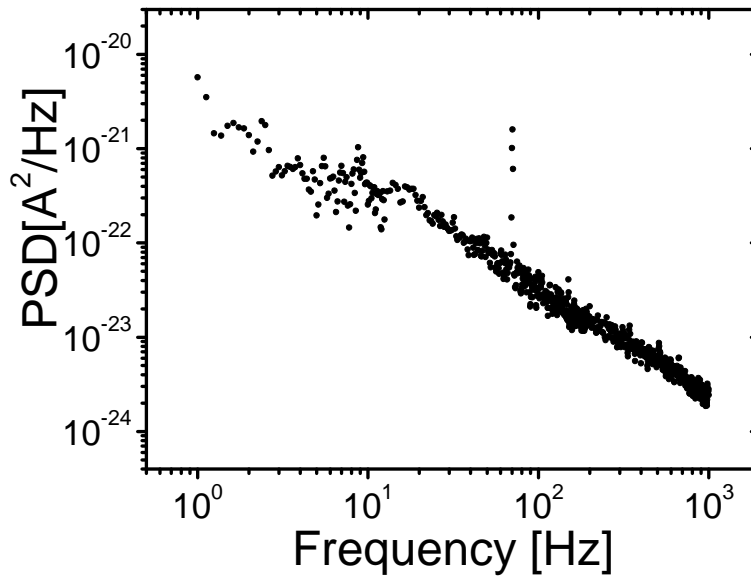
Figure 4.13. Power spectral density of the MOSFET from the chip Q11 (design A1) of the wafer 4972-4.

The noise power spectral density in Figure 4.13 was measured on the chip Q11 (design A1) of the wafer 4972-4. As we can notice, between 1 Hz and 1 kHz, the noise has pure 1/f behavior, in fact the thermal PSD for this device, and for all the other transistor designs, is on the order of 10^{-26} A^2/Hz. In Table 4.6, we report the input referred noise values integrated in the 1 Hz - 1 kHz bandwidth, for 4 different MOSFETS designs in the wafer 4972-4. As expected, the noise is lower for the transistor with longer channel.

MOSFET design	Chip name	Channel length [μm]	Integrated noise 1 Hz-10 kHz [pA]
A1	Q11	20	157 ± 3
A3	I11	20	190 ± 4
B1	L11	10	269 ± 5
B3	H11	10	291 ± 6

Table 4.6. Integrated noise values over the bandwidth 1 Hz-1kHz in 4 different chips.

4.3.4 – Sensitivity and resolution

The displacement and force sensitivities have been evaluated on-wafer, in a similar way like in the case of the piezoresistive cantilevers by using the AFM and a probe-card. A different probe-card, compatible with the MOSFET sensor, was design in CNM and fabricated in HTT.GmbH in Dresden. It was mounted on the micromanipulator on the AFM

chuck and it could contact all the pads of a single sensor while the AFM was performing a force curve. A stiff AFM probe (*k*=40 N/m) was used to deflect the cantilever at a length of 50 µm from the clamping edge. The force curve was performed in tapping mode (i.e the probe was vibrating at the resonance frequency) in order to better evaluate the contact point between the probe and the cantilever (i.e when the vibration amplitude decays to 0). Gate and drain were biased at 4 V while source and substrate at 0 V by using the internal voltage source of the LNA. A LNA internal offset current (*I_{OFF}*) equal to the drain current, *I_D*, was selected and the difference *I_D*-*I_{OFF}* was amplified by a sensitivity of 100 nA/V (Figure 4.12.A).

In Figure 4.14.A,B, we report the displacement sensitivity graphs for the same sensor Q11 (design A1 with L_{CH}=20 µm) from the wafers 4972-4 and 4972-9 and in Figure 4.14.C,D the deflection of the AFM probe during the sensitivity measurement. As first, we can notice that the sensitivities have opposite signs. For the chip of the wafer 4972-4, it is negative (i.e. *S_δ*= -190±34 nA/µm and *$(\Delta I_D/I_{D,0})/\delta$* = 0.22±0.04 µm^{-1}) while for the chip of the wafer 4972-9 is positive (i.e. *S_δ*= 165±30 nA/µm and *$(\Delta I_D/I_{D,0})/\delta$* = 0.38±0.07 µm^{-1}). In the first case the current decreases. This tells us that the channel of the transistor lays below the neutral plane in a region of compressive stress; in the second case the current increases and therefore the channel lays above the neutral plane in a region of tensile stress. We can notice a second difference in the AFM probe deflection: for the cantilever of the wafer 9 (Figure 4.14.D), the AFM probe deflects almost 5 times more than the cantilever of the wafer 4 (Figure 4.14.C). This means that the MOSFET cantilever is much stiffer in the wafer 9. These two differences cannot be explained by the different thermal treatment performed, which is the only nominal difference during the wafer processing. On the other hand, they can be explained easily by watching the Figure 4.8 Figure 4.9. In the wafer 9, at the end of the process there is still some buried oxide present under the cantilever. This stiffens the cantilever and modifies the position of the neutral plane (Figure 4.9.B) so that the channel lays above the neutral plane in a region of tensile stress and therefore *$\Delta I_D>0$*. In wafer 4972-4 there is no oxide below the cantilever so that the cantilever is softer and the channel lays below the neutral plane in a region of compressive stress and therefore *$\Delta I_D<0$*. In this case the position of the neutral plane is at $z_{0,CH}$=+ 84 nm (eq. (2.47))(the z origin is considered to be at the silicon surface where the channel is). We simulated the position of the neutral planes by FEM analysis. The simulated position, i.e. $z_{0,CH}{}^*$=- 98 nm (Figure 4.10.C), agrees well with the analytical model as the difference of +14 nm correspond to 1.5% of the total cantilever thickness. Considering the measured sensitivity of the chip Q11 of the wafer 4, we can calculate the piezoresistive coefficient of the n-channel (4.4) considering L$_2$=50 µm):

$$\pi_{11,Ch} = -82 \pm 15 \times 10^{-11} [Pa^{-1}]$$

and a tip sensitivity (considering L$_2$=200 µm):

$$S_{F,I} = -0.90 \pm 0.16 \ [pA/pN]$$

The piezoresistive coefficient is similar to the literature values at comparable transverse electric field (section 2.2.2.3). Taking into account a noise of 160 pA (Table 4.6), we can estimate a force resolution of:

$$MDF = 180 \pm 32 \ [pN]$$

A)

B)

C)

D)
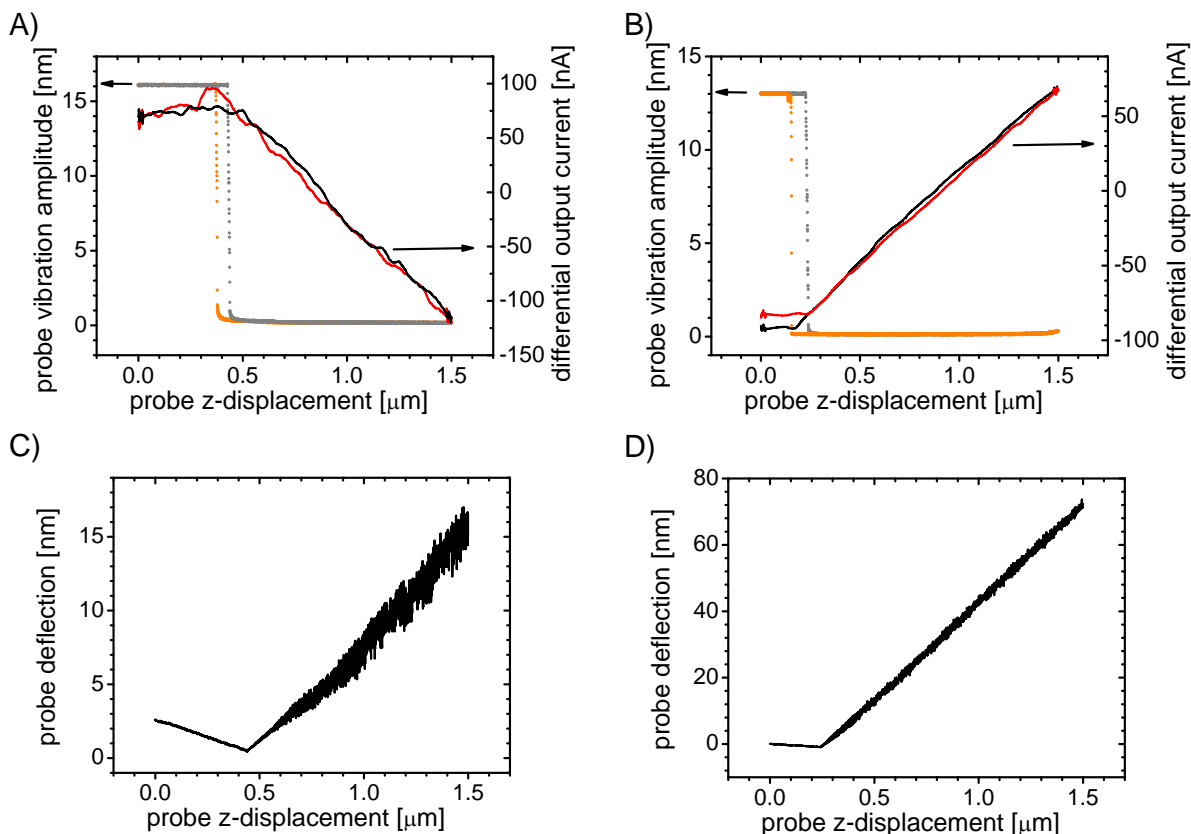
Figure 4.14. A,B) Sensitivity measurement of chip Q11 in the wafer 4972-4 and 4972-9 respectively. The sensitivities S_δ= -190±34 nA/μm and S_δ= 165±30 nA/μm are calculated taking into account the deflection of the AFM probe. The standard deviation is calculated considering that the measurement is performed pushing the cantilever at a length of 50±3 μm. C,D) Deflection of the AFM probe during the measurements.

The theoretical sensitivity, noise and resolution according to the model, calculated in Table 4.1, were respectively, $S_{F,I}$ = -0.67, $I_{D,H}$ = 184 pA and *MDF* = 277 pN. The theoretical sensitivity is 26% lower than the measured one and this derives from a higher measured drain current (I_D = 88 μA vs 52 μA).

Several sensors in both wafers were characterized and we noticed that the relative change of the drain current per displacement unit, *($\Delta I_D/I_{D,0})/\delta$*, could vary up to 30 times for both A and B designs. In Figure 4.15, it is reported the sensitivity of the chip G11 with a design A4 (i.e. L_{CH}=20 μm), which is very similar to design A1, and should have also similar sensitivity. On the contrary, we can see that it has almost 20 times less sensitivity (S_δ≈ 10 nA/μm and *($\Delta I_D/I_{D,0})/\delta$* =0.012 μm^{-1}). This can be explained vey easily watching the optical

micrograph of the cantilever (Figure 4.8.C,D). It is possible to see that the transistor channel lays in part onto the cantilever (around 13 μm) and part on the substrate (around 7 μm). On the other hand, for the chip Q11, the MOSFET lays completely on the cantilever in the position of maximum stress. This issue is due to the different etching speed of the DRIE used to etch the bulk silicon. As explain previously in section 3.2.3, it is possible to have undercut differences of up to 10 μm between two points in a wafer. Additionally there could be also some thin layer of buried oxide underneath the cantilever. In fact, also the HF vapor etching has not homogenous etching speed across the wafer and therefore can happen that some particles of BOX remain below the MOSFET, reducing the reciprocal distance between the neutral axis and the channel and therefore the sensitivity. Considering these two particular fabrication steps, the integration of a very short deflection transducer (i.e. 10 μm or 20 μm) is much more challenging than the integration of a long piezoresistor because the sensors can have very big performance deviation.

Finally, performing the measurement at different points from the clamping edge and on different sensors across the wafer we noticed also that the drain current could vary in a sinusoidal way before and during the contact (Figure 4.16). This issue invalidated many measurements and especially the ones from the cantilever that had less sensitivity. This signal can be fitted nicely with a sine of period of 1.4 μm which is two time higher than the AFM laser wavelength (λ=670 nm). This effect could be related to the interference or to the diffraction pattern of the laser onto the cantilever, which is also the substrate of the transistor, or onto the gate or drain of the transistor [15, 16]. Nevertheless, refocusing the laser onto the AFM probe and performing the force curves at 50 μm from the clamping edge (i.e. near the MOSFET) decreased this effect and increased the electromechanical response respectively (Figure 4.14.A,B and Figure 4.15).
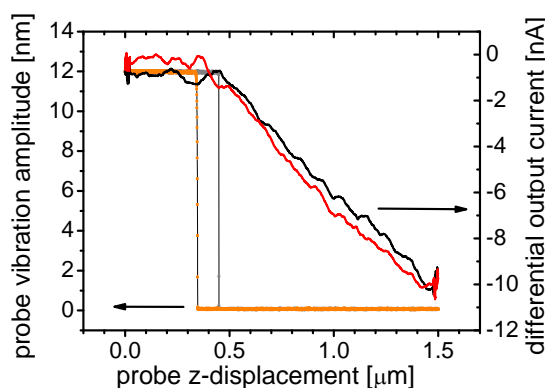
Figure 4.15. Sensitivity measurement of the chip G11 of the wafer 4972-4. The relative current variation ($\Delta I_D/I_{D,0}$)/δ =0.012±0.04 μm^{-1} is ten times lower than for the chip Q11 of the same wafer.
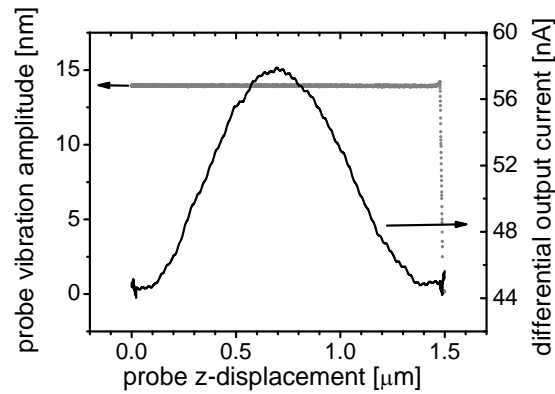
Figure 4.16. Drain current variation due to vertical displacement of the probe. The current varies in a sinusoidal way also before the deflection of the cantilever.

Concluding, taking into consideration a resolution of 19 pN (wafer 4974-4, design 2x250 for a bandwidth of 1 kHz) and 180 pN for piezoresistive and MOSFET cantilevers, respectively, the first ones offer much better force resolution (> 9 times). However, considering that the spring constant is almost 6 times lower (i.e 0.62 mN/m and 3.57 mN/m), for similar *k*, the MOSFET cantilever would have just 1.6 times lower sensitivity. Finally, in view of power consumption (1.3 mW and 0.35 mW), MOSFET cantilever can result advantageous having approximately three times higher resolution than piezoresistive ones.

Summary and future research directions

Piezoresistive metal-oxide-semiconductor field effect transistors (MOSFET) represent an alternative to bulk piezoresistor as deflection transducers. Therefore, cantilever with embedded a MOSFET have been developed at the same time as the cantilever with embedded piezoresistors.

The aim of the work presented in this chapter was:

- the development of the technological processes to obtain force sensors based on cantilever with embedded piezoresistive MOSFET deflection transducer.
- to measure the sensitivity and noise and extract important materials parameters like the piezoresistive factor of silicon inversion layer.
- to compare the performances of MOSFET and piezoresistive cantilever and to select the best one to be used in biomolecule recognition.

As first, the electromechanical model has been developed in order to optimize the different variables (i.e. cantilever and MOSFET dimensions). From it, we saw that it is possible to obtain comparable force resolution like for the cantilevers with embedded piezoresistors, but relatively thicker SOI wafer should be used (i.e. 1 μm thick device layer).

The mask layout and the fabrication process were presented next. The process flow is very similar to the one used in the production of cantilever with embedded piezoresistors and therefore they had similar fabrication issues. However, in this case, the issues have stronger effect on the performance variations: the sensitivity can vary up to 30 times in a wafer.

The techniques for the electro-mechanical characterization have been presented together with the results from two wafers. For the best sensor, we measured a sensitivity of $S_{F,I}$= - 0.9±0.16 pA/pN and a noise of $I_{D,noise}$= 157±3 pA (1 Hz- 1 kHz bandwidth), which lead to a resolution of MDF= 180±32 pN. From the sensitivity measurements, the longitudinal piezoresistive coefficient for the n-type silicon inversion layer in the <100> direction was extracted: π_{11}= 82±15 x 10^{-11} Pa^{-1}. This is in very good accordance with the literature values. Even though the resolution is almost two orders of magnitude lower than for the piezoresistive cantilevers, for similar spring constant and similar power dissipation, the MOSFET cantilever can represent a good alternative.

Considering the higher standard deviation of the electrical characteristics, the strong effects of the fabrication issues on the performance and in general the more difficult integration of the MOSFET into the cantilever, respect to a piezoresistor, we decided to focus all the efforts just on the piezoresistive cantilevers.

Considering that the MOSFET cantilever can represent a good alternative in cantilever based force sensors and that a deep recent study about the piezoresistive characteristics of MOSFET transistors is missing, I would suggest an extensive study of the piezoresistivity of the MOSFET technology at IMB-CNM on structures much easier to fabricate than cantilevers.

References

1. Akiyama, T., et al., *Integrated atomic force microscopy array probe with metal-oxide-semiconductor field effect transistor stress sensor, thermal bimorph actuator, and on-chip complementary metal-oxide-semiconductor electronics.* Journal of Vacuum Science & Technology B, 2000. **18**(6): p. 2669-2675.

2. Tark, S.-H., et al., *Nanomechanoelectronic signal transduction scheme with metal-oxide-semiconductor field-effect transistor-embedded microcantilevers.* Applied Physics Letters, 2009. **94**(10): p. 104101-104101-3.

3. Shekhawat, G., S.H. Tark, and V.P. Dravid, *MOSFET-embedded microcantilevers for measuring deflection in biomolecular sensors.* Science, 2006. **311**(5767): p. 1592-1595.

4. Wang, J., et al., *100 n-type metal-oxide-semiconductor field-effect transistor-embedded microcantilever sensor for observing the kinetics of chemical molecules interaction.* Applied Physics Letters, 2009. **95**: p. 124101.

5. Singh, P., et al., *Microcantilever sensors with embedded piezoresistive transistor read-out: Design and characterization.* Sensors and Actuators A: Physical, 2011. **171**(2): p. 178-185.

6. Li, X., *1/f Noise in MOSFETs*, 1993, Technische Universiteit Eindhoven.

7. Wortman, J.J. and R.A. Evans, *Young's Modulus, Shear Modulus, and Poisson's Ratio in Silicon and Germanium.* Journal of Applied Physics, 1965. **36**(1): p. 153-156.

8. Halg, B. *On a nonvolatile memory cell based on micro-electro-mechanics*. in *Micro Electro Mechanical Systems, 1990. Proceedings, An Investigation of Micro Structures, Sensors, Actuators, Machines and Robots. IEEE*. 1990.

9. Kapels, H., et al. *Full Characterization and Long-Term Stability of Standard CMOS Materials for Integrated Micromechanical Applications*. in *Solid-State Device Research Conference, 1999. Proceeding of the 29th European*. 1999. IEEE.

10. Zhao, J.-H., et al., *Measurement of elastic modulus, Poisson ratio, and coefficient of thermal expansion of on-wafer submicron films.* Journal of Applied Physics, 1999. **85**(9): p. 6421-6424.

11. Guohua, W., et al. *A Comprehensive Study on Nanomechanical Properties of Various SiO2-Based Dielectric Films*. in *Microelectronics and Electron Devices (WMED), 2010 IEEE Workshop on*. 2010.

12. Kabe, Y., H. Tanimoto, and H. Mizubayashi, *Elasticity study of nanostructured Al and Al-Si (Cu) films.* Materials Transactions, 2004. **45**(1): p. 119-124.

13. Haque, M.A. and M.T. A Saif, *Mechanical behavior of 30-50 nm thick aluminum films under uniaxial tension.* Scripta Materialia, 2002. **47**(12): p. 863-867.

14. Blaum, A., et al., *A new robust on-wafer 1/f noise measurement and characterization system.* Proceedings of IEEE 2001 International Conference On Microelectronic Test Structures, 2001. **14**: p. 125-130.

15. Werner, R., C. Zimmermann, and A. Kalz, *Light dependence of partially depleted SOI-MOSFET's using SIMOX substrates.* Electron Devices, IEEE Transactions on, 1995. **42**(9): p. 1653-1656.

16. Bosch, M.A., D. Herbst, and S.K. Tewksbury, *The influence of light on the properties of NMOS Transistors in laser Âμ-zoned crystallized silicon layers.* Electron Device Letters, IEEE, 1984. **5**(6): p. 204-206.

Chapter V

Biomolecule recognition

Biomolecule recognition

In order to apply the developed sensor to detect biomolecules at single molecule resolution, we evaluated that the most straightforward was the detection of the intermolecular forces between ligands and receptors, using the AFS measuring approach. Preliminary experiments were carried out in IMB-CNM, but due to the lack of knowledge of this technique, the experiments were not successful: no unbinding event was detected. In this perspective, it was of key importance to start an intensive collaboration with a group that had strong knowledge on this subject, in order to learn the AFS technique, integrate the piezoresistive sensor in an AFM and to perform AFS experiments with the new set up. Therefore, after a positive answer from Prof. Salvatore Cannistraro of the Biophysics and NanoScience center at Tuscia University of Viterbo, Italy, I obtained a COST action scholarship that financed me a short stay of three months in his lab.

In this section, the set-up (AFM and substrate sample) used in the experiments; the sensitivity and noise measurements; the functionalization procedures and finally the successful detection of the unbinding forces related to the biomolecule recognition between neutravidin and biotin molecules are presented.

5.1 – Set up

In the previous chapter 3, we showed that we achieved force sensors, which are capable of sub-10 pN resolution in liquid environment (see also section 5.2). These are appropriate to study the interaction involved in the formation of a molecular complex using the AFS measuring approach. For this purpose highly controlled displacements during the F-z curves are needed. In collaboration with the research group headed by Prof. Salvatore Cannistraro, we decided to integrate the sensor into a PicoLe 5100 AFM, from Agilent Technologies, to take advantage of the high mechanical stability of this equipment and the highly reliable displacement of the piezo actuator. Even though we choose this microscope, the sensors can be easily integrated in other AFMs, as for example we did in the Cervantes fullmode AFM from Nanotec Electronica S.A. The pre-requisite is that the AFM has a break-out box by which the deflection signal from the position sensitive photodiode can be substituted by the differential output voltage of the integrated deflection transducer of the piezoresistive sensor.

5.1.1 – PicoLe 5100 AFM

In order to use our sensor in the PicoLe 5100 AFM we had to mechanically and electronically integrate the chip into the microscope.

The commercial probe holder (also called nose cone) of the PicoLe uses a clip to hold firmly a standard AFM chip. Unfortunately, this was not suitable to hold the chip without causing any damage to sensitive parts of the encapsulated die (i.e nitride passivation or wire bonding). In this perspective, a custom AFM nose cone was designed and made by rapid prototyping at IMB-CNM (Figure 5.1.A,B). The silicon dies were glued and ultrasonically wire bonded on a custom made 0.4 mm thick printed circuit board (PCB) (Figure 5.1.C). On the PCB backside, it was glued also a 0.1 mm magnetic thick steel sheet. All the conductors were passivated by a mono component room temperature curable silicone coating (3140 RTV from Dow Corning®). The board was held firmly by a neodymium magnet embedded in the nose cone and inserted into a low profile zero insertion force (ZIF) connector (Figure 5.1.A,B,C). Thanks to this new design, the positioning of the sensor was much easier, with no danger to damage the chip during the mounting process and at the same time very stable.

The concept of the developed set-up was to simplify and to make as small as possible the path from the sensor to the electronic equipment. For this purpose, the ZIF connector with the lowest profile available in the market was selected (54550-0694 from Molex). This connector is very small (4.7 mm x 3.6 mm x 1mm) and has 6 pins with a pitch of 0.5 mm. Normally, they are used to create electrical connection with Flat Flexible Cable (FFC), which have a thickness of 0.3 mm, however we could insert the PCB, which is 0.4 mm thick, without any problem or drawback. Choosing this connector allowed us to downscale sensibly also the PCB dimensions: 15 mm x 3.7 mm x 0.4 mm. Due to the reduce weight of the PCB and of the connector, the magnetic force between the small magnet (N35D34 from laboutiquedeliman.com with a diameter of 3 mm and a height of 4 mm) and the thin iron foil (10 mm x 3.5 mm x 0.1 mm) was sufficient to guarantee high stability during the AFS measurements. The 3140 RTV silicone coating used to passivate all the metallic parts, inclusive the wire bondings, was chosen because it has high dielectric constant, is mono-component, does not require heat for curing, and has good thixotropic properties: it behaves as viscous under static conditions but flow relatively easy under shear stress. These characteristics are excellent in order to easily make a good quality passivation with a very low profile with no risk to damage the wirebondings (Figure 5.1.C). In Figure 5.2.A-D, then we can see the nosecone mounted into the AFM head, the substrate chip (see next section) placed into the fluid cell on the sample holder and the final assembly.

Regards to the electronic integration, unshielded copper cables with a diameter of 0.25 mm (Kynar) and a length of 15 cm were soldered at the terminals of the ZIF connector and glued by an epoxy resin (5-minutes Epoxy from Araldite) to improve the strength of the connection (Figure 5.1.B). The wires were shielded altogether by aluminum foil and at the other terminal we soldered a standard 6 position header with a pitch of 1.25 mm (Molex). In this way the cables could be connected easily to a "coaxial box" (Figure 5.2.D). This box was developed to null the differential output voltage of the sensor, using two wirewound potentiometers (1 kΩ from Bourns) (Figure 5.2.E) and to pass the signals from unshielded cables to shielded BNC cables. For future experiments, I would suggest to use an on-board

low noise amplifier that can be integrated into this box, which it has been already designed and is under production. The coaxial box was then connected to the external low noise amplifier (SR560 from Stanford Research) with two 50 cm long BNC cables. The sensors were biased by 4 AA rechargeable batteries (Eneloop - Sony) that provided a low noise constant voltage of 5 V. The output differential voltage was amplified 2000 times and low pass filtered at 10 kHz. The resulting signal was used as feedback to approach the cantilever to the sample substrate. To this purpose we introduced the amplified piezoresistive signal into the "error signal" of the controller via the break out box, which is a device that allows to monitor or change the internal signals between the AFM and the controller (Figure 5.2.E). Under normal working conditions the error signal, is the signal coming from the photodetector related to the deflection of the cantilever.
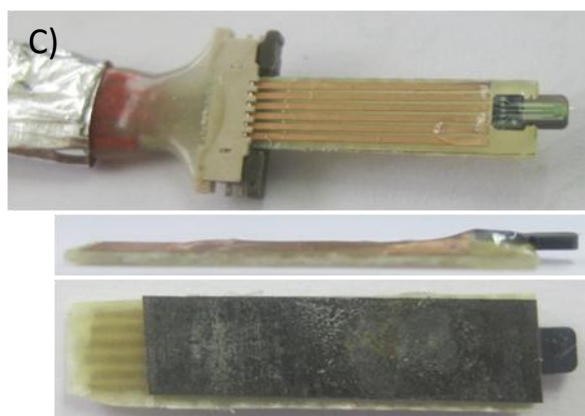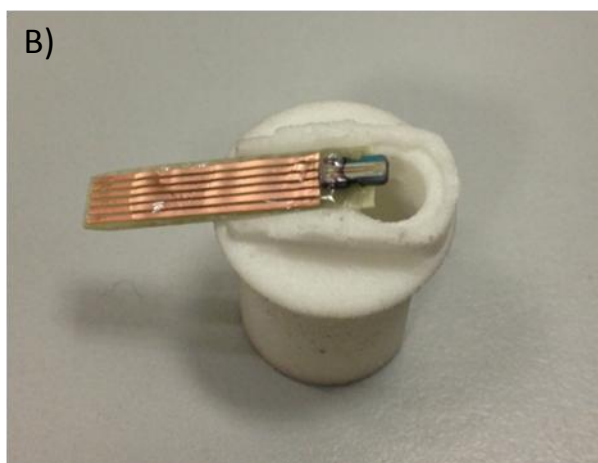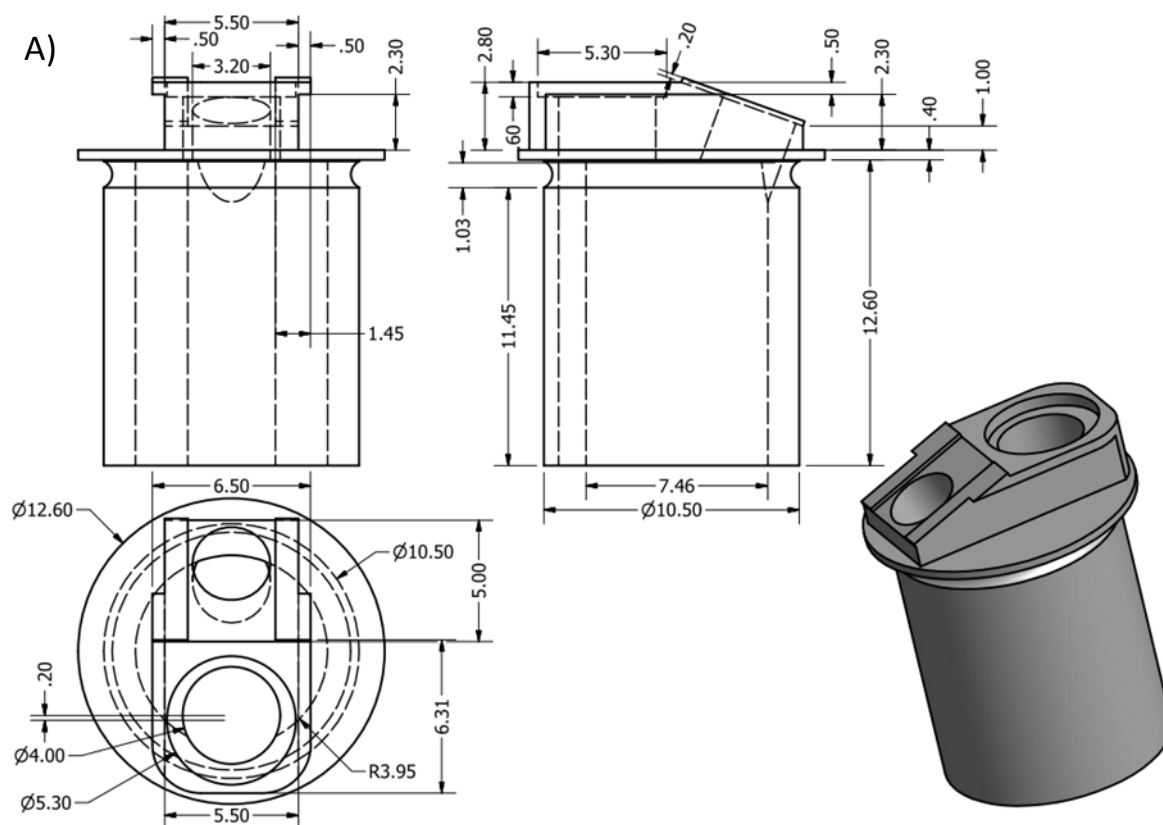
Figure 5.1. A) Top, lateral and isometric views of the custom AFM nose cone design. B) Nose cone made by rapid prototyping with a chip install onto it. C) Front, side and back view of the die wire bonded on the PCB and passivated by silicone. In the top view the PCB is inserted into the ZIF connector. The red cables are soldered on the ZIF terminals and epoxy resist is applied to strength the connections. The cables are shielded altogether by aluminum foil. In the side view we can appreciate the height of each components: the PCB is 0.4 mm thick and the die is 0.5 mm thick. The passivation of the wire bonding has to be as thin as possible to avoid any interaction with the substrate when the chip is mounted on the AFM. On the back view, a steel foil glued on the PCB is visible.
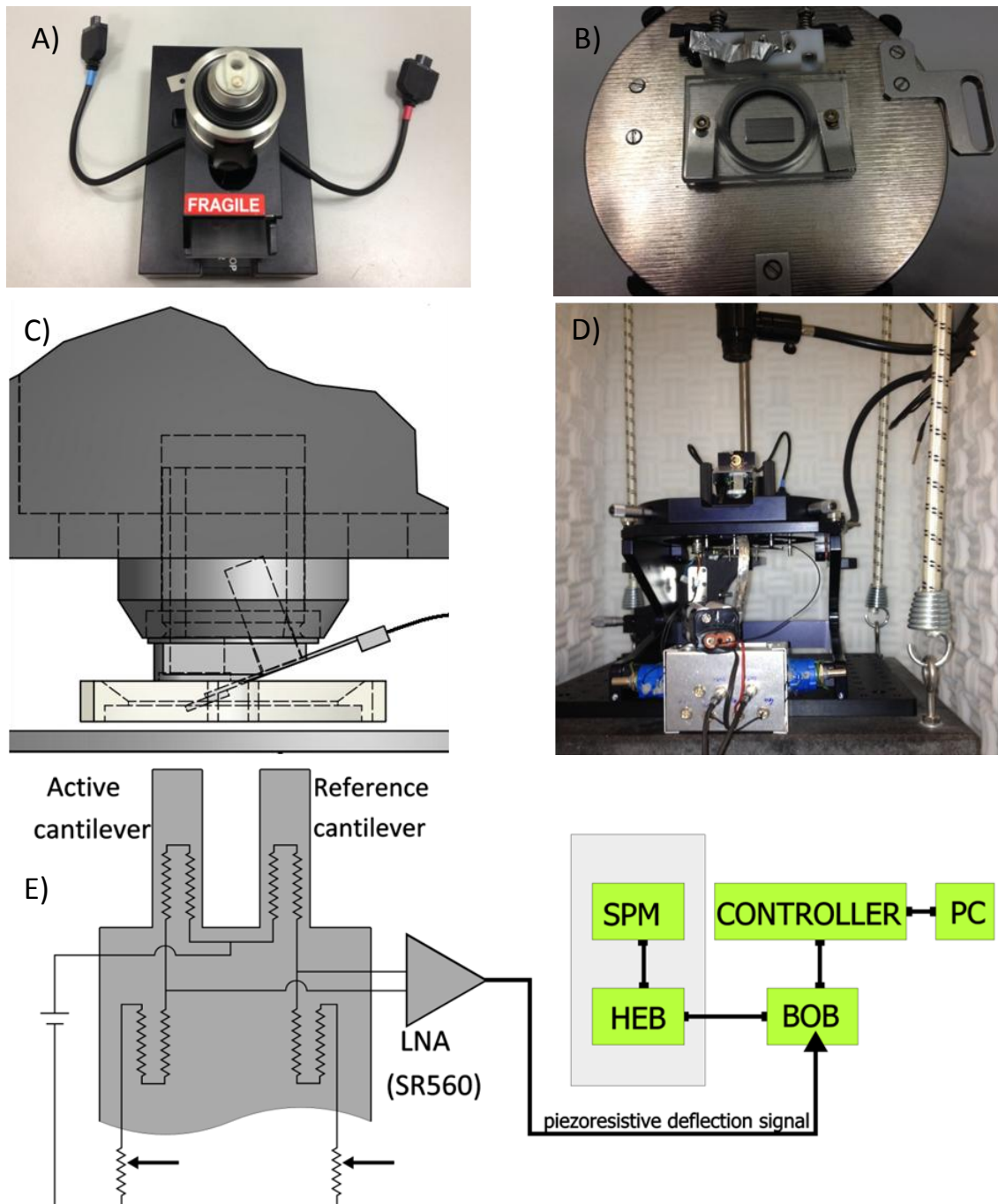
Figure 5.2. A) The nose cone is installed in the AFM head. B) The fluid cell and the substrate chip are placed on the sample holder. C) Design of the assembly with all the components. The PCB, which is inserted in the ZIF connector, is held by the magnet embedded into the nose cone. The nose cone is inserted into the AFM head. The fluid cell and the substrate chips are placed beneath the nose cone. D) Picture of the final set up. Up is visible the optical microscope of the AFM. Below there is the AFM head and in front there are the coaxial box with the potentiometers and the batteries. E) Electrical scheme of the set up. The Wheatstone bridge can be balanced by 2 potentiometers. The output differential voltage is amplified by a low noise voltage amplifier and is introduced into the AFM controller by the break out box (BOB). This signal substitutes the error signal coming from the photodiode, related to the deflection of the cantilever and normally used to approach the cantilever to the substrate.

5.1.2 – Substrate chip

In this section we will discuss the microfabrication of the substrate chips with sharp tips for the molecule atomic force spectroscopy measurements. As it is pointed out in the introduction (chapter 1.4) it is of key importance that just small areas between the cantilever and the substrate interact during this measurement to allow the interaction of just few molecules. In standard AFS measurements the typical AFM probes have a tip radius of 50 nm, while the substrate is a flat glass substrate. In our case the cantilevers don't have a real tip because we started from SOI device layer of 340 nm in order to optimize the resolution. We could have started from a thicker SOI wafer but the microfabrication of a tip would have made the process far more complex. Additionally thicker SOI wafer have also higher thickness standard deviation which would have been an issue for nano-thick cantilevers. However, it is not strictly needed to fabricate a sharp tip perpendicular to the cantilever but it could be microfabricated also in-plane, as reported by other researchers [1]. I would suggest this option for the future.

A set of two masks was designed.

1. The fist mask (Figure 5.3.A) is used to define a round area for the tip and a bigger area which has a U shape and can be used as visual reference for optical alignment during AFS measurements (see next paragraphs). The tip area is a circle with a diameter of 3 or 5 μm.
2. The second mask (Figure 5.3.B) is used to define pillars with a squared cross-section of 50x50 μm or 30x30 μm and the same U-shaped reference.

In Figure 5.3.C, we reported the masks overlapping for a single chip, which has the following dimensions: 10 mm x 5 mm.

The process [2] starts with a 500 μm thick p-doped silicon wafer with a resistivity of 1-10 Ωcm (Figure 5.4.A). A layer of approximately 1 μm of oxide was deposited via tetraethylorthosilicate(TEOS)/O_2-plasma enhanced chemical vapor deposition (PECVD) at 400º C in the Applied Materials Precision 5000 CVD equipment. The first photolithography, is performed to define the tip area and the oxide is etched via CHF_3/C_2F_6 reactive ion etching (RIE) in Drytek QUAD 484 etcher (OXI-QUAD conditions) (Figure 5.4.B). Afterwards, a layer of 6 μm of resist is spinned and the second photolithography is performed to define the mask for the pillars (Figure 5.4.C). Using the resist as etching mask, 100 μm of bulk silicon are etched via SF_6/C_4F_8 Bosch deep reactive ion etching process (DRIE) in an Alcatel 601 etcher (P601DEEP conditions) (Figure 5.4.D). After the cleaning in an O_2 plasma asher, a series of two DRIE in the Alcatel 601 is performed. The first etching is somehow "isotropic", it has a horizontal: vertical etching ratio of 1:2 and is used to etch horizontally the silicon (NANO2BISMOD conditions) (Figure 5.4.E-F). After measuring the vertical etching speed (2 μm/min), we etched the wafer for 2'20". During this step almost all the silicon under the oxide disk is etched and a proto-tip is formed. We stopped the process just after the first oxide protective disks fall down in the external part of the wafer (Figure 5.5.C). This happens

because not all the disks have the same dimensions due to deviations in the photolithographic process and because the etching speed can vary around 6% across the wafer. The second etching (NANO1 conditions) is highly anisotropic and is used to vertically etch the tip for 5 μm, using the oxide disk as mask (Figure 5.4.G-H). Then, oxidation of 400 nm at 1100°C (Figure 5.4.I-L) and oxide etching by SiOetch solution (Figure 5.4.M-N, Figure 5.5.D-F) are performed to obtain a sharper apex. A final oxide of 50 nm is grown at 1000°C to protect the tip. After the end of the microfabrication, the wafers are protected by hard backed photoresist and saw cut.
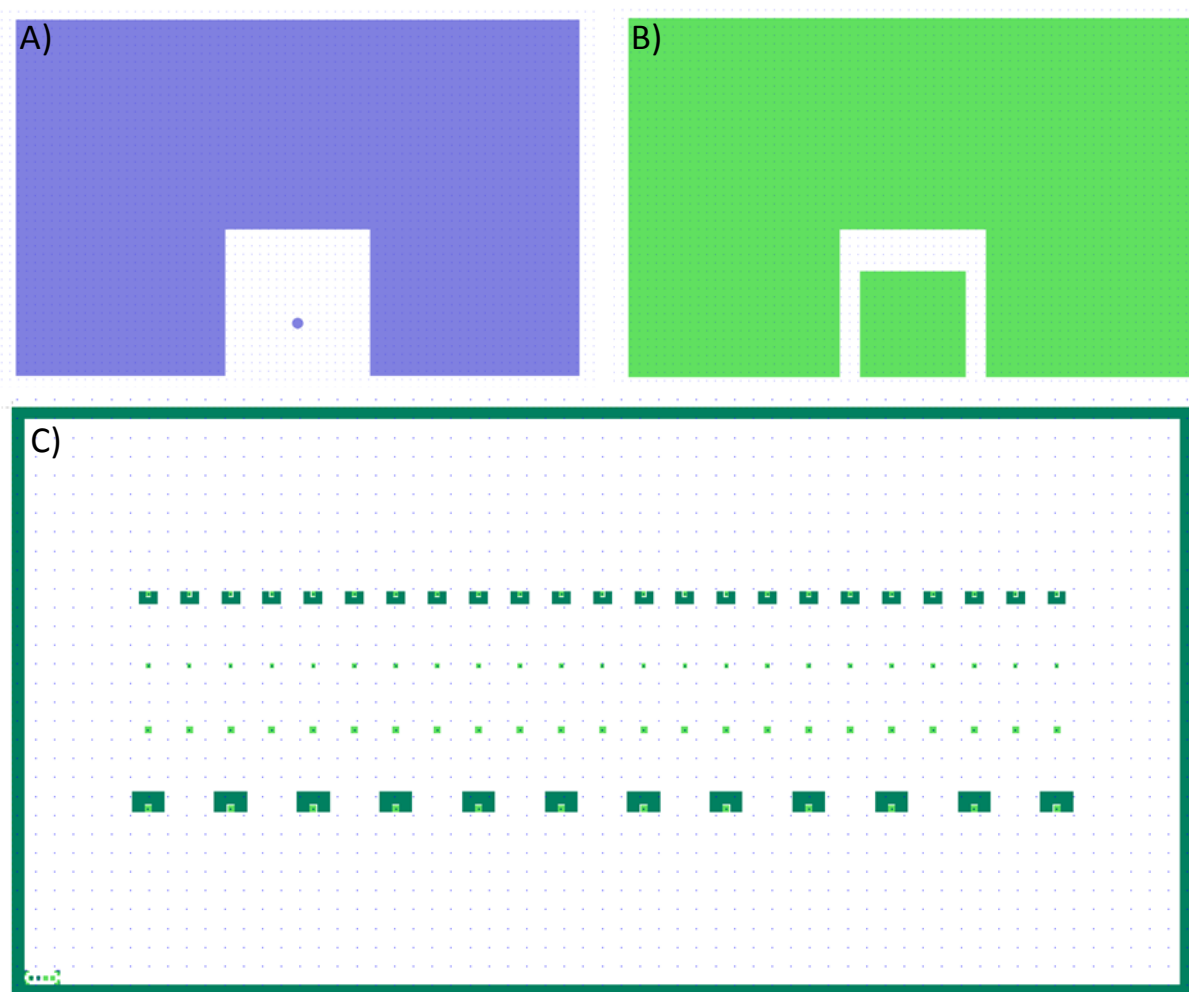
Figure 5.3. A) Detail of the mask to define the tip region and U reference area. B) Mask to define the pillar and the U reference area. C) Overlapping of the 2 mask levels for a single chip: there are four rows of tips on pillars, two with and two without U reference.
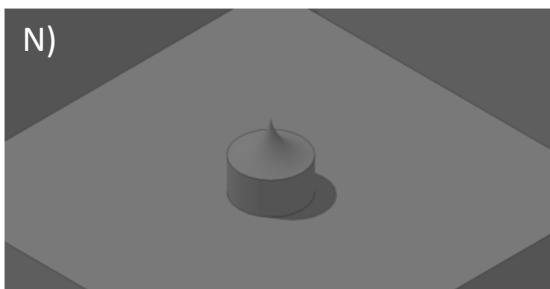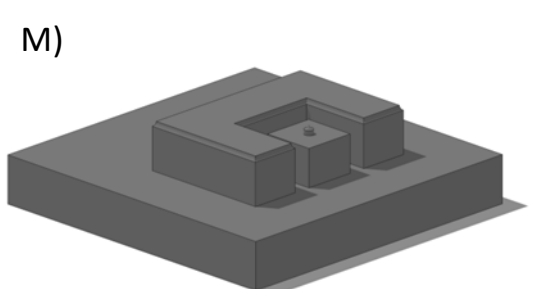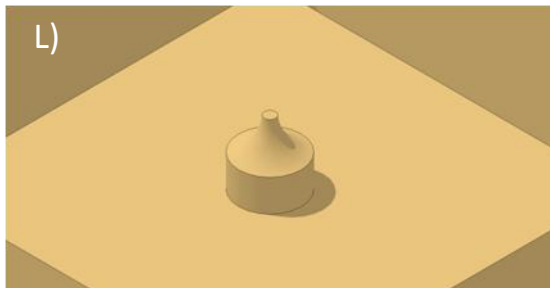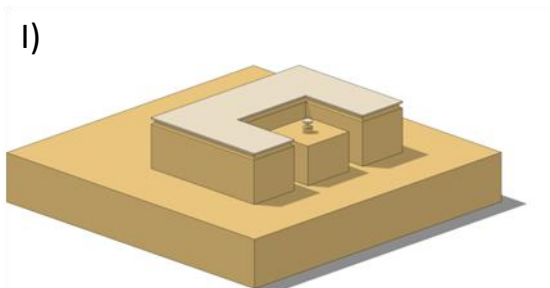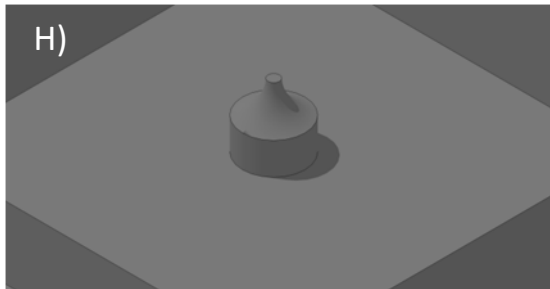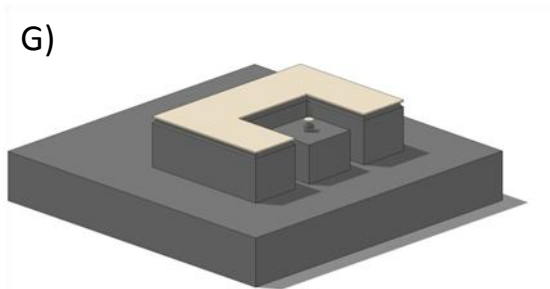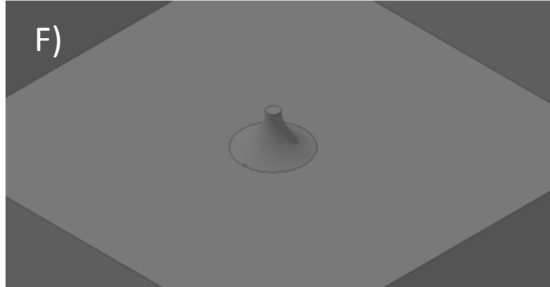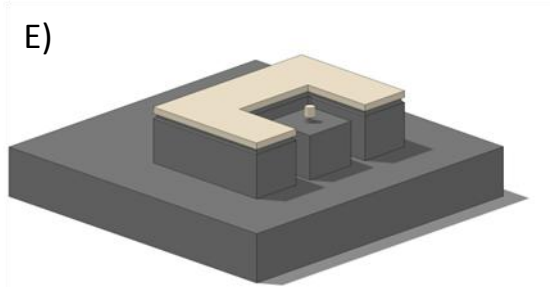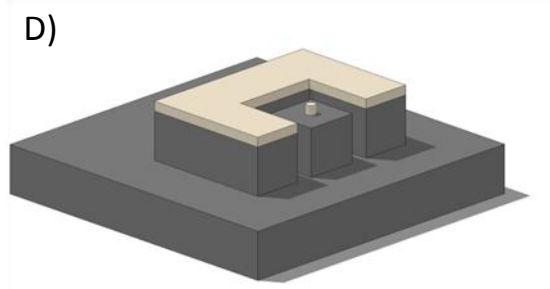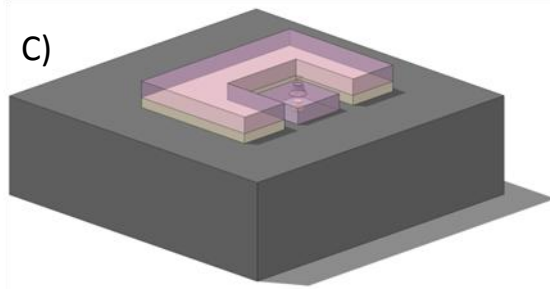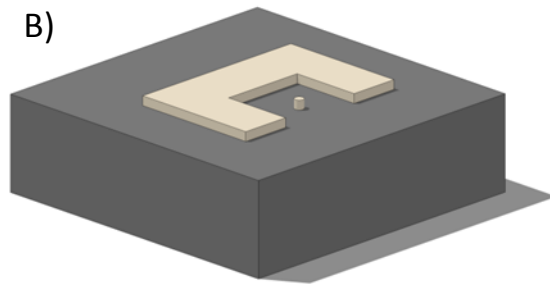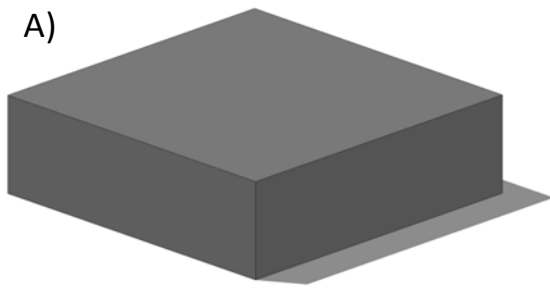
Figure 5.4. Process flow to fabricate the substrate chip. A) starting silicon wafer; B) Oxide deposition, photolithography and etching to define the tip area; C) photolithography to define the pillar area; D) DRIE of the pillar; E,F) "isotropic" silicon RIE with and without the oxide protective disk; G-H) Silicon DRIE of the tip to increase its aspect ratio; I-L) Silicon oxidation to sharpen the tip; M-N) Final tip after oxide etching
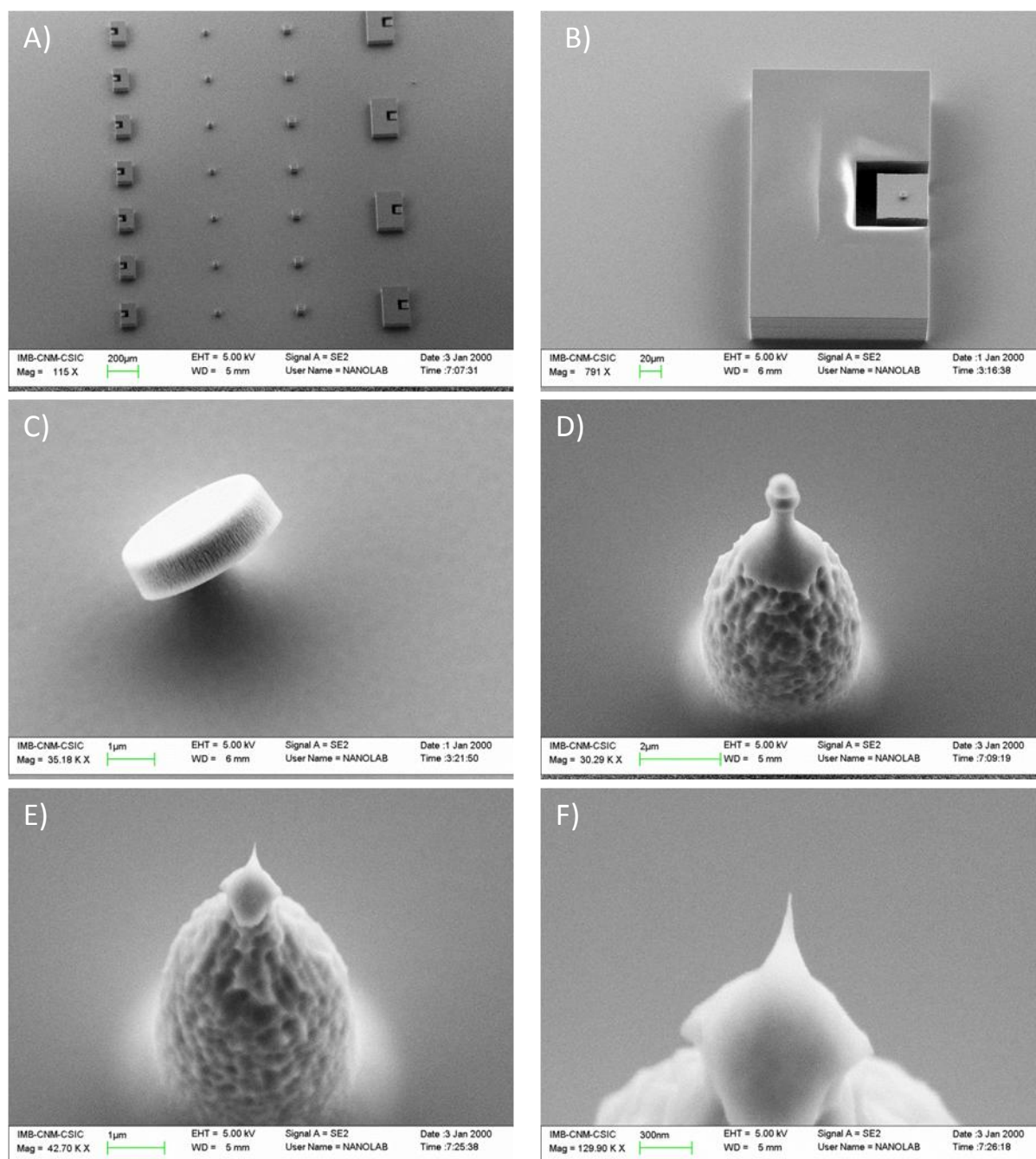
Figure 5.5. SEM images of substrate chip at different fabrication stages. A-C) Chip after the isotropic silicon etching. D-F) Final tips: the tip radius can vary between few hundreds and few tens of nm.

5.2 – Sensitivity and noise in air and liquid

In this section F-z curves and noise measurements of sensors from wafer 6481-3 and 6481-4 will be presented. While the sensors from the wafer 3 performed very good, there were some issues related to chips from wafer 4.

The sensors (wafer 6481-3) were tested in air, de-ionized water (milli-Q water) and PBS (phosphate buffer saline solution) for several hours in order to verify their performance in liquid medium by using the new set-up. Several F-z curves were recorded in order to calculate their sensitivity (Figure 5.6.A). In the Picole AFM, the set point to engage the cantilever to the substrate is fixed and it is 0 V. We found that unbalancing the bridge to start the engage procedure with -2 V in air and -0.1 V in liquid could lead to reliable engaging. The motor displaced the substrate until the signal increased to 0 V. This means that the signal from the chip varies around 1 mV in air and just 50 µV in water, considering that the signal is amplified 2000 times. Somehow the cantilever in air deflects already before engaging the substrate. This is probably due to potential difference between the cantilever and the substrate and to the water meniscus formation at the contact point between the cantilever and the substrate. Figure 5.6.A shows the typical difference between the F-z curves in air and in liquid environment for the cantilevers of the wafer 6481-3. During the approach in air, there is a jump-to-contact preceded by a region of attractive forces. During the retraction, the restoring force of the cantilever does not exceed the adhesion force and therefore the cantilever remains in contact [3]. In water, instead, there is neither jump-on-contact nor jump-off-contact. As expected, no significant sensitivity variation in liquid respect to air was observed, i.e. 354 µV/µm and 359 µV/µm, respectively.

A) B)
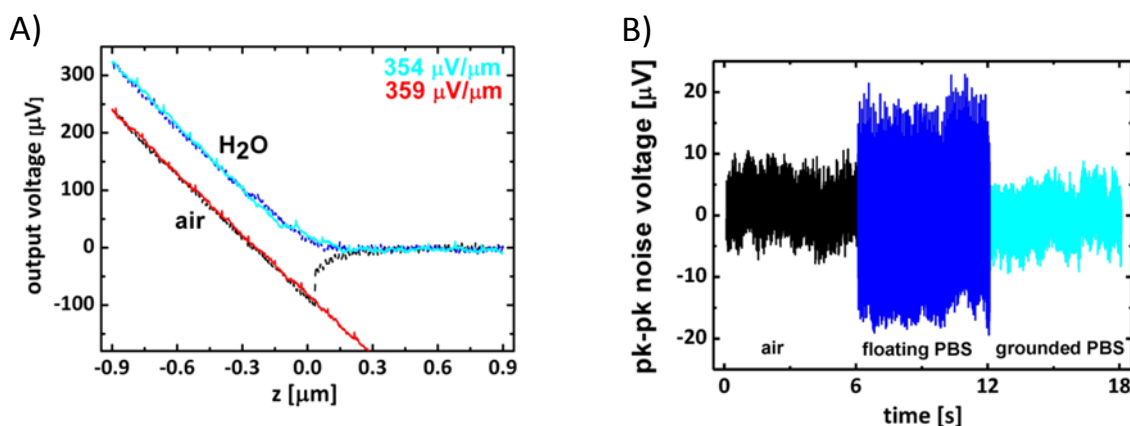
Figure 5.6. (A) F-z measurement in air (black and red curves) and water (blue and light blue). Approaching the sample in air, a jump-on contact event is detected (black line). Retracting the cantilever for 1 µm is not sufficient to overcome the adhesion force, therefore there is no jump-off-contact (red curve). In water, instead, there are no jump phenomena and the sensitivity has no significant variation. From the slopes we calculated sensitivities of 354 µV/µm and 359 µV/µm for air and water environments, respectively. (B) The peak to peak noise has a value of 18 µV in air (between 0 and 6 s) and in grounded PBS solution (between 12 and 18 s). When the solution is not grounded (between 6 and 12 s) the noise is more than 2 times higher. There is no significant noise variation between air and grounded PBS.

The peak-to-peak noise (Figure 5.6.B) did not change significantly when the liquid was grounded (ground represented by the batteries ground). If the water had floating potential, we noticed instead a relevant increase in the 50 Hz peaks with noise average level rising from 18 µV to 42 µV. Such low noise of the set up is due to the good nitride cantilever passivation on one side, and to the fact that the AFM provide a good shielding against the electromagnetic external interferences (Figure 5.2). These sensitivity and noise values are in good agreement with the values extracted from the on-wafer characterization.

In Figure 5.7.A, we report typical F-z curves in air of a sensor from the wafer 6481-4. This curve shows a very strange behavior of the cantilever in contact with the substrate. In the approach curve we cannot see a precise contact point; instead the slope varies continuously, between z=+200 nm and -200 nm, until a constant slope of 550 mV/µm is reached between z=-200 nm and z=-800 nm. At z= -800 nm the signal decay for about 0.4 V and then increases again with the same slope. In the retract curve, the slope is constant and has the same value between -900 nm and -600 nm, but then changes continuously. This behavior is probably due to buried oxide "network" present on the cantilever at the end of the fabrication process (section 3.2, Figure 3.30). In order to solve this problem we tried to clean the surface inserting the cantilever tip into a glass microcapillary with a diameter of 90 µm (see section 5.3) that was previously filled with 5% HF solution. Even though the HF etches the glass of the capillary, this could widthstand for several tens of minutes with no damage, due to the fact that solution was very diluted and had very small volume. After an etching of 2 minutes we performed again the F-z curve and the graph improved a lot (Figure 5.7.B). Then we performed an F-z curve in water (Figure 5.7.C) but in the approaching curve were visible two different slopes. The cantilever tip, probably, was still "dirty" and this was presumably due to the fact that the HF solution lost the main fluoride content dissolving the glass of the capillary. However, we used this cantilever for biomolecule recognition experiments (section 5.4), but with no success. We tried to clean several cantilevers in glass capillaries with the same negative result. We tried also to clean them in plastic micropipettes, but unfortunately these had bigger diameter (250 µm) so that the HF could evaporate on the cantilever and etch away the silicon nitride; using glass microcapillaries with a diameter <100 µm, we didn't noticed any evaporation instead.

Out of these experiments, therefore, I would suggest not to use a RIE to release a cantilever during the fabrication process, because it does not remove completely the oxide (section 3.2). If cleaning of cantilever should be performed, it should be done in HF resistant plastic microcapillaries with a diameter of less than 100 µm, to reduce HF evaporation.

A second issue encountered in some chip of both wafers was the unreliable passivation of the aluminum interconnections. In some sensor, the water corroded the aluminum some minutes after the application of a 5 V bias (Figure 5.8.A). This happened mostly at the height steps near the contact windows of the chips (Figure 5.8.B). This was probably due to the aluminum etching issues in the RUN 6481. This is an additional reason to choose lift-off technique to define the interconnections.

163

A)

B)

C)
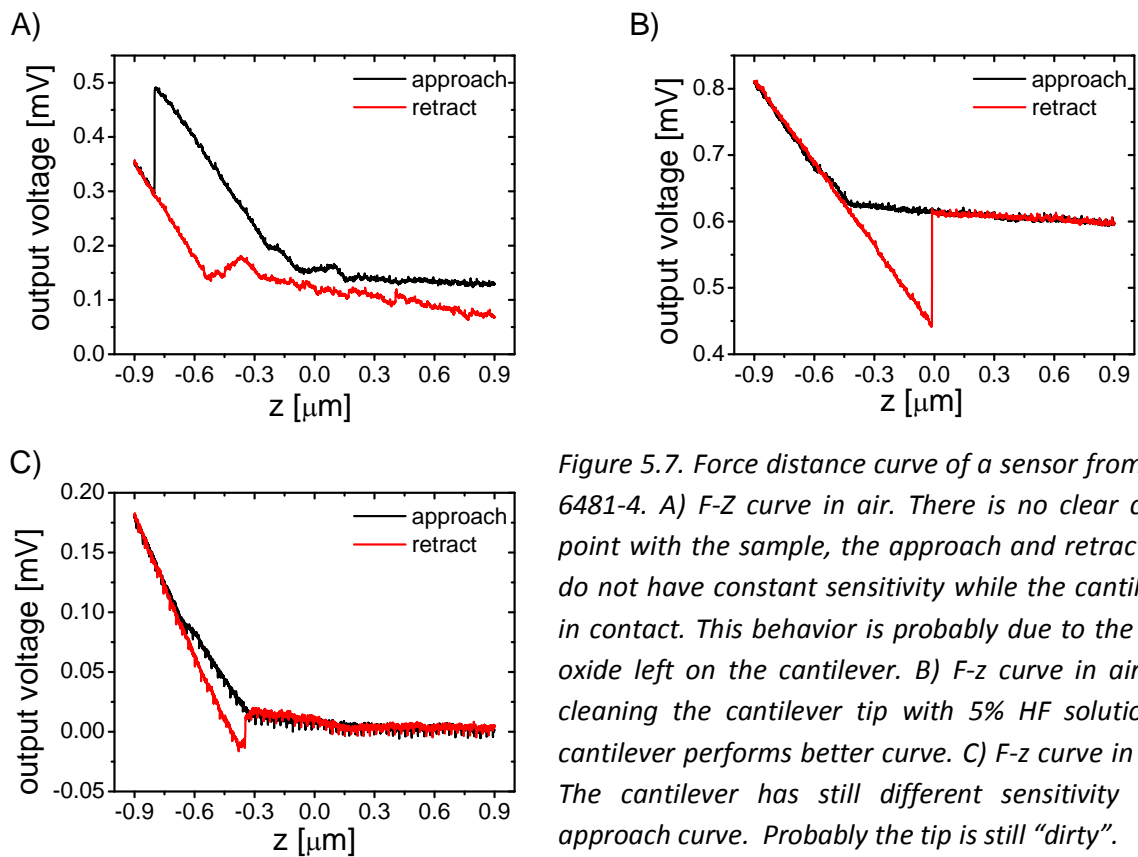
Figure 5.7. Force distance curve of a sensor from wafer 6481-4. A) F-Z curve in air. There is no clear contact point with the sample, the approach and retract curve do not have constant sensitivity while the cantilever is in contact. This behavior is probably due to the buried oxide left on the cantilever. B) F-z curve in air. After cleaning the cantilever tip with 5% HF solution, the cantilever performs better curve. C) F-z curve in water. The cantilever has still different sensitivity in the approach curve. Probably the tip is still "dirty".
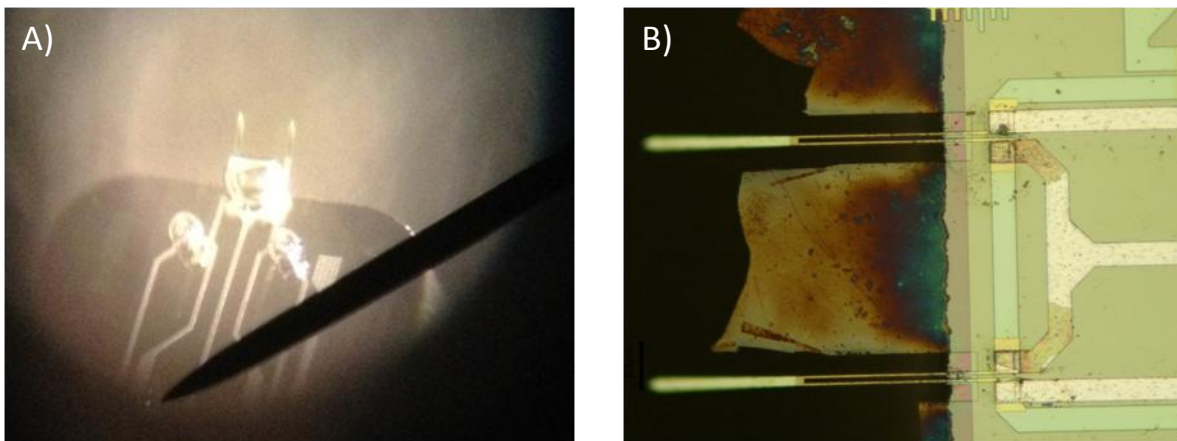
Figure 5.8. A) Optical micrograph of a biased sensor immersed in the water. 3 bubbles are visible. These are due to the aluminum corrosion which release hydrogen. B) It is visible that the aluminum interconnections are partially corroded.
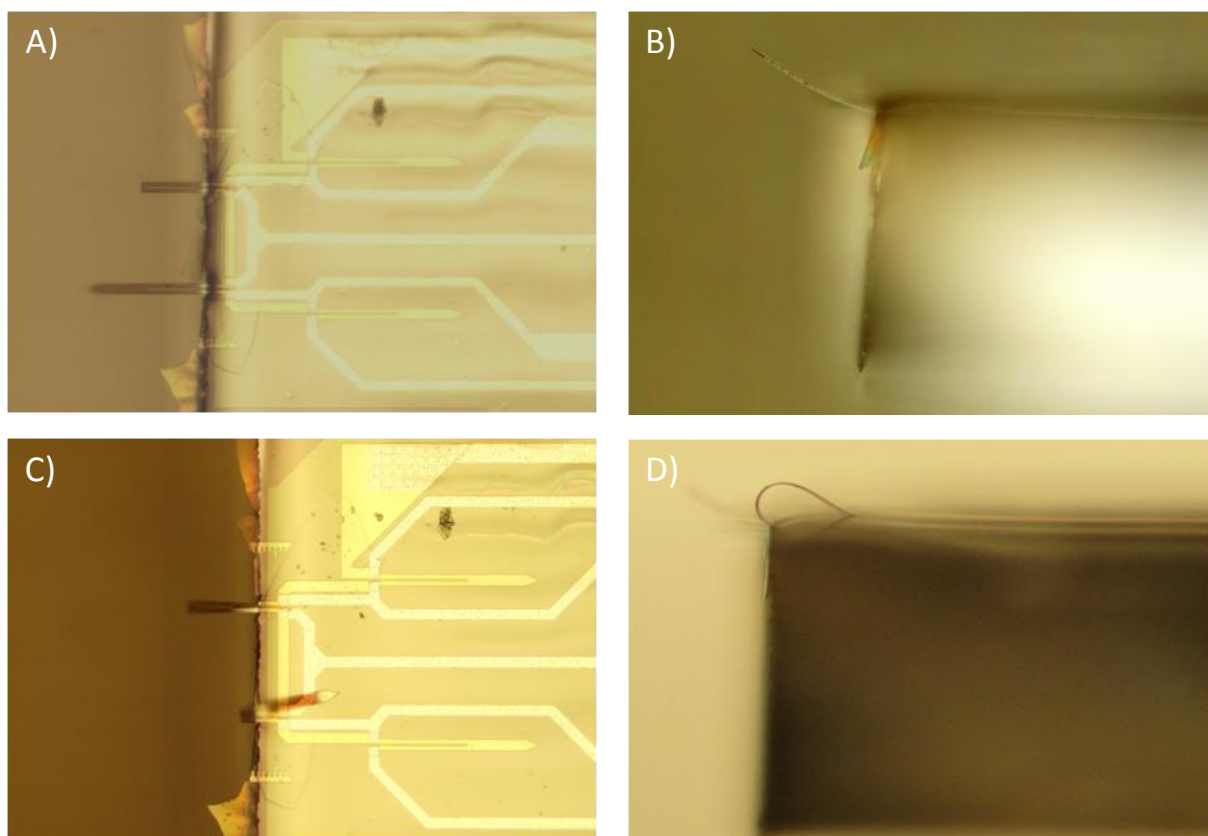
Figure 5.9. Front and side view of the chip before (A-B) and after (C-D) immersion in water. The cantilever is deflected upwards due to residual stresses of the different layers. The die is passivated by silicone. After the immersion in water, the long cantilever is adhering strongly on the chip while the reference cantilever is still suspended.

We decided therefore to passivate somehow the die. We found that the use of silicone or the epoxy resin were excellent to this purpose. However, the use of silicone had a drawback: once the chip was retracted from the water, the cantilever stuck permanently to the die (Figure 5.9.C-D). On the other hand, cantilevers adhere to the uncoated die but once the water evaporates they spring back (Figure 5.9.A-B). The cantilevers spring back, also in the case of passivation using epoxy resist. We decided therefore to passivate all the aluminum interconnections by epoxy resin using a "doctor blade" technique, therefore with no risk to coat the cantilevers. The performances of the coated sensors were unchanged (Figure 5.6) and could function in liquid medium for several hours with no deterioration.

5.3 – Cantilever and substrate functionalization

We decided to use the developed set-up to investigate the biorecognition processes in the well-studied avidin-biotin complex [4-6]. For this purpose we used a functionalization procedure previously developed at the Biophysics and Nanoscience Center in Viterbo [7].

Substrates and cantilevers were cleaned by hot acetone, exposed to UV light to expose hydroxyl groups and then covalently functionalized with biotinylated bovine serum albumin (b-BSA) and neutravidin, respectively. In both cases the proteins were linked to the aldehyde groups of the glutaraldehyde that was linked to the amino groups of the (3-aminopropyl)triethoxysilane (APTES) (Figure 5.10). Non-specific binding sites were blocked by ethanolamine.

All the starting materials were purchased from Sigma-Aldrich. The PBS used for the functionalization or washing had a strength of 50 mM with a pH of 7.5. All the cleanings and functionalizations were performed by immersing the substrate in Petri dishes and the cantilevers into microcapillaries by using a micromanipulator [8] (Figure 5.11). The microcapillaries were fabricated starting from standard borosilicate glass capillaries by using a micropipette puller to achieve a final diameter of ≈100 μm. This diameter is ideal, because it allows an easy cantilever insertion and the wetting of a small part of the beam. If the diameter is of 250 μm, instead, we found that the cantilever would completely get wet.

At the beginning, substrates and cantilever were washed in acetone for 10 minutes. The immobilization procedures for both consisted of 5 steps:

- hydroxyl group exposure
- silanization
- linker molecule deposition
- receptor, or ligand, coupling
- passivation of active linker

CANTILEVER

The hydroxyl groups of the silicon oxide were formed by exposing the cantilevers to UV light (200W Hg-Xe lamp) for 30 minutes. Subsequently the cantilever were immersed into freshly prepared 6.3% v/v 99% APTES solution in chloroform for 3 minutes, washed in chloroform (3 x 5 min) and dried under nitrogen. The linker molecule deposition was carried out in 1% v/v grade II 25% glutaraldehyde solution in milli-Q water for 3 minutes. Later, the cantilevers were cleaned in milli-Q water (3 X 5 min) and dried under nitrogen. The incubation of the receptor was performed overnight via a 10 μM neutravidin solution in PBS. The cantilevers were cleaned in PBS (3 x 5 min) and in milli-Q water (1 x 5 min). The active sites of the glutaraldehyde that didn't react with the neutravidin, were blocked by immersing the cantilevers into 60% wt ethanolamine hydrochloride solution in water for 5 minutes. Finally the cantilevers were washed with PBS and with milli-Q water.

SUBSTRATE

The functionalization of the substrate followed similar steps. The chips were exposed to UV light for 30 min, immersed in 2% APTES solution in chloroform for 3 hours, washed in chloroform (3 x 5 min) and dried under nitrogen. Afterwards, they were immersed into 1% v/v glutaraldehyde solution in milli-Q water for 3 minutes, washed with water (3 x 5 min)

and dried under nitrogen. Finally the samples were immersed into a 10 μM biotinylated bovine serum albumin (b-BSA) solution in PBS, washed with PBS and with water.

Cantilevers and substrate were used for atomic force spectroscopy measurements just after the functionalization.
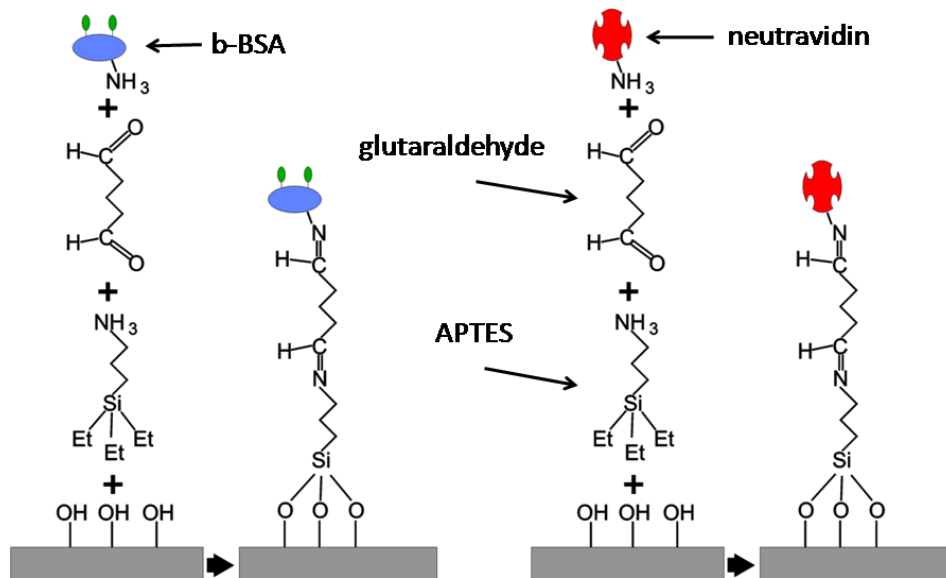
Figure 5.10. Immobilization strategies of the substrate (left) and probe (right) functionalization. The b-BSA and the neutravidin were linked to the aldehyde groups of the glutaraldehyde that was linked to the amino groups of the (3-aminopropyl)triethoxysilane (APTES).
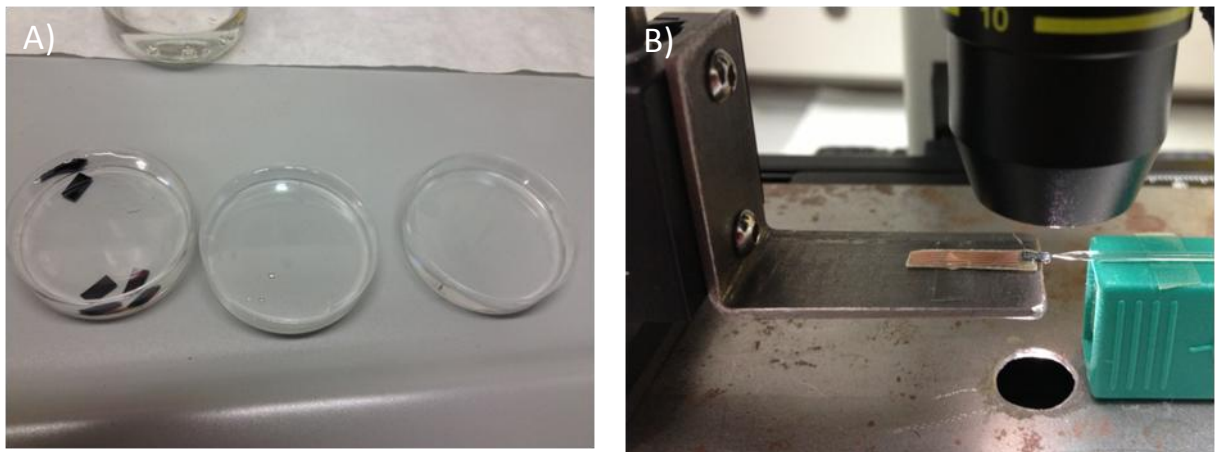
Figure 5.11. Functionalization of the substrate chips (A) and of the cantilevers (B). The sensor is placed onto a micropositioner in a optical microscope. On the right is placed a microcapillary with the functionalization solution. The cantilever is inserted inside the capillary by using the micropositioner.

5.4 – Single biomolecule recognition

In this section, the final results of the biomolecule atomic force spectroscopy measurements and the issues encountered during such experiments are presented.

Just after the functionalization, the sensor and the sample were placed in the nose cone and in the AFM fluid cell, respectively (Figure 5.1.B, Figure 5.2.A, B). After pouring 500 µL of PBS solution into the cell, the cantilever and the substrate were aligned using the optical microscope and the micromanipulators of the AFM (Figure 5.12). The cantilever was subsequently engaged to the sample surface, approached further to the sample for 0.9 µm at a constant speed of 1 µm/s for a maximum force of around 500 pN, and after 100 ms, retracted for 1.8 µm at a loading rate of 4.3 nN/s. At the same time the differential output voltage of the sensor was recorded (Figure 5.13). Hundreds of curves were acquired for each experiment. In most of them no unbinding event is visible since the retraction curve follows faithfully the approach curve (Figure 5.13.A). The jump-off event in Figure 5.13.B should be attributed to a non-specific adhesion between the substrate and the cantilever since the curve has a constant slope [9]. In Figure 5.13.C, instead, the slope is changing before the jump-off-contact. In this case, the average unbinding force resulted to be 44 ± 12 pN. Unbinding forces between 50 pN and 100 pN for biotin-avidin complex and similar loading conditions have been reported in the literature (Figure 5.14)[4], therefore this value could arise from specific unbinding events occurring between biotin and neutravidin. Due to the fact that the probe spring constant is 3 orders of magnitude lower than the one of the typical probes used in the AFS experiments, the jump-off contact occurs at a length between 200 and 300 nm, which is higher than the literature values [4].
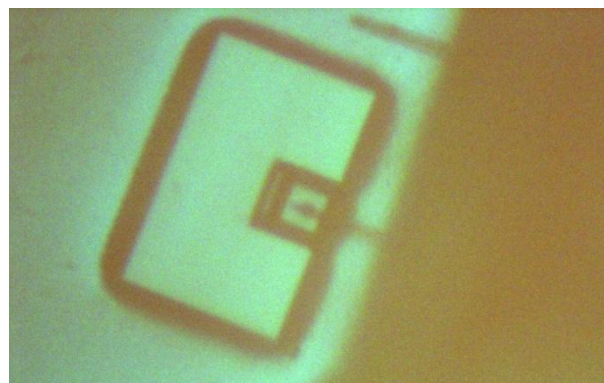
Figure 5.12. The cantilever and the tip of the substrate are aligned using the micromanipulators of the AFM
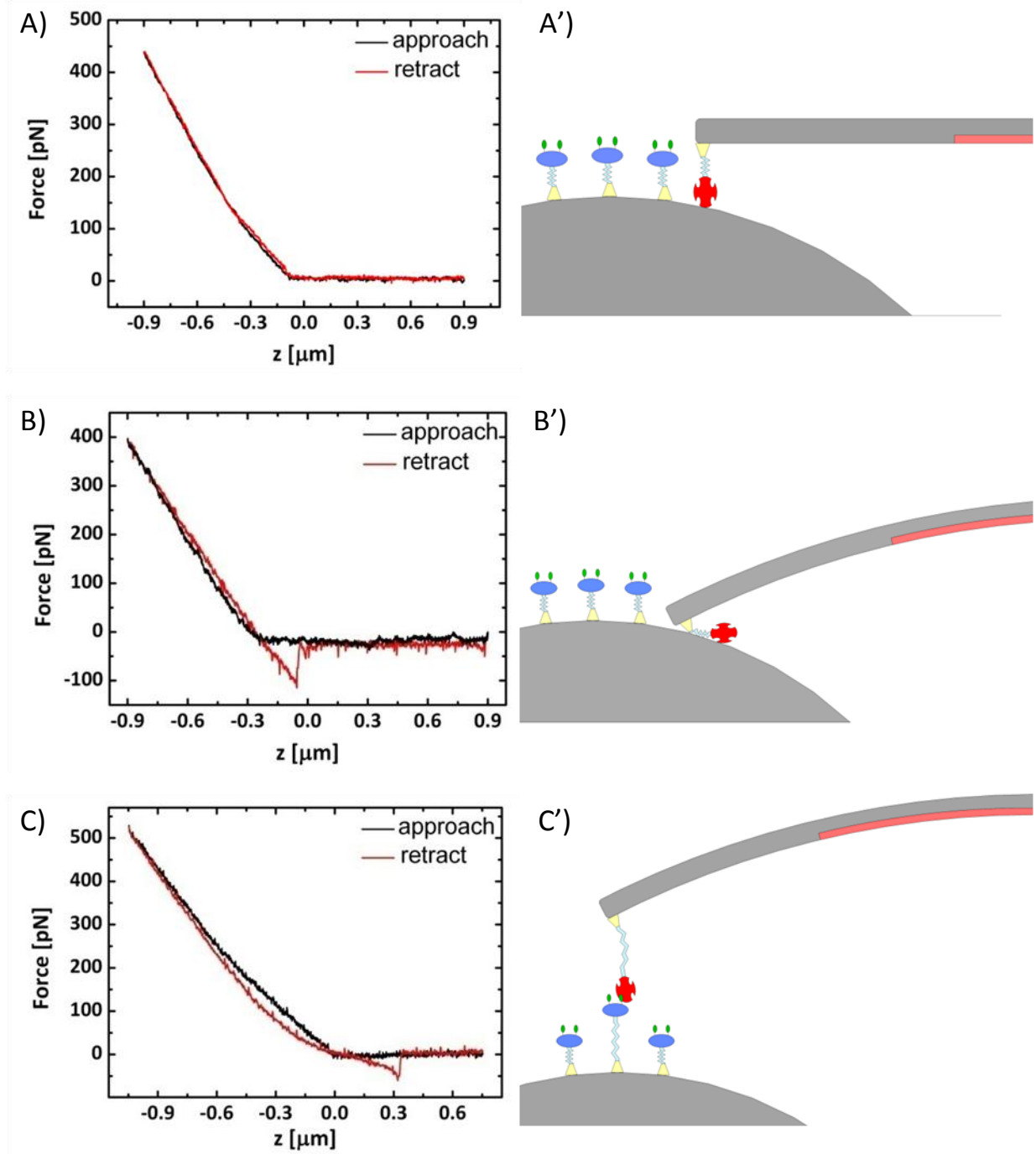
Figure 5.13. A-C: AFS curves obtained functionalizing the cantilever by b-BSA and the substrate by neutravidin. (A) No event is detected. (B) Non-specific event. The slope of the retract curve is constant before the jump-off. (C) Specific unbinding event between biotin and neutravidin. The slope of the retract curve varies before the jump off. The unbinding force is around 70 pN. A'-C': schematic representation of the three measurements.
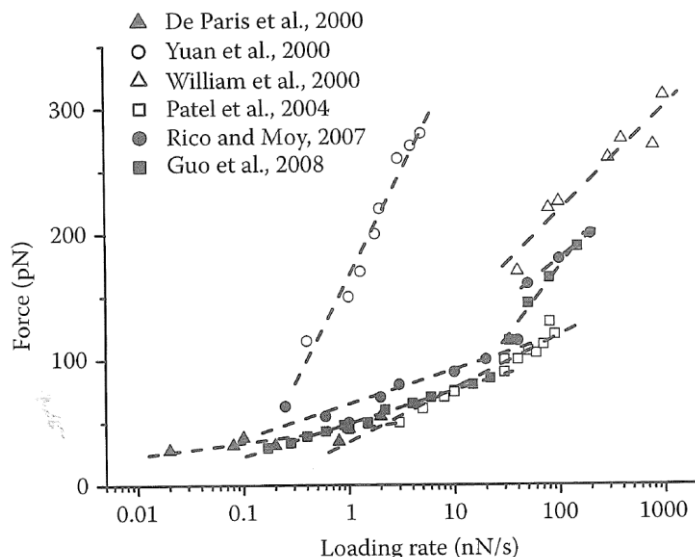
Figure 5.14. Overlay of unbinding forces as a function of the logarithm of the loading rate for the avidin-biotin complex [4]. The dashed lines are obtained by a fit through eq. (1.3). Data are from [10-15].
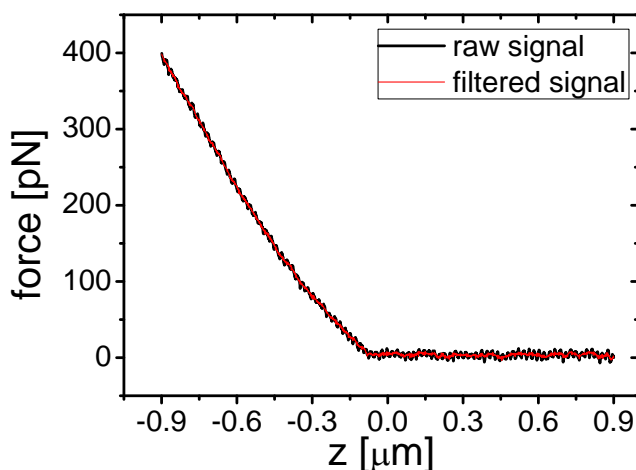
Figure 5.15. Approach curve of the Figure 5.13.A. The black curve represents the raw data. After removing the 50 Hz, 100 Hz and 150 Hz interferences, we obtain the red curve.

To obtain the graphs in Figure 5.13, we post processed the data by applying a filter to remove the signals at 50 Hz, 100 Hz and 150 Hz (Figure 5.15). In fact, during the days of biorecognition experiments, we found a higher 50 Hz noise, even though the PBS in the liquid cell was grounded. This can be due to several factors like deterioration in the coaxial cables and in the wiring in general and interactions between the ground of the batteries and of the AFM. We noticed, in fact, that sometimes the PBS, grounded by the batteries, could reach metal parts of the AFM, which was grounded by the electrical line.

The specific events were detected in two different experiments performed during the last days of the short stay in Viterbo, highlighting the repeatability of the measurement.

Even though we performed several hundreds of force curves, we achieved an overall low unbinding frequency (n° events/total F-Z curves) of ≈3%. This can be due to several facts: not optimal functionalization procedure for this set up, not perfectly clean cantilever (section 3.2), too low cantilever spring constant, possible denaturation of the molecules due to the temperature increase and too high electromagnetic interference. In this perspective a study and simulation about the temperature should be performed; a tip should be integrated into the cantilever; a dedicated set-up should be developed and the sensor should be integrated into a microfluid cell; the cantilever should have possibly higher spring constant, in fact the best AFS results are generally obtained using cantilevers with spring constant around $k_C=20$ mN/m, and this is the first time that AFS experiments are performed with such compliant cantilever ($k_C<1$ mN/m). About this aspect, further improvements in the microfabrication process would enable cantilevers with higher spring constant and sub-10 pN resolution.

Finally, it is worth nothing that, in comparison with similar piezoresistive force cantilevers fabricated by other groups, we offer a probe which is compatible with liquid media [16], which has higher resolution [17, 18] and it is produced by more straightforward fabrication process [19, 20].

These results open a new perspective in high sensitive label free biomarkers detection in nearly physiological conditions. In contraposition with the past, when the mass or the surface stress caused by the molecule binding to the cantilever was revealed, now we are able to achieve much higher resolution, down to a single molecule, detecting the intermolecular force between an analyte molecule and the receptor partner. Even though this was already possible with the atomic force microscope, the peculiarity of this sensor it is that the deflection transducer is integrated into the sensors. The sensor, therefore, can be used with no restrictions in opaque media, it can be easily integrated in microfluidic cells and displays a high multiplexing potentiality. These characteristics make this force sensor a very good candidate for a new type of biosensor.

Summary and future research directions

In this chapter the integration of the sensor into a commercial AFM, the substrate chip fabrication, the functionalization procedure and the biomolecule recognition experiments have been presented.

In order to perform biomolecule recognition experiments, high mechanical stability and highly reliable displacements are needed, therefore we integrated the sensor into a PicoLe 5100 AFM, from Agilent Technologies. To this purpose a custom made probe-holder was designed and made for the correct positioning of the sensor. The piezoresistive deflection signal was integrated into the AFM electronics by means of a break out box, substituting the error signal coming from the photodiode.

In the single molecule atomic force spectroscopy experiments, standard AFM cantilevers with a tip radius of 50 nm are normally used. This is necessary so that just small areas interact between the cantilever and the substrate. In this way, it is minimized the risk of multiple bindings of ligand-receptors pairs. Substrate chips with sharp tip have been therefore fabricated.

Afterwards, we tested the sensors in air and de-ionized water (milli-Q water) for several hours in order to verify their performance in liquid medium by using the new set-up. The sensitivity and noise values agree well with the values extracted from the on-wafer characterization and the sensors were functioning in liquid environment for several hours.

The biomolecular recognition experiments were performed after the functionalization of cantilevers and substrates with neutravidin and biotin, respectively. We successfully detected the forces related to the avidin-biotin complex formation, highlighting the possibility of biomolecule label-free recognition in nearly physiological conditions and at single molecule resolution. Besides the very high sensitivity attained, the sensor can be used with no restrictions in opaque media; it can be easily integrated in microfluidic cells and displays a high multiplexing potentiality. These results, therefore, open a new perspective in highly sensitive label free biomarkers detection in nearly physiological conditions.

Improvements in the cantilever design as well as in the set up could be made in the future, as pointed out in the text:

- Use of on board amplifier placed near the sensor in order to reduce as much as possible the external electromagnetic interference.
- Fabrication of a tip on the cantilever. This can be out of plane or better in plane for easier fabrication.
- Development of microfluidic systems for better functionalization and easier detection. This would be the first step towards a real biosensor based on the detection technique shown in this chapter.
- Explore different and maybe easier detection schemes: the pulling of the molecule may be achieved by means of receptor functionalized magnetic

particles, on which acts a magnetic force [21]. In this case the cantilever doesn't need a substrate, so that the system would result simpler.

References

1. Ried, R.P., et al., *6-mhz 2-N/m piezoresistive atomic-force microscope cantilevers with incisive tips.* Microelectromechanical Systems, Journal of, 1997. **6**(4): p. 294-302.
2. Villanueva, G., et al., *Deep reactive ion etching and focused ion beam combination for nanotip fabrication.* Materials Science and Engineering: C, 2006. **26**(2): p. 164-168.
3. Cappella, B. and G. Dietler, *Force-distance curves by atomic force microscopy.* Surface Science Reports, 1999. **34**(1): p. 1-104.
4. Bizzarri, A.R. and S. Cannistraro, *Dynamic Force Spectroscopy and Biomolecular Recognition*2012: CRC Press, Boca Raton.
5. Moy, V.T., E.L. Florin, and H.E. Gaub, *Intermolecular forces and energies between ligands and receptors.* Science, 1994. **266**(5183): p. 257-259.
6. Izrailev, S., et al., *Molecular dynamics study of unbinding of the avidin-biotin complex.* Biophysical Journal, 1997. **72**(4): p. 1568-1581.
7. Bizzarri, A.R., et al., *Interaction of an anticancer peptide fragment of azurin with p53 and its isolated domains studied by atomic force spectroscopy.* International Journal of Nanomedicine, 2011. **6**: p. 3011-3019.
8. Bietsch, A., et al., *Rapid functionalization of cantilever array sensors by inkjet printing.* Nanotechnology, 2004. **15**(8): p. 873-880.
9. Bizzarri, A.R. and S. Cannistraro, *The application of atomic force spectroscopy to the study of biological complexes undergoing a biorecognition process.* Chemical Society Reviews, 2010. **39**(2): p. 734-749.
10. De Paris, R., et al., *Force Spectroscopy and Dynamics of the Biotin-Avidin Bond Studied by Scanning Force Microscopy.* Single Molecules, 2000. **1**(4): p. 285-290.
11. Guo, S., et al., *Effects of multiple-bond ruptures on kinetic parameters extracted from force spectroscopy measurements: Revisiting biotin-streptavidin interactions.* Biophysical Journal, 2008. **95**(8): p. 3964-3976.
12. Patel, A.B., et al., *Influence of Architecture on the Kinetic Stability of Molecular Assemblies.* Journal of the American Chemical Society, 2004. **126**(5): p. 1318-1319.
13. Rico, F. and V.T. Moy, *Energy landscape roughness of the streptavidin-biotin interaction.* Journal of Molecular Recognition, 2007. **20**(6): p. 495-501.
14. Williams, P.M., et al., *On the dynamic behaviour of the forced dissociation of ligand-receptor pairs.* Journal of the Chemical Society. Perkin Transactions 2, 2000(1): p. 5-8.
15. Yuan, C., et al., *Energy landscape of streptavidin-biotin complexes measured by atomic force microscopy.* Biochemistry, 2000. **39**(33): p. 10219-10223.
16. Harley, J.A. and T.W. Kenny, *High-sensitivity piezoresistive cantilevers under 1000 Å thick.* Applied Physics Letters, 1999. **75**(2): p. 289-291.
17. Aeschimann, L., et al., *Scanning probe arrays for life sciences and nanobiology applications.* Microelectronic Engineering, 2006. **83**(4-9): p. 1698-1701.
18. Polesel-Maris, J., et al., *Piezoresistive cantilever array for life sciences applications.* Journal of Physics: Conference Series, 2007. **61**(1): p. 955-959.
19. Doll, J.C., *Advances in high bandwidth nanomechanical force sensors with integrated actuation*, 2012, Stanford University.
20. Doll, J.C., et al., *Faster than the Speed of Hearing: Nanomechanical Force Probes Enable the Electromechanical Observation of Cochlear Hair Cells.* Nano Letters, 2012. **12**(12): p. 6107-6111.

21. Baselt, D.R., et al., *A high-sensitivity micromachined biosensor.* Proceedings of the IEEE, 1997. **85**(4): p. 672-679.

Chapter VI

Conclusions

Conclusions

The main objective of this thesis has been the development of a force sensor based on a self-sensing cantilever compatible with liquid environment endowed with pN force resolution and its application in biomolecule recognition. In this respect, two different approaches have been studied: cantilevers with embedded piezoresistors or piezoresistive MOSFET transistors.

For the cantilevers with embedded piezoresistors, an electromechanical analytical model has been developed in order to optimize the different parameters to achieve the desired resolution. According to this model, it is possible to obtain a resolution of less than 10 pN for a bandwidth of 10 kHz, if the cantilevers have length, arm width and thickness of 250 μm, 2 μm and 325 nm respectively, and a piezoresistor with the following dimensions: 125 μm, 2 μm and 100 nm. Afterwards, a previously developed fabrication process (developed by Dr. Luis Guillermo Villanueva) has been improved in order to obtain the desired probes with high fabrication yield. Different process solutions have been tried and force sensors with excellent characteristics (resolution of 6 pN and yield of 90%-100%) have been obtained. For these results, three different key process steps have been optimized. A relatively low temperature arsenic activation thermal treatment at 950 °C for 75 minutes allowed obtaining a junction depth of around 100 nm. A combination of dry etching and wet etching has been used for the back end of line process to avoid any possible damage of the piezoresistors so to improve the noise characteristics. A custom made HF vapor etcher has been upgraded to provide fast and homogeneous buried oxide etching across the wafer.

At the same time, the second option of cantilever with an embedded piezoresistive MOSFET transistor has been explored. The specific two dimensional conduction mechanism of the transistor can be beneficial to the sensitivity because the conduction is on the surface of the silicon where the stress is the highest. An electromechanical model has been developed to evaluate the effect of each variable on the sensitivity and on the noise. According to this model, good resolution in the order of few tens of pN can be achieved for cantilever thicknesses of around 1 μm. A fabrication process has been developed and MOSFET with good electrical characteristics have been successfully embedded on cantilevers. Probes with a resolution of 180 pN for a bandwidth of 1 kHz have been obtained. Even though, the resolution is worse than piezoresistive cantilevers, it should be pointed out that the silicon thickness was not the optimal one in this case. According to this result, for similar spring constant and power consumption, the integration of MOSFET cantilever can represent a good alternative having 3 times higher resolution with respect to the piezoresistive cantilever.

Alongside the modeling and fabrication work, much job has been done in the characterization of the sensors. New set-ups and techniques have been developed in order to perform highly precise and high-throughput measurements of the noise and sensitivity characteristics. In view of the success of the project, this has been a very important point. It

has allowed extensive validation of the technological processes involved in production as well as the characterization of all the devices used in the biomolecular experiments. In particular, the integration of a probe-card into an AFM has allowed a fast and precise on-wafer sensitivity measurement and the use of a preamplifier and a spectrum analyzer with a probe-station have allowed a reliable on-wafer noise characterization. A sensitivity measurement can be performed in 2 minutes and a noise measurement can last from tenths of second to several minutes, depending on the requested precision. These new set ups have allowed the calibration of a considerable number of sensors in a relatively short time and directly on-wafer. This constitutes a definite improvement with the way these measurements have been done up to date, where the chip was normally pulled apart from the wafer, attached on a PCB board and wire bonded, which was a time consuming, risky and not robust processes. This characterization procedure offers also another advantage that is the selection of the sensors with better performance before the encapsulation.

During the last months of the experimental work, much effort has been put into the biorecognition experiments. This part of the thesis has been done in close collaboration with the research group of the Prof. Salvatore Cannistraro at Tuscia University, in which I have been hosted for 3 months. The piezoresistive force sensors have been mechanically and electronically integrated into a commercial PicoLe 5100 AFM to take advantage of the high mechanical stability of this equipment and the highly reliable displacement of the piezo actuator. To this purpose a new custom made probe holder has been designed and made for correct and robust positioning of the PCB, on which the sensor has been encapsulated. A substrate with very sharp tips has been microfabricated to allow the interaction of very small areas between the cantilever and the substrate. This fact is essential for single molecule biorecognition. Finally, we have successfully detected biorecognition specific events underlying the biotin-avidin complex formation. This result highlights the possibility of biomolecule label-free recognition in nearly physiological conditions and at single molecule resolution.

Perspectives

Alongside the text I pointed out some advices about improvement in the sensors and about future research directions on this topic:

- Improvement of the piezoresistive and noise properties of doped bulk silicon (or of MOSFET) in structures that are much easier to fabricate than cantilevers.
- Improvement of the electromechanical model considering the real concentration profile of the doping atoms. This would require also process simulations and related experiments.
- Fabrication of the chip metal interconnections by lift-off process, avoiding all the problems associated with the metal etching.

- Use a commercial HF vapor etcher to etch in a more uniform way the BOX.
- Fabrication of a tip on the cantilever.
- Use of low noise specifically designed on board amplifier, to reduce the electromagnetic external interference during the biomolecular experiments.
- Development of microfluidic systems for better functionalization and easier detection. This would be the first step towards a real biosensor based on the developed force sensors.
- Explore different and maybe easier detection schemes based on the same force measurement principle.

Appendices

Appendix A – Piezoresistive coefficients of MOSFETs

Author	Year	n-MOSFET			p-MOSFET			n-MOSFET <110>			p-MOSFET <110>			V_G [V]	$E_T \times 10^5$ [V]
		π_{11}	π_{12}	π_{44}	π_{11}	π_{12}	π_{44}	π_L	π_T	π_S	π_L	π_T	π_S		
Bulk silicon		-102	53	-14	7	-1	138	-31	-18	-49	72	-66	6		
Colman [1]	1968				-1	24	128								
Dorey [2]	1969				"half of Colman results"										
Dorda [3]	1970	-100	49	-11										1	
		-75	5	-26										25	
Dorda [4]	1972				-12	35								-1	
					6	30								-50	
Canali [5]	1979	-84	34	-18				-34	-19	-53				1	
		-67	0	-35				-50	-19					30	
					-13	28	104				60	-50	10	-1	
					-6	28					60	-45		-30	
Mikoshiba [6]	1980	-100	55	-10										1	
		-62	5	-40										16	
					-10	45	125							-1	
					-5	35	125							-7	
Zaima [7]	1989	-85	40	-15										2	
		-75	18	-22										16	

185

Author	Year	n-MOSFET			p-MOSFET			n-MOSFET $<110>$			p-MOSFET $<110>$			V_G [V]	$E_T \times 10^5$ [V]
		π_{11}	π_{12}	π_{44}	π_{11}	π_{12}	π_{44}	π_L	π_T	π_S	π_L	π_T	π_S		
Schoerner [8]	1990										43			2	1
											52			5	10
Wang [9]	1993	−90	40	−10											−1
		−75	5	−20											−10
					−15	30	115								
					0	28	110								
Bradley [10]	2001			−10						−80				IBM	
				−7						−57				Texas Instr.	
				−15						−85				Lucent Tech.	
							95						5	IBM	
							80						3	Texas Instr.	
							100						20	Lucent Tech.	
Gallon [11]	2004			−27				−49	−21	−70				Bulk Si	
				−27				−58	−31	−89				SOI	
							98				60	−38	22	Bulk Si	
							120				78	−42	35	SOI	

Author	Year	n-MOSFET			p-MOSFET			n-MOSFET <110>			p-MOSFET <110>			V_G [V]	$E_T \times 10^5$ [V]
		π_{11}	π_{12}	π_{44}	π_{11}	π_{12}	π_{44}	π_L	π_T	π_S	π_L	π_T	π_S		
Uchida [12]	2004	−93						−43							20
		−46						−50							100
					−19						71				−10
					−19						78				−80
Uchida [13]	2005	−86	38	−10											20
		−46	10												80
Vatedka [14]	2007							−30						0.5	
								−42						4.0	
Chang [15]	2009							−48	−30		77	−56			

References

1. Colman, D., R.T. Bate, and J.P. Mize, *Mobility anisotropy and piezoresistance in silicon p-type inversion layers.* Journal of Applied Physics, 1968. **39**(4): p. 1923-1931.
2. Dorey, A.P. and T.S. Maddern, *The effect of strain on MOS transistors.* Solid State Electronics, 1969. **12**(3): p. 185-189.
3. Dorda, G., *Piezoresistance in quantized conduction bands in silicon inversion layers.* Journal of Applied Physics, 1971. **42**(5): p. 2053-&.
4. Dorda, G., H. Friedrich, and E. Preuss, *Band Structure Investigation on p-Type Silicon Inversion Layers by Piezoresistance and Mobility Measurements.* Journal of Vacuum Science and Technology, 1972. **9**(2): p. 759-761.
5. Canali, C., et al., *Piezoresistivity effects in MOS-FET useful for pressure transducers.* Journal of Physics D-Applied Physics, 1979. **12**(11): p. 1973-1983.
6. Mikoshiba, H., *Stress-sensitive properties of silicon-gate MOS devices.* Solid State Electronics, 1981. **24**(3): p. 221-232.
7. Zaima, S., T. Maruyama, and Y. Yasuda, *Piezoresistance in n-channel inversion layers of Si MOSFET's.* Applied surface science, 1989. **41**: p. 433-438.
8. Schorner, R., *First and second order longitudinal piezoresistive coefficients of n-type metal-oxide-semiconductor field effect transistors.* Journal of Applied Physics, 1990. **67**(9): p. 4354-4357.
9. Wang, Z.Z., J. Suski, and D. Collard, *Piezoresistive simulation in MOSFETs.* Sensors and Actuators A: Physical, 1993. **37-38**: p. 357-364.
10. Bradley, A.T., et al., *Piezoresistive characteristics of short-channel MOSFETs on (100) silicon.* IEEE Transactions on Electron Devices, 2001. **48**(9): p. 2009-2015.
11. Gallon, C., et al., *Electrical analysis of external mechanical stress effects in short channel MOSFETs on (001) silicon.* Solid-State Electronics, 2004. **48**(4): p. 561-566.
12. Uchida, K., et al. *Experimental study of biaxial and uniaxial strain effects on carrier mobility in bulk and ultrathin-body SOI MOSFETs.* in *Electron Devices Meeting, 2004. IEDM Technical Digest. IEEE International*. 2004.
13. Uchida, K., et al. *Physical mechanisms of electron mobility enhancement in uniaxial stressed MOSFETs and impact of uniaxial stress engineering in ballistic regime*. in *Electron Devices Meeting, 2005. IEDM Technical Digest. IEEE International*. 2005.
14. Vatedka, R., et al., *Effect of high drain voltage on stress sensitivity in nMOSFETs.* Sensors and Actuators a-Physical, 2007. **140**(1): p. 89-93.
15. Chang, W.T. and J.A. Lin, *Piezoresistive coefficients of <1 1 0> silicon-on-insulator MOSFETs with 0.135/0.45/10 micrometers channel length with external forces.* Microelectronic Engineering, 2009. **86**: p. 1965-1968.

Appendix B – List of publications and participation in conferences

Peer reviewed articles

1. <u>G. Tosolini</u>, F. Scarponi, S. Cannistraro, and J. Bausells, "Biomolecule recognition using piezoresistive nanomechanical force probes," ***Applied Physics Letters,* vol. 102, 2013**, pp. 253701-253701-5. DOI: 10.1063/1.4812469.

2. <u>G. Tosolini</u>, L. G. Villanueva, F. Perez-Murano, and J. Bausells, "Fast on-wafer electrical, mechanical, and electromechanical characterization of piezoresistive cantilever force sensors," ***Review of Scientific Instruments,* vol. 83, 2012,** pp. 015002-015002-7. DOI: 10.1063/1.3673603.

3. <u>G. Tosolini</u>, G. Villanueva, F. Perez-Murano, and J. Bausells, "Silicon microcantilevers with MOSFET detection," ***Microelectronic Engineering,* vol. 87, 2010,** pp. 428-431. DOI: 10.1016/j.mee.2009.11.125.

Conference proceedings

1. <u>G. Tosolini</u>, L. G. Villanueva, F. Perez-Murano, and J. Bausells, "A novel high-throughput on-wafer electromechanical sensitivity characterization system for piezoresistive cantilevers," in ***IEEE International Conference on Microelectronic Test Structures,* 2012**, pp. 55-60. DOI: 10.1109/ICMTS.2012.6190613.

2. <u>G. Tosolini</u>, and L. G. Villanueva, F. Perez-Murano, J. Bausells, "Self sensing cantilevers for the measurement of (biomolecular) forces," in ***Electron Devices (CDE), 2011 Spanish Conference on,* 2011**, pp. 1-4. DOI: 10.1109/SCED.2011.5744171.

3. <u>G. Tosolini</u>, G. Villanueva, and J. Bausells, "Silicon Microcantilevers with Piezoresistive and MOSFET Detection," ***Proceedings of the 2009 Spanish Conference on Electron Devices,*** pp. 428-431, 2009. DOI: 10.1109/SCED.2009.4800525.

Attendance at conferences

1. <u>G. Tosolini</u>, F. Scarponi, S. Cannistraro, and J. Bausells, "Piezoresistive nanomechanical force probe in single biomolecule recognition". **Poster presentation** at the International Workshop on Nanomechanical Sensing (NMC). 1-3 May 2013, Stanford, USA.

2. <u>G. Tosolini</u>, J. M. Michalik, R. Cordoba, J. M. de Teresa, F. Perez-Murano, J. Bausells, "Magnetic properties of cobalt micro-wires measured by piezoresistive cantilever magnetometry". **Poster presentation** at the International Conference on Micro and Nano Engineering (MNE). 16-20 September 2012, Toulouse, France.

3. <u>G. Tosolini</u>, and L. G. Villanueva, F. Perez-Murano, J. Bausells, "A novel high-throughput on-wafer electromechanical sensitivity characterization system for

piezoresistive cantilevers". **Oral presentation** at the International Conference on Microelectronic Test Structures (ICMTS). 19-22 March 2012, San Diego, USA.

4. <u>G. Tosolini</u>, and L. G. Villanueva, F. Perez-Murano, J. Bausells, "Fast and reliable on-wafer electromechanical characterization technique for piezoresistive cantilevers". **Poster presentation** at International Workshop on Nanomechanical Sensing (NMC). 11-13 May 2011, Dublin, Ireland.

5. <u>G. Tosolini</u>, and L. G. Villanueva, F. Perez-Murano, J. Bausells, "Self Sensing Cantilevers for the Measurement of (biomolecular) Forces". **Oral presentation** at Spanish conference on electron devices (CDE). 8-11 February 2011, Palma de Mallorca, Spain.

6. <u>G. Tosolini</u>, and L. G. Villanueva, F. Perez-Murano, J. Bausells, "Optimization of piezoresistive and MOSFET cantilever for measuring forces". **Oral presentation** at Fuerzas y Tunel Conference. 27-29 September 2010, Tarragona, Spain.

7. <u>G. Tosolini</u>, and L. G. Villanueva, F. Perez-Murano, J. Bausells, "Silicon microcantilever with MOSFET detection". **Poster presentation** at International Conference on Micro and Nano Engineering (MNE). 28 September – 1 October 2009, Ghent, Belgium.

8. <u>G. Tosolini</u>, G. Villanueva, and J. Bausells, "Silicon microcantilevers with piezoresistive and MOSFET detection". **Oral presentation** at Spanish Conference on Electron Devices (CDE). 11-13 February 2009, Santiago de Compostela, Spain.